



Title	Construction of Metal-organic Frameworks Based Materials for Visible Light Photocatalysis
Author(s)	史, 力
Citation	北海道大学. 博士(理学) 甲第12916号
Issue Date	2017-09-25
DOI	10.14943/doctoral.k12916
Doc URL	<a href="http://hdl.handle.net/2115/67436">http://hdl.handle.net/2115/67436</a>
Type	theses (doctoral)
File Information	Li_Shi.pdf



[Instructions for use](#)

# **Construction of Metal-organic Frameworks Based Materials for Visible Light Photocatalysis**

(可視光応答型金属有機構造体の創成と光触媒特性に関する研究)

Li Shi

Functional Materials Chemistry Unit

Graduate School of Chemical Sciences and Engineering

Hokkaido University

2017

# Contents

---

## Contents

<b>Contents</b>	I
<b>Abstract</b>	1
<b>Chapter 1 Introduction</b>	4
1.1 General introduction	4
1.2 Rational design of MOFs based photocatalysts	7
1.3 The applications of MOFs based photocatalysts	10
1.3.1 MOFs based photocatalysts for degradation of organic molecules	10
1.3.2 MOFs based photocatalysts for hydrogen evolution	13
1.3.3 MOFs based photocatalysts for water oxidation	15
1.3.4 MOFs based photocatalysts for CO <sub>2</sub> reduction	17
1.3.5 MOFs based photocatalysts for Cr(VI) reduction	20
1.4 Modification of MOFs based photocatalysts for superior performances	22
1.4.1 Organic linkers or metal clusters modulations	22
1.4.2 Dye sensitization	25
1.4.3 Heterojunction construction	26
1.5 Research motivation and thesis organization	29
References	32
<b>Chapter 2 Construction of an amine-functionalized iron(III) metal-organic framework as efficient visible-light photocatalyst for Cr(VI) reduction</b>	37
2.1 Introduction	37
2.2 Experimental section	40
2.2.1 Materials	40
2.2.2 Synthesis of photocatalysts	40
2.2.3 Characterization	41
2.2.4 Photoelectrochemical Measurement	41
2.2.5 Photocatalytic experiments	42
2.3 Results and discussion	42

# Contents

---

2.3.1 Characterization of MOF photocatalysts	42
2.3.2 Evaluation of photocatalytic activity	45
2.3.3 Clarification of the mechanism	51
2.4 Conclusion	60
References	60
<b>Chapter 3 Construction of nano-sized g-C<sub>3</sub>N<sub>4</sub> nanosheet/UiO-66 composite photocatalyst for enhanced photocatalytic CO<sub>2</sub> Reduction</b>	<b>65</b>
3.1 Introduction	65
3.2 Experimental section	67
3.2.1 Materials	67
3.2.2 Preparation of photocatalysts	67
3.2.3 Characterization	68
3.2.4 Photocatalytic experiments	69
3.3 Results and discussion	69
3.3.1 Characterization of photocatalysts	69
3.3.2 CO <sub>2</sub> adsorption and electron transfer behaviors	77
3.3.3 Evaluation of photocatalytic activity	80
3.3.4 Clarification of the mechanism	82
3.4 Conclusion	85
References	86
<b>Chapter 4 Implantation of Iron(III) in Porphyrinic Metal Organic Frameworks for Highly Improved Photocatalytic Performance</b>	<b>88</b>
4.1 Introduction	88
4.2 Experimental section	90
4.2.1 Synthesis of photocatalysts	90
4.2.2 Characterization	92
4.2.3 Photoelectrochemical Measurement	92
4.2.4 The measurement of H <sub>2</sub> O <sub>2</sub>	93
4.2.5 Photocatalytic experiments	93
4.3 Results and discussion	94
4.3.1 Characterization of photocatalysts	94

# Contents

---

4.3.2 Photocatalytic performance	102
4.3.3 Mechanism investigation	108
4.4 Conclusion	117
References	118
<b>Chapter 5 Boosting charge separation <i>via</i> single cobalt atom implantation in MOFs for efficient visible-light driven CO<sub>2</sub> reduction</b>	121
5.1 Introduction	121
5.2 Experimental section	123
5.2.1 Materials	123
5.2.2 Synthesis of MOF-525	123
5.2.3 Postmetalation of MOF-525 to form MOF-525-Co and MOF-525-Zn	123
5.2.4 Characterization	123
5.2.5 Photocatalytic Experiments	124
5.2.6 X-ray absorption data collection, analysis, and modelling	124
5.2.7 Photoelectrochemical measurements	125
5.2.8 Computational methods	125
5.3 Results and discussion	126
5.3.1 Characterization of photocatalysts	126
5.3.2 Photocatalytic CO <sub>2</sub> reduction	134
5.3.3 Clarification of mechanism	139
5.4 Conclusion	144
References	145
<b>Chapter 6 General conclusions and future prospects</b>	148
6.1 General conclusions	148
6.2 Future prospects	150
<b>Acknowledgement</b>	153

# Abstract

---

## Abstract

Metal-organic frameworks (MOFs) have received much research interest in the field of photocatalysis because of their advantages, such as high surface area, visible light absorption, tunable electronic structure, etc. However, due to the fast electron-hole recombination rate and the low light absorption capability, the photocatalytic performances of the MOFs based photocatalysts are still moderate. In this thesis, the research object is to construct efficient MOFs based photocatalysts to explore their potential applications as well as understand the corresponding mechanism of photocatalysis. Three strategies, including amine functionalization, heterojunction fabrication and metal ions implantation, were proposed to enhance the photocatalytic performances of the MOFs based photocatalysts.

In chapter 1, a general background of photocatalysis and photocatalytic materials is introduced. Then the recent development of the MOFs based photocatalysts is also introduced.

In chapter 2, an iron(III) MOF based photocatalyst, named as MIL-88B (Fe), was constructed and explored for photocatalytic Cr(VI) reduction under visible light. An organic ligand modification strategy, namely amine functionalization, was demonstrated to be effective for enlarging the light absorption and improving the carrier separation and transfer efficiency of MIL-88B (Fe). It was found that in addition to the direct excitation of  $\text{Fe}_3\text{-}\mu_3\text{-oxo}$  clusters in MIL-88B (Fe), the amine functionalized organic linker could also be excited and then transferred an electron to  $\text{Fe}_3\text{-}\mu_3\text{-oxo}$  clusters to reduce Cr(VI). As a result, the amine functionalized MIL-88B (Fe) showed much enhanced photocatalytic activity for Cr(VI) reduction than bare MIL-88B (Fe).

In chapter 3, a MOF based heterostructure photocatalyst that composed of a zirconium MOF (UiO-66) and g- $\text{C}_3\text{N}_4$  nanosheet (CNNS) was constructed for photocatalytic  $\text{CO}_2$  reduction under visible light. Due to the well match of the energy level between UiO-66 and CNNS, a heterojunction structure in UiO-66/CNNS hybrid photocatalyst could be formed. As evidenced by the quenching of the

## Abstract

---

photoluminescence intensity and increase of fluorescence lifetime in UiO-66/CNNS compared with bare CNNS, the electrons from photoexcited CNNS could transfer to UiO-66. Such electron transfer could substantially suppress the electron-hole pairs recombination in the CNNS, and also supply long-lived electrons for the reduction of CO<sub>2</sub> molecules adsorbed in UiO-66. As a result, the UiO-66/CNNS heterostructure photocatalyst exhibited a CO yield of 59.4 μmol g<sub>CN</sub><sup>-1</sup> after visible light illumination for 6 hours, which was 3.4-fold higher than that of CNNS.

In chapter 4, a porphyrinic MOF, named as PCN-224, was employed as a visible-light-active photocatalyst for isopropanol (IPA) oxidation. Coordinatively unsaturated Fe(III) ions were implanted into porphyrin units and a new hybrid structure Fe@PCN-224 was constructed. The implantation of coordinatively unsaturated Fe(III) sites into the porphyrin units of PCN-224 could not only greatly boost the electron-hole separation efficiency, but also construct a Fenton reaction to convert the *in situ* photogenerated H<sub>2</sub>O<sub>2</sub> into active oxygen-related radicals ( $\cdot\text{OH}$  and  $\cdot\text{O}_2^-$ ) during the photocatalytic IPA oxidation reaction. As a result, the newly developed Fe@PCN-224 exhibited significantly enhanced photocatalytic activity, which was equivalent to an 8.9-fold improvement in acetone evolution rate and 9.3-fold enhancement in CO<sub>2</sub> generation rate compared with the PCN-224.

In chapter 5, a porphyrinic MOF, named as MOF-525, was constructed for photocatalytic CO<sub>2</sub> reduction under visible light. The modular optimization of MOF-525 was realized by incorporation of coordinatively unsaturated single cobalt atom into its matrix. The presence of single cobalt atom in the MOF-525 could greatly boost the electron-hole separation efficiency in porphyrin units. Directional migration of photogenerated exciton from porphyrin to catalytic cobalt centers was witnessed, and thus achieved the long-lived electrons for the reduction of CO<sub>2</sub> molecules that were adsorbed on cobalt centers. As a result, MOF-525 comprising atomically dispersed catalytic centers exhibited significantly enhanced photocatalytic conversion of CO<sub>2</sub>, which was equivalent to a 3.1-fold improvement in CO evolution rate (200.6 μmol g<sup>-1</sup>h<sup>-1</sup>) and 5.9-fold enhancement in CH<sub>4</sub> generation rate (36.7 μmol g<sup>-1</sup>h<sup>-1</sup>) compared with bare MOF-525.

## Abstract

---

In chapter 6, an overall summary of this dissertation work was provided. This thesis carried out a systematic study on the construction of efficient MOFs based photocatalysts for visible light photocatalytic reactions, including Cr(VI) reduction, CO<sub>2</sub> reduction and IPA oxidation. Organic ligand modification, heterojunction fabrication and metal ion implantation were proved to be effective strategies to improve the photocatalytic efficiencies of the constructed MOFs based photocatalysts. The findings in this study present some potential applications of MOFs based materials, aid to understand the mechanism of photocatalysis, and more importantly, highlight some universal design principles to the efficient MOFs based photocatalysis.

## Chapter 1 Introduction

### 1.1 General introduction

Nowadays, energy shortages have raised awareness of potential global crisis. Solar energy is regarded as an important energy source for the sustainable development of society, economy and environment. The search for the advanced techniques of converting solar energy to chemical energy that is easy to use, transport and store is indispensable for the wide utilization of solar energy. Semiconductor photocatalysis provides an environmentally friendly approach for the solar-to-chemical energy conversion by mimicking photosynthesis in nature and thus has been considered as one of the most promising solution for counteracting the energy shortage and realizing environmental remediation.<sup>1-4</sup> The potential applications of photocatalysis can be found in the four main fields: (1) photo-splitting of water to produce H<sub>2</sub> and O<sub>2</sub>; (2) photo-reduction of CO<sub>2</sub>; (3) photo-decomposition of organic pollutant or photo-reduction of inorganic hazardous substances; (4) photo-electrochemical conversion, etc.<sup>5-8</sup>

Generally, the process of photocatalytic reactions comprises three steps, as shown in Figure 1.1.<sup>4</sup> Firstly, the photocatalyst is excited by light of energy greater than its bandgap to induce a transition of electrons from the valence band (VB) to the conduction band (CB), leaving an equal number of holes. This stage is referred to the “photo-excited state” of semiconductors. Secondly, the photogenerated electrons and holes will partially recombine in the semiconductors and the rest will migrate to the surface of the semiconductors. Thirdly, the electrons and holes on the surface will react with the electron acceptors (A) and the electron donors (D), respectively.

# Chapter 1

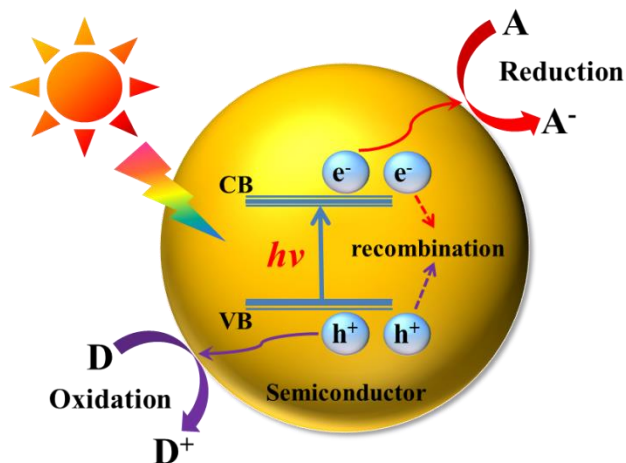


Figure 1.1 Schematic illustration of photocatalytic process.

The search for suitable materials as photocatalysts has dominated the study of photocatalysis in history. According to the photocatalytic principles, a photocatalyst must own suitable positions of valence band and conduction band to involve oxidation and reduction reactions simultaneously. Specifically, for a semiconductor to be a photocatalyst to split water, the bottom level of the conduction band has to be more negative than the redox potential of  $H^+/H_2$  (0 V vs. NHE, pH 0), while the top level of the valence band has to be more positive than the redox potential of  $O_2/H_2O$  (1.23 V vs. NHE, pH 0).<sup>1</sup> Besides the suitable positions of valence and conduction band, the bandgap of a semiconductor that determines the light absorption range is another important factor to be considered for seeking novel photocatalysts. It is worth noting that the bandgap of a photocatalyst should be small to absorb visible light as much as possible to achieve high solar energy conversion efficiency, since visible light contributes about 50% of solar radiation.<sup>9</sup> However, a small bandgap of photocatalyst as a result of a low conduction band position and/or a high valence band position would lead to a weak driving force for the transfer of charge carriers between a semiconductor and a redox couple, which would result in low photocatalytic efficiency. Therefore, there is a compromise between the bandgap and the desired properties of charge carriers for seeking novel photocatalysts. What is more, an ideal photocatalyst should also be low-cost, highly stable and environmentally friendly.<sup>4</sup>

# Chapter 1

---

The discovery of photoelectrochemical water splitting on TiO<sub>2</sub> electrode by Fujishima and Honda in 1972 has been regarded as the landmark event that opened the investigations of solar-to-chemical energy conversion by photocatalytic process.<sup>10</sup> Since then, intense research about the photocatalysis has been carried out on TiO<sub>2</sub> semiconductor material, because of its many outstanding characteristics, such as excellent stability, nontoxicity and high photocatalytic activities.<sup>11-13</sup> The research about the TiO<sub>2</sub> photocatalysis has been mainly focused on the investigation of the photocatalytic mechanism, improving the photocatalytic efficiency and enlarging the application area.<sup>14-16</sup> However, TiO<sub>2</sub> can only absorb the UV light occupying no more than 5% in solar light because of its large bandgap (3-3.2 eV), leading to a photoconversion efficiency of less than 2.2% under (AM) 1.5 solar illumination, far from the satisfaction in practical applications. In this context, over the past decades, great efforts have been devoted to make the TiO<sub>2</sub> based photocatalyst active under visible light. One of the most useful strategies is to narrow the bandgap of TiO<sub>2</sub> photocatalyst by substitutional doping with metal species (Fe, Co, Cu, Mn, *et al.*)<sup>17-20</sup> or with nonmetal elements (P, S, N, *et al.*)<sup>21-23</sup>. The foreign elemental doping into TiO<sub>2</sub> can introduce impurity levels (either a donor level above the original valence band or an acceptor level below the original conduction band) in the forbidden band to narrow the bandgap and to make the TiO<sub>2</sub> photocatalyst respond to visible light. In addition to TiO<sub>2</sub> based photocatalysts, many photocatalysts have also been investigated, even without using above modification technology (elemental doping). To date, most of the reported photocatalysts are based on metal oxides, phosphate, vanadate, sulfide, nitride or oxynitride semiconductors consisting of metal cations with d<sup>0</sup> (W, V, Nb, Ta, Mo, *et al.*) or d<sup>10</sup> (Cu, Ag, Zn, Cd, Ga, In, *et al.*) electronic configurations.<sup>1, 24-34</sup>

Recent research on new photocatalytic materials, either semiconductor or not, has delivered a number of possible substitutes. Metal organic frameworks (MOFs) based photocatalyst is one of novel and unconventional photocatalytic material that have received much research interest.<sup>35-38</sup> For inorganic semiconductor photocatalysts, when they are excited by light of energy greater than their bandgaps, the electrons will move to the conduction band (CB) and an equal number of holes will be left on the valence band (VB) which reacts with the adsorbed reactant separately. The MOFs based photocatalysts can be

# Chapter 1

---

considered to undergo a similar reaction process as inorganic semiconductors but the energy level is described as the highest occupied molecular orbital (HOMO) and the lowest unoccupied molecular orbital (LUMO).<sup>37</sup> MOFs are a class of hybrid porous materials composed of metal-oxo clusters and organic building blocks. Compared with the traditional photocatalysts, the superiority of MOFs is based on their desirable topology and high surface area, which is beneficial for fast transport and good accommodation of guest molecules.<sup>36</sup> Moreover, the band gap of MOFs is closely related to the HOMO-LUMO gap, which may be flexibly tuned through rational modification of the inorganic unit or the organic linker during synthetic procedures, thus the efficient light harvesting can be realized.<sup>38</sup> Importantly, MOFs also offer the opportunity to integrate both light-harvesting and catalytic components in a single solid platform to enable the conversion of solar energy to chemical energy *via* artificial photosynthesis. Therefore, the MOFs based photocatalysts have been regarded as promising materials that offers new opportunities in the field of artificial photosynthesis.

## 1.2 Rational design of MOFs based photocatalysts

MOFs are class of crystalline materials that are constructed from well-defined molecular building blocks and metal or metal-cluster connecting nodes. The synthetic methodology of MOFs generally consists of mixing two solutions containing the hydrophilic metal and the hydrophobic organic component (organic linker), using hydrothermal or solvothermal techniques. A key structural feature of MOFs is the ultrahigh porosity (up to 90% free volume) and incredibly high internal surface areas, extending beyond a Langmuir surface area of  $10000 \text{ m}^2 \text{ g}^{-1}$ , which play a crucial role in functional applications.<sup>39</sup> One of the most distinct applications of MOFs based materials is photocatalysis. MOFs based materials have been proposed as potential photocatalysts since the late 1990's and the early 2000's.<sup>35</sup> Some MOFs based materials are believed to be analogous to inorganic semiconductors, because they exhibit a broad UV-vis absorption with an edge falling into the range of typical semiconductor band gap values, although the structures of MOFs are formed by linking bridging ligands and metal connecting nodes that are different from inorganic semiconductors. However, the optical absorption properties of

# Chapter 1

MOFs cannot be taken as strong evidence to support the description of MOFs as semiconductors, as such an absorption band in MOFs can also be assigned to a metal-to-ligand charge transfer (MLCT) transition or a localized ligand-to-metal charge transfer (LMCT) or a  $\pi-\pi^*$  transition of the aromatic ligand. For most MOFs, the charge separation over a long distance will not be observed upon excitation because of their insulating nature, although they exhibit typical semiconductor-like optical transition. Therefore, to design MOFs based materials as efficient photocatalysts, their charge mobility and electronic conductivity should be carefully considered. Moreover, the poor stability of MOFs derived from the reversible nature of coordination bonds is commonly regarded as the major drawback for their practical applications. The stability issue of MOFs should be specially considered in practical photocatalytic applications. As a MOFs based photocatalyst, it should be stable in photocatalytic reaction system. Recently, the explored MOFs based photocatalysts are mainly focused on three types of MOFs, namely Zr, Fe and Ti based MOFs (Table 1.1).<sup>40-47</sup>

Table 1.1. Some typical Zr, Fe and Ti based MOFs photocatalysts and their applications.

	Structure	Photocatalytic applications	reference
Zr based MOFs photocatalysts	NH <sub>2</sub> -UiO-66	oxidation of organic compounds	45
	PCN-222	CO <sub>2</sub> reduction	43
	UiO-67	trifluoroethylation of styrenes	42
	UiO-66 (AN)	degradation of methyl orange	47
Fe based MOFs photocatalysts	MIL-53	decolorization of methylene blue	44
	MIL-100	benzene hydroxylation to phenol	40
	MIL-68	benzene hydroxylation to phenol	40
Ti based MOFs photocatalysts	NH <sub>2</sub> -MIL-125	oxidation of amine to imine	46

A Zr based MOF,  $Zr_6(\mu_3-O)_4(\mu_3-OH)_4(BDC)_6$  (UiO-66, UiO stands for the University of Oslo) with 12-coordinated  $Zr_6(\mu_3-O)_4(\mu_3-OH)_4(CO_2)_{12}$  clusters was firstly discovered by Cavka *et al.*<sup>48</sup> The structure

# Chapter 1

---

of UiO-66 exhibits unprecedented stability, especially hydrothermal stability beyond most reported MOFs. From then on, the discovery of MOFs based on Zr(IV) ions (Zr based MOFs), mostly Zr(IV) carboxylates, has emerged, such as MOF-808 and PCN-56.<sup>49, 50</sup> Moreover, diverse strategies have been adopted to modify their structures and properties, and various functions and applications being explored. Due to the high stability, the research about the Zr based MOFs for application of catalysis has received much interest. Among these zirconium based MOFs, UiO-66 has been extensively studied for the applications of photocatalysis, due to its semiconducting properties and much higher stability.

In addition to the Zr based MOFs, another high-valence metal ion, such as Fe<sup>3+</sup>, has also been exploited to synthesize water stable MOFs. A series of Fe based MOFs structured as MILs (MIL for materials of institute Lavoisier), such as MIL-100, MIL-88B, MIL-53, and MIL-101 have been successfully synthesized.<sup>51-53</sup> The structure of MIL-100(Fe) was firstly determined by Horcajada et al., which showed the formula of Fe<sub>3</sub>F(H<sub>2</sub>O)<sub>2</sub>-O(btc)<sub>2</sub> (1,3,5-btc = benzene tricarboxylic or trimesic acid), and possessed two types of mesoporous cages of free apertures of *ca.* 25 and 29 Å, respectively.<sup>52</sup> The permanent porosity of this porous solid was measured by N<sub>2</sub> adsorption experiments performed in liquid nitrogen, revealing an adsorption isotherm characteristic of microporosity. The thermal stability of MIL-100(Fe) has been determined by X-ray thermodiffraction to be up to 270 °C. Other types of Fe based MOFs (MIL-88B, MIL-53 and MIL-101) are all constructed from Fe<sup>III</sup> and bdc organic linker (bdc=1,4-benzenedicarboxylic acid or terephthalic acid) but have different structures. In the MIL-88B and MIL-53 frameworks, the Fe<sup>III</sup> analogue of MIL-53, chains of FeO<sub>6</sub> octahedra are connected by benzenedicarboxylate anions. Thus, rhomb-shaped one-dimensional (1D) channels are formed that run along the *a* axis of the structure. The hexagonal 3D structure of MIL-88B is built up from trimers of FeO<sub>6</sub> octahedra linked to benzenedicarboxylate anions. Thus, the 3D pore system of MIL-88B consists of tunnels along the *c* axis connected by bipyramidal cages.<sup>54</sup> The structure of MIL-101(Fe) shows formula of Fe<sub>3</sub>-(μ<sub>3</sub>-O)Cl(H<sub>2</sub>O)<sub>2</sub>(BDC)<sub>3</sub> and this hybrid solid is built up from super tetrahedral building units,

# Chapter 1

---

which are formed by rigid terephthalate ligands and Fe(III) octahedral clusters.<sup>55</sup> Recently, the application of these Fe based MOFs as photocatalyst has emerged.

Ti based MOFs structured as MIL-125 has also been used as an efficient photocatalyst. The synthetic procedure of MIL-125 (Ti) was firstly reported by Meenakshi Dan-Hardi in 2009, using an appropriate choice of solvent mixtures (dimethylformamide (DMF) and methanol) and titanium tetraisopropoxide at 150°C, and a well crystallized white hybrid solid denoted MIL-125 or  $\text{Ti}_8\text{O}_8(\text{OH})_4(\text{O}_2\text{C}-\text{C}_6\text{H}_4-\text{CO}_2)_6$ , could be isolated.<sup>56</sup> The MIL-125 (Ti) has good stability, and rehydration at 300 K does not change the X-ray powder pattern. MIL-125 (Ti) is also thermally robust, and is resistant to change in crystallinity up to 290°C. Interestingly, MIL-125 (Ti) exhibits a reversible photochromic behavior induced by alcohol adsorption. UV-visible irradiation can promote the formation of a Ti(III)-Ti(IV) mixed valence in MIL-125, and simultaneously oxidize the adsorbed alcohol molecules. MIL-125(Ti) also shows semiconductor properties and owns a charge mobility of  $\sim 10^{-5} \text{ cm}^2 \text{ V}^{-1} \text{ s}^{-1}$  upon 340 nm light illumination.<sup>57</sup> Its high photonic sensitivity and charge mobility, offer ample scope for new microporous hybrid solids capable of fitting applications in photocatalysis.

## 1.3 The applications of MOFs based photocatalysts

### 1.3.1 MOFs based photocatalysts for degradation of organic molecules

Photocatalytic degradation of organic pollutants is one of the intensely studied topics in environmental science. Some reports demonstrated that MOFs based materials can be used as photocatalysts for decomposing organic dye molecules that are used as surrogates for organic pollutants. Based on the richness of organic bridging linkers and the controllability of the synthesis, it is easy to construct MOFs with tailorable capacity to absorb visible light, thereby initiating desirable photocatalytic reactions for specific applications in the degradation of organic dye molecules. In 2015, Pu *et al.* reported a new UiO-66-type Zr based MOFs material UiO-66(AN) that was prepared by using chromophoric anthracene-9,10-dicarboxylic acid as linker.<sup>47</sup> The large-sized conjugate  $\pi$ -system in the ligand results in the bathochromic shift of the absorption peaks into the visible light region in the absorption spectrum of

# Chapter 1

---

UiO-66(AN), compared to those of UiO-66 made of terephthalate linker. It was found that UiO-66(AN) was shown to be an efficient photocatalyst for degradation of methyl orange under visible light. This finding shows promises for the development of more efficient MOFs as photocatalysts by using chromophoric conjugate ligands.

Fe based MOFs have also been used as photocatalysts for photocatalytic degradation of organic pollutants. In 2013, Laurier and coworkers firstly reported the photocatalytic reactions of Fe based MOFs under visible light.<sup>58</sup> The Fe based MOFs that consist of  $\text{Fe}_3\text{-}\mu_3\text{-oxo}$  clusters, such as MIL-100, MIL-88B, and MIL-101, could be used as photocatalysts for photocatalytic degradation of an organic dye (Rhodamine 6G) in an aqueous solution under visible light illumination. The highest overall visible light photocatalytic activity was measured for the Fe based MOF structured as MIL-88B. MIL-88B is composed of  $\text{Fe}_3\text{-}\mu_3\text{-oxo}$  clusters interconnected by oxidation-stable terephthalate linkers resulting in a 3D network. Since the linker does not absorb any visible light, the  $\text{Fe}_3\text{-}\mu_3\text{-oxo}$  cluster in the MOF is responsible for the visible light absorption and the associated photocatalytic activity. Further studies indicated that the organic linker and the framework topology of the Fe based MOFs determine the overall photocatalytic activity. The diffractograms study indicated that the crystallinity of these Fe based MOFs was reasonably maintained after photocatalytic reactions, resulting in the assumption of a stable structure. Ai *et al.* also reported the photocatalytic reactions of a Fe based MOF, MIL-53.<sup>59</sup> They demonstrate that an iron terephthalate MOF MIL-53 synthesized by a facile solvothermal reaction was capable of activating hydrogen peroxide ( $\text{H}_2\text{O}_2$ ) to achieve high efficiency in photocatalytic process. It could completely decompose the  $10 \text{ mg L}^{-1}$  Rhodamine B (RhB) in the presence of a certain amount of  $\text{H}_2\text{O}_2$  under visible light irradiation within 50 min. The reusability test shows that the performance of MIL-53 photocatalyst remains almost unchanged after three recycles, as shown in Figure 1.2a. The catalytic activities were found to be strongly affected by the various operating parameters, such as solution pH, initial dye concentration, and  $\text{H}_2\text{O}_2$  dosage. Interestingly, catalytic degradation of RhB proceeded about 4.3- and 4.6-fold faster in the MIL-53/visible light/ $\text{H}_2\text{O}_2$  system relative to the MIL-53/visible light system and MIL-53/ $\text{H}_2\text{O}_2$  system, respectively. This enhanced catalytic activity was considered to be

# Chapter 1

arisen from the synergistic effects by combination of MIL-53 and  $\text{H}_2\text{O}_2$  under visible light irradiation, which was confirmed by the results of detection of hydroxyl radicals ( $\cdot\text{OH}$ ) and transient photocurrent responses (Figure 1.2b). The ability of such iron-based MOFs to activate  $\text{H}_2\text{O}_2$  may enable rational design of advanced MOF-based catalysts for environmental remediation.

A Ti based MOF,  $\text{Ti}_2(\text{Hdhbdc})_2(\text{H}_2\text{dhbdc})$  (NTU-9,  $\text{H}_4\text{dhbdc} = 2,5$ -dihydroxyterephthalic acid), was also reported recently as an active photocatalyst for dye degradation.<sup>60</sup> NTU-9 was obtained as red and its absorption reaches up to 750 nm (Figure 1.3c). NTU-9 was proved to be a semiconductor with p-type conductivity. NTU-9 showed good photocatalytic activity in the degradation of rhodamine B (RB) in aqueous solution under visible light irradiation ( $\lambda > 420$  nm). Photodegradation of RB was complete after 80 min. During the 6 h testing period, NTU-9 exhibited persistent high photoactivity and good photostability (Figure 1.2d). This study presents a novel MOFs photocatalyst, and suggests that Ti based MOFs could be promising candidates for the development of efficient visible light photocatalysts.

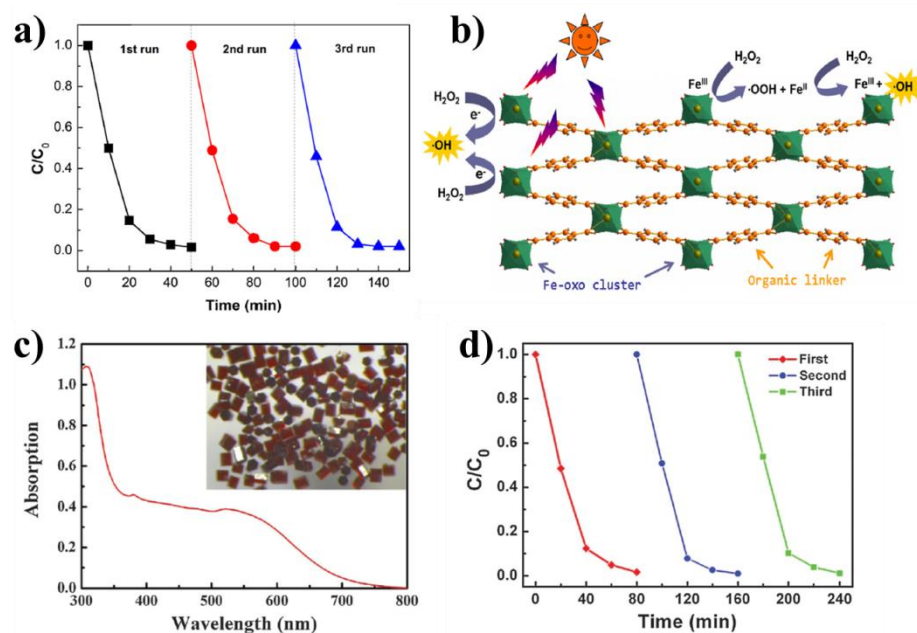


Figure 1.2 (a) The cycling runs of the degradation of RhB ( $10 \text{ mg L}^{-1}$ ) over MIL-53(Fe)/visible light/ $\text{H}_2\text{O}_2$  system. (b) Proposed mechanism for the activation of  $\text{H}_2\text{O}_2$  by MIL-53(Fe) under visible light irradiation.<sup>59</sup> (c) Diffuse reflectance spectra of NTU-9. (d) Recycling test on NTU-9 for photo-degradation of RB under visible light irradiation ( $\lambda > 420$  nm).<sup>60</sup>

## 1.3.2 MOFs based photocatalysts for hydrogen evolution

H<sub>2</sub> becomes a significant energy source in the upcoming years, by virtue of its clean combustion characteristics in energy conversion. The production of H<sub>2</sub> fuels by using sunlight is an attractive and sustainable solution to the global energy and environmental problem. Various MOFs based photocatalysts have been developed in the past decades for hydrogen evolution reactions. In 2010, Silva and co-workers used highly stable Zr based MOFs (UiO-66) for water reduction.<sup>61</sup> Mott-Schottky plots reveal an n-type semiconductor feature of UiO-66, and confirmed the conduction band of UiO-66 is estimated to be ~0.6 V vs NHE, which is negative to the redox potential of H<sup>+</sup>/H<sub>2</sub> (~0.41 V vs NHE at pH = 7), conforming the possibility of UiO-66 for H<sub>2</sub> production. The MOF-catalyzed hydrogen generation was evaluated with a UV irradiation (>300 nm) and methanol as the sacrificial electron donor. Laser-flash photolysis has allowed detecting for UiO-66 the photochemical generation of a long lived charge separated state whose decay is not complete 300 ms after the laser flash. In this case, UiO-66 has been used both as photosensitizers and as catalysts for proton reduction reaction with sacrificial reductants. Moreover, they showed that this photocatalytic activity can be increased by rational design of the material via amino group introduction and by adding Pt as hydrogen evolution co-catalyst. This study indicates that the influence of the amino group producing a bathochromic shift in the optical spectrum shows promises for the development of more efficient MOFs for water splitting.

In addition to the Zr based MOFs photocatalysts, Ti based MOFs photocatalysts can also be used for photocatalytic H<sub>2</sub> evolution. In 2012, Yu Horiuchi and co-workers reported the hydrogen production from an aqueous medium over Pt loaded amino-functionalized Ti(IV) metal-organic framework (Ti-MOF-NH<sub>2</sub>) under visible-light irradiation.<sup>62</sup> The XRD patterns show that Ti-MOF-NH<sub>2</sub> and Pt/Ti-MOF-NH<sub>2</sub> exhibit MIL-125 structure. The UV-vis spectra demonstrate that Ti-MOF-NH<sub>2</sub>, containing BDC-NH<sub>2</sub> units as the organic linker, is a visible-light absorbing MOF. Mechanism study indicates that the photocatalytic hydrogen production reactions using Pt/Ti-MOF-NH<sub>2</sub> and Ti-MOF-NH<sub>2</sub> proceed through a pathway involving light absorption by the BDC-NH<sub>2</sub> chromophore and subsequent efficient electron

# Chapter 1

transfer to the titanium-oxo cluster. The observations made in this investigation should offer new insight into the design of efficient visible light active MOFs based photocatalysts.

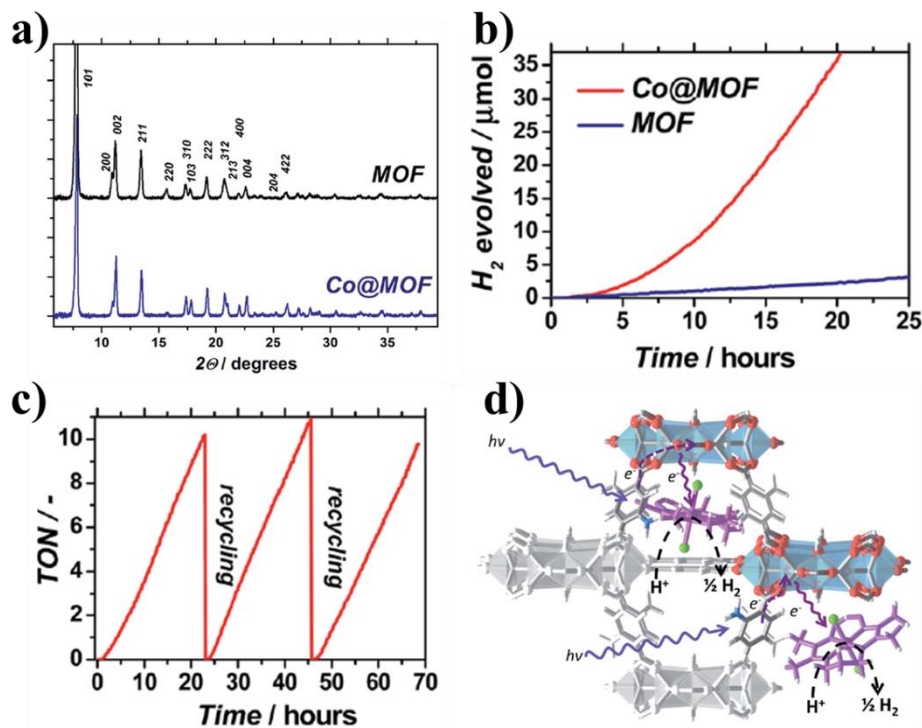


Figure 1.3 (a) Powder X-ray diffraction patterns of pristine NH<sub>2</sub>-MIL-125(Ti) (black) and Co@MOF (blue). (b) Photocatalytic proton reduction using MOF and Co@MOF. (c) Recycling tests on Co@MOF bearing medium cobalt loading. Conditions: 5 mg catalyst, 5 mL CH<sub>3</sub>CN, 1 mL TEA, 0.1 mL H<sub>2</sub>O, 500 W Xe/Hg lamp using  $\lambda > 408$  nm. (d) Concept of photocatalytic H<sub>2</sub> production using a multifunctional MOF-based composite.<sup>63</sup>

MOFs have been proven to be photoactive and their optical properties can be easily tuned towards visible light operation. The current challenge lies in the development of more appropriate active sites for the desired photocatalytic cycle. In this context, M. A. Nasalevich and co-workers present a synthetic strategy for the efficient encapsulation of a derivative of a well-defined cobaloxime proton reduction catalyst within a photo-responsive metal–organic framework (NH<sub>2</sub>-MIL-125(Ti)).<sup>63</sup> As shown in Figure 1.3a, the encapsulation of a derivative of a well-defined cobaloxime proton reduction catalyst did not change the crystal structure of Ti based MOF. It is found that the introduction of the cobaloxime-derived

# Chapter 1

---

active sites into the cavities of the framework resulted in a 20-fold enhanced photocatalytic activity compared to the pristine NH<sub>2</sub>-MIL-125(Ti) used as a benchmark (Figure 1.3b). The prepared hybrid system Co@MOF is an efficient and fully recyclable noble metal-free catalyst system for light driven hydrogen evolution from water under visible light illumination (Figure 1.3c). The mechanism of this hybrid system is studied by ESR measurement. It indicates that upon photon-absorption by the MOF linker, charge separation takes place to generate Ti<sup>3+</sup> and a hole at the organic linker. The hole then reacts with the electron donor, TEA, while the electron is rapidly injected into the cobalt species, leading to reduction of Co(III) to Co(II), which is likely to play an important role in photocatalytic activity of the whole system (Figure 1.3d). This finding provides an example of synergetic action between a MOF and a molecular catalyst for application in photocatalysis.

### 1.3.3 MOFs based photocatalysts for water oxidation

Although many MOFs based photocatalysts have been reported to own the ability to split water to produce H<sub>2</sub>, fewer MOFs based photocatalysts have been reported for the other half reaction of water splitting, namely water oxidation. This is probably due to the instability of most MOFs under water oxidation conditions (aqueous buffer solution, strong oxidant, etc.). The first work about water oxidation by MOFs based photocatalyst was performed by Lin and coworkers in 2011.<sup>64</sup> It was reported that three iridium-based water oxidation catalysts, [Cp\*Ir<sup>III</sup>(dcppy)Cl], [Cp\*Ir<sup>III</sup>(dcbpy)Cl]Cl, and [Ir<sup>III</sup>(dcppy)<sub>2</sub>(H<sub>2</sub>O)<sub>2</sub>]OTf, (dcppy = 2-phenylpyridine-5,40-dicarboxylic acid; dcbpy = 2,2'-bipyridine-5,5'-dicarboxylic acid) can be doped into the a Zr based MOF (UiO-67) without changing its structure. The photocatalytic water oxidation reaction were investigated with Ce<sup>4+</sup> (cerium ammonium nitrate) as an oxidant and the resulting MOFs are highly effective water oxidation catalysts with turnover frequencies (TOFs) as high as 4.8 h<sup>-1</sup>. The photocatalytic activity must come from the doped iridium-based water oxidation catalysts since the parent UiO-67 MOF does not show any activity for water oxidation. However, the doped MOFs show lower activities than their homogeneous counterparts. The lower activities can be ascribed to the fact that the photocatalytic water oxidation reactions only take place by the iridium-based water oxidation

# Chapter 1

catalysts on the MOF particle surface, since cerium ammonium nitrate is apparently too large ( $\sim 11.3$  Å in diameter for the cerium nitrate anions from the crystal structure) to enter the MOF channels ( $\sim 6.7$  Å in diameter). This work illustrates another example of combining molecular catalysts and MOF structures in developing highly active photocatalysts for solar energy utilization.

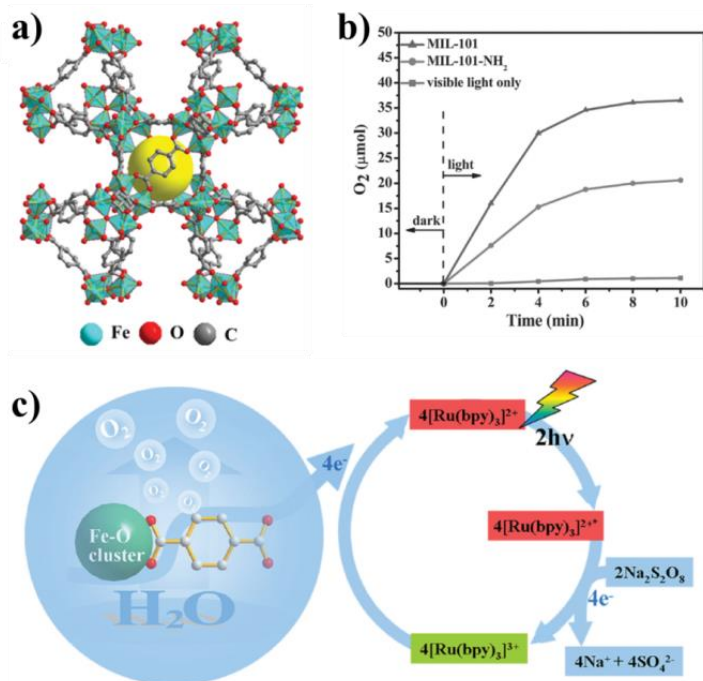


Figure 1.4 (a) Schematic of the crystal structure of MIL-101(Fe). (b) Kinetics of O<sub>2</sub> evolution of the photocatalytic system with different catalysts (MIL-101(Fe), MIL-101-NH<sub>2</sub>(Fe)), and visible light only. (c) The processes of photocatalytic water oxidation catalyzed by Fe-based MOFs.<sup>65</sup>

Fe based MOFs photocatalysts have also been explored for photocatalytic O<sub>2</sub> evolution. Very recently, Chi *et al.* explored three types of Fe based MOFs (MIL-53, MIL-88B, and MIL-101) and their aminofunctionalized derivatives as water oxidation catalysts.<sup>65</sup> Among the as-obtained MOFs, MIL-101 exhibits excellent oxygen evolution reaction catalytic activity in basic solution (Figure 1.4a, b). O<sub>2</sub> evolution by photocatalytic water oxidation was examined with [Ru(bpy)<sub>3</sub>]<sup>2+</sup> as a photosensitizer and Na<sub>2</sub>S<sub>2</sub>O<sub>8</sub> as an electron acceptor in the presence of catalysts under visible light irradiation (Figure 1.4c). MIL-101 showed the much higher photocatalytic activity than other types of Fe based MOFs, and the

# Chapter 1

---

initial quantum yield was also determined to be as high as 20.56%. This study demonstrated that Fe based MOFs as efficient water oxidation catalysts are promising candidates for photocatalytic water oxidation process.

## 1.3.4 MOFs based photocatalysts for CO<sub>2</sub> reduction

Photocatalytic reduction of CO<sub>2</sub> through artificial photosynthesis is of significant interest since it offers the potential to produce valuable hydrocarbon fuels to meet the increasing energy demands while also mitigate the rising CO<sub>2</sub> levels. Based on the tailor ability of the framework as well as the controllability of synthesis, it is easy to construct MOFs with tunable capacity of light and gas molecules adsorption, thereby initiating desirable photocatalytic properties for specific application in CO<sub>2</sub> reduction. The study of MOFs applications in this topic thus has a bright future even though it has not been so widely explored up to date. In 2012, Zhaohui Li and co-workers reported the photocatalytic reduction of CO<sub>2</sub> to HCOO<sup>-</sup> under visible light irradiation over a photoactive Ti-containing MOF, NH<sub>2</sub>-MIL-125(Ti).<sup>66</sup> A significant change in NH<sub>2</sub>-MIL-125 (Ti) induced by the amino functionality was its optical absorption, which showed an obvious red shift from the adsorption band edge of 350 nm to around 550 nm, falling in the visible region. The photocatalytic reduction of CO<sub>2</sub> over photocatalyst NH<sub>2</sub>-MIL-125 (Ti) was carried out in acetonitrile (MeCN) with TEOA as sacrificial agent under visible light irradiation. A temporal concentration change of HCOO<sup>-</sup> with the time of irradiation shows that the amount of HCOO<sup>-</sup> formed reached 8.14 μmol in 10 h. The inactivity of the parent MIL-125(Ti) under otherwise similar conditions confirms that the visible light photocatalytic activity for CO<sub>2</sub> reduction over NH<sub>2</sub>-MIL-125(Ti) was actually induced by the amino functionality. The mechanism study shows that, upon light absorption, a long-lived excited charge separation state occurs by transferring an electron from an organic ligand to Ti<sup>4+</sup>. This process is similar to the generation of electrons and holes over photoexcited metal oxide semiconductors. Ti<sup>4+</sup> is thus reduced to Ti<sup>3+</sup> whereas TEOA acts as an electron donor. Therefore, a complete photocatalytic cycle can be achieved by reduction of CO<sub>2</sub> to HCOO<sup>-</sup> by Ti<sup>3+</sup> in the presence of TEOA as electron donor. Although the current activity for the reduction of CO<sub>2</sub> over the NH<sub>2</sub>-MIL-

# Chapter 1

125(Ti) catalyst is very low, considering the versatile coordination chemistry of the metal cations, the availability of different organic linkers, and the possibility to modulate the composition, structure, and properties of the MOFs, it is believed that high-efficient MOFs based photocatalysts for the reduction of  $\text{CO}_2$  can be obtained.

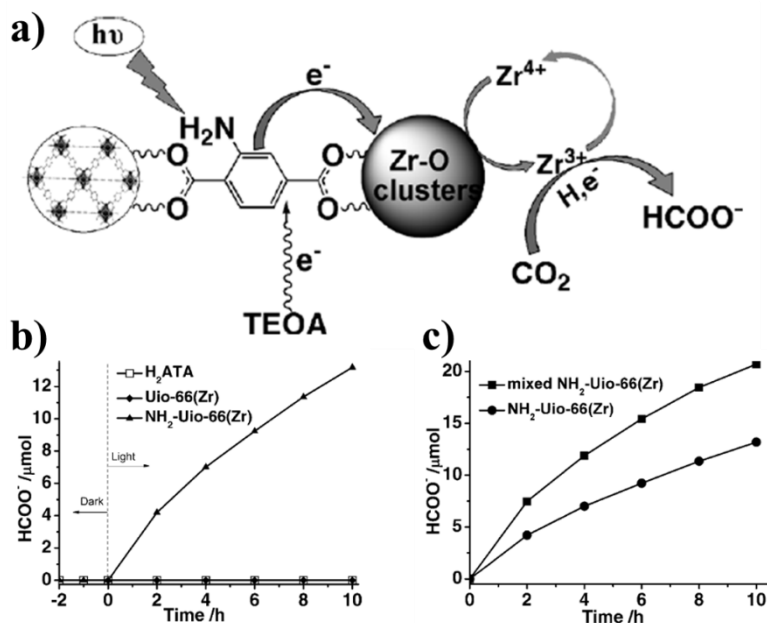


Figure 1.5 Proposed mechanism for photocatalytic  $\text{CO}_2$  reduction over  $\text{NH}_2\text{-Uio-66(Zr)}$  under visible-light irradiation. (b) Amount of  $\text{HCOO}^-$  produced as a function of irradiation time over  $\text{NH}_2\text{-Uio-66(Zr)}$ ,  $\text{Uio-66(Zr)}$  and  $\text{H}_2\text{ATA}$ . The solutions were irradiated with an Xe lamp and filters producing light in the range of 420–800 nm. Photocatalyst: 50 mg,  $\text{MeCN/TEOA}$  (5/1), solution volume: 60 mL. (c) Amount of  $\text{HCOO}^-$  produced as a function of irradiation time over  $\text{NH}_2\text{-Uio-66(Zr)}$  and mixed  $\text{NH}_2\text{-Uio-66(Zr)}$ .<sup>67</sup>

Later on, using a similar strategy, Li and coworkers reported photocatalytic  $\text{CO}_2$  reduction catalyzed by  $\text{NH}_2\text{-Uio-66(Zr)}$  with TEOA as a sacrificial agent under visible-light irradiation.<sup>67</sup> Photoluminescence studies indicate that photoinduced electrons can transfer from the excited 2-aminoterephthalate organic linker to Zr oxo clusters in  $\text{NH}_2\text{-Uio-66(Zr)}$ , resulting in the formation of  $\text{Zr}^{\text{III}}$ . The photocatalytic cycle can be achieved by reduction of  $\text{CO}_2$  to  $\text{HCOO}^-$  by  $\text{Zr}^{\text{III}}$  in the presence of TEOA as electron donor (Figure 1.5a). The concentration change of  $\text{HCOO}^-$  over  $\text{NH}_2\text{-Uio-66(Zr)}$  with the irradiation time shows

# Chapter 1

---

that the amount of  $\text{HCOO}^-$  produced reached  $13.2 \mu\text{mol}$  in 10 h (Figure 1.5b). This value is higher than that over irradiated  $\text{NH}_2\text{-MIL-125(Ti)}$  ( $8.14 \mu\text{mol}$ ) under similar reaction conditions. In addition, facile partial substitution of the organic linker 2-aminoterephthalate by 2,5-diaminoterephthalate in  $\text{NH}_2\text{-UiO-66(Zr)}$  could further improve its photocatalytic performance in  $\text{CO}_2$  reduction due to enhanced light absorption in the visible region and increased  $\text{CO}_2$  adsorption (Figure 1.5c).

Fe based MOFs photocatalysts can also be applied for photocatalytic  $\text{CO}_2$  reduction. In 2014, Li and co-workers reported the photocatalytic  $\text{CO}_2$  reduction over three typical Fe-based MOFs ( $\text{MIL-101(Fe)}$ ,  $\text{MIL-53(Fe)}$ , and  $\text{MIL-88B(Fe)}$ ) and their amino-functionalized derivatives.<sup>68</sup> These Fe-based MOF materials contain a similar organic linker, BDC (BDC = benzene-1,4-dicarboxylate), but have quite different structures. The photocatalytic reduction of  $\text{CO}_2$  over Fe-based MOF was performed under visible light irradiation in the presence of TEOA as a sacrificial agent. The results show that  $\text{MIL-101(Fe)}$  exhibits much higher activity than  $\text{MIL-53(Fe)}$  and  $\text{MIL-88B(Fe)}$ , due to the existence of the coordination unsaturated Fe sites in its structure. In order to further increase the activity, the Fe based MOFs with amine functionality, named as  $\text{NH}_2\text{-MIL-101(Fe)}$ ,  $\text{NH}_2\text{-MIL-53(Fe)}$ , and  $\text{NH}_2\text{-MIL-88B(Fe)}$ , are prepared by similar methods expect that BDC is replaced with  $\text{NH}_2\text{-BDC}$ . The XRD patterns of the as-prepared amino-functionalized MOFs are similar to those of the parent MOFs. As expected, amino-functionalized Fe-based MOF materials show enhanced absorption in the visible light region and improved photocatalytic  $\text{CO}_2$  reduction activities compared with the non-functionalized MOFs. The improved activities can be ascribed to the synergetic effect of dual excitation pathways: i.e., an exciting  $\text{NH}_2$  functionality followed by an electron transfer from the excited organic linker to the Fe center and the direct excitation of Fe–O clusters. This study for the first time elucidates a dual-excitation pathway for the photocatalytic  $\text{CO}_2$  reduction, and gives us a better understanding of the photocatalytic  $\text{CO}_2$  reduction over MOF-based materials.

## 1.3.5 MOFs based photocatalysts for Cr(VI) reduction

The increasing toxic heavy metal pollution in water system has become a serious issue faced by all the governments in the world, which triggers intense attention over the advanced technology for water treatment. Efficient removal of inorganic pollutants from wastewater has become a hot research topic due to its ecological and environmental importance. Cr(VI) is a typical heavy metal ion contaminant in the waste water arising from some industrial process, such as leather tanning, paint-making, or steel manufacturing. Traditional water treatment methods, such as adsorption, coagulation and membrane separation, suffer from high operating costs and even the generation of secondary pollutants. The reduction of Cr(VI) to Cr(III) is considered as an efficient strategy for the removal of Cr(VI) in the waste water, because Cr(III) is environmentally friendly and vital to plants and human life. Recent studies indicate that photocatalysis on MOFs based photocatalysts has demonstrated efficiency in reduction of Cr(VI).

Zr based MOFs, acting as photocatalysts, are effective in the photocatalytic degradation of inorganic pollutants, especially for the reduction of hexavalent chromium Cr(VI). Shen *et al.* reported the photocatalytic Cr(VI) reduction over amino group functionalized Zr based MOFs (NH<sub>2</sub>-UiO-66).<sup>69</sup> It was found that the NH<sub>2</sub>-UiO-66 showed efficient photocatalytic activity for Cr(VI) reduction under visible light. It has been determined that the flat-band potential ( $V_{fb}$ ) of the NH<sub>2</sub>-UiO-66 is around -0.80 V vs Ag/AgCl and it was more negative than the Cr(VI)/Cr(III) potential (+1.15 V, pH 3.0), confirming that the photogenerated electrons on the conduction band of NH<sub>2</sub>-UiO-66 were able to reduce Cr(VI) thermodynamically. Moreover, highly dispersed Pd nanoparticles of about 3–6 nm in diameter are immobilized in the amino group functionalized UiO-66 via a facile one pot hydrothermal method. As shown in Figure 1.6a, the resulting Pd@NH<sub>2</sub>-UiO-66 nanocomposite exhibits an excellent and higher visible light photocatalytic activity for reducing Cr(VI) compared with NH<sub>2</sub>-UiO-66 and N-doped TiO<sub>2</sub>. Further mechanism study indicated that the enhanced activity could be due to the high dispersion of Pd

# Chapter 1

nanoparticles and their close contact with the matrix, which lead to the enhanced light harvesting and more efficient separation of photogenerated electron-hole pairs (Figure 1.6b).

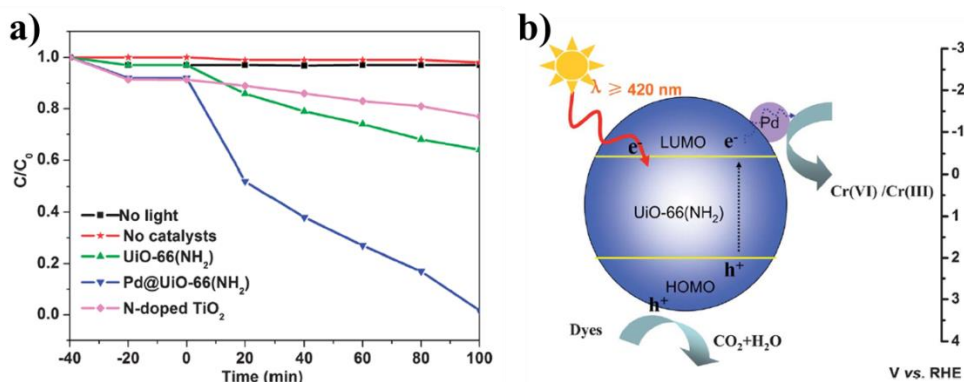


Figure 1.6 (a) Reaction profiles of photocatalytic reduction of Cr(VI). (b) Possible mechanism of photocatalytic reduction of Cr(VI) over Pd@NH<sub>2</sub>-UiO-66.<sup>69</sup>

Ti based MOFs photocatalyst, NH<sub>2</sub>-MIL-125(Ti), can also be applied for photocatalytic Cr(VI) reduction. In 2015, Wang and co-workers systematically studied the photocatalytic Cr(VI) reduction over NH<sub>2</sub>-MIL-125(Ti).<sup>70</sup> It is revealed that the introduction of amino group in the MIL-125(Ti) can make it responsive to visible light, and the visible-light absorption of NH<sub>2</sub>-MIL-125(Ti) can be up to 520 nm, which was associated with the chromophore (amino group) in the organic linker. Compared with MIL-125(Ti), NH<sub>2</sub>-MIL-125(Ti) exhibited more efficient photocatalytic activity for Cr(VI) reduction under visible-light irradiation. The addition of hole scavenger and the pH value of the reaction solution played important roles in the photo-catalytic reduction of Cr(VI). Lower pH value of the reaction solution results in higher activity, and the ethanol is the best hole scavenger for the photocatalytic Cr(VI) reduction. The mechanism study indicates that the presence of Ti<sup>3+</sup>-Ti<sup>4+</sup> intervalence electron transfer was the main reason for photo-excited electrons transportation from titanium-oxo clusters to Cr(VI), facilitating the Cr(VI) reduction under the acid condition. This study gives another efficient MOFs based material as photocatalyst for water purification.

## 1.4 Modification of MOFs based photocatalysts for superior performances

MOFs based photocatalysts exhibit lots of advantages in comparison with traditional inorganic semiconductors in photocatalysis, due to their inherent structural characteristics (large surface area and porous structure) and the tunable organic linkers/metal clusters. However, the photocatalytic efficiency of MOFs based photocatalysts is still very low and cannot satisfy the practical needs. To further promote the photocatalytic performance of MOFs based photocatalysts, various strategies have been adopted via either modulation of their organic linkers/metal clusters or incorporation with dye/ semiconductor catalysts for enlarged visible light absorption, better charge separation, and efficient reactant activation (Figure 1.7).<sup>71-</sup>

75

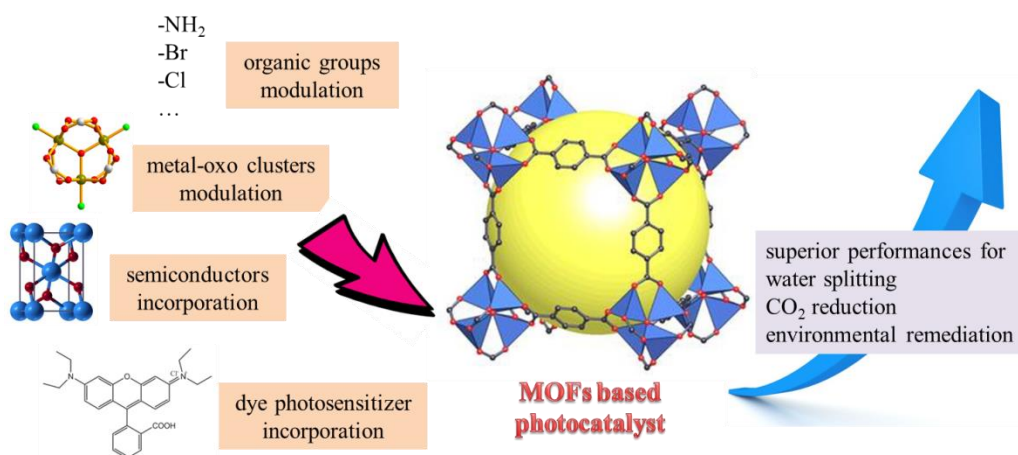


Figure 1.7 Modification of MOFs based photocatalysts for superior performances.

### 1.4.1 Organic linkers or metal clusters modulations

The first step in photocatalytic system is light-harvesting by a chromophore, that is, a light absorbing component. This chromophore should efficiently absorb and convert the incoming solar energy into an excited state that can transfer an electron to an acceptor for the creation of a charge-separated state, thus generating the required thermodynamic driving force for the desired chemical reactions. For the cases where the MOFs work as a sensitizer agent, the organic ligands serve as antennae to harvest light and sensitize metal nodes, energy transfer processes such as localized ligand-to-metal charge transfer (LMCT)

# Chapter 1

---

or metal-to-ligand charge transfer (MLCT) transition or a  $\pi$ - $\pi^*$  transition of the aromatic ligand are always applied. By adjusting the functional organic linkers of MOFs, the light absorption can be effectively enlarged. In 2013, Aron Walsh and co-authors performed a combined experimental and computational study to elucidate the band structure of titanium-containing MIL-125 and the impact of functional groups on the 1,4-benzenedicarboxylate (bdc) linker and explain the specific role of the  $-\text{NH}_2$  group of the monoaminated 1,4-benzenedicarboxylate (bdc- $\text{NH}_2$ ) linker in lowering the optical band gap of the MIL-125- $\text{NH}_2$ .<sup>76</sup> DFT calculations show that the upper valence band (VB) of MIL-125 is composed of bdc aromatic 2p orbitals. Introducing a single bdc- $\text{NH}_2$  linker per unit cell (i.e., to give 10%-MIL-125- $\text{NH}_2$ ) breaks the original  $I4/mmm$  symmetry and splits the VB into a high energy occupied state, which confirmed that electronic modifications of the aromatic motifs are localized and directly control the optical properties through modification of the valence band. This work illustrates that the optical response of MIL-125 may be tailored toward absorption in the visible region through rational selection of substituents of the aromatic bdc linker. The diaminated bdc- $(\text{NH}_2)_2$  linker is expected to demonstrate the most significant red shift of the optical absorption edges.

MOFs can not only be realized by modification on the organic ligands but also metal ions, due to the versatile coordination chemistry of the metal cations and the availability of different organic linkers. In 2014, Yang and his coworkers demonstrated the systematic substitution engineering of band gap and optical properties of MOF-5 via substitution of  $\text{Zn}_4\text{O}$  with  $\text{X}_4\text{Y}$  ( $\text{X} = \text{Zn}, \text{Cd}, \text{Be}, \text{Mg}, \text{Ca}, \text{Sr}, \text{Ba}$ ;  $\text{Y} = \text{O}, \text{S}, \text{Se}, \text{Te}$ ) in the node from density functional theory calculations.<sup>77</sup> Results show that it can tune the band gaps of MOF-5 ranging from 1.7 to 3.6 eV, and the corresponding minimum absorption wavelength varied from 345 to 724 nm. Although the above findings are only predicted by the theory calculation, it gives important hint for exploring band engineered MOF for more visible-light absorption via metal clusters modulation in MOFs. In 2015, Sun and his co-workers experimentally demonstrated that metal clusters modification in MOFs structure could be beneficial for photocatalytic performance.<sup>78</sup> They prepared the Ti-substituted  $\text{NH}_2$ -Uio-66(Zr) (denoted as  $\text{NH}_2$ -Uio-66(Zr/Ti)) by exposing  $\text{NH}_2$ -Uio-66(Zr)

# Chapter 1

to DMF solution containing  $\text{TiCl}_4(\text{THF})_2$ . To study the influence of Ti substitution on the photocatalysis of  $\text{NH}_2\text{-Uio-66}(\text{Zr})$ , the photocatalytic performance for  $\text{CO}_2$  reduction over the as-prepared  $\text{NH}_2\text{-Uio-66}(\text{Zr}/\text{Ti})$  was investigated. Triethanolamine (TEOA) was chosen as a sacrificial agent, which acts as both an electron donor and a hydrogen donor and provides the basic environment to facilitate the photocatalytic  $\text{CO}_2$  reduction. Results show that  $\text{NH}_2\text{-Uio-66}(\text{Zr}/\text{Ti})$  exhibits much higher photocatalytic  $\text{CO}_2$  reduction and  $\text{H}_2$  evolution activities than  $\text{NH}_2\text{-Uio-66}(\text{Zr})$ , which indicates that the incorporated Ti moiety is beneficial for the photocatalysis over  $\text{NH}_2\text{-Uio-66}(\text{Zr}/\text{Ti})$  (Figure 1.8a,b). Both the ESR measurement and the DFT calculation suggest a favorable electron transfer from excited organic linker to the Ti moiety to form  $(\text{Ti}^{3+}/\text{Zr}^{4+})_6\text{O}_4(\text{OH})_4$  in Ti-doped  $\text{NH}_2\text{-Uio-66}(\text{Zr})$ . After that,  $\text{Ti}^{3+}$  donates an electron to  $\text{Zr}^{4+}$  to promote the formation of  $\text{Zr}^{3+}$ . The mechanism study indicates that the substituted Ti center in  $\text{NH}_2\text{-Uio-66}(\text{Zr}/\text{Ti})$  acts as a mediator during the photocatalysis over  $\text{NH}_2\text{-Uio-66}(\text{Zr}/\text{Ti})$ , and helps to improve the interfacial charge transfer from excited organic linker to  $\text{Zr-O}$  oxo-clusters, which is beneficial for visible light photocatalysis (Figure 1.8c).

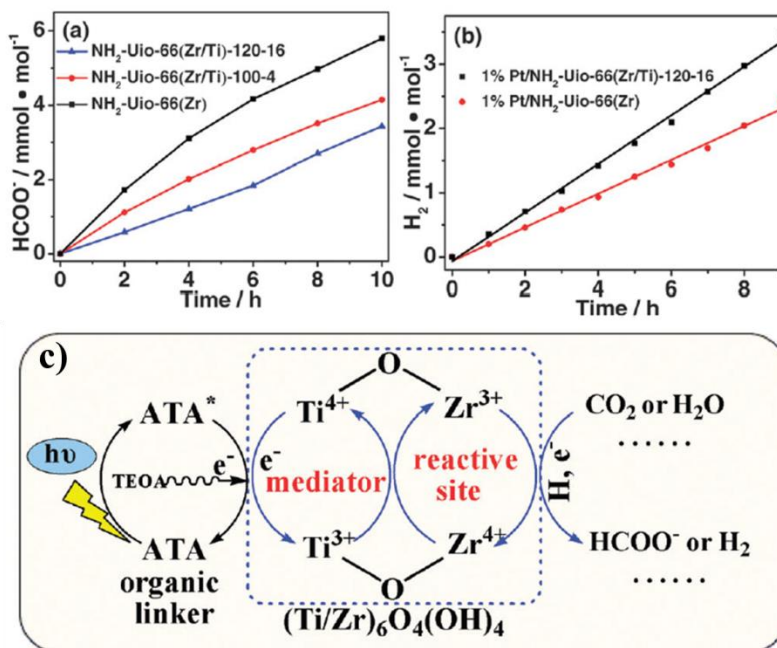


Figure 1.8 (a) Amount of  $\text{HCOO}^-$  produced as a function of irradiation time over different samples (photocatalyst: 50 mg, MeCN/TEOA (5/1), solution volume: 60 mL). (b) amount of hydrogen evolved

# Chapter 1

during the photocatalytic reactions over different samples (photocatalyst: 50 mg, solvent: H<sub>2</sub>O, H<sub>2</sub>O/TEOA (5/1), solution volume: 60 mL). (c) Proposed enhanced mechanism for the photocatalytic reactions over NH<sub>2</sub>-UiO-66(Zr/Ti).<sup>78</sup>

## 1.4.2 Dye sensitization

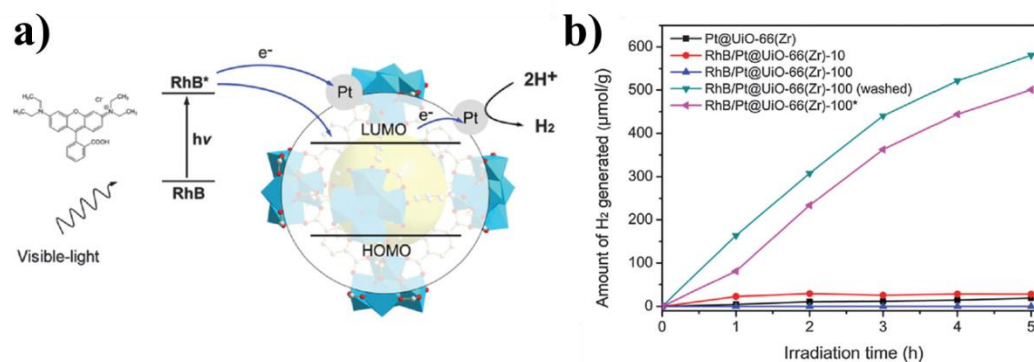


Figure 1.9 (a) Proposed mechanism of photocatalytic H<sub>2</sub> production over RhB sensitized Pt@UiO-66(Zr) under visible-light. (b) Photocatalytic H<sub>2</sub> production over Pt@UiO-66(Zr) and RhB-sensitized Pt@UiO-66(Zr) under visible-light.<sup>79</sup>

Alternative promising approach to realize efficient visible light photo response is to construct dye-sensitized system, which has also been applied in MOFs based visible light photocatalysis. Taking into account that both MOFs and dyes containing benzene ring, it is expected that there exists a strong  $\pi$ - $\pi$  stacking and Van Der Waals interaction between MOFs and dyes, which is very important for efficient electron transfer in dye-sensitized photocatalytic system. One of this works was reported by He and coworkers in 2014, they used rhodamine B (RhB) dye to sensitize UiO-66 for photocatalytic H<sub>2</sub> production.<sup>79</sup> Pt was used as co-catalyst and RhB dye was used as a sensitizer to absorb visible-light. The redox potentials of RhB and excited RhB\* are 0.95 V and -1.42 V vs. NHE, respectively. Considering the potential of LUMO in UiO-66 (-0.60 V vs. NHE), direct electron transfer from RhB\* to UiO-66(Zr) is thermodynamically favorable (Figure 1.9 a). The photocatalytic activities of the catalysts were evaluated in the presence of triethanolamine (TEOA) as an electron donor. Results showed that the adsorbed and directly added dye extremely enhanced the photocatalytic activity to 30 and 26 times the value afforded

# Chapter 1

---

by bare Pt@UiO-66(Zr), respectively, as shown in Figure 1.9b. Although the H<sub>2</sub> generation rate in this dye-photosensitized Pt@UiO-66(Zr) is lower, it is believed that the simple strategy demonstrated here could be extended to other MOFs and other dyes.

Another more stable Erythrosin B (denoted as ErB) dye has also been used as light absorbing antenna, and an active hydrogen production system over ErB-sensitized UiO-66 has been demonstrated to be feasible, as reported by Xue and his co-workers in 2014.<sup>80</sup> As the LUMO potential of ErB is -0.9 V vs NHE, which is higher than the LUMO potential (-0.6 V) of UiO-66, and thus, the electron transfer is thermodynamically favourable from the photo-excited ErB dye to the UiO-66, and then to the Pt active sites for H<sub>2</sub> production. The electron transfer process is studied by PL measurement, and it shows an obvious fluorescence quenching. The photocatalytic H<sub>2</sub> production activity have been evaluated under visible light, and L-ascorbic acid (0.1 M, pH=4.0) was used as the sacrificial reagent. The pristine Pt-UiO-66 sample shows no activity for H<sub>2</sub> production under visible light, owing to its UV light absorption nature. Also, ErB dye suspension (5 mg) with H<sub>2</sub>PtCl<sub>6</sub> solution addition produces trace amount of H<sub>2</sub>, demonstrating that ErB dye can be photoexcited and the electrons from ErB dye can produce H<sub>2</sub>. Upon adding of 5 mg ErB dye (denoted as UiO-66-5, the number 5 indicates the amount of added ErB dye) into the reaction solution, a H<sub>2</sub> evolution rate of  $\sim 0.7 \mu\text{mol}\cdot\text{h}^{-1}$  was achieved, suggesting the positive sensitization effect of ErB dye on UiO-66 for H<sub>2</sub> production. The photocatalytic H<sub>2</sub> production can be further enhanced up to  $4.6 \mu\text{mol}\cdot\text{h}^{-1}$  by increasing ErB dye amount to 30 mg (Pt-UiO-66-30). The quantum efficiency (QE) of the present H<sub>2</sub> production system is measured to be  $\sim 0.25\%$  at 420 nm, which is also very low compared with some traditional photocatalysts. Further research should focus on the exploration of efficient dyes-sensitized MOFs photocatalytic system for H<sub>2</sub> production.

### 1.4.3 Heterojunction construction

Even though the light absorption can be enhanced *via* either structural modulation or dye sensitization, the low efficiency in exciton generation and charge separation largely limited the practical application for the most MOFs based photocatalysts. Therefore, another effective strategy to optimize the

# Chapter 1

MOFs based photocatalysts with improved photocatalytic efficiency is needed. Fabricating photocatalysts with heterojunction structure, which can effectively suppress the photogenerated electron-hole recombination probability, is one of the most effective methods to improve the photocatalytic efficiency of photocatalysts, and has been widely applied in traditional inorganic photocatalysts. For MOFs based photocatalysts, it is also feasible to construct heterostructure via integration of MOFs materials with traditional semiconductors for higher photocatalytic performance.

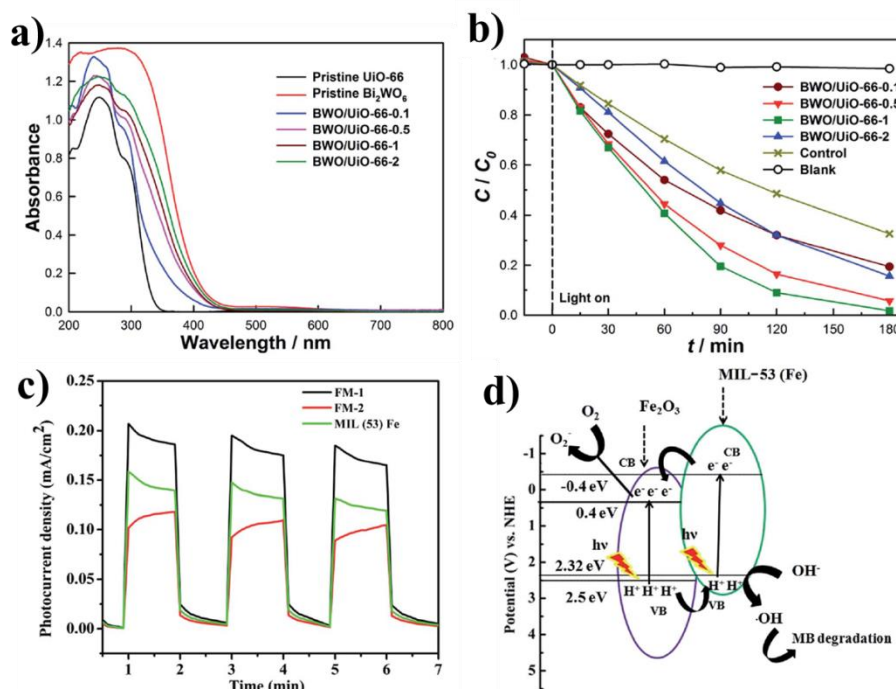


Figure 1.10 (a) UV-Vis diffuse reflectance spectra of pristine UiO-66, pristine Bi<sub>2</sub>WO<sub>6</sub> (BWO), and Bi<sub>2</sub>WO<sub>6</sub>/UiO-66 composites with different Bi<sub>2</sub>WO<sub>6</sub> contents. (b) Photocatalytic degradation of RhB in the presence and absence (blank) of different catalysts (BWO/UiO-66-0.1, BWO/UiO-66-0.5, BWO/UiO-66-1, and BWO/UiO-66-2) under visible-light irradiation.<sup>81</sup> (c) Photocurrent response experiment of Fe<sub>2</sub>O<sub>3</sub>/MIL-53(Fe) composite and MIL-53(Fe). (d) Charge transfer mechanism of Fe<sub>2</sub>O<sub>3</sub>/MIL-53(Fe) heterojunction.<sup>82</sup>

# Chapter 1

---

One of MOFs based heterostructure photocatalysts was reported by Sha and coworkers in 2014.<sup>81</sup> They reported the synthesis of a series of  $\text{Bi}_2\text{WO}_6/\text{UiO-66}$  composites with different  $\text{Bi}_2\text{WO}_6$  contents by incorporating UiO-66 with  $\text{Bi}_2\text{WO}_6$  through a convenient hydrothermal method, which could be used as photocatalysts for dye degradation. The formation of composite can improve the visible light absorption ability of UiO-66 (Figure 1.10a). In the rhodamine B (RhB) degradation experiment, The  $\text{Bi}_2\text{WO}_6/\text{UiO-66}$  composite exhibited enhanced photocatalytic activity under visible-light irradiation than bare  $\text{Bi}_2\text{WO}_6$  or UiO-66 (Figure 1.10b). In the recycled dye degradation experiments, most activity of the composite is reserved, and the structure and morphology of the composite do not vary after the experiment of dye degradation, which demonstrates the good catalyst stability. Because of the well match of the energy band between  $\text{Bi}_2\text{WO}_6$  and UiO-66, a heterostructure has been formed, which may promote the separation of the photogenerated electron-hole pairs, leading to the enhanced photocatalytic activity. The mechanism of photocatalytic degradation of RhB by the  $\text{Bi}_2\text{WO}_6/\text{UiO-66}$  composite was also investigated, and the results implied that  $\text{O}_2^{\cdot-}$  and  $\text{h}^+$  were two main active species involving in the degradation process of RhB.

Very recently, Ramdayal Panda and coworkers reported another MOFs based heterostructure photocatalyst,  $\text{Fe}_2\text{O}_3/\text{MIL-53(Fe)}$  composite, that was prepared by partial and complete thermal decomposition of MIL-53(Fe) for photocatalytic degradation of methylene blue in both UV and visible light.<sup>82</sup> The photocurrent response experiment depicts excellent photogenerated electron hole separation ability of  $\text{Fe}_2\text{O}_3/\text{MIL-53(Fe)}$  composite compare to both pure  $\text{Fe}_2\text{O}_3$  and pure MIL-53 (Fe) by its much higher transient photocurrent density (Figure 1.10c). This could be explained by the fact that  $\text{Fe}_2\text{O}_3$  and MIL-53(Fe) create a heterojunction which may enhance the electron hole separation ability. A possible charge transfer mechanism for  $\text{Fe}_2\text{O}_3/\text{MIL-53(Fe)}$  heterostructure photocatalytic system can be described as follows: At the initial stage, the light is absorbed by the MIL-53(Fe) and the photogenerated electrons are excited to the conduction band (CB) with simultaneous hole remained in the valence band (VB) (Figure 1.10d). The photogenerated electrons from CB of MIL-53(Fe) are migrated to CB of  $\text{Fe}_2\text{O}_3$  due to

# Chapter 1

---

difference of band gap, resulting in an electron-rich locale at the CB of  $\text{Fe}_2\text{O}_3$ . Essentially, the accumulation of photogenerated holes in the VB of  $\text{Fe}_2\text{O}_3$  transfer to the VB of MIL-53(Fe), creating a hole-rich locale. Subsequently, the combination of  $\text{Fe}_2\text{O}_3$  and MIL-53(Fe) act as powerful photocatalytic oxidant and reductant respectively by composition of two narrow-bandgap semiconductors. As a result, the prepared  $\text{Fe}_2\text{O}_3/\text{MIL-53(Fe)}$  composite shows much higher photocatalytic methylene blue degradation efficiency than both pure  $\text{Fe}_2\text{O}_3$  and pure MIL-53 (Fe). The study of the MOFs based heterostructure photocatalysts provides one of design principles to the efficient MOFs based photocatalysis.

## 1.5 Research motivation and thesis organization

Overall, the development of MOFs based photocatalysts related to water-splitting,  $\text{CO}_2$  photoreduction, and water purification, has been under intensive investigation due to the unique characteristics of MOFs based materials, which demonstrated them to be a new class of photocatalysts for potential applications in the environmental and energy field. Compared with conventional inorganic photocatalysts, the MOFs photocatalysts have three advantages: (i) versatile synthetic strategies, including solvothermal, vapor diffusion, emulsion-assistant precipitation, and even post-synthesis modification, allow a high degree of crystalline quality of MOFs photocatalysts; (ii) the well-defined crystalline structures of MOFs are beneficial in the characterization and study of the structure–property relationship and thus help us to understand the photocatalytic mechanisms; (iii) the modular nature of the MOFs synthesis allows the rational design and fine tuning of these photocatalysts at the molecular level, including the incorporation of active sites, the introduction of visible-light chromophore, and thus provides us a unique platform to mimic the natural photosynthesis systems.

In this dissertation, I focus on the construction of MOFs based materials to explore their photocatalytic applications, to enhance the photocatalytic efficiency, and to understand the photocatalytic mechanisms. Three strategies have been proposed to enhance the photocatalytic activities of MOFs based photocatalysts, namely amine functionalization, heterojunction fabrication and metal ions implantation. The remaining five chapters is as follows:

# Chapter 1

---

## **Chapter 2 Construction of an amine-functionalized iron(III) metal-organic framework as efficient visible-light photocatalyst for Cr(VI) reduction**

Iron(III) MOFs based materials show great potential in photocatalysis because of their small band gap enabling visible light excitation. In this chapter, one of the iron(III) MOFs based materials named as MIL-88B was constructed, and its photocatalytic performance for Cr(VI) reduction under visible-light irradiation was investigated. Due to the direct excitation of  $\text{Fe}_3\text{-}\mu_3\text{-oxo}$  clusters in MIL-88B under visible light, the photocatalytic performance for Cr(VI) reduction could be achieved. The MIL-88B functionalized with amine groups was expected to the improved light absorption and carrier separation. During the photocatalytic reactions, in addition to the direct excitation of  $\text{Fe}_3\text{-}\mu_3\text{-oxo}$  clusters, the amine functionality in MIL-88B can also be excited and then transferred an electron to  $\text{Fe}_3\text{-}\mu_3\text{-oxo}$  clusters, and thus the enhanced photocatalytic activity for Cr(VI) reduction can be expected over amine-functionalized MIL-88B.

## **Chapter 3 Construction of nano-sized g-C<sub>3</sub>N<sub>4</sub> nanosheet/UiO-66 heterojunction photocatalyst for enhanced photocatalytic CO<sub>2</sub> Reduction**

A Zr based MOF named as UiO-66 has been demonstrated to be an excellent photocatalyst. Nevertheless, the relatively wide band gap of UiO-66 may limit its optical adsorption in the visible light region. To prepare UiO-66 based visible-light active photocatalysts, an ideal solution would be to incorporate UiO-66 together with a visible-light active photosensitizer, such as narrow bang gap semiconductors, to form a heterostructure photocatalyst. In this chapter, a novel hybrid photocatalyst that composed of g-C<sub>3</sub>N<sub>4</sub> nanosheet (CNNS) and UiO-66 was constructed for photocatalytic CO<sub>2</sub> reduction under visible light. Due to the well match of the energy level between UiO-66 and CNNS, a heterojunction structure in UiO-66/CNNS hybrid photocatalyst could be formed. It can be expected that the electrons from photoexcited carbon nitride nanosheet can transfer to UiO-66, which could substantially suppress electron-hole pairs recombination in the carbon nitride nanosheet, and also supply long-lived electrons for the reduction of CO<sub>2</sub> molecules adsorbed in UiO-66. Therefore, the prepared

# Chapter 1

---

heterostructure photocatalyst may exhibit much higher photocatalytic activity for the CO<sub>2</sub> conversion than bare g-C<sub>3</sub>N<sub>4</sub> nanosheet.

## **Chapter 4 Implantation of iron(III) in porphyrinic metal organic frameworks for highly improved photocatalytic performance**

The porphyrinic MOF named as PCN-224 should show rather promising in photocatalysis due to its high photoresponse in visible light and its high stability. In this chapter, the photocatalytic performance of PCN-224 was explored for isopropanol (IPA) oxidation under visible light. The implantation of Fe(III) ions in the PCN-224 is expected to realize two purpose. Firstly, the Fe(III) sites in the PCN-224 can capture electrons from the excited PCN-224, which would induce the efficient separation of electron-hole pairs. Secondly, a Fenton reaction could be constructed on Fe(III) implanted PCN-224 photocatalyst, in which the light energy was used as power, PCN-224 photocatalyst acted as an in situ and robust H<sub>2</sub>O<sub>2</sub> generator, and the modified Fe(III) acted as a trigger of H<sub>2</sub>O<sub>2</sub> conversion to produce considerably abundant oxygen-related radicals. Therefore, the enhanced photocatalytic activity for IPA oxidation can be expected over Fe(III) implanted PCN-224.

## **Chapter 5 Boosting charge separation *via* single cobalt atom implantation in MOFs for efficient visible-light driven CO<sub>2</sub> reduction**

The separation efficiency of the photoinduced charge carriers and the highly directional excitons transfer play important roles for the final photocatalytic activity. In this chapter, I aim to realize the modular optimization of a porphyrinic MOFs based photocatalyst by incorporation of coordinatively unsaturated single atom into the porphyrin unit. The presence of single cobalt atom in the MOF is expected to greatly boost its electron-hole separation efficiency. Directional migration of photogenerated exciton from porphyrin to catalytic cobalt centers can also be expected. Thus the newly developed MOFs can achieve the supply of long-lived electrons for the reduction of CO<sub>2</sub> molecules that are adsorbed on cobalt centers, leading to the enhanced photocatalytic CO<sub>2</sub> reduction.

# Chapter 1

---

## Chapter 6 General conclusion and future prospects

This chapter gives an overall summary of the achievements of this dissertation, and presents the prospects for future work.

## References

1. X. B. Chen, S. H. Shen, L. J. Guo, S. S. Mao, *Chem. Rev.*, **2010**, *110*, 6503-6570.
2. D. J. Martin, G. G. Liu, S. J. A. Moniz, Y. P. Bi, A. M. Beale, J. H. Ye, J. W. Tang, *Chem. Soc. Rev.*, **2015**, *44*, 7808-7828.
3. A. Kudo, Y. Miseki, *Chem. Soc. Rev.*, **2009**, *38*, 253-278.
4. H. Tong, S. X. Ouyang, Y. P. Bi, N. Umezawa, M. Oshikiri, J. H. Ye, *Adv. Mater.*, **2012**, *24*, 229-251.
5. X. J. Lang, X. D. Chen, J. C. Zhao, *Chem. Soc. Rev.*, **2014**, *43*, 473-486.
6. T. Ohno, L. Bai, T. Hisatomi, K. Maeda, K. Domen, *J. Am. Chem. Soc.*, **2012**, *134*, 8254-8259.
7. Q. Liu, Y. Zhou, J. H. Kou, X. Y. Chen, Z. P. Tian, J. Gao, S. C. Yan, Z. G. Zou, *J. Am. Chem. Soc.*, **2010**, *132*, 14385-14387.
8. S. N. Habisreutinger, L. Schmidt-Mende, J. K. Stolarczyk, *Angew. Chem. Int. Ed.*, **2013**, *52*, 7372-7408.
9. N. Zhang, R. Ciriminna, M. Pagliaro, Y. J. Xu, *Chem. Soc. Rev.*, **2014**, *43*, 5276-5287.
10. A. Fujishima, K. Honda, *Nature*, **1972**, *238*, 37.
11. R. Asahi, T. Morikawa, T. Ohwaki, K. Aoki, Y. Taga, *Science*, **2001**, *293*, 269-271.
12. A. L. Linsebigler, G. Q. Lu, J. T. Yates, *Chem. Rev.*, **1995**, *95*, 735-758.
13. M. Takeuchi, K. Sakamoto, G. Martra, S. Coluccia, M. Anpo, *J. Phys. Chem. B*, **2005**, *109*, 15422-15428.
14. S. G. Kumar, L. G. Devi, *J. Phys. Chem. A*, **2011**, *115*, 13211-13241.
15. R. Daghrir, P. Drogui, D. Robert, *Ind. Eng. Chem. Res.*, **2013**, *52*, 3581-3599.

# Chapter 1

---

16. L. W. Zhang, H. B. Fu, Y. F. Zhu, *Adv. Funct. Mater.*, **2008**, *18*, 2180-2189.
17. C. Y. Wang, C. Bottcher, D. W. Bahnemann, J. K. Dohrmann, *J. Mater. Chem.*, **2003**, *13*, 2322-2329.
18. M. Iwasaki, M. Hara, H. Kawada, H. Tada, S. Ito, *J. Colloid Interf Sci.*, **2000**, *224*, 202-204.
19. G. Colon, M. Maicu, M. C. Hidalgo, J. A. Navio, *Appl. Catal. B-Environ.*, **2006**, *67*, 41-51.
20. V. D. Binas, K. Sambani, T. Maggos, A. Katsanaki, G. Kiriakidis, *Appl. Catal. B-Environ.*, **2012**, *113*, 79-86.
21. K. S. Yang, Y. Dai, B. B. Huang, *J. Phys. Chem. C*, **2007**, *111*, 18985-18994.
22. T. Ohno, T. Mitsui, M. Matsumura, *Chem. Lett.*, **2003**, *32*, 364-365.
23. M. Sathish, B. Viswanathan, R. P. Viswanath, C. S. Gopinath, *Chem. Mater.*, **2005**, *17*, 6349-6353.
24. F. G. Wang, C. Di Valentin, G. Pacchioni, *Chemcatchem*, **2012**, *4*, 476-478.
25. K. L. Zhang, C. M. Liu, F. Q. Huang, C. Zheng, W. D. Wang, *Appl. Catal. B-Environ.*, **2006**, *68*, 125-129.
26. Z. F. Zhu, F. Yu, Y. Man, Q. Y. Tian, Y. He, N. Z. Wu, *J. Solid State Chem.*, **2005**, *178*, 224-229.
27. M. S. Jeon, W. S. Yoon, H. Joo, T. K. Lee, H. Lee, *Appl. Surf. Sci.*, **2000**, *165*, 209-216.
28. H. Kato, H. Kobayashi, A. Kudo, *J. Phys. Chem. B*, **2002**, *106*, 12441-12447.
29. M. Hara, T. Kondo, M. Komoda, S. Ikeda, K. Shinohara, A. Tanaka, J. N. Kondo, K. Domen, *Chem. Commun.*, **1998**, 357-358.
30. P. Wang, B. B. Huang, X. Y. Qin, X. Y. Zhang, Y. Dai, J. Y. Wei, M. H. Whangbo, *Angew. Chem. Int. Ed.*, **2008**, *47*, 7931-7933.
31. C. G. Tian, Q. Zhang, A. P. Wu, M. J. Jiang, Z. L. Liang, B. J. Jiang, H. G. Fu, *Chem. Commun.*, **2012**, *48*, 2858-2860.
32. H. J. Yan, J. H. Yang, G. J. Ma, G. P. Wu, X. Zong, Z. B. Lei, J. Y. Shi, C. Li, *J. Catal.*, **2009**, *266*, 165-168.
33. T. Hisatomi, K. Miyazaki, K. Takanabe, K. Maeda, J. Kubota, Y. Sakata, K. Domen, *Chem. Phys. Lett.*, **2010**, *486*, 144-146.

# Chapter 1

---

34. Z. Y. Wang, B. B. Huang, Y. Dai, X. Y. Qin, X. Y. Zhang, P. Wang, H. X. Liu, J. X. Yu, *J. Phys. Chem. C*, **2009**, *113*, 4612-4617.
35. T. Zhang, W. B. Lin, *Chem. Soc. Rev.*, **2014**, *43*, 5982-5993.
36. M. A. Nasalevich, M. van der Veen, F. Kapteijn, J. Gascon, *Crystengcomm*, **2014**, *16*, 4919-4926.
37. Y. Li, H. Xu, S. X. Ouyang, J. H. Ye, *Phys. Chem. Chem. Phys.*, **2016**, *18*, 7563-7572.
38. J. L. Wang, C. Wang, W. B. Lin, *Acs Catal.*, **2012**, *2*, 2630-2640.
39. Q. L. Zhu, Q. Xu, *Chem. Soc. Rev.*, **2014**, *43*, 5468-5512.
40. D. K. Wang, M. T. Wang, Z. H. Li, *Acs Catal.*, **2015**, *5*, 6852-6857.
41. C. Wang, K. E. deKrafft, W. B. Lin, *J. Am. Chem. Soc.*, **2012**, *134*, 7211-7214.
42. X. Yu, S. M. Cohen, *J. Am. Chem. Soc.*, **2016**, *138*, 12320-12323.
43. H. Q. Xu, J. H. Hu, D. K. Wang, Z. H. Li, Q. Zhang, Y. Luo, S. H. Yu, H. L. Jiang, *J. Am. Chem. Soc.*, **2015**, *137*, 13440-13443.
44. J. J. Du, Y. P. Yuan, J. X. Sun, F. M. Peng, X. Jiang, L. G. Qiu, A. J. Xie, Y. H. Shen, J. F. Zhu, *J. Hazard. Mater.*, **2011**, *190*, 945-951.
45. J. L. Long, S. B. Wang, Z. X. Ding, S. C. Wang, Y. E. Zhou, L. Huang, X. X. Wang, *Chem. Commun*, **2012**, *48*, 11656-11658.
46. D. R. Sun, L. Ye, Z. H. Li, *Appl. Catal. B-Environ*, **2015**, *164*, 428-432.
47. S. Pu, L. Xu, L. Sun, H. B. Du, *Inorg. Chem. Commun.*, **2015**, *52*, 50-52.
48. J. H. Cavka, S. Jakobsen, U. Olsbye, N. Guillou, C. Lamberti, S. Bordiga, K. P. Lillerud, *J. Am. Chem. Soc.*, **2008**, *130*, 13850-13851.
49. H. Furukawa, F. Gandara, Y. B. Zhang, J. C. Jiang, W. L. Queen, M. R. Hudson, O. M. Yaghi, *J. Am. Chem. Soc.*, **2014**, *136*, 4369-4381.
50. H. L. Jiang, D. W. Feng, T. F. Liu, J. R. Li, H. C. Zhou, *J. Am. Chem. Soc.*, **2012**, *134*, 14690-14693.
51. S. Surble, C. Serre, C. Mellot-Draznieks, F. Millange, G. Ferey, *Chem. Commun*, **2006**, 284-286.
52. P. Horcajada, S. Surble, C. Serre, D. Y. Hong, Y. K. Seo, J. S. Chang, J. M. Greneche, I. Margiolaki, G. Ferey, *Chem. Commun*, **2007**, 2820-2822.

# Chapter 1

---

53. P. Horcajada, C. Serre, G. Maurin, N. A. Ramsahye, F. Balas, M. Vallet-Regi, M. Sebban, F. Taulelle, G. Ferey, *J. Am. Chem. Soc.*, **2008**, *130*, 6774-6780.
54. C. Scherb, A. Schodel, T. Bein, *Angew. Chem. Int. Ed.*, **2008**, *47*, 5777-5779.
55. K. M. L. Taylor-Pashow, J. Della Rocca, Z. G. Xie, S. Tran, W. B. Lin, *J. Am. Chem. Soc.*, **2009**, *131*, 14261.
56. M. Dan-Hardi, C. Serre, T. Frot, L. Rozes, G. Maurin, C. Sanchez, G. Ferey, *J. Am. Chem. Soc.*, **2009**, *131*, 10857.
57. M. A. Nasalevich, M. G. Goesten, T. J. Savenije, F. Kapteijn, J. Gascon, *Chem. Commun*, **2015**, *51*, 961-962.
58. K. G. M. Laurier, F. Vermoortele, R. Ameloot, D. E. De Vos, J. Hofkens, M. B. J. Roeffaers, *J. Am. Chem. Soc.*, **2013**, *135*, 14488-14491.
59. L. H. Ai, C. H. Zhang, L. L. Li, J. Jiang, *Appl. Catal. B-Environ*, **2014**, *148*, 191-200.
60. J. K. Gao, J. W. Miao, P. Z. Li, W. Y. Teng, L. Yang, Y. L. Zhao, B. Liu, Q. C. Zhang, *Chem. Commun*, **2014**, *50*, 3786-3788.
61. C. Gomes Silva, I. Luz, F. X. Llabres i Xamena, A. Corma, H. Garcia, *Chemistry*, **2010**, *16*, 11133-11138.
62. Y. Horiuchi, T. Toyao, M. Saito, K. Mochizuki, M. Iwata, H. Higashimura, M. Anpo, M. Matsuoka, *J. Phys. Chem. C*, **2012**, *116*, 20848-20853.
63. M. A. Nasalevich, R. Becker, E. V. Ramos-Fernandez, S. Castellanos, S. L. Veber, M. V. Fedin, F. Kapteijn, J. N. H. Reek, J. I. van der Vlugt, J. Gascon, *Energy Environ. Sci.*, **2015**, *8*, 364-375.
64. C. Wang, Z. Xie, K. E. deKrafft, W. Lin, *J. Am. Chem. Soc.*, **2011**, *133*, 13445-13454.
65. L. Chi, Q. Xu, X. Y. Liang, J. D. Wang, X. T. Su, *Small*, **2016**, *12*, 1351-1358.
66. Y. H. Fu, D. R. Sun, Y. J. Chen, R. K. Huang, Z. X. Ding, X. Z. Fu, Z. H. Li, *Angew. Chem. Int. Ed.*, **2012**, *51*, 3364-3367.
67. D. R. Sun, Y. H. Fu, W. J. Liu, L. Ye, D. K. Wang, L. Yang, X. Z. Fu, Z. H. Li, *Chem-Eur. J*, **2013**, *19*, 14279-14285.

# Chapter 1

---

68. D. K. Wang, R. K. Huang, W. J. Liu, D. R. Sun, Z. H. Li, *Acs Catal.*, **2014**, *4*, 4254-4260.
69. L. Shen, W. Wu, R. Liang, R. Lin, L. Wu, *Nanoscale*, **2013**, *5*, 9374-9382.
70. H. Wang, X. Z. Yuan, Y. Wu, G. M. Zeng, X. H. Chen, L. J. Leng, Z. B. Wu, L. B. Jiang, H. Li, *J. Hazard Mater.*, **2015**, *286*, 187-194.
71. J. J. Zhou, R. Wang, X. L. Liu, F. M. Peng, C. H. Li, F. Teng, Y. P. Yuan, *Appl. Surf. Sci.*, **2015**, *346*, 278-283.
72. T. W. Goh, C. X. Xiao, R. V. Maligal-Ganesh, X. L. Li and W. Y. Huang, *Chem Eng Sci*, **2015**, *124*, 45-51.
73. S. B. Wang, X. C. Wang, *Appl. Catal. B-Environ*, **2015**, *162*, 494-500.
74. C. C. Hou, T. T. Li, S. Cao, Y. Chen, W. F. Fu, *J. Mater. Chem. A*, **2015**, *3*, 10386-10394.
75. X. L. Liu, R. Wang, M. Y. Zhang, Y. P. Yuan, C. Xue, *Apl. Mater.*, **2015**, *3*.
76. C. H. Hendon, D. Tiana, M. Fontecave, C. Sanchez, L. D'arras, C. Sassoeye, L. Rozes, C. Mellot-Draznieks, A. Walsh, *J. Am. Chem. Soc.*, **2013**, *135*, 10942-10945.
77. L. M. Yang, G. Y. Fang, J. Ma, E. Ganz, S. S. Han, *Cryst. Growth Des.*, **2014**, *14*, 2532-2541.
78. D. R. Sun, W. J. Liu, M. Qiu, Y. F. Zhang, Z. H. Li, *Chem. Commun.*, **2015**, *51*, 10765-10765.
79. J. He, J. Wang, Y. Chen, J. Zhang, D. Duan, Y. Wang, Z. Yan, *Chem. Commun.*, **2014**, *50*, 7063-7066.
80. Y. P. Yuan, L. S. Yin, S. W. Cao, G. S. Xu, C. H. Li, C. Xue, *Appl. Catal. B-Environ*, **2015**, *168*, 572-576.
81. Z. Sha, J. L. Sun, H. S. O. Chan, S. Jaenicke, J. S. Wu, *Rsc Adv.*, **2014**, *4*, 64977-64984.
82. R. Panda, S. Rahut, J. K. Basu, *Rsc Adv.*, **2016**, *6*, 80981-80985.

# **Chapter 2 Construction of an amine-functionalized iron(III) metal-organic framework as efficient visible-light photocatalyst for Cr(VI) reduction**

## **2.1 Introduction**

The increasing toxic heavy metal ions contamination in natural water has become a serious issue faced by all the governments in the world, which stimulates intense research on the advanced technology for water treatment.<sup>1,2</sup> Hexavalent chromium (Cr(VI)) is a typical heavy metal ion contaminant in the waste water arising from some industrial process, such as leather tanning, paint-making or steel manufacturing.<sup>3,4</sup> Cr(VI) is highly toxic to organisms, carcinogenic in human beings, and is mobile in the nature due to its high solubility in water.<sup>5</sup> Therefore, Cr(VI) has been listed as one of the priority controlled pollutants and its concentration in drinking water has been strictly regulated by many countries. Various techniques for removing Cr(VI) from waste water have been developed, including chemical precipitation, ion exchange, membrane separation, adsorption and reduction.<sup>6-8</sup>

The reduction of Cr(VI) to Cr(III) is considered as an efficient strategy for the removal of Cr(VI) in the waste water, because Cr(III) is environmentally friendly and vital to plants and human life.<sup>5</sup> Meanwhile, Cr(III) is mostly immobile, which can be precipitated or sorbed on a variety of substrates in neutral or alkaline solutions.<sup>8</sup> Reduction of Cr(VI) to Cr(III) by semiconductor photocatalysis is a relatively effective method for the removal of Cr(VI) in the waste water. This photocatalytic method is based on the electron-hole pairs ( $e^-$  -  $h^+$ ) generated in the semiconductor materials under illumination by light of energy greater than the semiconductor band gap.<sup>9</sup> These electrons, which migrate to the

## Chapter 2

---

semiconductor surface, are capable of reducing Cr(VI) to Cr(III) in the solution. Many researchers have reported the photocatalytic reduction of Cr(VI) over TiO<sub>2</sub>.<sup>10-13</sup> However, the application of TiO<sub>2</sub> is limited by its wide band gap (3-3.2 eV), which can only absorb the UV light occupying no more than 5% in solar light.<sup>14</sup> In recent years, many efforts have been devoted to searching for other efficient photocatalysts that are active under visible-light irradiation. The photocatalytic reduction of Cr(VI) over visible-light active photocatalysts such as CdS, SnS<sub>2</sub>, Ag<sub>2</sub>S and WO<sub>3</sub> has been widely reported.<sup>15-18</sup> But unfortunately, the activity of these photocatalyst for the reduction of Cr(VI) is not very high and the reduction process usually takes a long time. On the other hand, sulfide materials are normally not stable enough to be used as photocatalysts due to the photocorrosion problem, and may cause secondary pollution because of their high toxicity.<sup>19</sup> Thereby, to explore novel visible-light active photocatalysts with stable and high photocatalytic ability for the reduction of Cr(VI) is desperately needed.

Metal-organic frameworks (MOFs) are a class of hybrid porous materials composed of metal-oxo clusters and organic building blocks, which have shown a variety of potential applications.<sup>20-23</sup> Especially, the application of MOFs in photocatalysis is emerging as an interesting topic recently.<sup>24</sup> Compared with the traditional photocatalysts, the superiority of MOFs is based on their desirable topology and high surface area, which is beneficial for fast transport and good accommodation of guest molecules. Moreover, the band gap of MOFs is closely related to the HOMO-LUMO gap, which may be flexibly tuned through rational modification of the inorganic unit or the organic linker during synthetic procedures, thus the efficient light harvesting can be realized.<sup>25</sup> In this context, Gascon et al. observed that the band gap energy of MOF-5 can be tuned by changing the organic linker.<sup>26</sup> A theoretical study from Walsh et al. also revealed that the optical response of a Ti-based MOF could be successfully tuned through rational functionalization of the linking unit.<sup>27</sup> These studies demonstrated the high potential of MOFs as photocatalysts. In fact, some MOFs such as titanium, zirconium and iron based MOFs have already been demonstrated to have photocatalytic activities for dye degradation, water splitting and CO<sub>2</sub> reduction.<sup>28-34</sup> The proposed photocatalytic mechanism involves an photoinduced electron transfer from the photoexcited organic linker to the metal-oxo clusters within MOFs and the direct excitation of metal-oxo

## Chapter 2

---

cluster.<sup>34</sup> Despite the great progress achieved so far, the photocatalytic performance of MOFs have not been fully exploited. In particular, little work has been reported on application of MOFs for the photocatalytic reduction of Cr(VI) with high performance and good stability.

Herein, I reported the photocatalytic reduction of Cr(VI) over an amine-functionalized iron(III) MOF (NH<sub>2</sub>-MIL-88B) under visible-light irradiation. It was found that NH<sub>2</sub>-MIL-88B (Fe) exhibited an excellent reusability and much higher photocatalytic activity for Cr(VI) reduction than that of MIL-88B (Fe) under visible-light irradiation. Importantly, the visible-light activity of NH<sub>2</sub>-MIL-88B (Fe) is even higher than widely used photocatalyst P25 irradiated under UV-visible light. Furthermore, iron(III) based MOFs with mixed 1, 4-benzenedicarboxylic acid (BDC) and 2-amino- benzenedicarboxylic acid (BDC-NH<sub>2</sub>) ligands were prepared, and those MOFs all exhibited MIL-88B structure. The introduction of amino group in iron(III) based MOFs can enhance efficiency for the photocatalytic Cr(VI) reduction, the more the better. A dual excitation pathways mechanism for photocatalytic reduction of Cr(VI) over NH<sub>2</sub>-MIL-88B(Fe) was proposed: i.e., photoinduced exciting of amine functionality followed by electron transfer from the excited organic linker to the Fe<sub>3</sub>-μ<sub>3</sub>-oxo clusters and the direct excitation of Fe<sub>3</sub>-μ<sub>3</sub>-oxo clusters. The electron transfer phenomenon was revealed by photoluminescence (PL), electron spin resonance (ESR) and transient photocurrent studies. The effect of amine functionalization in the other two Iron(III)-based MOFs (MIL-53 (Fe) and MIL-101 (Fe) ) on the visible light photocatalytic activity for the reduction of Cr(VI) was also studied. The same trend was observed, namely all of the amine functionalized MOFs showed enhanced activity for photocatalytic Cr(VI) reduction compared with those of their parent MOFs. This work provides us with better understanding of photocatalytic behavior over MOFs photocatalyst and also demonstrates the promising potential of MOFs as high stable and efficient photocatalysts.

### 2.2 Experimental section

#### 2.2.1 Materials

N, N-dimethylformamide (DMF), ferric chloride hexahydrate ( $\text{FeCl}_3 \cdot 6\text{H}_2\text{O}$ ), 1, 4-benzenedicarboxylic acid (BDC) and 2-amino-benzenedicarboxylic acid ( $\text{BDC-NH}_2$ ) were purchased from Wako Co. All reagents were analytical grade and used without further purification. Deionized water (18.2 M $\Omega$ ) used throughout all experiments was produced using a Millipore Direct-Q System.

#### 2.2.2 Synthesis of photocatalysts

Iron(III) based MOFs MIL-88B (Fe) and amine-functionalized MIL-88B (Fe) ( $\text{NH}_2\text{-MIL-88B (Fe)}$ ) crystals were produced from a rapid microwave-assisted solvothermal synthesis method. For the synthesis of MIL-88B (Fe), BDC (3mmol, 0.49839g) and  $\text{FeCl}_3 \cdot 6\text{H}_2\text{O}$  (3mmol, 0.8109g) were dissolved in DMF (50 mL). After vigorously stirred for 10 min, this solution was placed in a sealed vessel and heated by microwave at 400W for 15 min at 150°C. After cooling to room temperature, the resulting particles were isolated by centrifugation, washed with ethanol and deionized water several times, and then dried at 343 K under vacuum overnight.  $\text{NH}_2\text{-MIL-88B (Fe)}$  was achieved by replacing BDC with  $\text{BDC-NH}_2$ , while keeping all other synthetic conditions unchanged. Mixed MIL-88B (Fe) was prepared using a similar procedure as above except that a certain percentage of BDC was replaced with  $\text{BDC-NH}_2$ . Other two visible light active MOF photocatalysts  $\text{NH}_2\text{-Uio-66-Zr}$  and  $\text{NH}_2\text{-MIL-125-Ti}$  were synthesized according to the literatures previously reported.<sup>32, 33</sup> Iron(III) based MOFs MIL-53, MIL-101 and their amine functionalized derivatives were synthesized according to the literatures.<sup>46-48</sup> Briefly, MIL-53 (Fe) was synthesized from a mixture of  $\text{FeCl}_3 \cdot 6\text{H}_2\text{O}$ , BDC and DMF with a molar ratio of 1:1:280, then the mixture was heated at 150°C for 15 hours with a heating ramp of 1 hour. The amine functionalized  $\text{NH}_2\text{-MIL-53 (Fe)}$  was synthesized by hydrothermal treatment of a mixture of 0.9 g (5 mmol) of  $\text{BDC-NH}_2$ , 50 mL of  $\text{H}_2\text{O}$ , and 1.35 g (5 mmol) of  $\text{FeCl}_3 \cdot 6\text{H}_2\text{O}$  at 150°C for three days. MIL-101 (Fe) was synthesized via a hydrothermal reaction of a mixture of  $\text{FeCl}_3 \cdot 6\text{H}_2\text{O}$ , BDC and DMF with a molar ratio of 2:1:560 at 110°C for 24 h.  $\text{NH}_2\text{-MIL-101(Fe)}$  was prepared similarly to MIL-101(Fe) except that BDC was replaced

## Chapter 2

---

by BDC-NH<sub>2</sub>. All the as-synthesized Iron(III) based MOFs were obtained by centrifugation, washed with water and ethanol several times, and then dried at 343 K under vacuum overnight. g-C<sub>3</sub>N<sub>4</sub> was prepared by heating melamine to 550°C for 4 hours under air condition in a crucible.

### 2.2.3 Characterization

The X-ray diffraction (XRD) patterns of the prepared samples were recorded on an X-ray diffractometer (Shimadzu, XRD-7000) with monochromatized Cu K $\alpha$  radiation ( $\lambda=1.54178 \text{ \AA}$ ), under 40kV and 30 mA. UV-visible diffuse reflectance spectra were measured on UV-visible spectrophotometer (Hitachi U-3900) with BaSO<sub>4</sub> as the reflectance standard reference. X-ray Photoelectron Spectroscopy (XPS) were performed on Thermo ESCALAB250 using monochromatized Al K $\alpha$  at  $h\nu = 1486.6 \text{ eV}$ . The morphology and size of the samples were observed with a scanning electron microscope (SEM, JSM-6701F, JEOL Co., Japan). The PL spectra were recorded on a JASCO FP-6500 spectrofluorometer. Electron spin resonance (ESR) characterizations were carried out with JEOL JES-FA-200 at room temperature under vacuum.

### 2.2.4 Photoelectrochemical Measurement

To prepare the photoelectrodes, 10 mg iron(III) based MOFs was added into 1 ml of ethanol. The as-prepared solution was stirred for one hour to ensure that the iron (III) based MOFs were uniformly dispersed in the solution. 10  $\mu\text{l}$  of the 10 mg/ml iron (III) based MOFs solution was dropped onto the surface of ITO substrate, which had an exposed area of  $1.0 \times 1.0 \text{ cm}^2$ , and then dried under vacuum condition for 1 h at 80°C. This step was repeated five times to ensure a uniform coverage of iron(III) based MOFs on ITO. Photocurrent measurements were performed with an electrochemical station (ALS/CH model 650A, Japan) using a three-electrode mode with 0.5 M Na<sub>2</sub>SO<sub>4</sub> solution (pH=7.0) as the electrolyte. The iron (III) based MOFs photoanodes were used as working electrodes; a Pt wire served as a counter electrode. The Ag/AgCl electrode was used as the reference electrodes. A 500 W Xe lamp with

## Chapter 2

---

a UV-cutoff filter (420nm) was used as the visible light source. The Mott-Schottky measurements were performed at a frequency of 1000 Hz in the dark.

### 2.2.5 Photocatalytic experiments

The photocatalytic activities of iron (III) based MOFs were evaluated by photocatalytic reduction of Cr(VI) under visible-light irradiation of a 300 W Xe arc lamp with a 420 nm cutoff filter and cooling water filter. Potassium dichromate ( $K_2Cr_2O_7$ ) was selected as a Cr(VI) compound. The photocatalytic reduction of Cr(VI) was performed at about 30°C in a quartz reactor containing 20 mg photocatalyst and 40 ml of Cr(VI) solution (8 mg L<sup>-1</sup> based on Cr in a dilute  $K_2Cr_2O_7$  solution). The solution was stirred for 40 min in the dark to reach adsorption equilibrium and then was exposed to visible light irradiation. The Cr content in the reaction solution was determined using the diphenylcarbazide (DPC) method.<sup>17</sup> The photocatalytic efficiency was determined by dividing  $C/C_0$ , where C is the remained Cr(VI) concentration and  $C_0$  is the starting Cr(VI) concentration.

## 2.3 Results and discussion

### 2.3.1 Characterization of MOF photocatalysts

Metal-organic framework MIL-88B (Fe) and  $NH_2$ -MIL-88B (Fe) were produced through a rapid microwave-assisted solvothermal synthesis method. The crystallographic structure of the products was determined by powder X-ray diffraction (PXRD). As shown in Figure 2.1a, the well-defined diffraction peaks revealed the high crystallinity of the products, which are in good agreement with the simulated MIL-88B structure. The MIL-88B(Fe) and  $NH_2$ -MIL-88B(Fe) exhibits the same diffraction pattern, indicating that the crystal phase structure is retained after amine functionalization. The MIL-88B frameworks are built up from  $Fe_3-\mu_3$ -oxo clusters interconnected by oxidation stable terephthalate linkers (Figure 2.1b).  $Fe_3-\mu_3$ -oxo cluster exhibits an octahedral structure with three iron atoms, four oxygen atoms from the bidentate dicarboxylates, one  $\mu_3O$  oxygen atom and one oxygen from terminal ligand (water molecular or halogenide ligand).<sup>35</sup> The morphology and particle size of these obtained MIL-88B (Fe) and

## Chapter 2

NH<sub>2</sub>-MIL-88B (Fe) crystals were observed by scanning electron microscopy (SEM). Figure 2.2 (a) and (b) show that MIL-88B (Fe) crystals have a spindle-shaped morphology with an average size of 5.5 μm in length and 3.2 μm in diameter. In comparison, the NH<sub>2</sub>-MIL-88B (Fe) crystals were needle-shaped with a length of about 1.6 μm and a diameter of 260 nm (Figure 2.2 c, d). In order to elucidate the semiconductor properties of NH<sub>2</sub>-MIL-88B (Fe) and MIL-88B (Fe), Mott-Schottky measurements have been conducted. As shown in Figure 2.3, the flat-band potential of MIL-88B (Fe) is determined to be 0.13 V vs. NHE, which is more negative than the Cr(VI)/Cr(III) potential (+1.15 V, pH 3.0).<sup>36</sup> This indicates that MIL-88B (Fe) has potential for the reduction of Cr(VI) to Cr(III). The flat-band potential of NH<sub>2</sub>-MIL-88B (Fe) is also around 0.13 V vs. NHE, which means that the incorporation of amine group in MIL-88B (Fe) framework has little effect on the conduction band position. This can be explained that the conduction band of Iron(III)-based MIL-88B MOFs is mainly constructed from Fe 3d and O 2p states and the N 2p state from the amine group participates in the construction of valance band because of the strong electron-donating characteristics of aromatic amines.<sup>27</sup>

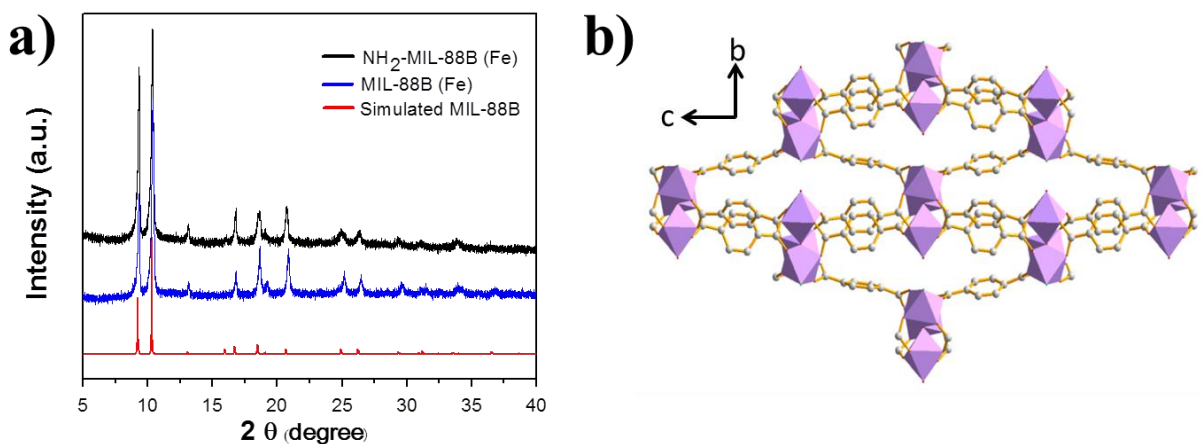


Figure 2.1. (a) XRD patterns of MIL-88B (Fe), NH<sub>2</sub>-MIL-88B (Fe) and simulated MIL-88B; (b) MIL-88B (Fe) structure viewed along *a* axis.

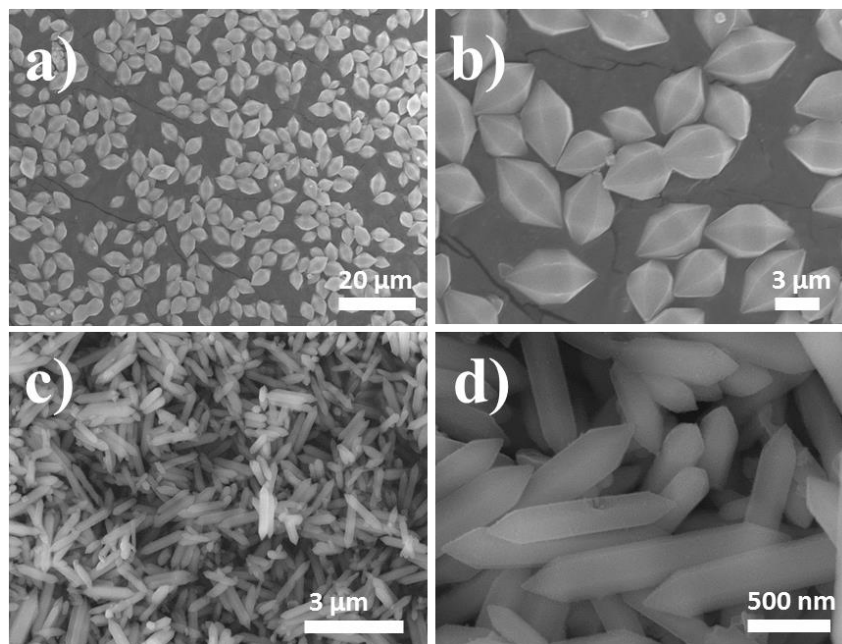


Figure 2.2. SEM images of (a)-(b) MIL-88B (Fe) and (c)-(d) NH<sub>2</sub>-MIL-88B (Fe).

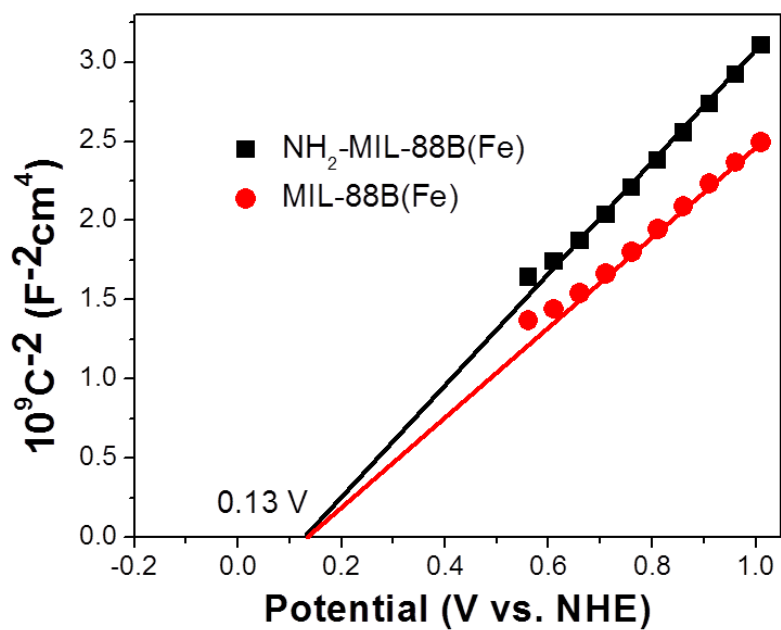


Figure 2.3. Mott-Schottky plot of MIL-88B (Fe) and NH<sub>2</sub>-MIL-88B(Fe).

## Chapter 2

---

### 2.3.2 Evaluation of photocatalytic activity

The photocatalytic reduction of Cr(VI) was performed over MIL-88B (Fe) and NH<sub>2</sub>-MIL-88B (Fe) under visible light irradiation. The photocatalytic reaction was evaluated through monitoring the decolorizing of the UV-vis adsorption spectra of DPC- Cr(VI) complex solutions. Figure 2.4a displays the time dependent spectral changes of DPC- Cr(VI) complex solution at various exposure times in the presence of NH<sub>2</sub>-MIL-88B (Fe) at pH 2. It shows that the reaction solution achieves the adsorption-desorption equilibrium after a presetting of 40 min in the dark. With the increase of irradiation time, the absorption peak at 540nm ascribed to the DPC- Cr(VI) complex decreases gradually, and it almost disappears after 45 min, which demonstrates the photocatalytic reduction of Cr(VI) over NH<sub>2</sub>-MIL-88B (Fe). Previous studies reported that the pH value of the solution had a great effect on the reduction rate of aqueous Cr(VI) over photocatalyst.<sup>36-37</sup> To investigate the influence of pH value on the photocatalytic reduction of Cr(VI), controlled experiments of photocatalytic reduction of Cr(VI) over NH<sub>2</sub>-MIL-88B (Fe) have been carried out with different pH values. Figure 2.4b presents the time dependence of the photocatalytic reduction of Cr(VI) catalyzed by NH<sub>2</sub>-MIL-88B (Fe) at different pH values. The pH value of the K<sub>2</sub>Cr<sub>2</sub>O<sub>7</sub> solution was adjusted in the range from 2 to 4 by addition of requisite amount of 0.2 M H<sub>2</sub>SO<sub>4</sub>. It shows that the lower pH value results in better photocatalytic performance. This catalysed effect of the acidified pH values is consistent with the previously reported results that the photocatalytic reduction of Cr(VI) is an acid-catalysed behavior.<sup>36-38</sup> At pH 2-4, the predominating species of chromium is Cr<sub>2</sub>O<sub>7</sub><sup>2-</sup>, and the Cr(VI) reduction reaction could be expressed as follows:<sup>36</sup>



The obtained performance of photocatalytic reduction of Cr(VI) over NH<sub>2</sub>-MIL-88B (Fe) was compared to those of MIL-88B (Fe), and two typical visible-light active MOF photocatalysts (NH<sub>2</sub>-Uio-66-Zr and

## Chapter 2

NH<sub>2</sub>-MIL-125-Ti). The formations of NH<sub>2</sub>-Uio-66-Zr and NH<sub>2</sub>-MIL-125-Ti have been confirmed by their XRD patterns (Figure 2.5). Figure 2.6a displays the time dependence of the photocatalytic reduction of Cr(VI) over different types of MOFs photocatalysts. It is obvious that the reduction of Cr(VI) hardly occurred in the absence of photocatalysts and NH<sub>2</sub>-MIL-88B (Fe) exhibits much higher activity than that of other visible-light MOFs photocatalysts. The obtained performance of photocatalytic reduction of Cr(VI) over NH<sub>2</sub>-MIL-88B (Fe) was also compared to those of N-doped TiO<sub>2</sub>, g-C<sub>3</sub>N<sub>4</sub>, commercial CdS and widely used photocatalyst P25 (Figure 2.7). It can be seen that the visible light photocatalytic performance of NH<sub>2</sub>-MIL-88B (Fe) is much higher than N-doped TiO<sub>2</sub> and g-C<sub>3</sub>N<sub>4</sub>. Importantly, NH<sub>2</sub>-MIL-88B (Fe) also showed even higher visible-light photocatalytic activity than that of P25, which is conducted under UV-visible light irradiation. This demonstrates that NH<sub>2</sub>-MIL-88B (Fe) exhibits superior photocatalytic activity for the reduction of Cr(VI).

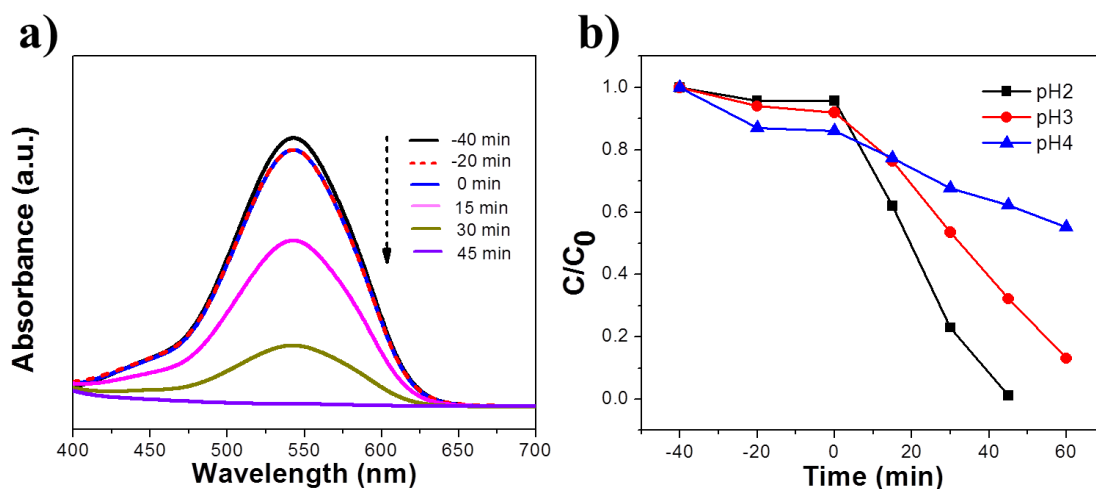


Figure 2.4. (a) Time-dependent absorption spectral pattern of DPC- Cr(VI) complex solutions after reduction over NH<sub>2</sub>-MIL-88B (Fe) at pH 2; (b) photocatalytic reduction of Cr(VI) over NH<sub>2</sub>-MIL-88B (Fe) at different pH values. Reaction condition: 20 mg photocatalyst, 40 ml of 8 ppm Cr(VI), reaction temperature is 30°C, visible light.

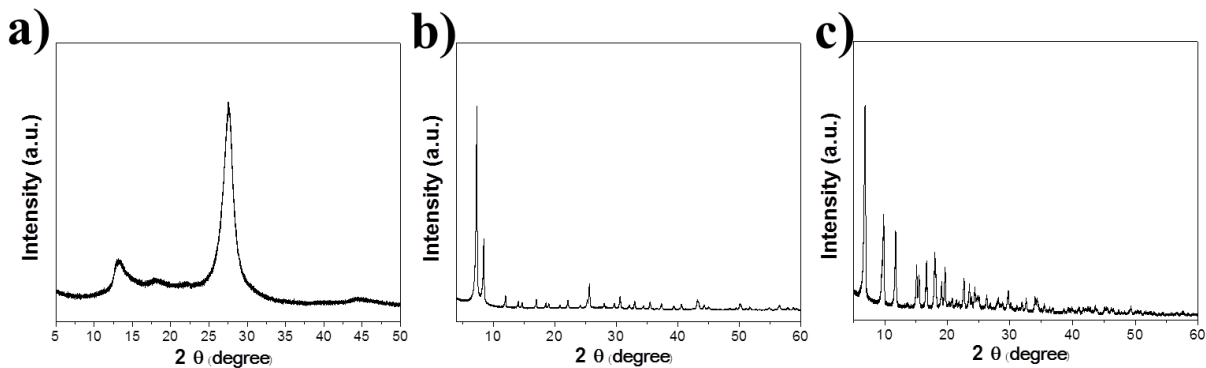


Figure 2.5. XRD patterns of (a)  $g\text{-C}_3\text{N}_4$ , (B)  $\text{NH}_2\text{-Uio-66-Zr}$  and (C)  $\text{NH}_2\text{-MIL-125-Ti}$ .

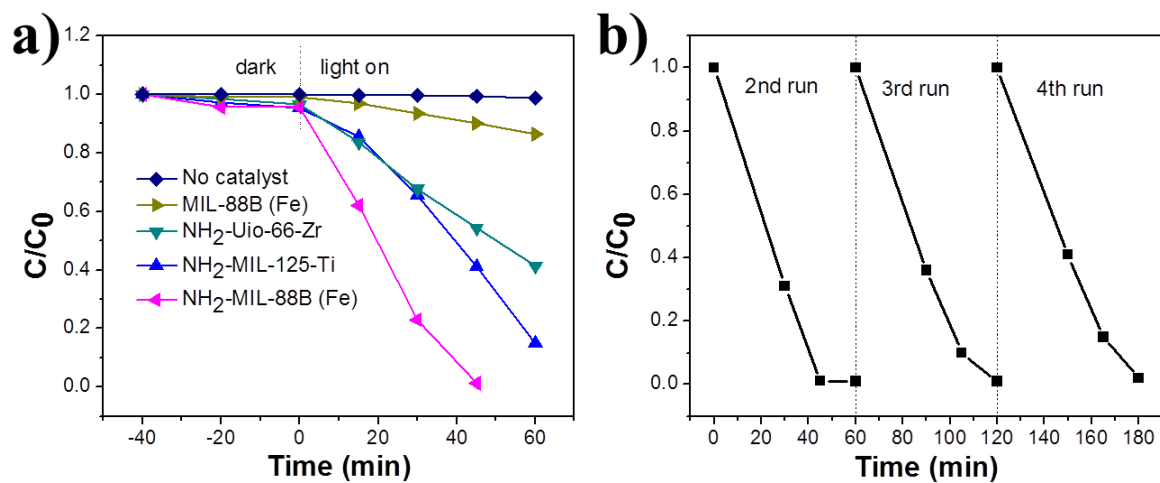


Figure 2.6. (a) Reduction profiles of photocatalytic reduction of  $\text{Cr(VI)}$  over various photocatalysts; (b) recycling test on  $\text{NH}_2\text{-MIL-88B (Fe)}$  for photocatalytic reduction of  $\text{Cr(VI)}$ . Reaction condition: 20 mg photocatalyst, 40 ml of 8 ppm  $\text{Cr(VI)}$ , reaction temperature is  $30^\circ\text{C}$ ,  $\text{pH}=2$ .

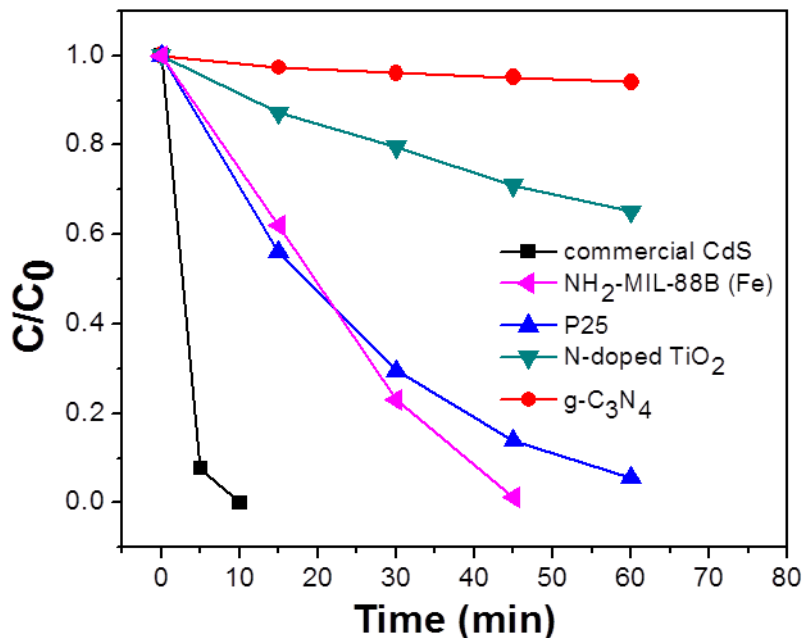


Figure 2.7. Reduction profiles of photocatalytic reduction of Cr(VI) over various photocatalysts. Reaction condition: 20 mg photocatalyst, 40 ml of 8 ppm Cr(VI), reaction temperature is 30°C, pH=2. P25 is conducted in UV-visible light and the other photocatalysts are conducted in visible light. The solution is stirred for 40 min in the dark and then is exposed to visible light irradiation.

It is well-known that the stability and reusability of the photocatalysts are very important from an economic point of view. The used photocatalyst can be recovered by filtration, washing with water and ethanol and then drying under vacuum. SEM images after photocatalytic reaction at different pH values were measured and shown in Figure 2.8. It is obvious that the morphology of NH<sub>2</sub>-MIL-88B (Fe) can almost retain at pH 2-4. However, the lower pH values (pH 1.7 and 1.5) result in the deterioration of morphology, and NH<sub>2</sub>-MIL-88B (Fe) can be totally dissolved when the pH value is adjusted to 1. Thus, the photocatalytic performance of NH<sub>2</sub>-MIL-88B (Fe) was tested under pH 2-4 conditions and the stability of the photocatalysts was further investigated at the reaction condition of pH 2. The XRD pattern of NH<sub>2</sub>-MIL-88B (Fe) after the photocatalytic reaction reveals almost no deterioration in the crystal structure (Figure 2.9), and the FTIR spectra of the photocatalyst after the reaction did not show obvious

## Chapter 2

changes (Figure 2.10). Inductively-coupled plasma analysis of the photocatalyst before and after the reaction revealed that only 0.9% iron ions leak from NH<sub>2</sub>-MIL-88B (Fe). All of the data indicate the stability of the photocatalyst in this reaction conditions.

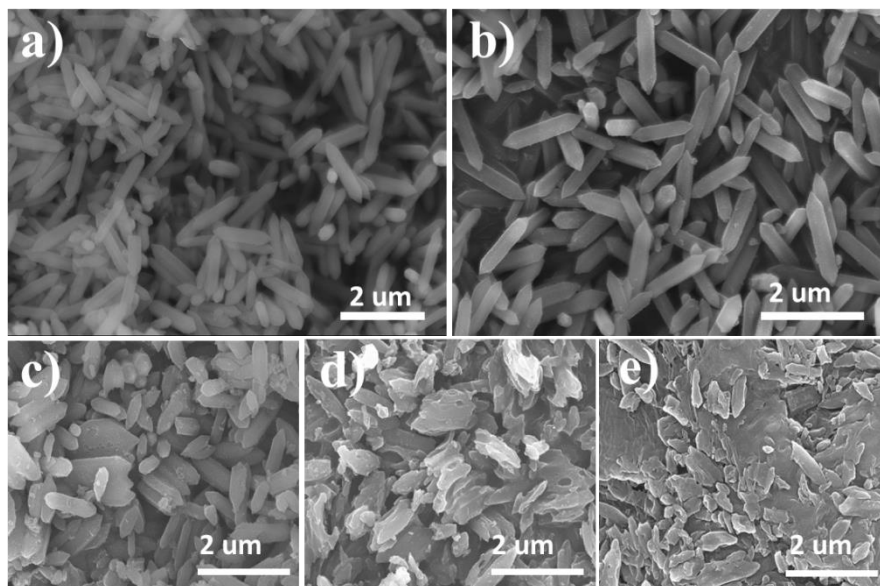


Figure 2.8. SEM images of NH<sub>2</sub>-MIL-88B (Fe) after photocatalytic reaction at different pH values: (a) 4; (b) 3; (c) 2; (d) 1.7; (e) 1.5.

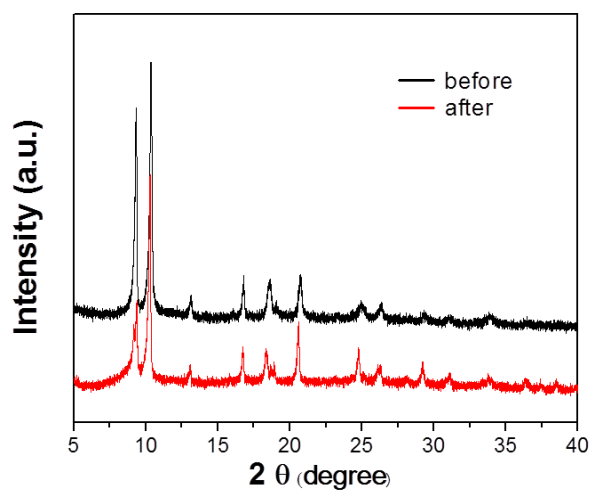


Figure 2.9. XRD patterns of NH<sub>2</sub>-MIL-88B (Fe) before and after photocatalytic reaction.

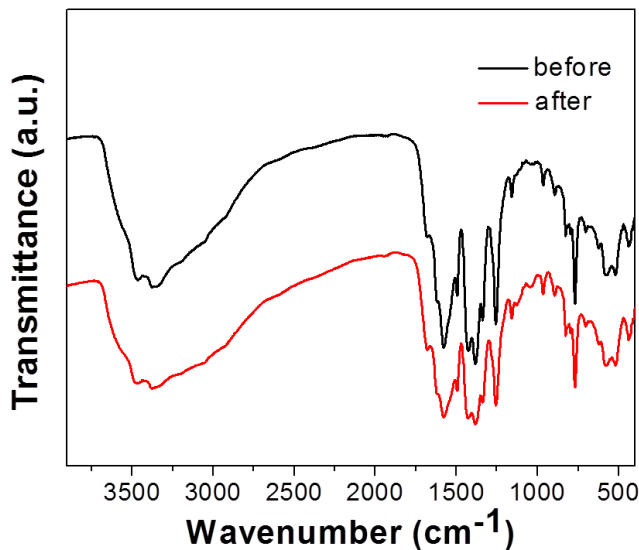


Figure 2.10. FTIR spectra of NH<sub>2</sub>-MIL-88B (Fe) before and after photocatalytic reaction.

The XPS results further confirm the stability of the photocatalyst. As shown in Figure 2.11, the XPS spectra of samples measured before and after photocatalytic reaction are almost the same. Fe 2p peaks of NH<sub>2</sub>-MIL-88B (Fe) at binding energy  $\sim 711$  eV and  $\sim 725$  eV are assigned to Fe 2p<sub>3/2</sub> and Fe 2p<sub>1/2</sub> for iron(III) oxide, which is consistent with the iron(III) based MOFs previously reported.<sup>39</sup> The N 1s XPS spectrum locates at 399.1 eV, and this is the same as BDC-NH<sub>2</sub> ligand.<sup>40</sup> Interestingly, in the XPS spectra of NH<sub>2</sub>-MIL-88B (Fe) after photocatalytic reaction, a weak peak located at 577.1 eV can be observed. This peak corresponds to Cr 2p and resembles the Cr(III) in Cr(OH)<sub>3</sub>.<sup>36</sup> This further confirm the reduction of Cr(VI) to Cr(III) over NH<sub>2</sub>-MIL-88B (Fe). Moreover, the weak intensity of Cr 2p XPS signal indicates that the Cr(III) can be removed by simply washing the sample, which is beneficial for reusability of the photocatalyst. I have further studied the reusability of the photocatalyst NH<sub>2</sub>-MIL-88B (Fe) by collecting and reusing the photocatalyst for four times. As shown in Figure 2.6b, the photocatalyst NH<sub>2</sub>-MIL-88B (Fe) can retain its good photocatalytic activity even after four cycles of reaction. Only insignificant decrease in photocatalytic activity is observed, which might be partly caused by loss of photocatalyst during each collection.

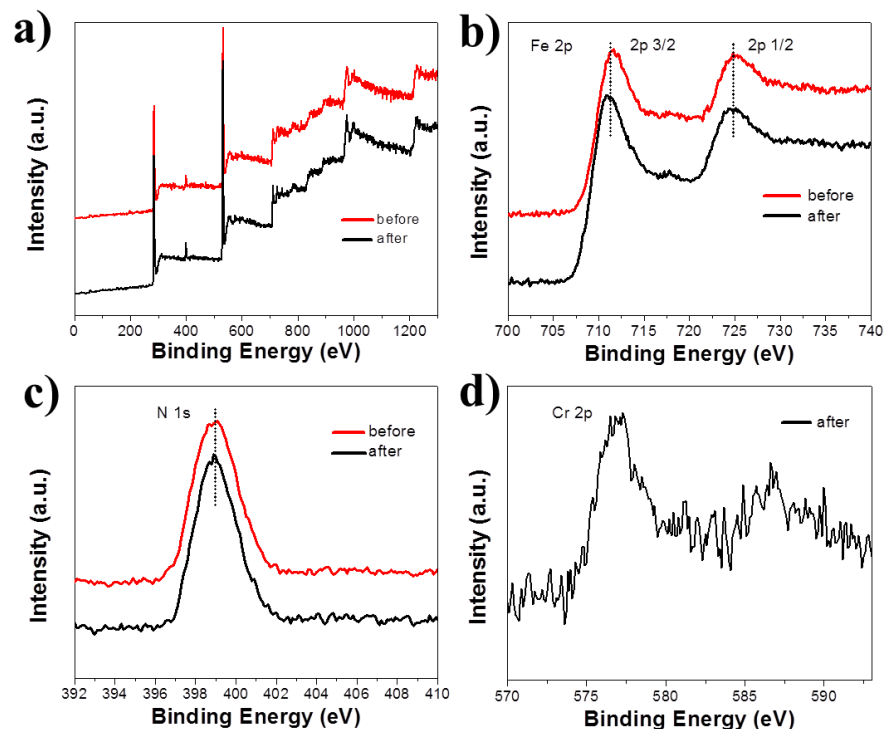


Figure 2.11. XPS patterns of  $\text{NH}_2\text{-MIL-88B (Fe)}$  before and after photocatalytic reaction.

### 2.3.3 Clarification of the mechanism

Iron(III)-based MOFs, containing Fe-oxo clusters, have already been demonstrated to have semiconductor properties for the photocatalytic degradation of Rhodamine B, which can be ascribed to the direct excitation of Fe-oxo clusters.<sup>41-42</sup> In this work,  $\text{NH}_2\text{-MIL-88B (Fe)}$  displays much higher visible light photocatalytic performance than  $\text{MIL-88B (Fe)}$ . Taking into account that  $\text{MIL-88B (Fe)}$  and  $\text{NH}_2\text{-MIL-88B (Fe)}$  contain the same  $\text{Fe}_3\text{-}\mu_3\text{-oxo}$  clusters and reduction potential, the amine group from the linkers contributes to the enhanced photocatalytic performance. Previous studies found that linker modification were beneficial for the UV-light active MOF photocatalysts based on titania or zirconia clusters, due to the ligand-to-metal charge transfer (LMCT) mechanism.<sup>32-33</sup> The photoluminescence (PL) has been proved as a powerful technique to study the LMCT mechanism in MOFs.<sup>32,43</sup> For  $\text{NH}_2\text{-MIL-88B (Fe)}$ , there also exists the electron transfer from the  $\text{BDC-NH}_2$  organic linker to  $\text{Fe}_3\text{-}\mu_3\text{-oxo}$  clusters, and

## Chapter 2

such electron-transfer process was studied by PL spectra. Actually, as displayed in Figure 2.12, when excited at 350nm, BDC-NH<sub>2</sub> showed a broad luminescence band centered at 540 nm, which is attributed to its local excitation.<sup>32</sup> However, NH<sub>2</sub>-MIL-88B (Fe) did not show any PL signal around 540 nm, thus suggesting the electron transfer from the excited BDC-NH<sub>2</sub> organic linker to the Fe<sub>3</sub>-μ<sub>3</sub>-oxo clusters. To gain further evidence of LMCT process, electron spin resonance (ESR) studies were also carried out. As shown in Figure 2.13a, when BDC-NH<sub>2</sub> was irradiated with visible light, an ESR signal with a g value of 2.004 was observed. According to literature, the new signal was produced by the space confined amine group upon irradiation.<sup>32</sup> In contrast, when NH<sub>2</sub>-MIL-88B (Fe) was irradiated with visible light, the above signal was not detected. Moreover, as shown in Figure 2.13b, NH<sub>2</sub>-MIL-88B (Fe) shows a typical ESR signal with a g value of 1.996 in the dark, which can be ascribe to Fe<sup>3+</sup>.<sup>44</sup> The ESR signal intensities of Fe<sup>3+</sup> decreased upon visible light irradiation. Also, when the irradiation was stopped, the intensity of this ESR signal recovered. The decrease of Fe<sup>3+</sup> ESR signal intensity could be attributed to the trapping of electrons by Fe<sup>3+</sup> site in Fe<sub>3</sub>-μ<sub>3</sub>-oxo clusters.<sup>44</sup> The disappearance of the ESR signal at g value of 2.004 and the decrease of the ESR signal at g value of 1.996 suggest the electron transfer from excited amine group to Fe<sub>3</sub>-μ<sub>3</sub>-oxo clusters in NH<sub>2</sub>-MIL-88B (Fe) irradiated with visible light.

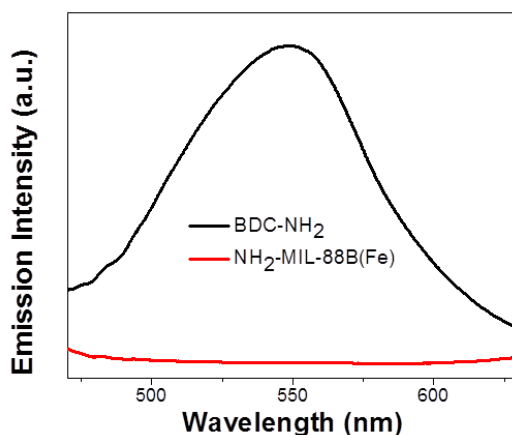


Figure 2.12. PL properties of NH<sub>2</sub>-MIL-88B (Fe) and BDC-NH<sub>2</sub> at excitation wavelength of 350 nm. The PL study was carried out on NH<sub>2</sub>-MIL-88B (Fe) and BDC-NH<sub>2</sub> powders.

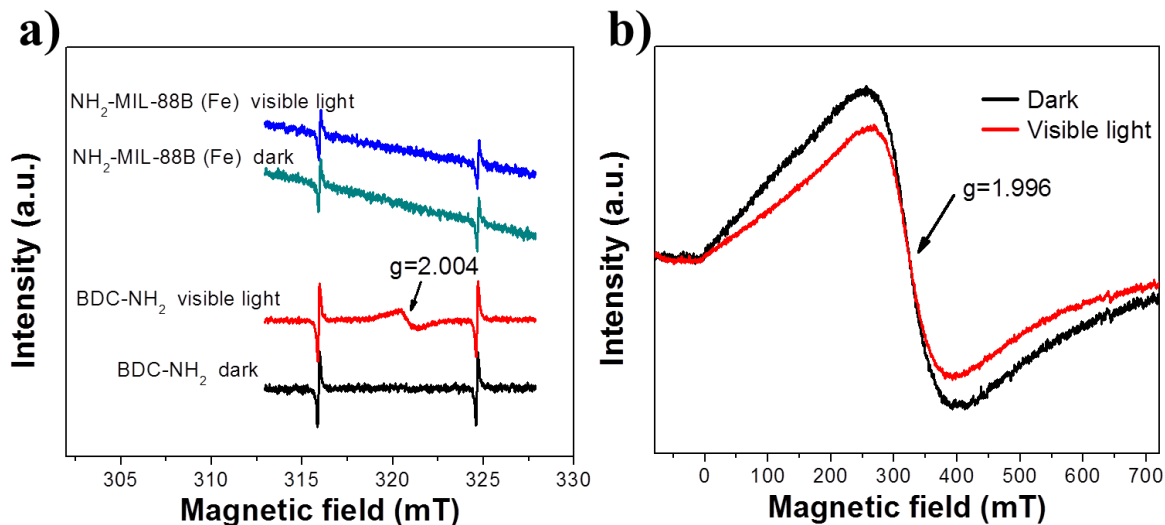


Figure 2.13. (a) ESR spectra of BDC-NH<sub>2</sub> and NH<sub>2</sub>-MIL-88B (Fe) measured before and after visible light irradiation; (b) ESR spectra of NH<sub>2</sub>-MIL-88B (Fe) measured before and after visible light irradiation.

The Iron(III)-based MOF had been proven to be a robust motif that was amenable to carboxylate ligand exchange.<sup>45</sup> In order to further confirm that the amino group play a key role in enhancing the photocatalytic ability, I partly substituted BDC in MIL-88B (Fe) by BDC-NH<sub>2</sub> to obtain Iron(III)-based MOFs with mixed BDC and BDC-NH<sub>2</sub> ligands. (See experimental sections) Three mixed Iron(III)-based MOFs were synthesized by varying the ratio of BDC and BDC-NH<sub>2</sub> linkers, which were named as MOF-1, MOF-2 and MOF-3, i.e., 15%, 30% and 60% molar ratio of BDC in MIL-88B (Fe) structure is replaced with BDC-NH<sub>2</sub>, respectively. As shown in Figure 2.14, the three prepared mixed Iron(III)-based MOFs exhibited the similar XRD patterns, and were in good agreement with the simulated MIL-88B structure. SEM images (Figure 2.15) showed that the mixed Iron(III)-based MOFs remained the similar morphologies compared with MIL-88B (Fe) and NH<sub>2</sub>-MIL-88B (Fe). Figure 2.16a displays the diffuse-reflectance UV/Vis spectrum of the prepared MIL-88B (Fe), NH<sub>2</sub>-MIL-88B (Fe) and mixed MIL-88B (Fe). It shows that the introduction of amino group in the organic linker of Iron(III)-based MOF can enhance its light absorption in the visible region. This observation indicates that the more amine group incorporated into the Iron(III)-based MOF, the more electron-hole pairs can be generated via excitation of amine functionality under visible-light irradiation, which might lead to enhance photocatalytic activity.

## Chapter 2

Figure 2.16b shows the transient photocurrent responses of MIL-88B (Fe), NH<sub>2</sub>-MIL-88B (Fe) and mixed MIL-88B (Fe) under intermittent visible light illumination. It can be seen that the photocurrent density of Iron(III)-based MOF with 100%, 60%, 30%, 15% and 0% BDC-NH<sub>2</sub> incorporation are about 6, 5, 3.5, 3 and 2 μA/cm<sup>2</sup>, respectively. The incorporation of amino group in the Iron(III)-based MOF can enhance the photocurrent significantly. This indicates that the separation efficiency of photoinduced electron-hole (e<sup>-</sup> h<sup>+</sup>) pairs and the lifetime of the photogenerated charge carriers are improved, and this can be explained by the excitation of amine functionalized organic linker and then the excited electrons transfer to Fe<sub>3</sub>-μ<sub>3</sub>-oxo clusters.

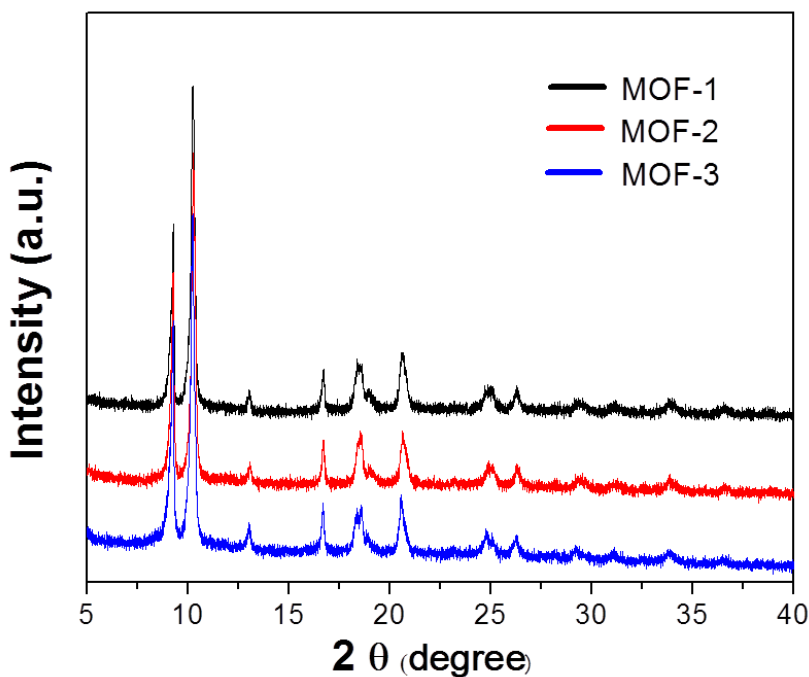


Figure 2.14. XRD patterns of mixed MIL-88B (Fe) with different percentage of BDC-NH<sub>2</sub> incorporation.

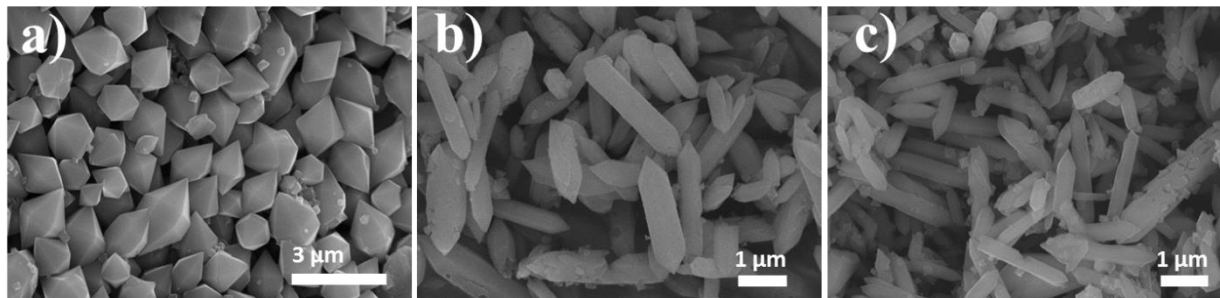


Figure 2.15. SEM images of (a) MOF-1; (b) MOF-2 and (c) MOF-3.

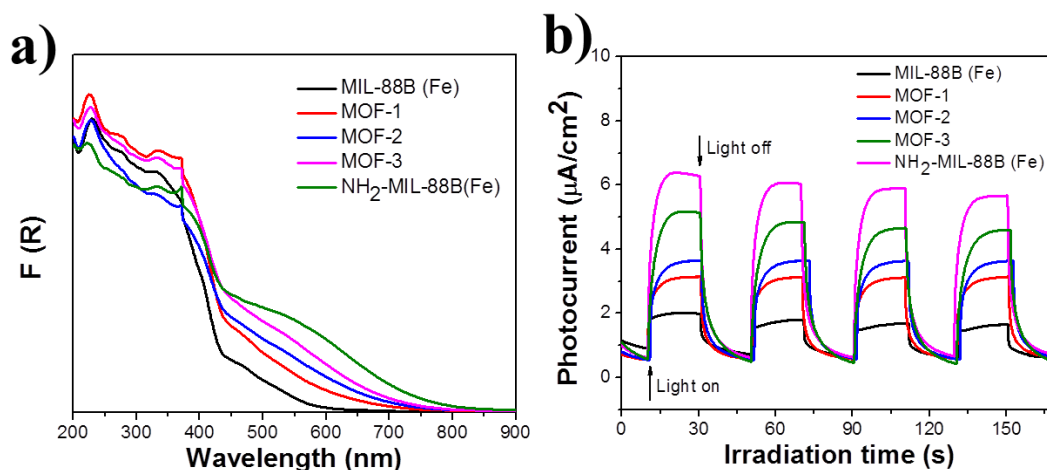


Figure 2.16. (a) The diffuse-reflectance UV/Vis spectrum and (b) the transient photocurrent responses of the prepared MIL-88B (Fe), NH<sub>2</sub>-MIL-88B (Fe) and mixed MIL-88B (Fe).

The influence of amine group incorporated in the Iron(III)-based MOF on the visible light photocatalytic activity was investigated by testing the photocatalytic performance for Cr(VI) reduction over MIL-88B (Fe), NH<sub>2</sub>-MIL-88B (Fe), and mixed MIL-88B (Fe). Meanwhile, the photocatalytic ability of organic linker BDC-NH<sub>2</sub> was also performed. As expected, the MIL-88B (Fe) photocatalyst with higher amino groups incorporation exhibited better photocatalytic performance for Cr(VI) reduction under visible light irradiation (Figure 2.17), which is due to the enhanced light absorption and efficient electron transfer as discussed above. Interestingly, organic linker BDC-NH<sub>2</sub> also exhibits photocatalytic activity for Cr(VI) reduction, which demonstrates that the amine functionality can be excited under

## Chapter 2

visible-light irradiation. Significantly,  $\text{NH}_2\text{-MIL-88B (Fe)}$  shows much higher activity than that of  $\text{BDC-NH}_2$  and  $\text{MIL-88B (Fe)}$ , which means that the electron transfer phenomenon plays a key role in enhancing the photocatalytic activity, because the electron transfer can reduce the chance for electron-hole pairs recombination. On the basis of the above discussion, a mechanism of the photocatalytic reduction of  $\text{Cr(VI)}$  over  $\text{NH}_2\text{-MIL-88B (Fe)}$  was proposed, as shown in **Scheme 2.1**. Under visible-light irradiation, both of amine functionalized organic linker and  $\text{Fe}_3\text{-}\mu_3\text{-oxo}$  clusters in the  $\text{NH}_2\text{-MIL-88B (Fe)}$  structure were excited. The electrons from the excited  $\text{Fe}_3\text{-}\mu_3\text{-oxo}$  clusters can reduce the  $\text{Cr(VI)}$  to  $\text{Cr(III)}$ , and at the same time, the photogenerated electrons in the organic linker transfer to the  $\text{Fe}_3\text{-}\mu_3\text{-oxo}$  clusters, which is also responsible for the reduction of  $\text{Cr(VI)}$ . The introduction of amino group in the  $\text{MIL-88B (Fe)}$  structure can promote the electron transfer and reduce the chance for electron-hole pairs recombination, thus result in the enhanced photocatalytic performance.

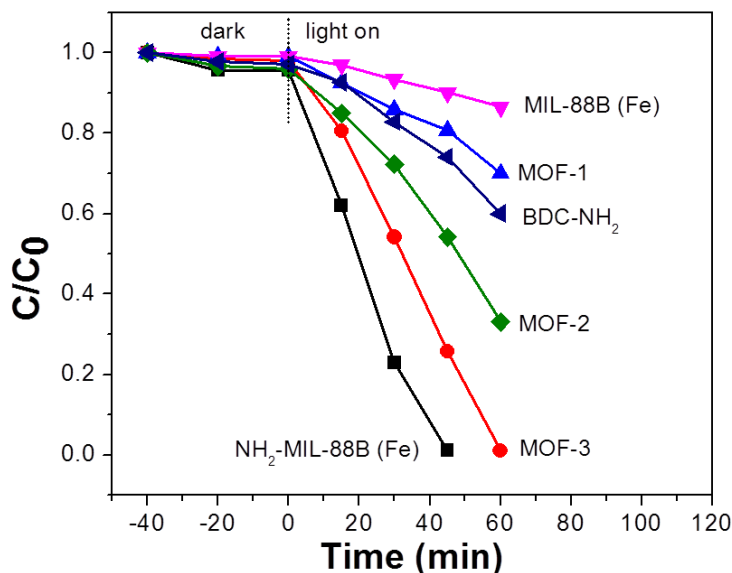
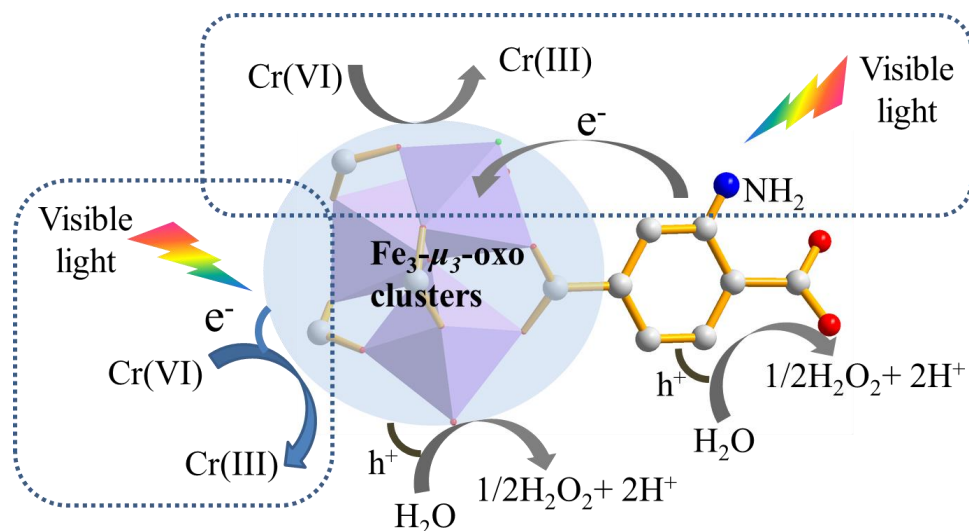


Figure 2.17. Reduction profiles of photocatalytic reduction of  $\text{Cr(VI)}$  over  $\text{MIL-88B(Fe)}$ ,  $\text{NH}_2\text{-MIL-88B(Fe)}$ , mixed  $\text{MIL-88B(Fe)}$  and organic linker  $\text{BDC-NH}_2$ . Reaction condition: 20 mg photocatalyst, 40 ml of 8 ppm  $\text{Cr(VI)}$ , reaction temperature is  $30^\circ\text{C}$ ,  $\text{pH}=2$ .



Scheme 2.1. Proposed dual excitation pathways mechanism for photocatalytic reduction of Cr(VI) over NH<sub>2</sub>-MIL-88B(Fe).

Since the amine functionality in NH<sub>2</sub>-MIL-88B (Fe) have an great effect on the photocatalytic performance for the reduction of Cr(VI), it is very interesting to investigate the photocatalytic performance of other Iron(III)-based MOFs photocatalysts. MIL-53 (Fe) and MIL-101 (Fe) were selected because these two kind of Iron(III)-based MOFs have been proven to be stable photocatalysts and both contain the BDC organic linker similar to that in MIL-88B (Fe) but have different structures.<sup>34</sup> Moreover, amine functionalized NH<sub>2</sub>-MIL-53 (Fe) and NH<sub>2</sub>-MIL-101 (Fe) can also be obtained through organic linker substitution. The formation of these MOFs have been confirmed by their XRD patterns (Figure 2.18). Those XRD patterns were in good agreement with as-synthesized Iron(III)-based MOFs that were previously reported.<sup>46-48</sup> The photocatalytic reduction of Cr(VI) was also investigated over MIL-53 (Fe), NH<sub>2</sub>-MIL-53 (Fe), MIL-101 (Fe) and NH<sub>2</sub>-MIL-101 (Fe). Amine functionalized NH<sub>2</sub>-MIL-53 (Fe) shows an enhanced visible light absorption and improved photocatalytic performance compared to MIL-53 (Fe) without amine functionalization (Figure 2.19a, Figure 2.20). The same trend was also observed for MIL-101 (Fe) MOF with and without amine functionalization (Figure 2.19b, Figure 2.20). This observation indicated that amine functionalization in Iron(III)-based MOFs could be a general method to improve the

## Chapter 2

photocatalytic performance for the reduction of Cr(VI). However, I observed a significant difference in the activity enhancement for NH<sub>2</sub>- MIL-53 (Fe), NH<sub>2</sub>- MIL-101 (Fe) and NH<sub>2</sub>-MIL-88B (Fe) compared with their unfunctionalized MOFs. The difference may be ascribed to the different structures and electron transfer efficiency of these Iron(III)-based MOFs photocatalysts.

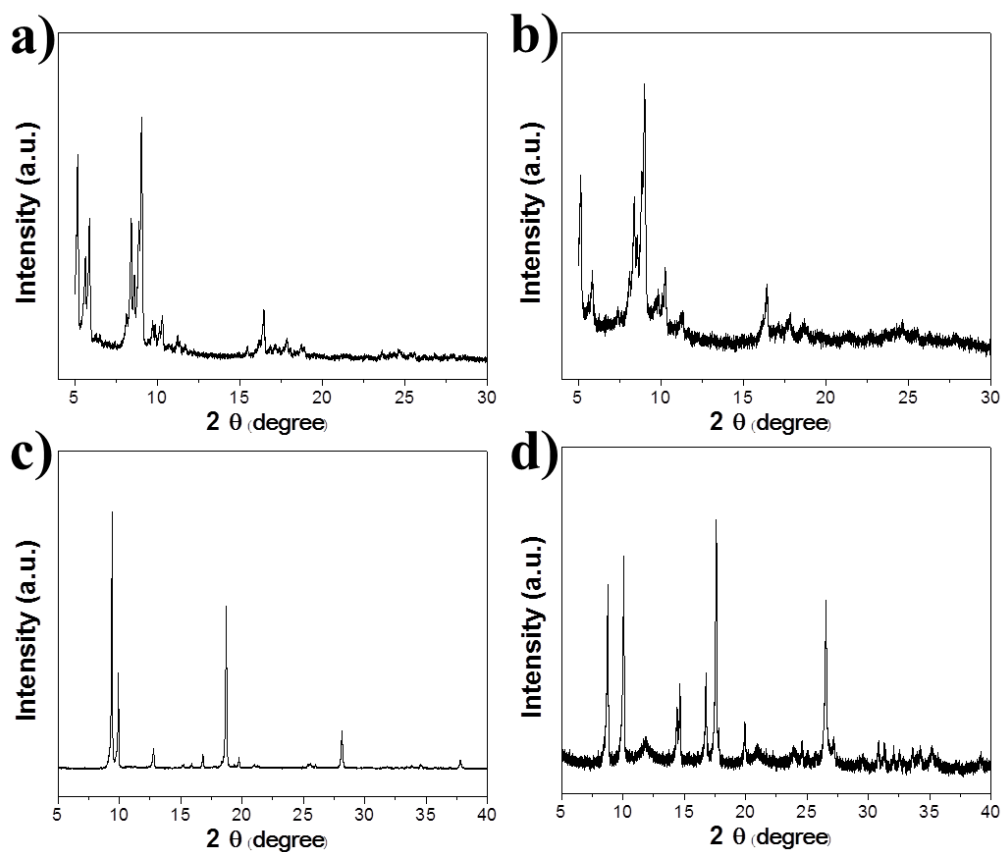


Figure 2.18. XRD patterns of as-synthesized (a) MIL-101 (Fe); (b) NH<sub>2</sub>-MIL-101 (Fe); (c) MIL-53 (Fe) and (d) NH<sub>2</sub>-MIL-53 (Fe).

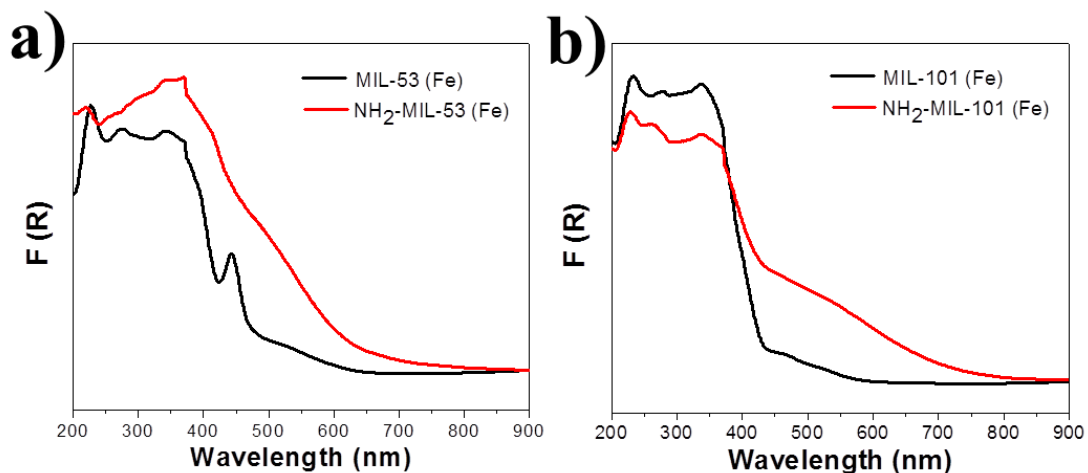


Figure 2.19. The diffuse-reflectance UV/Vis spectra of (a) MIL-53 (Fe) and (b) MIL-101 (Fe) with and without amine functionalization.

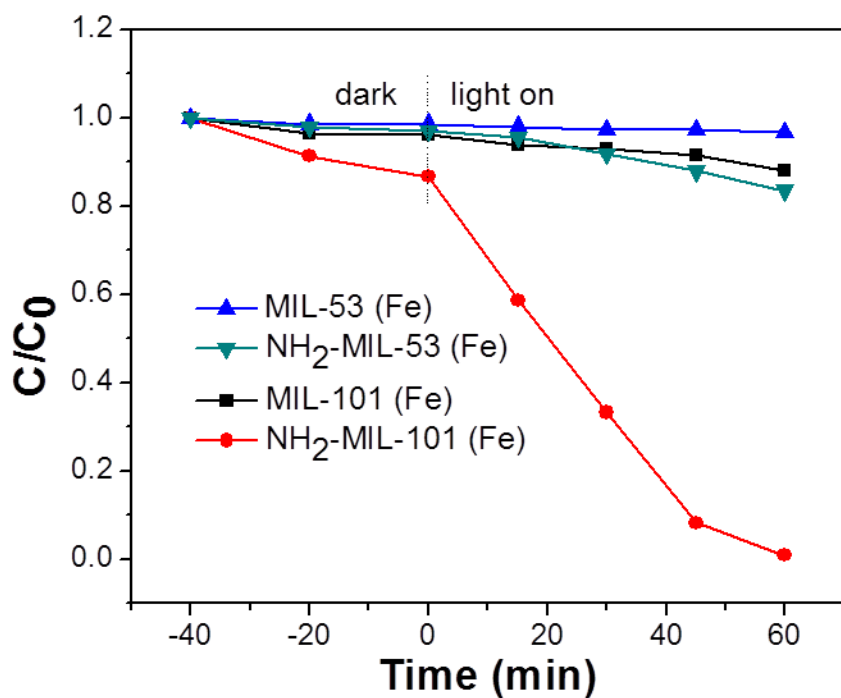


Figure 2.20. Reduction profiles of photocatalytic reduction of Cr(VI) over MIL-101 (Fe), NH<sub>2</sub>-MIL-101 (Fe), MIL-53 (Fe) and NH<sub>2</sub>-MIL-53 (Fe). Reaction condition: 20 mg photocatalyst, 40 ml of 8 ppm Cr(VI), reaction temperature is 30°C, pH=2.

### 2.4 Conclusion

In summary, iron(III) based MOFs structured as MIL-88B structure were successfully produced through a rapid microwave-assisted solvothermal synthesis method. The prepared amino-functionalized NH<sub>2</sub>-MIL-88B (Fe) shows high stability and efficiency for the photocatalytic Cr(VI) reduction under visible-light irradiation. The visible-light activity of NH<sub>2</sub>-MIL-88B (Fe) was even higher than that of P25 under UV-visible light irradiation. It was observed that the incorporation of amino group in the iron(III) based MOFs resulted in enhanced photocatalytic activity for Cr(VI) reduction, which was due to the enhanced light absorption and efficient charge transfer from organic linker to Fe<sub>3</sub>-μ<sub>3</sub>-oxo clusters. The effect of amine functionalization in the other two Iron(III)-based MOFs (MIL-53 (Fe) and MIL-101 (Fe) ) on the visible light photocatalytic activity for the reduction of Cr(VI) was also studied. The same trend was observed, namely all of the amine functionalized MOFs showed enhanced activity for photocatalytic Cr(VI) reduction compared with those of their parent MOFs. This work elucidated the mechanism of iron(III) based MOFs as photocatalysts for Cr(VI) reduction. It also proved that MOFs can serve as stable and efficient photocatalysts and the light harvesting efficiency can be flexibly tuned by simply modifying the organic linker in the MOFs structure.

### References

1. D. Z. Li, Z. X. Chen, Y. L. Chen, W. J. Li, H. J. Huang, Y. H. He, X. Z. Fu, *Environ. Sci. Technol.*, **2008**, 42, 2130.
2. J. S. Hu, L. L. Ren, Y. G. Guo, H. P. Liang, A. M. Cao, L. J. Wan, C. L. Bai, *Angew. Chem. Int. Ed.*, **2005**, 44, 1269.
3. R. J. Kieber, J. D. Willey, S. D. Zvalaren, *Environ. Sci. Technol.*, **2002**, 36, 5321.
4. J. J. Testa, M. A. Grela, M. I. Litter, *Environ. Sci. Technol.*, **2004**, 38, 1589.

## Chapter 2

---

5. S. Rengaraj, S. Venkataraj, J. –W. Yeon, Y. Kim, X. Z. Li, G. K. H. Pang, *Appl. Catal. B: Environ.*, **2007**, 77, 157.
6. L. Yang, Y. Xiao, S. Lin, Y. Li, Q. Cai, S. Luo, G. Zeng, *Appl. Catal. B: Environ.*, **2010**, 94, 142.
7. Y. Xing, X. Chen, D. wang, *Environ. Sci. Technol.*, **2007**, 41, 1439.
8. L. B. Khalil, W. E. Mourad, M. W. Rophael, *Appl. Catal. B: Environ.*, **1998**, 17, 267.
9. M. Gratzel, *Energy Resources through Photochemistry and Catalysis*, Academic Press, New York, 1983.
10. S. G. Schrank, H. J. José, R. F. P. M. Moreira, *J. Photochem. Photobiol. A: Chem.*, **2002**, 147, 71.
11. C. R. Chenthamarakshan, K. Rajeshwar, *Electrochem. Commun.*, **2000**, 2, 527.
12. G. Colón, M. C. Hidalgo, J. A. Navío, *Langmuir*, **2001**, 17, 7174.
13. H. Kyung, J. Lee, W. Choi, *Environ. Sci. Technol.*, **2005**, 39, 2376.
14. H. Tong, S. Ouyang, Y. Bi, N. Umezawa, M. Oshikiri, J. Ye, *Adv. Mater.*, **2012**, 24, 229.
15. X. Liu, L. Pan, T. Lv, G. Zhu, Z. Sun, C. Sun, *Chem. Commun.*, **2011**, 47, 11984.
16. Y. C. Zhang, J. Li, M. Zhang, D. D. Dionysiou, *Environ. Sci. Technol.*, **2011**, 45, 9324.
17. W. Yang, L. Zhang, Y. Hu, Y. Zhong, H. B. Wu, X. W. Lou, *Angew. Chem. Int. Ed.*, **2012**, 51, 11501.
18. H. Yoneyama, Y. Yamashita, H. Tamura, *Nature*, **1979**, 282, 817.
19. Y. Hu, X. Gao, L. Yu, Y. Wang, J. Ning, S. Xu, X. W. Lou, *Angew. Chem. Int. Ed.*, **2013**, 52, 5636.
20. T. Watanabe, D. S. Sholl, *Langmuir*, **2012**, 28, 14114.
21. Y. Mao, L. Shi, H. Huang, W. Cao, J. Li, L. Sun, X. Jin, X. Peng, *Chem. Commun.*, **2013**, 49, 5666.

## Chapter 2

---

22. D. Ma, B. Li, X. Zhou, Q. Zhou, K. Liu, G. Zeng, G. Li, Z. Shi, S. Feng, *Chem. Commun.*, **2013**, 49, 8964.
23. F. Ke, Y. -P. Yuan, L. -G. Qin, Y. -H. Shen, A. -J. Xie, J. -F. Zhu, X. -Y. Tian, L. -D. Zhang, *J. Mater. Chem.*, **2011**, 21, 3843.
24. J. -L. Wang, C. Wang, W. Lin, *ACS Catal.*, **2012**, 2, 2630.
25. L. Shen, S. Liang, W. Wu, R. Liang, L. Wu, *Dalton. Trans.*, **2013**, 42, 13649.
26. J. Gascon, M. D. Hernández-Alonso, A. R. Almeida, G. P. M. Klink, F. Kapteijn, G. Mul, *ChemSusChem.*, **2008**, 1, 981.
27. C. H. Hendon, D. Tiana, M. Fontecave, C. Sanchez, L. D'arras, C. Sassoia, L. Rozes, C. Mellot-Draziéks, A. Walsh, *J. Am. Chem. Soc.*, **2013**, 135, 10942.
28. J. Gao, J. Miao, P. -Z. Li, W. Y. Teng, L. Yang, Y. Zhao, B. Liu, Q. Zhang, *Chem. Commun.*, **2014**, 50, 3786.
29. W. -Q. Kan, B. Liu, J. Yang, Y. -Y. Liu, J. -F. Ma, *Cryst. Growth. Des.*, **2012**, 12, 2288.
30. Y. Horiuchi, T. Toyao, M. Saito, K. Mochizuki, M. Iwata, H. Higashimura, M. Anpo, M. Matsuoka, *J. Phys. Chem. C*, **2012**, 116, 20848.
31. C. Wang, Z. Xie, K. E. deKrafft, W. Lin, *J. Am. Chem. Soc.*, **2011**, 133, 13445.
32. D. Sun, Y. Fu, W. Liu, L. Ye, D. Wang, L. Yang, X. Fu, Z. Li, *Chem. Eur. J.* **2013**, 19, 14279.
33. Y. Fu, D. Sun, Y. Chen, R. Huang, Z. Ding, X. Fu, Z. Li, *Angew. Chem. Int. Ed.*, **2012**, 51, 3364.
34. D. Wang, R. Huang, W. Liu, D. Sun, Z. Li, *ACS Catal.*, **2014**, 4, 4254.
35. P. Horcajada, F. Salles, S. Wuttke, T. Devic, D. Heurtaux, G. Maurin, A. Vimont, M. Daturi, O.

## Chapter 2

---

- David, E. Magnier, N. Stock, Y. Filinchuk, D. Popov, C. Riekkel, G. Férey, C. Serre, *J. Am. Chem. Soc.*, **2011**, 133, 17839.
36. L. Shen, W. Wu, R. Liang, R. Lin, L. Wu, *Nanoscale*, **2013**, 5, 9374.
37. G. Chen, M. Sun, Q. Wei, Z. Ma, B. Du, *Appl. Catal. B: Environ.*, **2012**, 125, 282.
38. C. R. Chenthamarakshan, K. Rajeshwar, E. J. Wolfrum, *Langmuir*, **2000**, 16, 2715.
39. G. Srinivas, W. Travis, J. Ford, H. Wu, Z. -X. Guo, T. Yildirim, *J. Mater. Chem. A*, **2013**, 1, 4167.
40. J. Long, S. Wang, Z. Ding, S. Wang, Y. Zhou, L. Huang, X. Wang, *Chem. Commun.*, **2012**, 48, 11656.
41. L. Ai, C. Zhang, L. Li, J. Jiang, *Appl. Catal. B: Environ.*, **2014**, 148, 191.
42. K. G. M. Laurier, F. Vermoortele, R. Ameloot, D. E.D. Vos, J. Hofkens, M. B. J. Roeffaers, *J. Am. Chem. Soc.*, **2013**, 135, 14488.
43. M. Alvaro, E. Carbonell, B. Ferrer, F. X. L. i. Xamena, H. Garcia, *Chem. Eur. J.* **2007**, 13, 5106.
44. X. Li, P. -L. Yue, C. Kotal, *New J. Chem.*, **2013**, 27, 1264.
45. K. M. L. Taylor-Pashow, J. D. Rocca, Z. Xie, S. Tran, W. Lin, *J. Am. Chem. Soc.*, **2009**, 131, 14261.
46. S. Bauer, C. Serre, T. Devic, P. Horcajada, J. Marrot, G. Férey, N. Stock, *Inorg. Chem.*, **2008**, 47, 7568.
47. P. Horcajada, C. Serre, G. Maurin, N. A. Ramsahye, F. Balas, M. V. -Regi, M. Sebban, F. Taulelle, G. Férey, *J. Am. Chem. Soc.*, **2008**, 130, 6774.

## Chapter 2

---

48. T. Devic, P. Horcajada, C. Serre, F. Salles, G. Maurin, B. Moulin, D. Heurtaux, G. Clet, A.

Vimont, J. Grenèche, B. L. Ouay, F. Moreau, E. Magnier, Y. Filinchuk, J. Marrot, J. Lavalley, M.

Oaturi, G. Férey, *J. Am. Chem. Soc.*, **2010**, 132, 1127.

# Chapter 3 Construction of nano-sized g-C<sub>3</sub>N<sub>4</sub> nanosheet/UiO-66 composite photocatalyst for enhanced photocatalytic CO<sub>2</sub> Reduction

### 3.1 Introduction

The production of chemical fuels using CO<sub>2</sub> as carbon source has been regarded as an ideal solution to the energy shortage and the global warming problems.<sup>1</sup> Photocatalytic reduction of CO<sub>2</sub> through artificial photosynthesis is of significant interest since it offers the potential to produce valuable hydrocarbon fuels to meet the increasing energy demands while also mitigate the rising CO<sub>2</sub> levels.<sup>2</sup> A great deal of effort has been devoted to exploring photocatalysts that are capable of reducing CO<sub>2</sub>. In the photocatalytic processes, the photocatalyst is excited by light of energy greater than its bandgap to generate electron-hole pairs which are separated and then transferred to the catalytically active sites for redox reactions.<sup>3</sup> The CO<sub>2</sub> conversion efficiency of the photocatalysts essentially relies on the lifetime of photo-generated electron-hole pairs, separation efficiency of photoinduced charge carriers, CO<sub>2</sub> molecule adsorption and activation.<sup>4</sup> In particular, increasing the CO<sub>2</sub> adsorption ability of photocatalysts has been proved to be an effective strategy to improve the CO<sub>2</sub> conversion efficiency, as the effective electron transfer from the catalytically active sites of photocatalysts to CO<sub>2</sub> molecule largely relies on their intimate and stable binding. Therefore, in order to improve the photocatalytic CO<sub>2</sub> conversion, an ideal solution would be to incorporate a photocatalyst into the CO<sub>2</sub> sorbent materials. For instance, zeolites or mesoporous materials modified with TiO<sub>2</sub> photocatalysts have been widely studied for photocatalytic CO<sub>2</sub> reduction, which showed improved CO<sub>2</sub> adsorption ability and a higher photocatalytic CO<sub>2</sub> conversion efficiency compared with bare TiO<sub>2</sub>.<sup>5-6</sup> The role of the zeolites materials can be regarded as a so-called

## Chapter 3

---

“catch and release effect of CO<sub>2</sub>”, i.e., capture of CO<sub>2</sub> molecular and followed by the efficient diffusion of the CO<sub>2</sub> molecular onto the TiO<sub>2</sub> active site.<sup>7</sup> However, the improvements in the photocatalytic activity are quite limited, mainly due to the fact that zeolite itself cannot provide the active site for the photocatalytic CO<sub>2</sub> reduction and the photocatalytic efficiency largely depends on the efficient diffusion of the CO<sub>2</sub> molecular from zeolite to the active site of photocatalysts.

Metal-organic frameworks (MOFs) are a class of porous solid materials composed of metal containing clusters and organic building blocks, which have demonstrated wide application in drug delivery, catalysis, gas capture and separation.<sup>8-12</sup> UiO-66, a zirconium based MOF, have attracted intense research interest due to its higher chemical stability and thermostability compared to other types of MOFs.<sup>13</sup> UiO-66 has been considered as a promising material for CO<sub>2</sub> capture and storage.<sup>14</sup> Moreover, recent studies proved that UiO-66 exhibited semiconductor behavior, which can facilitate charge transfer or harvest solar light directly for photocatalytic reaction.<sup>15-18</sup> UiO-66 has also been demonstrated to have active sites for the photocatalytic reduction of CO<sub>2</sub>.<sup>19</sup> Nevertheless, the relatively wide band gap of UiO-66 may limit its optical adsorption in the visible light region. To prepare UiO-66 based visible-light active photocatalysts, an ideal solution would be to incorporate UiO-66 together with a visible-light active photosensitizer, such as narrow bang gap semiconductors, to form a heterogeneous photocatalyst. The key point to this heterogeneous photocatalyst is whether the photoexcited electron from the photosensitizer can be efficiently transferred to UiO-66.

Graphitic carbon nitride (CN), a metal-free and visible-light active photocatalyst, has attracted increasing attention and been reported to possess the photocatalytic performance of water splitting, organic degradation and transformation, and it has also been explored for the photocatalytic conversion of CO<sub>2</sub>.<sup>20-24</sup> However, the efficiency of bulk carbon nitride (bulk CN) is far from satisfaction, mainly due to the fast recombination of photogenerated electron-hole pairs. The exfoliation of bulk CN to 2D atomic carbon nitride nanosheet (CNNS) has been actively pursued to improve the photocatalytic activity, due to the synergistic effect of increased bandgap, enhanced electron transport ability and prolonged lifetime.<sup>25-27</sup> However, further improvement of the efficiency in the photocatalytic CO<sub>2</sub> reduction is limited, mainly

## Chapter 3

---

due to the fact that it remains challenging to efficiently capture CO<sub>2</sub> molecules by using carbon nitride. The integration of carbon nitride with UiO-66 may offer an attractive way to improve the efficiency of photocatalytic CO<sub>2</sub> reduction. The colloidal suspension of CNNS with highly flexible and soft nature, as well as negatively charged surface property, made it possible for self-assembly preparation of CNNS based heterogeneous photocatalysts with desired separation of photogenerated charge carriers.<sup>28-29</sup>

Herein, I report a facile self-assembly synthesis of UiO-66/CNNS heterostructure photocatalyst through electrostatic reaction between negatively charged nano-sized CNNS with positively charged UiO-66. To the best of our knowledge, the MOF/CNNS hybrid structure prepared from electrostatic self-assembly method has been rarely explored. In addition, the UiO-66/bulk CN heterostructure photocatalyst was also prepared via the same method. The photocatalytic CO<sub>2</sub> reduction was investigated over UiO-66/CNNS hybrid structure, CNNS, UiO-66/bulk CN hybrid structure and bulk CN. It is observed that CNNS shows higher activity than bulk CN, and the formation of hybrid structure can further improve the photocatalytic CO<sub>2</sub> conversion efficiency. These hybrid structures exhibit a large surface area and strong CO<sub>2</sub> capture ability. It was demonstrated that the electrons from photoexcited CNNS or bulk CN can transfer to UiO-66, which can substantially suppress electron-hole pairs recombination in the CNNS or bulk CN, as well as supply long-lived electrons for the reduction of CO<sub>2</sub> molecules adsorbed in UiO-66.

### 3.2 Experimental section

#### 3.2.1 Materials

Melamine, N, N-dimethylformamide (DMF), 1, 4-benzenedicarboxylic acid (BDC), zirconium chloride (ZrCl<sub>4</sub>), acetonitrile (MeCN) and triethanolamine (TEOA) were purchased from Wako Co. All reagents were analytical grade and used without further purification. Deionized water (18.2 MΩ) used throughout all experiments was produced using a Millipore Direct-Q System.

#### 3.2.2 Preparation of photocatalysts

Bulk CN was prepared by heating melamine to 550°C for 4 hours under air condition in a crucible. Nano-sized CNNS was obtained by liquid exfoliating of as-prepared bulk CN in water. Brief, 0.1 g bulk

## Chapter 3

---

CN powder was dispersed in 100 ml H<sub>2</sub>O, then ultrasonicated using a Branson-250 sonifier (Japan) at a water bath for 5 h with the output wattage of 48 W. After this process, the suspension was stayed overnight and then centrifuged at 9000 rpm for 10 min to remove the residual unexfoliated bulk CN and large-sized CNNS. The nano-sized CNNS was collected by evaporating the supernatant. UiO-66 was synthesized from a mixture of ZrCl<sub>4</sub>, BDC and DMF with a molar ratio of 1:1:650, then the mixture was heated at 120°C for 48 hours. The resulting white UiO-66 products were collected by centrifugation and washed with DMF and water several times, and then activated at 200°C for 12 hours under vacuum to remove the organic solvent. UiO-66/CNNS composite was prepared by mixing UiO-66 and nano-sized CNNS with a certain mass ratio in water. The suspension was ultrasonicated for 10 min and then stirred for 24 hours. After volatilization of water, the powder was obtained after drying at 100°C under vacuum. UiO-66/bulk CN composite was prepared similarly expect that bulk CN was used instead of CNNS.

### 3.2.3 Characterization

The prepared samples were characterized by powder XRD on an X-ray diffractometer (Rint 2000, Altima III, Rigaku Co. Japan) using a Cu K $\alpha$  source. UV–visible diffuse reflectance spectra were measured on UV–visible spectrophotometer (SHIMADZU, UV-2600) with BaSO<sub>4</sub> as the reflectance standard reference. The morphology and structure of the samples were examined with a scanning electron microscope (SEM, S4800, Hitachi Co., Japan) and transmission electron microscopy (TEM, 2100F, JEOL Co., Japan). CO<sub>2</sub> adsorption isotherms were measured at room temperature using a BEL SORP-mini II (BEL Japan INC., Japan). Nitrogen adsorption–desorption isotherms were recorded via nitrogen physisorption (Autosorb-iQ<sub>2</sub>-MP; Quantachrome Corp., U.S.A.). The thickness of CNNS was measured on a DFM (Nanocute H, Japan). The valence band analysis of the samples were performed by X-ray photoelectron spectroscopy (XPS, PHI Quantera SXM, ULVAC-PHI Inc., Japan). The zeta potential of samples was recorded on ELSZ-2000 (Otosuta Electronics), and the solvent is pure water. All the zeta potential measurements were repeated three times and the average values were used. The PL spectra were recorded on a JASCO FP-6500 spectrofluorometer. The decay time was measured by a fluorescent

## Chapter 3

---

spectrophotometer (Horiba Jobin Yvon, Fluorolog-3) with a nano-LED lamp (370 nm) as an excitation source (Horiba Jobin Yvon). The experiment detail of decay time measurements was described as below: the powder sample was transferred to a substrate and the decay time measurements were conducted directly on powder sample with an excitation light wavelength of 370 nm. Electron spin resonance (ESR) characterizations were carried out with JEOL JES-FA-200 at room temperature in the air.

### 3.2.4 Photocatalytic experiments

The photocatalytic activities of samples were carried out in a batch type reaction system with a total volume of about 330 ml. The sample was uniformly dispersed on a porous quartzose film in the reaction cell, and 5 ml solution (MeCN : TEOA=4 : 1) was injected into the cell. After evacuation of reaction system completely (no O<sub>2</sub> or N<sub>2</sub> can be detected), 80 kPa pure CO<sub>2</sub> gas was injected into the airtight system. A 300 W xenon arc lamp with a UV-cut filter to remove light with wavelengths less than 400 nm and an IR-cut filter to remove wavelengths longer than 800 nm light filters (400 nm <  $\lambda$  < 800 nm) was used as the light source. In the measurement, certain amount of powder samples were used (keeping the visible light photoactive materials carbon nitride at the same weight ). Prior to the test, the catalysts were degassed at 200°C for 12 hours under vacuum to remove any possible organic contaminants. The gas products were measured by using a gas chromatograph (GC-14B, Shimadzu Co., Japan). The isotope analysis of <sup>13</sup>C was analyzed by using a gas chromatographmass spectrum (JEOL-GCQMS, JMS-K9 and 6890N Network GC system, Agilent Technologies).

## 3.3 Results and discussion

### 3.3.1 Characterization of photocatalysts

The formation of UiO-66/CNNS hybrid structure involves a two step process, as shown in Figure 3.1a. Firstly, CNNS were obtained by a liquid exfoliation route from bulk CN in water. Secondly, a certain mass ratio of the as- prepared CNNS and UiO-66 were dispersed in water under vigorous stirring, and then these CNNS will spontaneously coat on UiO-66 through electrostatic self-assembly process. Figure

## Chapter 3

---

3.1b shows transmission electron microscopy (TEM) images of the exfoliated CNNS. It can be seen that the as-obtained CNNS are freestanding with a diameter of  $15 \pm 5$  nm. The high-resolution TEM (HRTEM) image shows that the edge of CNNS is nearly transparent, which indicates its ultrathin thickness (Figure 3.1b, inset). Atomic force microscopy (AFM) was performed to gain more information about the morphology and thickness of CNNS. A typical AFM image in Figure 3.1c,d shows the thickness of randomly measured nanosheet is about 3.6 nm, indicating the exfoliated CNNS only consist of ten C-N layers. The crystal and electronic structure of the CNNS were studied by their X-ray diffraction (XRD) patterns, optical absorption and photoluminescence (PL) spectra compared with bulk CN (Figure 3.2a, b, c). As presented in Figure 3.2a, the CNNS shows two peaks at  $13.1^\circ$  (100) and  $27.4^\circ$  (002), which is consistent with bulk CN, indicating that the CNNS basically exhibit the same crystal structure as bulk CN. Compared with bulk CN, the peak (002) in the CNNS slightly shifts from  $27.7^\circ$  to  $27.4^\circ$ , which can be attributed to the loose layered structure of CNNS swelled by water. Remarkably enough, in the case of CNNS, the peak at  $13.1^\circ$  becomes less pronounced, which can be ascribed to the simultaneously decreased planar size of the layers during exfoliation of bulk CN.<sup>25-26</sup> The UV-visible absorption spectra in Figure 3.2b shows that the intrinsic absorption edge of CNNS displays an obvious blue shift compared with that of bulk CN, and the bandgap of bulk CN of 2.63 eV increased to 2.78 eV for CNNS. Moreover, the PL spectrum shows that the emission peak of CNNS exhibits a blue shift of 21 nm in comparison with the bulk CN (Figure 3.2c). The reason for the larger bandgap and the blue shift of PL spectra in CNNS is attributed to the quantum confinement effect with the conduction and valence band edges shifting in opposite direction.<sup>28</sup>

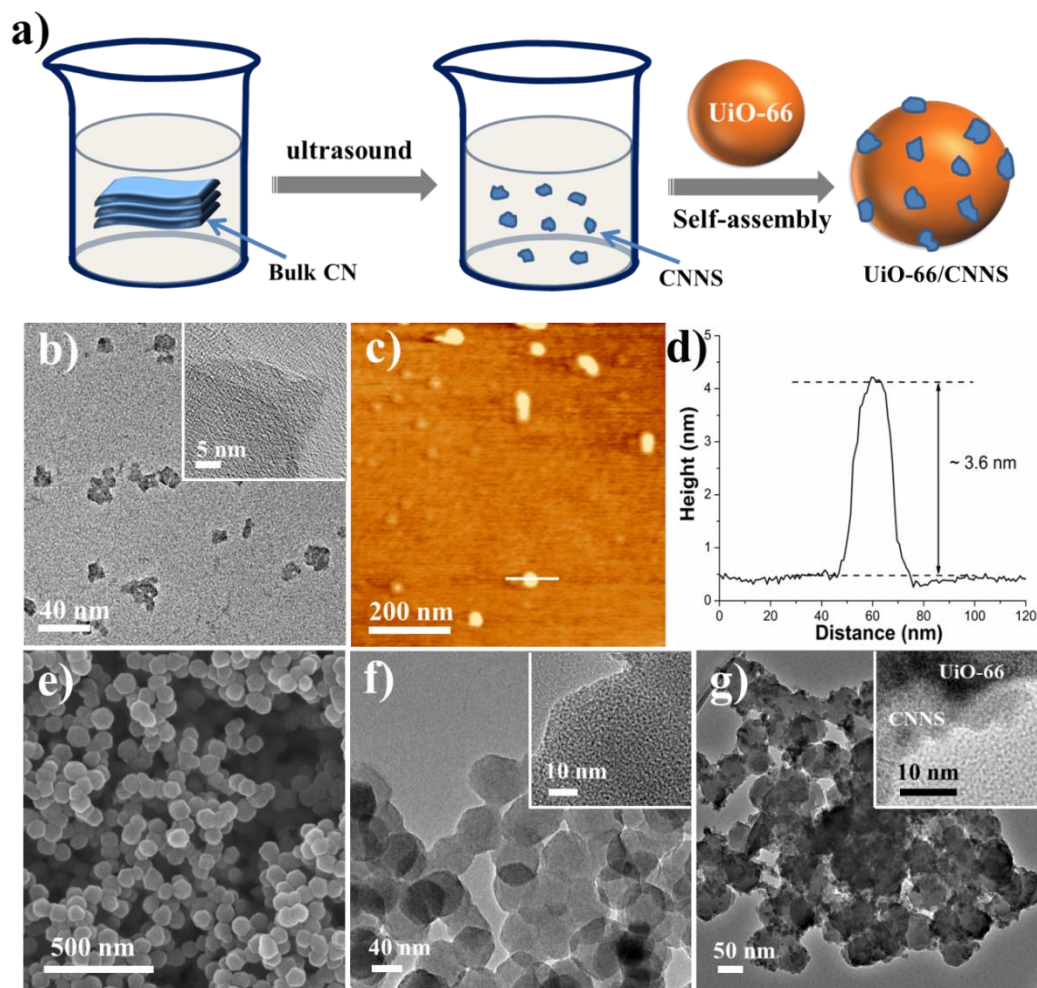


Figure 3.1. (a) Schematic illustration of the preparation of the UiO-66/CNNS heterogeneous photocatalyst. (b) TEM and HRTEM images of CNNS; (c) - (d) AFM and corresponding height images of CNNS. (e) - (f) SEM, TEM and HRTEM images of UiO-66. (g) TEM and HRTEM images of UiO-66/CNNS. The CNNS content in UiO-66/CNNS composite is 10 wt%.

## Chapter 3

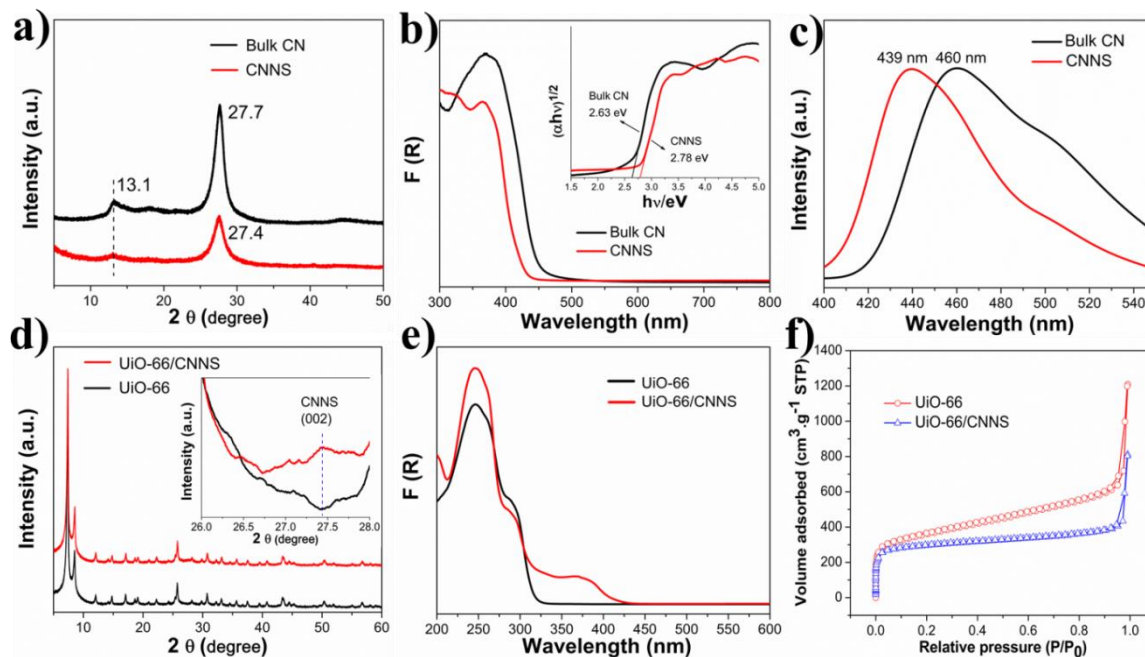


Figure 3.2. (a)-(c) XRD patterns, diffuse-reflectance UV/Vis spectrum and PL spectra of bulk CN and CNNS. (d)-(f) XRD patterns, diffuse-reflectance UV/Vis spectrum and  $N_2$  adsorption-desorption isotherms of UiO-66 and UiO-66/CNNS. The CNNS content in UiO-66/CNNS composite is 10 wt%.

The valence band X-ray photoelectron spectroscopy (VB-XPS) was carried out to investigate the VB top of bulk CN and CNNS. As shown in Figure 3.3, the energy level valence band maximum (VBM) of bulk CN and CNNS is 1.62 eV and 1.68 eV, respectively. Therefore, in our case, the CNNS has a larger bandgap by 0.15 eV as a result of a lower valence band edge by 0.06 eV and higher conduction band edge by 0.09 eV compared to bulk CN. According to the literature, the position of the conduction band edge for bulk CN is located at -1.3 V vs NHE at pH 7.<sup>30</sup> Therefore, it can be established that the position of the conduction band edge for CNNS is located at -1.39 V (vs. NHE, pH 7).

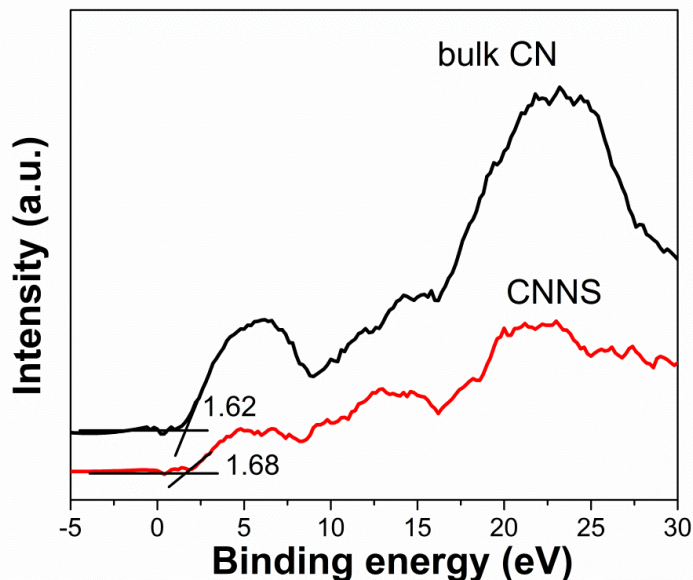


Figure 3.3. The XPS valence band spectra of bulk CN and CNNS.

The as-prepared CNNS could be coated on the surface of UiO-66, and this was confirmed by TEM images of UiO-66 MOF crystal and UiO-66/CNNS composite. The as-obtained UiO-66 MOF shows well-defined nanocrystals with a narrow size distribution (Figure 3.1e, f). The HRTEM image (Figure 3.1f, inset) indicates that the surface of UiO-66 crystal is rough, which is beneficial for loading CNNS. Figure 3.1g shows the TEM image of UiO-66/CNNS hybrid structure, indicating the CNNS were well coated on the surface of UiO-66 without much aggregation. Importantly, the HRTEM image (Figure 3.1g, inset) shows a distinguished and coherent interface between UiO-66 crystal and CNNS, indicating that a nano-junction of UiO-66/CNNS hybrid structure might be formed, which could result in efficient electron transfer within the hybrid structure. The elemental mapping analysis (Figure 3.4) clearly shows the well-defined spatial distribution of element Zr and N, which confirms that the CNNS were coated on the UiO-66 uniformly. In order to investigate the self-assembly mechanism between CNNS and UiO-66, zeta potential measurements were carried out. The dispersed CNNS in water is negatively charged, with a zeta potential of about -35.91 mV, while UiO-66 shows a zeta potential value of +7.71 mV, indicating its positively charged surface. The zeta potential measurements results demonstrate that the hybrid structure

## Chapter 3

---

between CNNS and UiO-66 is formed through electrostatic self-assembly process. The crystallographic structure of the products was determined by XRD patterns. As shown in Figure 3.2d, the peaks characteristic for UiO-66 can be clearly identified in UiO-66/CNNS composite, suggesting that the crystal phase structure of UiO-66 is retained after being coated by CNNS.<sup>15-18</sup> The enlarged XRD pattern in Figure 3.2d confirms that the sample is a hybrid structure between UiO-66 and CNNS. The optical absorption of UiO-66 MOF and UiO-66/CNNS hybrid structure was measured by UV-visible absorption spectra. As illustrated in Figure 3.2e, UiO-66 can only absorb UV-light in the wavelength shorter than 350nm, while UiO-66/CNNS hybrid structure has an absorption edge at about 440nm, which is similar to CNNS. The enhancement of light absorption in the visible region further confirms the formation of hybrid structure between UiO-66 and CNNS. Figure 3.2f shows the N<sub>2</sub> adsorption-desorption isotherms for the UiO-66 MOF and UiO-66/CNNS hybrid structure, respectively. The sample of bare UiO-66 MOF attains a Langmuir surface area of 1610.5 m<sup>2</sup> g<sup>-1</sup>, while the UiO-66/CNNS hybrid structure shows relatively low surface area (1315.3 m<sup>2</sup> g<sup>-1</sup>). The decrease in surface area after CNNS coating is reasonable, as the CNNS accounts for 10% of the total weight and exhibits much smaller surface area (Figure 3.5). The dispersed bulk CN in water was also negatively charged, with a measured zeta potential of -24.27 mV, thus UiO-66/bulk CN composite can also be formed through electrostatic self-assembly process. The XRD patterns and UV-visible absorption spectra demonstrate that the hybrid composite consisted of bulk CN and UiO-66 was formed successfully (Figure 3.6). Further information about the microstructure of UiO-66/bulk CN composite was obtained from TEM images. As shown in Figure 3.7, UiO-66 crystals are coated by bulk CN, thereby forming a nano-junction of UiO-66/bulk CN composite. The Langmuir surface area of UiO-66/bulk CN composite is 1340.9 m<sup>2</sup> g<sup>-1</sup>, which is close to that of UiO-66/CNNS composite.

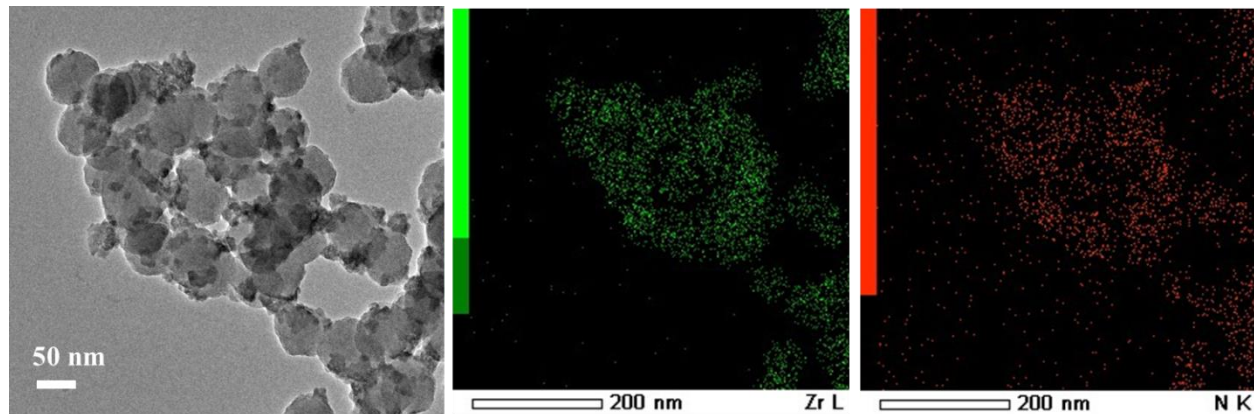


Figure 3.4. TEM image and corresponding elemental mapping images of UiO-66/CNNS. The CNNS content in UiO-66/CNNS composite is 10 wt%.

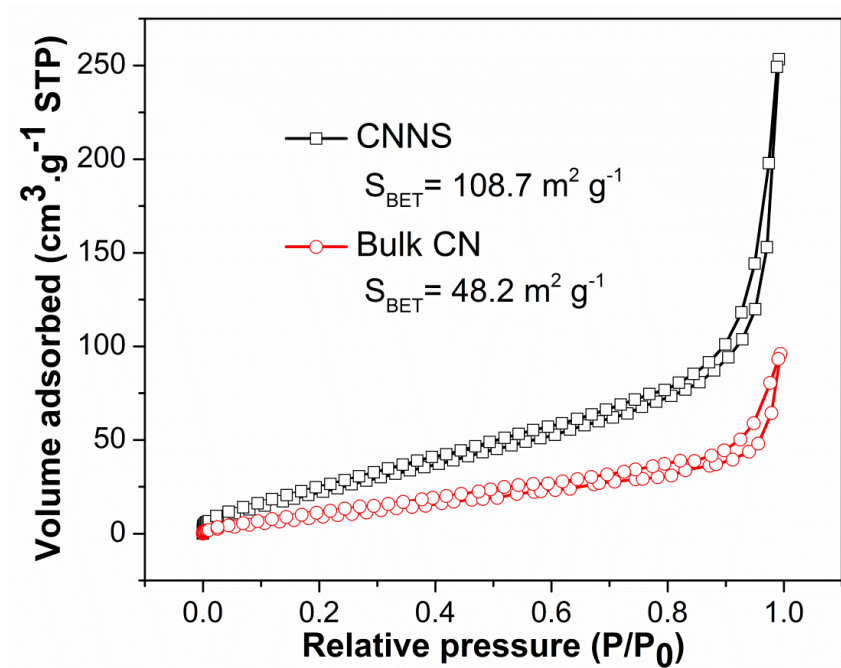


Figure 3.5.  $\text{N}_2$  adsorption-desorption isotherms of CNNS and bulk CN.

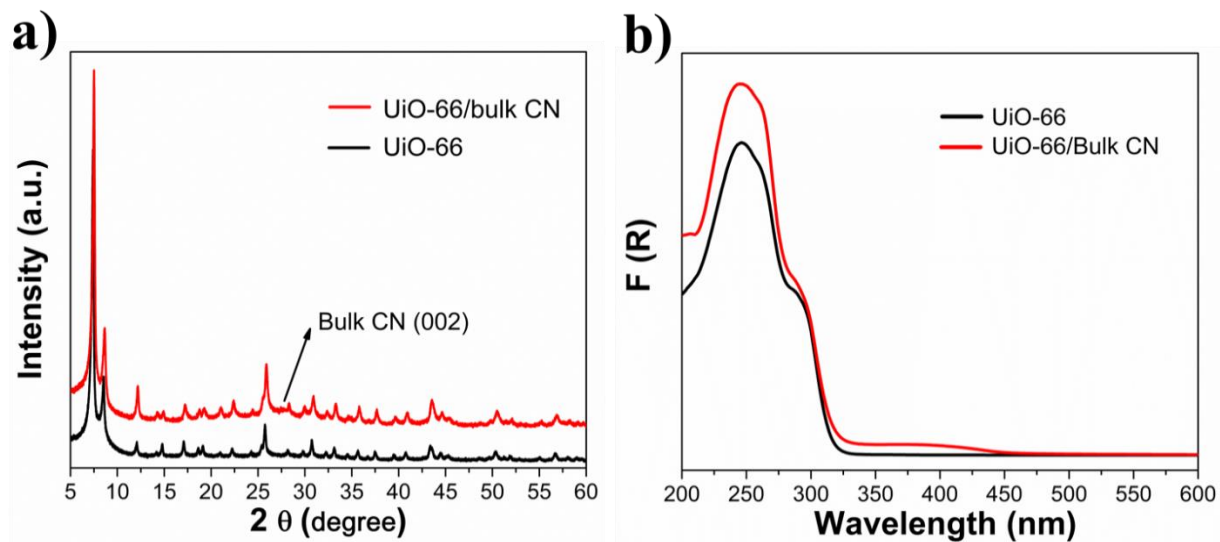


Figure 3.6. (a) XRD patterns and (b) diffuse-reflectance UV/Vis spectrum of UiO-66 and UiO-66/bulk CN. The bulk CN content in UiO-66/bulk CN composite is 10 wt%.

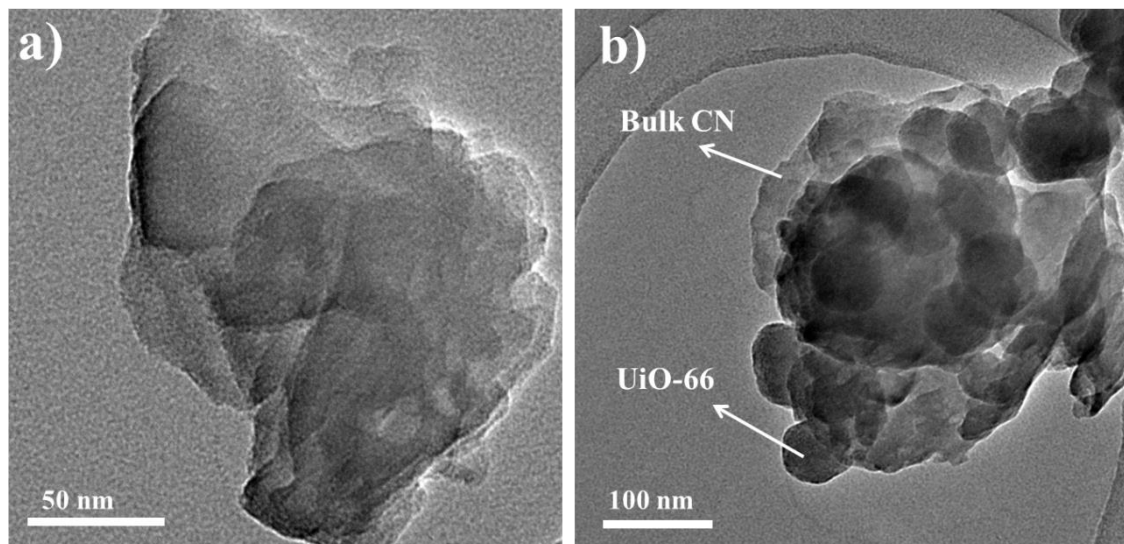


Figure 3.7. TEM images of (a) bulk CN and (b) UiO-66/bulk CN.

3.3.2 CO<sub>2</sub> adsorption and electron transfer behaviors

Figure 3.8a shows the CO<sub>2</sub>-adsorption behaviors of samples at room temperature. It can be seen that the maximum CO<sub>2</sub> uptake for UiO-66 MOF, UiO-66/CNNS composite and CNNS is 38.4 cm<sup>3</sup> g<sup>-1</sup>, 32.7 cm<sup>3</sup> g<sup>-1</sup> and 3.7 cm<sup>3</sup> g<sup>-1</sup>, respectively. The comparison of the CO<sub>2</sub>-adsorption behaviors of above three samples indicates that UiO-66/CNNS composite shows superior CO<sub>2</sub> uptake ability than that of CNNS due to the high adsorption capability of UiO-66 MOF. This suggests that the coating layers of CNNS are finely dispersed on the surface of UiO-66 avoiding the pore blockage of the UiO-66 and CO<sub>2</sub> molecules can be adsorbed on the microporous UiO-66 cores. The CO<sub>2</sub>-adsorption behaviors of UiO-66/bulk CN composite and bulk CN were also investigated and shown in Figure 3.9, the maximum CO<sub>2</sub> uptake for UiO-66/bulk CN composite is 35.9 cm<sup>3</sup> g<sup>-1</sup>, which is much higher than bulk CN (1.1 cm<sup>3</sup> g<sup>-1</sup>).

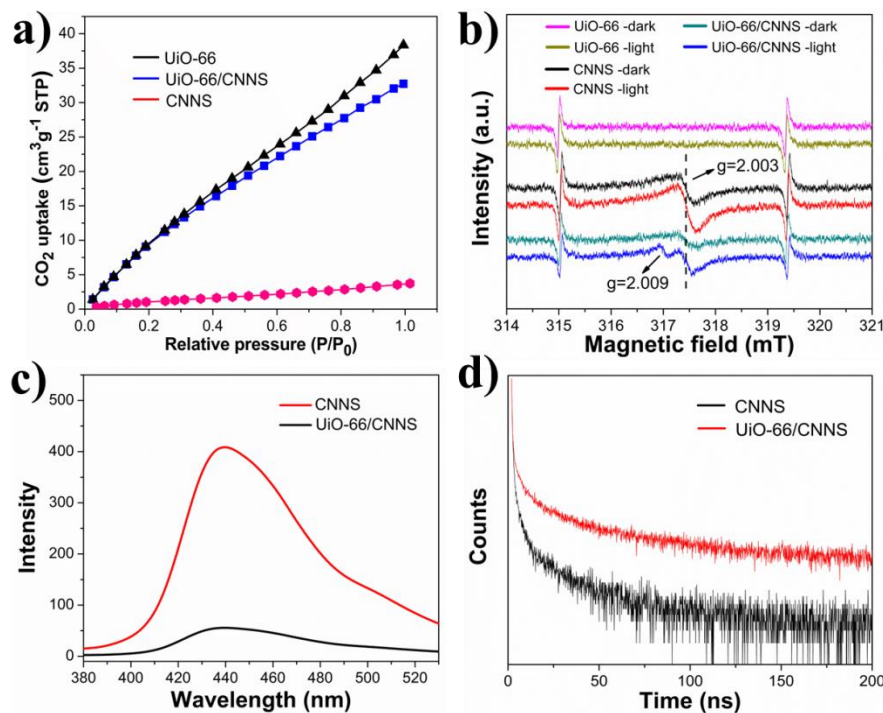


Figure 3.8. (a)-(b) CO<sub>2</sub> adsorption isotherms and ESR spectra of UiO-66, CNNS and UiO-66/CNNS. (c)-(d) PL spectra and decay curve of CNNS and UiO-66/CNNS. The CNNS content in UiO-66/CNNS composite is 10 wt%.

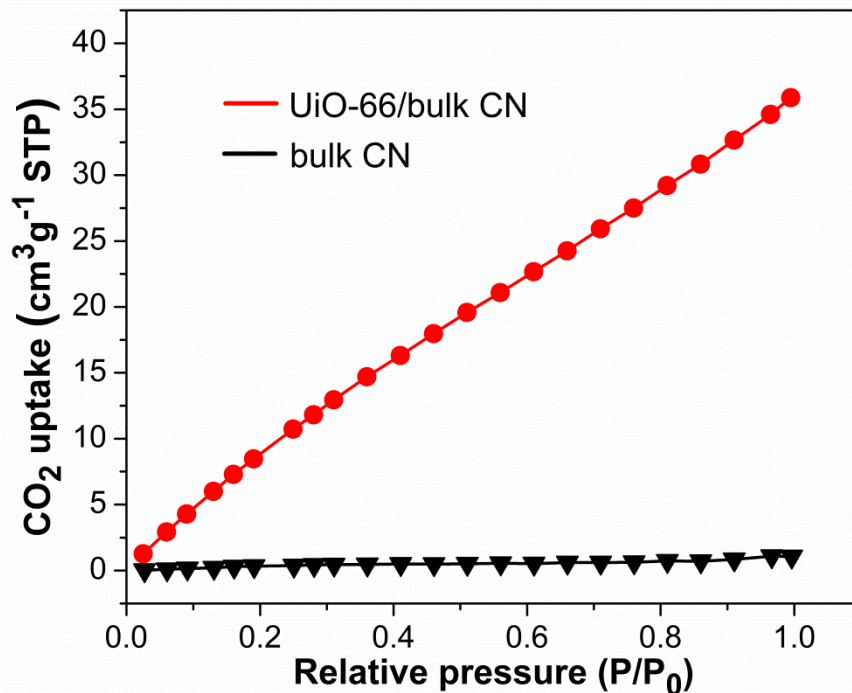


Figure 3.9. CO<sub>2</sub> adsorption isotherms of bulk CN and UiO-66/bulk CN. The bulk CN content in UiO-66/bulk CN composite is 10 wt%.

It is important to note that UiO-66 has been proven to be a semiconductor material with conduction band edge potential of -0.6 V (vs. NHE, pH=7), which is much lower than that of CNNS.<sup>18, 31</sup> Therefore, the nano-junction formed between UiO-66 and CNNS could result in efficient electron transfer within the hybrid structure and better separation of photo-induced charge carriers. Figure 3.8b shows electron spin resonance (ESR) spectra of UiO-66, CNNS and UiO-66/CNNS composite measured at room temperature under air atmosphere. For CNNS, a  $g$  value of 2.003 can be observed, which could be ascribed to the unpaired electrons on the carbon atoms of the aromatic rings within  $\pi$ -bonded nanosized clusters.<sup>32</sup> The intensity of this ESR signal increased under visible light illumination, which provides the clue of promoted photo-generation of radical pairs in the CNNS.<sup>32</sup> However, in the case of UiO-66/CNNS composite, except for the enhanced intensity of  $g$  value of 2.003, a new ESR signal with  $g$  value of 2.009 can be observed. According to the literature, the new signal can be attributed to  $O_2^{\bullet-}$  species formed from photogenerated electrons adsorbed in the UiO-66.<sup>17</sup> In contrast, when pristine UiO-66 was irradiated with visible light, the above ESR signal was not detected, due to the fact that UiO-66 has a large bandgap that

## Chapter 3

cannot be excited under visible light. The ESR results show that CNNS can act as photosensitizer to harvest visible light and the electrons generated from conduction band of CNNS transfer to UiO-66, and consequently transfer to the adsorbed oxygen molecules in the cage of UiO-66. Further insights into the electron transfer behavior were revealed by the PL quenching and fluorescence lifetime experiments (Figure 3.8c,d). The results show that in the presence of UiO-66, there is a significant quenching of the PL intensity and increase of fluorescence lifetime, indicating that the recombination of the photoexcited electron-hole pairs are significantly suppressed and the separation of electron-hole pairs are efficiently improved. The lengthening of the lifetime in the UiO-66/CNNS composite is ascribed to the electron transfer from the conduction band of CNNS to UiO-66 and then those electrons are localized in UiO-66. The electron transfer behavior in UiO-66/bulk CN composite was also confirmed by the quenching of the PL intensity and increase of fluorescence lifetime (Figure 3.10).

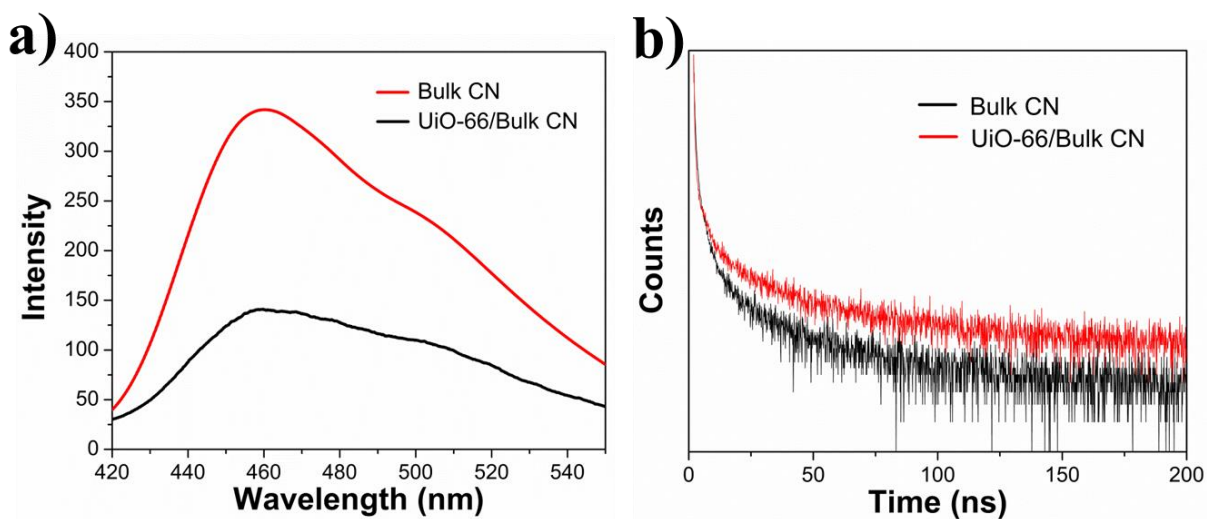


Figure 3.10. (a) PL spectra and (b) decay curve of bulk CN and UiO-66/bulk CN.

### 3.3.3 Evaluation of photocatalytic activity

The photocatalytic properties of samples were evaluated by photocatalytic reduction of CO<sub>2</sub>. The photocatalytic reduction of CO<sub>2</sub> was conducted in a reaction system using triethanolamine (TEOA) as an electron donor, under mild reaction conditions. The setup of the photocatalytic system was illustrated in Figure 3.11. After the photocatalytic reaction, neither H<sub>2</sub> nor hydrocarbon gases were detected, and CO was the main gas product from the CO<sub>2</sub> reduction. Figure 3.12a shows the time-dependent conversion yields of CO<sub>2</sub> into CO by our samples as photocatalysts under light irradiation. The generation of CO increased almost linearly with the irradiation time. It is apparent that CNNS exhibits higher efficiency in the CO<sub>2</sub> conversion than bulk CN. Furthermore, it is found that the CO yield was increased after UiO-66 was introduced. The UiO-66/CNNS composite shows the highest CO evolution rate and it rendered a CO yield of 59.4 μmol g<sub>CN</sub><sup>-1</sup> under light illumination for 6 hours, which is over three times than that of CNNS (17.1 μmol g<sub>CN</sub><sup>-1</sup>). The CO evolution amount of UiO-66/bulk CN composite reaches 19.3 μmol g<sub>CN</sub><sup>-1</sup> after 6 hours, which is 1.6-fold larger than those of bulk CN. This experiment demonstrates the superiority of the hybrid structure in the photocatalytic CO<sub>2</sub> conversion. When the experiment was conducted in the absence of photocatalysts or light illumination, no detectable CO was formed in the reaction system. To further validate the source of the generated CO product, an isotopic experiment using <sup>13</sup>CO<sub>2</sub> as substrate was performed under the identical photocatalytic reaction condition, and the products were analysed by gas chromatogram and mass spectra. As shown in Figure 3.13, the peak at m/z 29 was assigned to <sup>13</sup>CO, indicating that the carbon source of CO indeedly comes from CO<sub>2</sub>. The stability and reusability of the UiO-66/CNNS composite photocatalyst were investigated. After the reaction, the UiO-66/CNNS composite was removed from the reaction system and characterized by XRD pattern (Figure 3.14a) and morphology analyses (Figure 3.14b). The results show that the UiO-66/CNNS composite has strong resistance to crystal structure and morphology changes, which reflects its stable characteristics in the photocatalytic CO<sub>2</sub> conversion reaction. The reusability of the photocatalyst was studied by collecting and

## Chapter 3

reusing the photocatalyst for three times. As shown in Figure 3.12b, the UiO-66/CNNS composite photocatalyst exhibits fairly good photocatalytic activity stability in the recycling test.

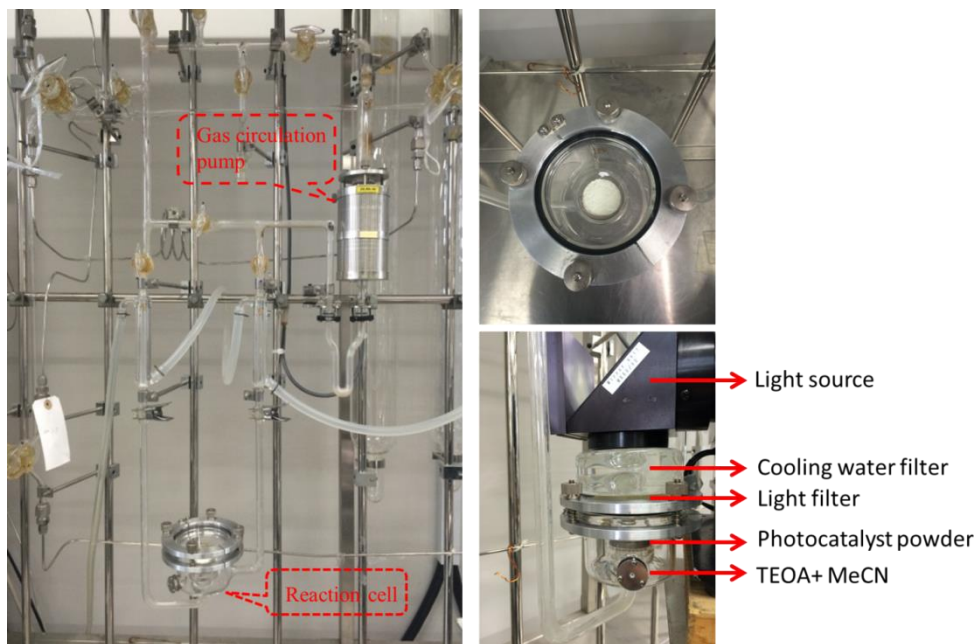


Figure 3.11. Setup of experiment.

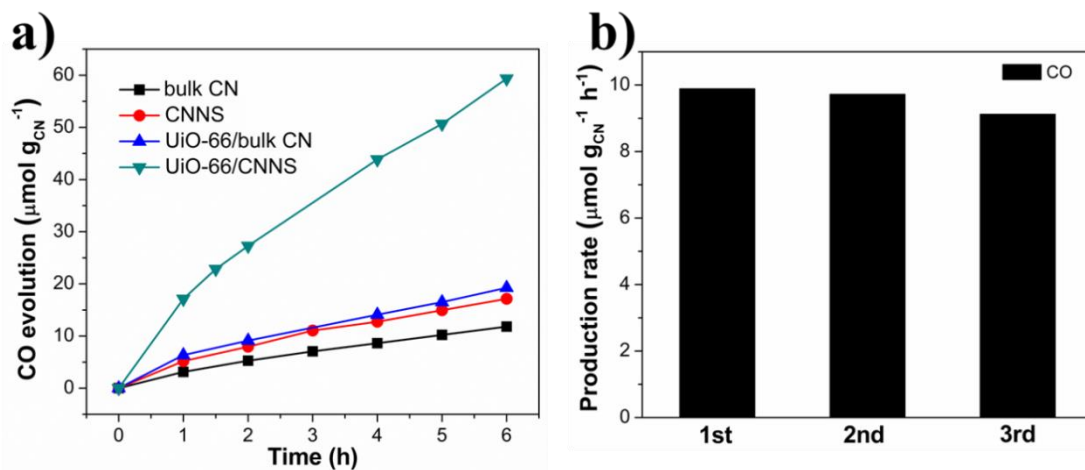


Figure 3.12. (a) Time course of CO evolution over bulk CN, CNNS, UiO-66/bulk CN and UiO-66/CNNS photocatalysts. (b) Production yields of CO over UiO-66/CNNS photocatalyst in the recycling tests. For hybrid structure photocatalysts, the carbon nitride content is 10 wt%.

## Chapter 3

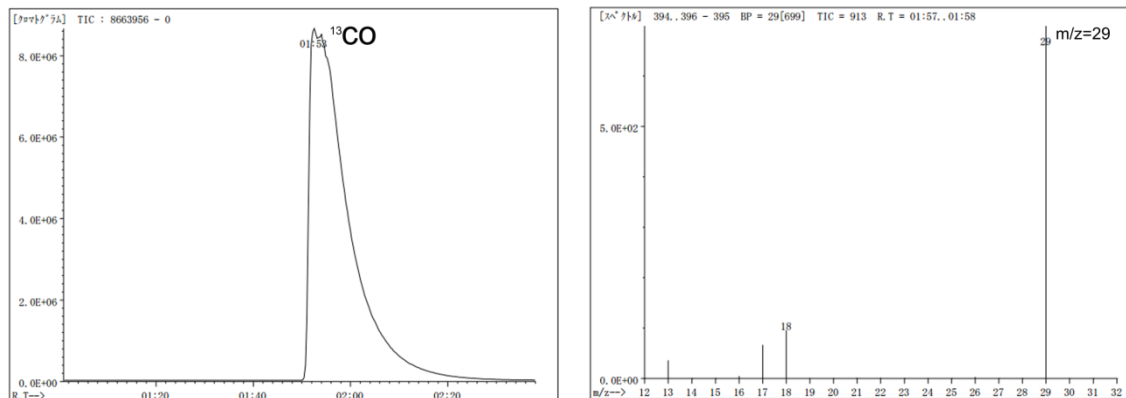


Figure 3.13. Gas chromatogram and mass spectra of  $^{13}\text{CO}$  ( $m/z=29$ ) produced over UiO-66/CNNS in the photocatalytic reduction of  $^{13}\text{CO}_2$ .

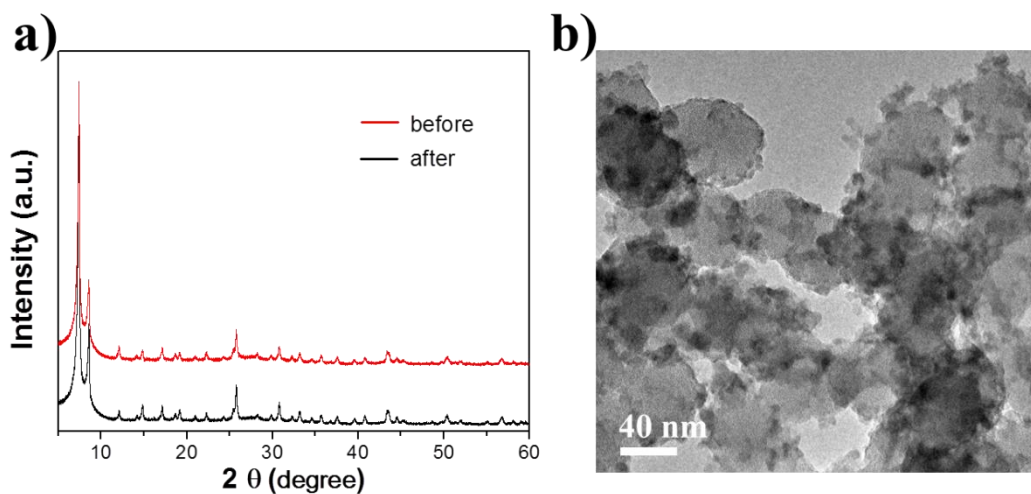


Figure 3.14. XRD patterns and TEM image of UiO-66/CNNS before and after photocatalytic  $\text{CO}_2$  reduction.

### 3.3.4 Clarification of the mechanism

The above information clearly shows the photocatalytic performance of  $\text{CO}_2$  reduction over CN and also demonstrates the improvement of photocatalytic activity over the hybrid structure formed by the integration of Zr-based MOF structured as UiO-66 with CN. I am now in a position to try to understand the mechanisms behind the function of the hybrid structure. It is well known that the band structure,

## Chapter 3

---

lifetime of photo-generated electron-hole pairs, separation efficiency of photoinduced charge carriers, CO<sub>2</sub> adsorption and activation are crucial factors that influence the photocatalytic CO<sub>2</sub> conversion efficiency.<sup>4</sup> It is important to note that the position of the conduction band for bulk CN is -1.3 V (*vs.* NHE, pH=7), which is negative enough to reach the corresponding reduction potential of CO<sub>2</sub> to produce CO (CO<sub>2</sub> + 2H<sup>+</sup> + 2e<sup>-</sup> → CO + H<sub>2</sub>O, -0.48 V *vs.* NHE at pH=7).<sup>4</sup> Both the theoretical prediction and experimental results have proven that the band gap enlargement of 0.15 eV in exfoliated CNNS could be ascribed to the shifting of conduction band and valence band in opposite directions, and thus shows higher conduction band edge and lower valence band edge compared with bulk CN to enhance the photoredox ability.<sup>28</sup> The enhancement of the photoredox ability in CNNS is responsible for its higher photocatalytic CO<sub>2</sub> reduction performance with respect to the bulk CN. Meanwhile, the CO<sub>2</sub> adsorption ability and lifetime of CNNS are higher than bulk CN, which is also responsible for its higher photocatalytic CO<sub>2</sub> reduction performance. The photocatalytic ability of CO<sub>2</sub> reduction can be further improved through the introduction of UiO-66. It was observed that UiO-66 itself did not show any detectable photocatalytic activity under visible light irradiation, due to its large bandgap that can only absorb UV light (Figure 3.2e). Therefore, the enhancement of the photocatalytic activity for the hybrid structure can be attributed to the synergistic effects of the enhanced CO<sub>2</sub> adsorption, separation efficiency of photoinduced charge carriers and prolonged lifetime of photo-generated electron-hole pairs as evidenced above.

However, I observe a significant difference in the activity improvement for UiO-66/CNNS composite and UiO-66/bulk CN composite compared with pristine CNNS and bulk CN. The CO evolution rate of UiO-66/CNNS composite shows 3.4-fold larger than that of CNNS, while UiO-66/bulk CN composite only shows 1.6 -fold larger than bulk CN. Taking into account that UiO-66/CNNS composite and UiO-66/bulk CN composite exhibit similar surface area and CO<sub>2</sub> adsorption ability, the significant difference in the activity enhancement can be ascribed to the different lifetime improvement. The lifetime of UiO-66/CNNS composite shows 75.8% improvement compared with CNNS, while UiO-66/bulk CN only shows 64.7% improvement compared with bulk CN. This suggests that the designed

## Chapter 3

---

UiO-66/CNNS hybrid system is much more robust in improving the efficiency of electron-hole separation, and this can be explained by three main reasons. First of all, compared to bulk CN, the CNNS has a larger bandgap by 0.15 eV as a result of higher conduction band and lower valence band, and this means that CNNS can provide a stronger driving force for the transfer of electrons to UiO-66 as a result of the larger energy level difference between the conduction band edge of CNNS and UiO-66. Secondly, it is well known that the electron transfer process in our hybrid structure involves two steps: photoexcited electrons in the CNNS or bulk CN migrate to the surface of CNNS or bulk CN, and subsequently transfer to UiO-66. Compared to bulk CN, the unique nanosheet structure of CNNS can shorten the electron transport distance between UiO-66 and the excitation center in the CNNS, thus facilitating efficient electron transfer and reducing the bulk recombination probability of charge carriers in CNNS. In addition, CNNS with flexible structure and soft nature, as well as more negatively charged surface, is much more easily adsorbed on the UiO-66 surface uniformly compared to bulk CN, which will increase the binding force between CNNS and UiO-66. It is thereby more easier for photogenerated electrons from CNNS to transfer to UiO-66 than bulk CN. The electrons localized in UiO-66 are sufficiently long-lived, resulting in higher electron density in UiO-66/CNNS composite, a feature that is also beneficial for the activation of CO<sub>2</sub> adsorbed in UiO-66, since the production of CO is a multi-electrons process.<sup>33</sup>

On the basis of the above discussion, a tentative mechanism of photocatalytic CO<sub>2</sub> reduction over UiO-66/CNNS composite was proposed, as shown in Figure 3.15. On visible light irradiation, electrons are promoted from the valence band of CNNS to its corresponding conduction band. Those photo-generated electrons migrate to the surface of CNNS and then transfer to UiO-66 across the interface between CNNS and UiO-66. The electrons in UiO-66 can reduce the adsorbed CO<sub>2</sub> to CO, and simultaneously, the holes remained on the valence band of CNNS were consumed by TEOA which acts as an electron donor.

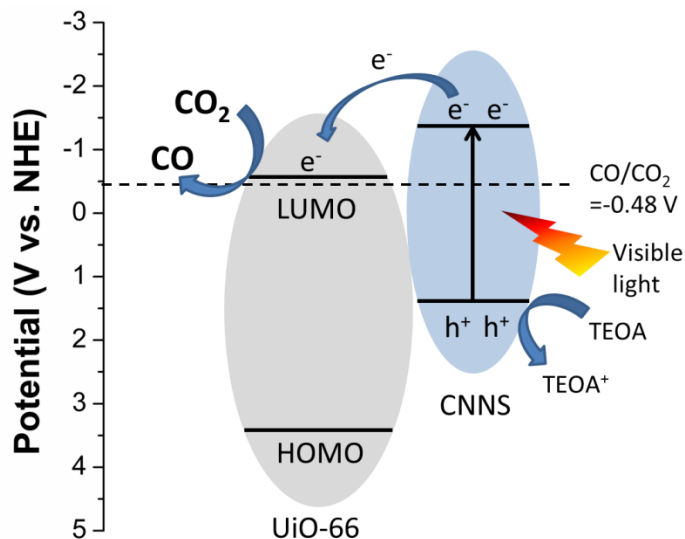


Figure 3.15. Proposed mechanism of photocatalytic reduction of  $\text{CO}_2$  by UiO-66/CNNS heterogeneous photocatalyst under visible light irradiation.

### 3.4 Conclusion

In summary, I have demonstrate a facile method to synthesize UiO-66/CNNS hybrid structure by electrostatic self-assembly of negatively charged CNNS with positively charged UiO-66. The designed hybrid structure possesses not only a large surface area and strong  $\text{CO}_2$  adsorption ability, but also an improved electron separation and prolonged lifetime of charge carriers as a result of efficient electron transfer across the interface between CNNS and UiO-66. As a result, the UiO-66/CNNS composite photocatalyst exhibited much higher photocatalytic activity for the  $\text{CO}_2$  conversion than bare CNNS under mild reaction conditions. Similarly, UiO-66/bulk CN hybrid structure was also prepared and showed enhanced activity for the photocatalytic reduction of  $\text{CO}_2$  compared with bulk CN, due to the strong  $\text{CO}_2$  adsorption ability of UiO-66 and the efficient charge transfer. It is anticipated that this work will provide a strategy to design more active photocatalysts for  $\text{CO}_2$  conversion reaction, as well as open up the opportunities to develop various MOFs based photocatalysts for gaseous reaction.

## Chapter 3

---

### References

1. S. C. Roy, O. K. Varghese, M. Paulose, C. A. Grimes, *ACS Nano*, **2010**, *4*, 1259.
2. X. Zhang, F. Han, B. Shi, S. Farsinezhad, G. P. Dechaine, K. Shankar, *Angew. Chem. Int. Ed.*, **2012**, *51*, 11778.
3. H. Tong, S. Ouyang, Y. Bi, N. Umezawa, M. Oshikiri, J. Ye, *Adv. Mater.*, **2012**, *24*, 229.
4. W. Tu, Y. Zhou, Z. Zou, *Adv. Mater.*, **2014**, *26*, 4607.
5. H. Yamashita, Y. Fujii, Y. Ichihashi, S. G. Zhang, K. Ikeue, D. R. Park, K. Koyano, T. Tatsumi, M. Anpo, *Catal. Today*, **1998**, *45*, 221.
6. M. Anpo, H. Yamashita, K. Ikeue, Y. Fujii, S. G. Zhang, Y. Ichihashi, D. R. Park, Y. Suzuki, K. Koyano, T. Tatsumi, *Catal. Today*, **1998**, *44*, 327.
7. M. Takeuchi, S. Sakai, A. Ebrahimi, M. Matsuoka, M. Anpo, *Top. Catal.*, **2009**, *52*, 1651.
8. P. Horcajada, C. Serre, G. Maurin, N. A. Ramsahye, F. Balas, M. V. -Reg í, M. Sebban, F. Taulelle, G. Férey, *J. Am. Chem. Soc.*, **2008**, *130*, 6774.
9. J. -L. Wang, C. Wang, W. Lin, *ACS Catal.*, **2012**, *2*, 2630.
10. J. R. Choi, T. Tachikawa, M. Fujitsuka, T. Majima, *Langmuir* **2010**, *26*, 10437.
11. T. M. McDonald, W. R. Lee, J. A. Mason, B. M. Wiers, C. S. Hong, J. R. Long, *J. Am. Chem. Soc.*, **2012**, *134*, 7056.
12. Y. Mao, L. Shi, H. Huang, W. Cao, J. Li, L. Sun, X. Jin, X. Peng, *Chem. Commun.*, **2013**, *49*, 5666.
13. J. H. Cavka, S. Jakobsen, U. Olsbye, N. Guillou, C. Lamberti, S. Bordiga, K. P. Lillerud, *J. Am. Chem. Soc.*, **2008**, *130*, 13850.
14. C. H. Lau, R. Babarao, M. R. Hill, *Chem. Commun.*, **2013**, *49*, 3634.
15. L. Shen, S. Liang, W. Wu, R. Liang, L. Wu, *J. Mater. Chem. A*, **2013**, *1*, 11473.
16. L. Shen, W. Wu, R. Liang, R. Lin, L. Wu, *Nanoscale*, **2013**, *5*, 9374.
17. J. Long, S. Wang, Z. Ding, S. Wang, Y. Zhou, L. Huang, X. Wang, *Chem. Commun.*, **2012**, *48*,

## Chapter 3

---

- 11656.
18. Z. Sha, J. Sun, H. S. O. Chan, S. Jaenicke, J. Wu, *RSC Adv.*, **2014**, *4*, 64977.
  19. D. Sun, Y. Fu, W. Liu, L. Ye, D. Wang, L. Yang, X. Fu, Z. Li, *Chem. Eur. J.* **2013**, *19*, 14279.
  20. X. Wang, K. Maeda, A. Thomas, K. Takanebe, G. Xin, J. M. Carlsson, K. Domen, M. Antonietti, *Nat. Mater.*, **2009**, *8*, 76.
  21. S. C. Yan, Z. S. Li, Z. G. Zou, *Langmuir*, **2010**, *26*, 3894.
  22. X. Chen, J. Zhang, X. Fu, M. Antonietti, X. Wang, *J. Am. Chem. Soc.*, **2009**, *131*, 11658.
  23. Z. Lin, X. Wang, *Angew. Chem. Int. Ed.*, **2013**, *52*, 1735.
  24. P. Niu, Y. Yang, J. C. Yu, G. Liu, H. –M. Cheng, *Chem. Commun.*, **2014**, *50*, 10837.
  25. S. Yang, Y. Gong, J. Zhang, L. Zhan, L. Ma, Z. Fang, R. Vajtai, X. Wang, P. M. Ajayan, *Adv. Mater.*, **2013**, *25*, 2452.
  26. P. Niu, L. Zhang, G. Liu, H. –M. Cheng, *Adv. Funct. Mater.*, **2012**, *22*, 4763.
  27. X. Lu, K. Xu, P. Chen, K. Jia, S. Liu, C. Wu, *J. Mater. Chem. A*, **2014**, *2*, 18924.
  28. X. Zhang, X. Xie, H. Wang, J. Zhang, B. Pan, Y. Xie, *J. Am. Chem. Soc.*, **2013**, *135*, 18.
  29. X. Zhang, H. Wang, H. Wang, Q. Zhang, J. Xie, Y. Tian, J. Wang, Y. Xie, *Adv. Mater.*, **2014**, *26*, 4438.
  30. Y. Cui, Z. Ding, P. Liu, M. Antonietti, X. Fu, X. Wang, *Phys. Chem. Chem. Phys.*, **2012**, *14*, 1455.
  31. J. He, J. Wang, Y. Chen, J. Zhang, D. Duan, Y. Wang, Z. Yan, *Chem. Commun.*, **2014**, *50*, 7063.
  32. Y. Zheng, L. Lin, X. Ye, F. Guo, X. Wang, *Angew. Chem. Int. Ed.*, **2014**, *53*, 1.
  33. R. Li, J. Hu, M. Deng, H. Wang, X. Wang, Y. Hu, H.-L. Jiang, J. Jiang, Q. Zhang, Y. Xie, Y. Xiong, *Adv. Mater.*, **2014**, *26*, 4783.

# Chapter 4 Implantation of Iron(III) in Porphyrinic Metal Organic Frameworks for Highly Improved Photocatalytic Performance

## 4.1 Introduction

The design and construction of efficient photocatalysts for maximizing the solar-light energy utilization remains crucial in the field of photocatalysis.<sup>1-4</sup> To meet the challenges, various photocatalysts have been developed, among which metal organic frameworks (MOFs) based photocatalysts have drawn considerable and increasing attention.<sup>5-7</sup> MOFs are class of crystalline materials that are constructed from well-defined molecular building blocks and metal or metal-cluster connecting nodes. Recently, many MOFs materials have shown semiconductor-like characters in photocatalysis, and have achieved potential applications in all kinds of photocatalytic areas, such as H<sub>2</sub>/O<sub>2</sub> evolution from water splitting,<sup>8-10</sup> organic pollutant photo-decomposition,<sup>11-12</sup> inorganic hazardous substances photo-reduction,<sup>13-15</sup> CO<sub>2</sub> reduction,<sup>16-20</sup> and so on. However, the photocatalytic efficiency of MOFs based photocatalysts is still very low and far from satisfaction for the practical needs, largely due to the low efficiency in light harvesting and the fast recombination of the photogenerated electron–hole pairs. In this context, great efforts have been devoted to improve the photocatalytic efficiency of MOFs based photocatalysts over past few years and most of the reported strategies were limited to a narrow range by either modulation of their organic linkers (e.g., tethering the ligand with one or two additional amine groups) or incorporation with dye/semiconductor catalysts for enlarged visible light absorption, better charge separation, and efficient reactant activation.<sup>21-28</sup> Developing novel strategies to dramatically boost the photocatalytic efficiency of MOFs based photocatalysts is desperately needed.

## Chapter 4

---

The modification of transition metal ions, such as Fe(III), on photocatalysts has been proved as an efficient way to realize high photocatalytic performance.<sup>29-30</sup> Because of the relative low redox potentials of Fe<sup>3+/2+</sup> compared with the conduction band positions of photocatalysts, the photogenerated electrons from photocatalysts can be easily scavenged by the modified Fe(III) ions, inducing the efficient separation of electron-hole pairs, which should be beneficial for the photocatalytic reactions.<sup>30</sup> Fe(III) ions were also be used as a reactant in light induced heterogeneous Fenton-like photocatalytic process to produce abundant and active oxygen-related species ( $\bullet\text{OH}$  and  $\bullet\text{O}_2^-$ ), which play an essential role in promoting the photocatalytic activities for oxidation of organic molecular.<sup>31-32</sup> The generally accepted free-radical-chain mechanism of Fenton reaction between Fe<sup>3+</sup>/Fe<sup>2+</sup> pair and H<sub>2</sub>O<sub>2</sub> is shown below:<sup>31</sup>



In most cases, however, extra H<sub>2</sub>O<sub>2</sub> must be added into the reaction system as a reactant to initiate those Fenton-like reactions, which is not cost-effective.<sup>32-34</sup> Very recently, it has been demonstrated that a Fenton reaction could be constructed on Fe(III) modified alkalized-C<sub>3</sub>N<sub>4</sub> photocatalyst even without adding extra H<sub>2</sub>O<sub>2</sub>, in which the light energy was used as power, alkalized-C<sub>3</sub>N<sub>4</sub> photocatalyst acted as an in situ and robust H<sub>2</sub>O<sub>2</sub> generator, and the modified Fe<sup>3+</sup> acted as a trigger of H<sub>2</sub>O<sub>2</sub> conversion to produce considerably abundant oxygen-related radicals.<sup>35</sup> To initiate this Fenton reaction, an indispensable issue that must be mentioned is the capability of photocatalysts to photogenerate H<sub>2</sub>O<sub>2</sub>. It has been reported that porphyrins and their derivatives owned the ability to effectively photogenerate H<sub>2</sub>O<sub>2</sub>.<sup>36-37</sup> I can reason that the photogeneration of H<sub>2</sub>O<sub>2</sub> might be realized via integration of porphyrins unites into MOFs structure. Bearing these in mind and motivated by the fact that the unique structural properties of porphyrins could provide the effective coordination sites to anchor individual metal ions,<sup>38-39</sup> I can reasonably expect that the Fe(III) could be rationally modified on porphyrinic MOFs based photocatalysts, which would result in much improved separation efficiency of electron-hole pairs, as well

## Chapter 4

---

as initiate the Fenton-like reactions to produce active oxygen-related species, and finally improve the photocatalytic activities.

In this work, I employed a very stable porphyrinic MOF, PCN-224, which integrate the  $Zr_6$  clusters and porphyrin based molecular units into 3D network, as a visible light active photocatalyst for isopropanol (IPA) oxidation. Coordinatively unsaturated Fe(III) ions are implanted into porphyrin unit and generate a new hybrid structure Fe@PCN-224. The introduction of Fe(III) ions in PCN-224 can not only improve the separation efficiency of photogenerated electron-hole pairs, but also construct a Fenton reaction to convert the *in situ* photogenerated  $H_2O_2$  into active oxygen-related radicals ( $\bullet OH$  and  $\bullet O_2^-$ ) during the photocatalytic reaction. As a direct result, the newly developed Fe@PCN-224 exhibits significantly enhanced photocatalytic oxidation of IPA, which is equivalent to an 8.9-fold improvement in acetone evolution rate and 9.3-fold enhancements in  $CO_2$  generation rate compared with the PCN-224. Furthermore, apart from PCN-224, such Fe(III) implantation-enhanced photocatalytic IPA oxidation performance could also be observed over another porphyrinic MOF, PCN-222, suggesting the generality of this strategy.

### 4.2 Experimental section

#### 4.2.1 Synthesis of photocatalysts

In the synthesis of PCN-224, 120 mg  $ZrOCl_2 \cdot 8H_2O$  (Wako Co.) was added to N, N-dimethylformamide (DMF, 50 mL) and stirred for thirty minutes. After that, 25 mg tetrakis(4-carboxyphenyl)-porphyrin (TCI, Tokyo Chemical Industry Co.) was added to the solution. After ten minutes further stirring, acetic acid (12.5 mL) was added to the solution. The solution was heated at 338 K for three days in the autoclave. The generated precipitate was collected by centrifugation, washed repeatedly by methanol and dried under vacuum at 80 °C. Fe@PCN-224 was prepared as follows: 100 mg of PCN-224 and 200 mg of  $FeCl_3$  were mixed together into 20 ml DMF solution and stirred for 30 min at room temperature. After that the solution was heated at 120 °C with stirring for 12 h, and the generated precipitate was collected by centrifugation, washed repeatedly by methanol and dried. The weight

## Chapter 4

---

percentage of the Fe in PCN-224 was measured by inductively coupled plasma (ICP)-elemental analysis, which was 4.1 wt.%. Fe@PCN-224 was prepared as follows: 100 mg of PCN-224, 13.5 mg FeCl<sub>3</sub> (4.1 wt.% Fe in Fe@PCN-224) and 3 ml ethanol were ground together in a mortar under room temperature. After the evaporation of ethanol, the powder sample was collected and then dried under 60 °C for 6 hours.

PCN-222 (also called MOF-545) was prepared according to a previous report with minor modifications. ZrOCl<sub>2</sub>·8H<sub>2</sub>O (75 mg) was added to DMF (20 mL) and stirred for thirty minutes. Following stirring, tetrakis(4-carboxyphenyl)-porphyrin (13 mg) was added to the solution. After a further ten minutes of stirring, formic acid (14 mL) was added to the solution. The solution was heated at 130 °C for three days in the autoclave, and then the generated precipitate was collected by centrifugation, washed repeatedly by methanol and dried under vacuum at 80 °C. Fe@PCN-222 was prepared similarly to Fe@PCN-224 except that PCN-224 was replaced by PCN-222.

NH<sub>2</sub>-MIL-125 was synthesized by adding 2-amino benzenedicarboxylic acid (6 mmol) and titanium isopropoxide (3 mmol) into a solution containing DMF (25 ml) and methanol (25 ml). The mixture was stirred at ambient temperature for 30 min, transferred to Teflon lined stainless steel autoclave, and heated 16 h at 423 K. After the reaction, the product of the synthesis was extracted by centrifugation, and washed with methanol. The obtained yellow solid was dried under vacuum overnight. NH<sub>2</sub>-UiO-66 was prepared as follows: ZrCl<sub>4</sub> (0.240 g) and 2-amino benzenedicarboxylic acid (0.186 g) were added into DMF (60 mL) solution at room temperature. The mixed solution was stirred at room temperature for 30 min and transferred to Teflon lined stainless steel autoclave and heated at 120°C for 48 h. After hydrothermal treatment, the resultant suspension was filtered, washed with DMF and methanol several times, and dried under vacuum overnight. For the synthesis of MIL-88B (Fe), benzenedicarboxylic acid (3mmol, 0.498g) and FeCl<sub>3</sub>·6H<sub>2</sub>O (3mmol, 0.811g) were dissolved in DMF (50 mL). After vigorously stirred for 10 min, this solution was placed in a sealed vessel and heated by microwave at 400W for 15 min at 150°C. After cooling to room temperature, the resulting particles were isolated by centrifugation, washed with ethanol

## Chapter 4

---

and deionized water several times, and then dried at 343 K under vacuum overnight. g-C<sub>3</sub>N<sub>4</sub> was prepared by heating melamine to 550°C for 4 hours under air condition in a crucible.

### 4.2.2 Characterization

The crystal structure of the samples were characterized by powder XRD (SmartLab). The UV-Vis spectra of the samples were measured on a UV-visible spectrophotometer (SHIMADZU UV-2600) and BaSO<sub>4</sub> was used as the reflectance standard reference. The morphology analysis of the as-prepared samples was conducted on a scanning electron microscope (SEM, S4800, Hitachi Co., Japan). TEM, HAADF-STEM, and elemental mapping images were taken on a transmission electron microscope (TEM, 2100F, JEOL Co., Japan). Nitrogen adsorption-desorption isotherms and BET surface areas were recorded using a Quantachrome Autosorb-iQ Automated Gas Sorption System at 77 K, and the pore size distributions were analyzed by density functional theory (DFT) model. Before nitrogen adsorption-desorption measurement, the samples were treated under vacuum at 150°C for 12h. The PL spectra of samples were recorded on the powder samples by using JASCO FP-6500 spectrofluorometer. The PL lifetime measurements were performed on a compact fluorescence lifetime spectrometer (Quantaaurus-Tau, C11367, HAMAMATSU). the chemical state of the samples were analyzed by X-ray photoelectron spectroscopy (XPS, PHI Quantera SXM, ULVAC-PHI Inc., Japan). The chemical structure of the samples was studied by FTIR spectra (Thermoscientific Nicolet 4700). The ESR measurements were carried out with JEOL JES-FA-200 at room temperature.

### 4.2.3 Photoelectrochemical Measurement

The photoelectrochemical measurements were carried out in an electrochemical station (ALS/CH model 650A, Japan). The as-prepared PCN-224 and Fe@PCN-224 photoanodes (1.0 × 1.0 cm<sup>2</sup>) were used as a working electrode, a Pt foil was used as a counter electrode, a Ag/AgCl electrode was used as the reference electrode, and a 0.5 M Na<sub>2</sub>SO<sub>4</sub> solution was used as the electrolyte. A 500 W Xe lamp with a UV-cutoff filter ( $\lambda > 400\text{nm}$ ) was used as the visible light source. The photocurrent was measured at -

## Chapter 4

---

0.5 V bias voltage *versus* Ag/AgCl. The Mott-Schottky plots were obtained in the dark at 1000 and 500 Hz. The electrochemical impedance spectra were measured under visible light.

### 4.2.4 The measurement of H<sub>2</sub>O<sub>2</sub>

The measurement of H<sub>2</sub>O<sub>2</sub> was conducted by using the colorimetric DPD method. The DPD method is based on the oxidation of N,N-diethyl-p-phenylenediamine (DPD) catalyzed with horseradish peroxidase (POD) by H<sub>2</sub>O<sub>2</sub>. Briefly, 0.1 g of DPD was dissolved in 10 ml 0.05 M H<sub>2</sub>SO<sub>4</sub>, denoted as solution A. 10 mg of peroxidase (POD) was dissolved in 10 ml water, denoted as solution B. 10 ml of 0.1 M Na<sub>2</sub>HPO<sub>4</sub> solution and 90 ml of 0.1 M NaH<sub>2</sub>PO<sub>4</sub> solution were mixed together to obtain solution C. Then 54 ml deionized water, 6 ml solution C, 24 μl methanol, 100 μl solution A and 100 μl solution B were mixed together to obtain solution D. The in-situ generated H<sub>2</sub>O<sub>2</sub> during the photocatalytic IPA oxidation was measured as follows: the 20 mg photocatalyst sample powder was irradiated under visible-light for 5 min in the reaction cell with gaseous IPA and air addition, and then was dispersed into solution D, 3 ml filtrates was used to measure the generated H<sub>2</sub>O<sub>2</sub>, which was monitored by the absorption of the solution at 551 nm and determined with UV-vis spectrophotometer. The time-dependent H<sub>2</sub>O<sub>2</sub> generation was measured in a similar above procedure expect that the irradiation time was set as 10, 15, 20, 25 minutes, respectively.

### 4.2.5 Photocatalytic experiments

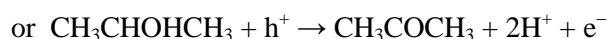
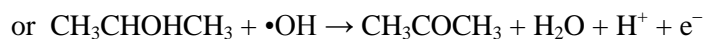
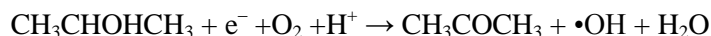
A 300 W Xe arc lamp (focus through a 45 × 45 mm shutter window) equipped with a UV light cutoff filter ( $\lambda > 400$  nm) and a cooling water filter was employed as the light source. 0.05 g of the sample was evenly spread over a dish with an area of 8.5 cm<sup>2</sup> in a 500 ml borosilicate glass vessel. The experimental facility can be seen from Figure S6. Then the vessel was pretreated by artificial air [V(O<sub>2</sub>):V(N<sub>2</sub>) = 1:4] for 5 min to remove the gaseous impurities. After the sample was sealed in the vessel, a certain amount of gaseous isopropanol (IPA) was injected into the vessel. Before exposed to the visible light irradiation, the reaction cell was kept in dark to ensure an adsorption–desorption equilibrium. The generated concentration of acetone and CO<sub>2</sub> was measured by using a gas chromatograph (GC-2014,

## Chapter 4

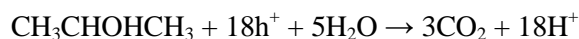
---

Shimadzu Corp., Japan) equipped with FID detectors and methanizer. The photocatalytic IPA oxidation undergoes two kinds of typical reaction processes as below:

(1) One-photon reaction:



(2) Multiphoton reaction:



### 4.3 Results and discussion

#### 4.3.1 Characterization of photocatalysts

Solvothermal treatment of zirconyl chloride octahydrate, tetrakis(4-carboxyphenyl)-porphyrin ( $\text{H}_2\text{T CPP}$ ) and acetic acid in DMF solution yielded dark red-colored crystals of PCN-224. PCN-224 crystallizes in space group  $\text{Im}\bar{3}\text{m}$ , and its framework consists of  $\text{Zr}_6$  clusters linked by the square planar  $\text{H}_2\text{T CPP}$  ligands.<sup>40</sup> Each  $\text{Zr}_6(\text{OH})_8$  core, in which all of the triangular faces in a  $\text{Zr}_6$ -octahedron are capped by  $\mu_3$ -OH groups, is connected to six  $\text{H}_2\text{T CPP}$  ligands (Figure 4.1a, Figure 4.2). The phase purity of the as-prepared sample was confirmed by X-ray powder diffraction, which is in good agreement with the simulated PCN-224 structure (Figure 4.1b). Cationic Fe(III) was incorporated into porphyrin unit (Figure 4.1a) and generate a hybrid structure Fe@PCN-224 by postsynthetic reaction between PCN-224 and  $\text{FeCl}_3$  in DMF solution. The XRD pattern in Figure 4.1b shows that the PCN-224 and Fe@PCN-224 exhibit the similar diffraction pattern, indicating that the crystal phase structure is retained after Fe(III) incorporation. The electron spin resonance (ESR) spectrum of Fe@PCN-224 in Figure 4.1c displays a

## Chapter 4

---

strong signal at  $g$  value of 1.996, which can be ascribed to the high-spin state Fe(III), confirming the incorporation of Fe(III) into PCN-224 structure.<sup>13</sup> The X-ray Photoelectron Spectroscopy (XPS) spectra were further recorded to determine the chemical state of the Fe species (Figure 4.3a). In the Fe 2p core level spectrum, the peak observed at around 711 eV can be assigned to Fe<sup>3+</sup>, which is consistent with the ESR results illustrated above.<sup>35</sup> The fourier transform infrared (FTIR) spectroscopy is shown in Figure 4.3b, compared with H<sub>2</sub>TCP ligand, the asymmetric vibrational absorption intensity of C=O and C–OH groups greatly decrease after coordination between Zr<sup>4+</sup> and –COOH groups in PCN-224, indicating that the –COOH groups in H<sub>2</sub>TCP ligands are participated in the coordination with Zr<sup>4+</sup>.<sup>41</sup> N–H bond absorption is observed in H<sub>2</sub>TCP and PCN-224, which confirms the existence of the uncoordinated nitrogen sites in the PCN-224.<sup>42</sup> By post-synthetic modification of PCN-224 with Fe(III) ions, it can be observed that there is no N–H bond adsorption in the as-synthesized Fe@PCN-224 (See the magnified FTIR spectra in Figure 4.3c). Moreover, an intense symmetric Fe–N stretching at around 1000 cm<sup>-1</sup> appears for Fe@PCN-224 (Figure 4.3d), further reflecting the metalation of porphyrin ring with Fe to form iron porphyrinate.<sup>42</sup> All the above results support the successful incorporation of Fe(III) into the porphyrin unit in PCN-224.

The obtained PCN-224 grows into big cubic crystals, which are distributed in the size of several micrometers, as revealed by scanning electron microscopy (SEM) images (Figure 4.4a, b). Incorporation of Fe(III) into PCN-224 would not significantly change its morphology (Figure 4.4c, d). Figure 4.4e-i show the high-angle annular dark-field scanning TEM (HAADF-STEM) image and the corresponding elemental mapping analysis of Fe@PCN-224. It clearly shows the well-defined spatial distributions of element Fe, N, Zr and O, which confirms that Fe is uniformly incorporated in the PCN-224. The existence of Fe element can also be evidenced by the energy dispersive X-ray spectrometer (EDS) spectrum (Figure 4.5). The N<sub>2</sub> adsorption-desorption measurements at 77 K for PCN-224 and Fe@PCN-224 show a type I isotherm (Figure 4.6). PCN-224 has the stronger ability for N<sub>2</sub> adsorption with the Brunauer-Emmett-Teller (BET) surface areas of 2726 m<sup>2</sup> g<sup>-1</sup>, which is higher than that of Fe@PCN-224 (2360 m<sup>2</sup> g<sup>-1</sup>). The

## Chapter 4

reason may be ascribed to the introduction of Fe sites, which can slightly diminish the surface area. Figure 4.7 shows the pore size distribution of PCN-224 and Fe@PCN-224. The desirable porous structures and high surface area of PCN-224 and Fe@PCN-224 allow for exposing active sites as much as possible and facilitating the accessibility of target reactants to the active sites, which might be advantageous for photocatalysis.

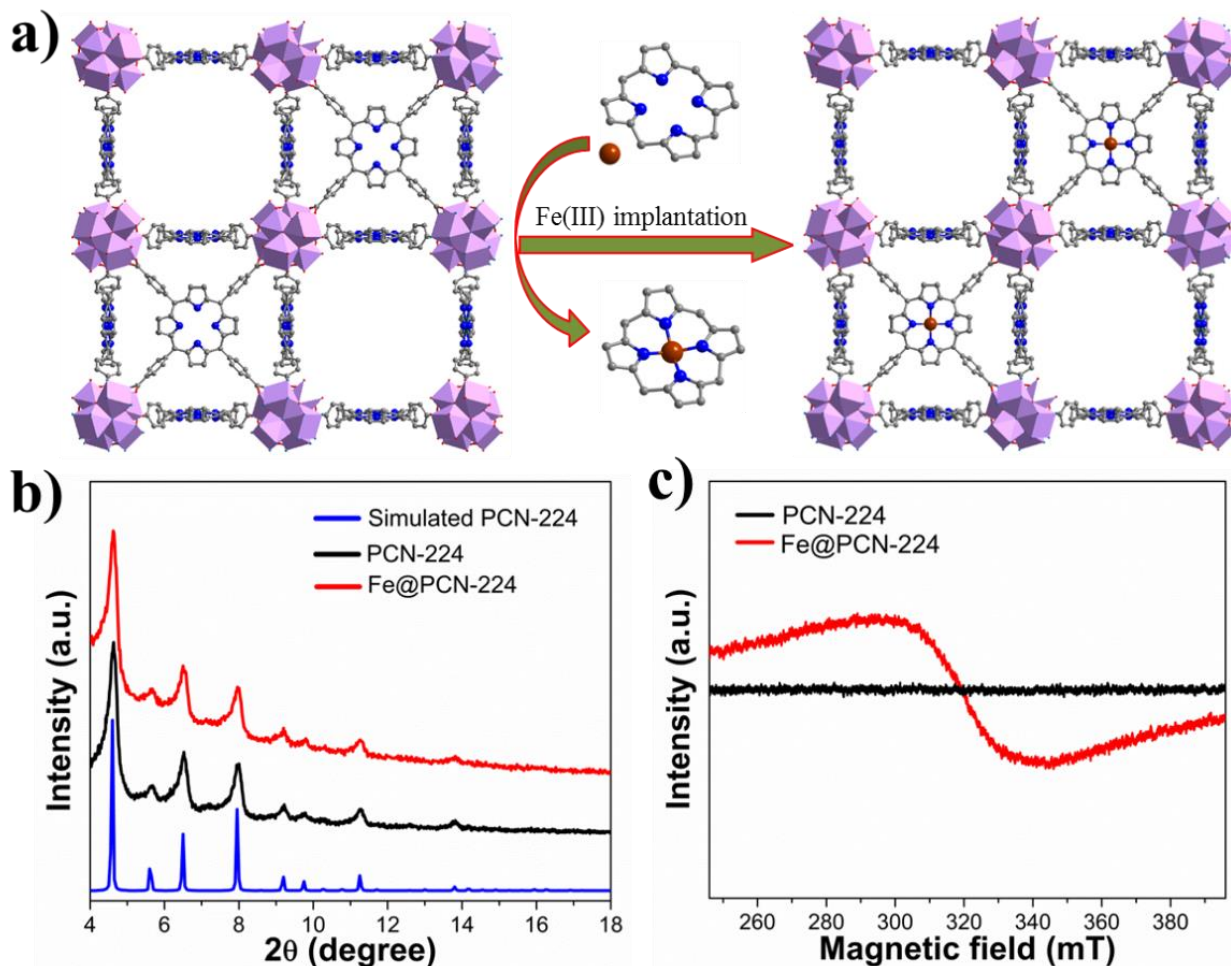


Figure 4.1. (a) View of the 3D network of PCN-224 featuring highly porous framework as well as the implantation of Fe(III) sites into the PCN-224 framework; (b) XRD patterns of PCN-224 and Fe@PCN-224; (c) ESR spectra of PCN-224 and Fe@PCN-224.

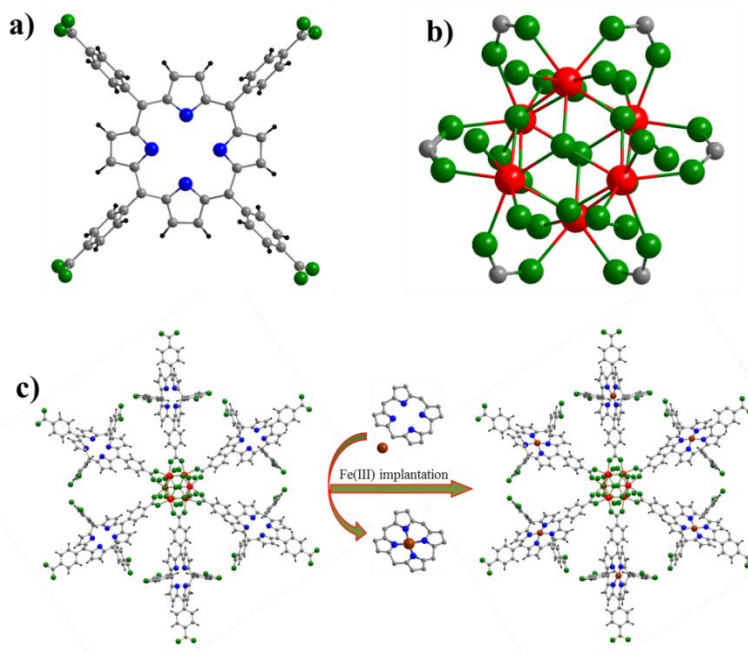


Figure 4.2. (a) The structure of  $H_2TCPP$  ligand; (b) the 6-connected  $D_{3d}$  symmetric  $Zr_6$  in PCN-224; (c) the  $Zr_6$  cluster is connected to six  $H_2TCPP$  ligands before and after Fe(III) implantation. C (gray), N (blue), O (green), Zr (red), Fe (brown).

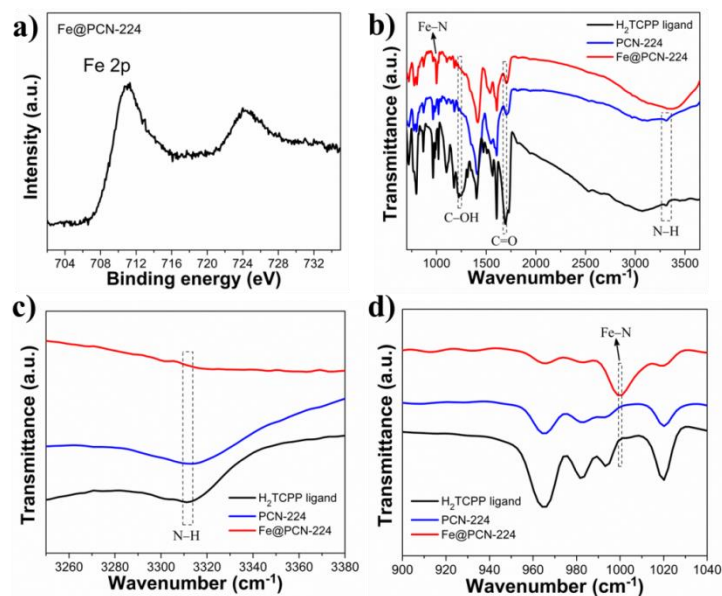


Figure 4.3. (a) high resolution Fe XPS spectrum of Fe@PCN-224; (b) FTIR spectra of  $H_2TCPP$  ligands, PCN-224 and Fe@PCN-224; (c)-(d) The magnified FTIR spectra of  $H_2TCPP$  ligands, PCN-224 and Fe@PCN-224.

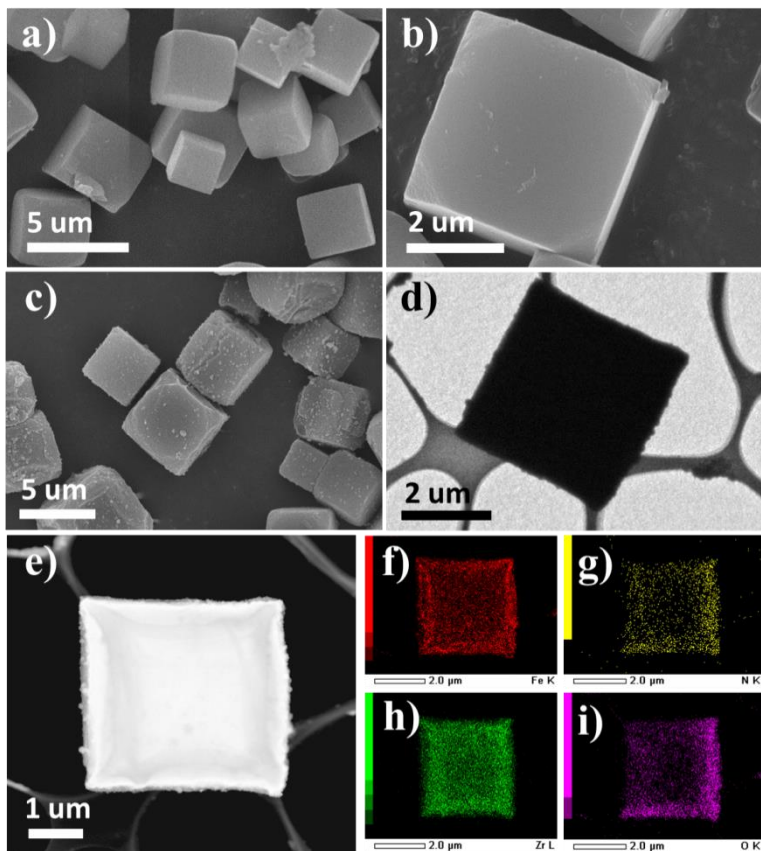


Figure 4.4. (a)-(b) SEM images of PCN-224; (c)-(d) SEM and TEM images of Fe@PCN-224, respectively; (e)-(i) HAADF-STEM image and its corresponding elemental mapping images of Fe@PCN-224. (f) Fe, (g) N, (h) Zr, (i) O.

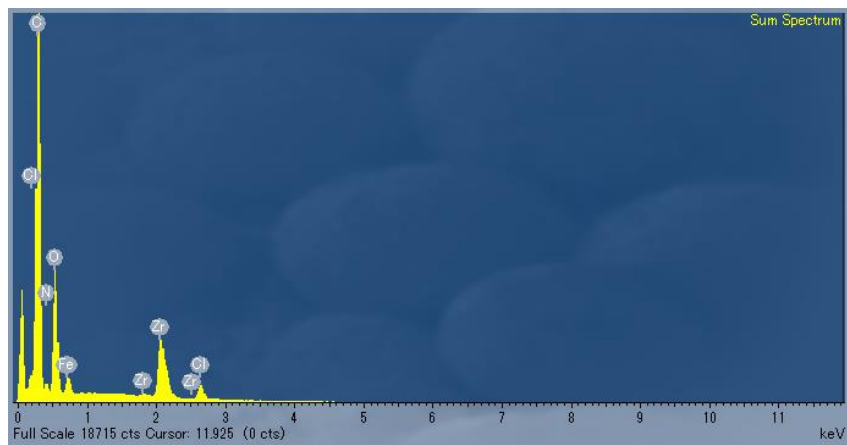


Figure 4.5. EDS spectrum of Fe@PCN-224.

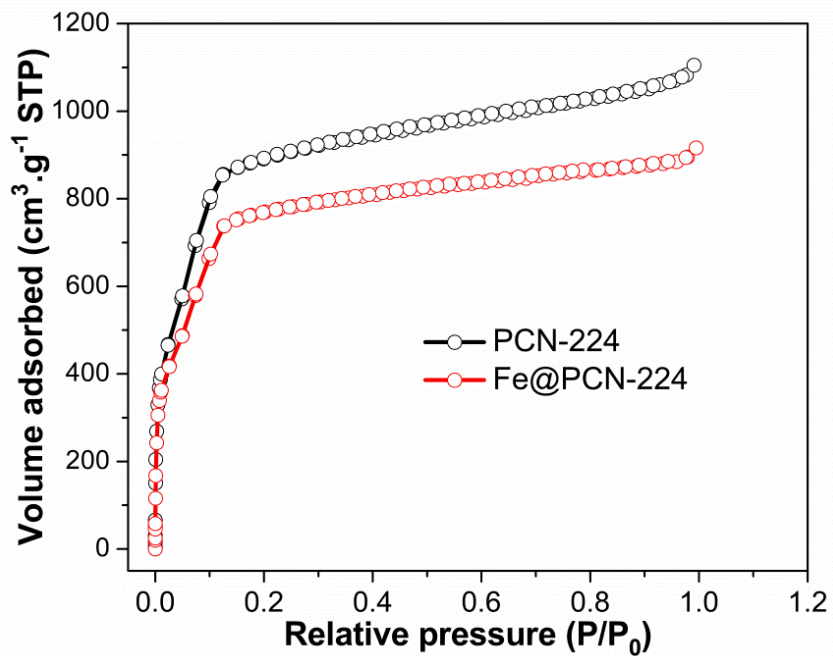


Figure 4.6. N<sub>2</sub> adsorption-desorption spectra of PCN-224 and Fe@PCN-224.

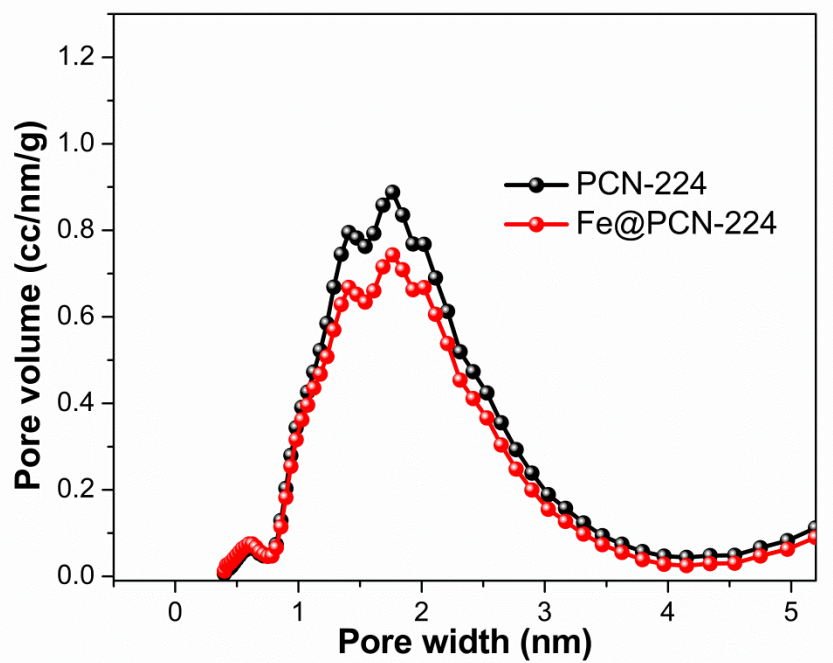


Figure 4.7. Pore size distribution of PCN-224 and Fe@PCN-224.

## Chapter 4

The incorporation of Fe(III) into PCN-224 would induce the color change from dark red to brown (Figure 4.8a, inset). The UV-Vis spectra in Figure 4.8a indicates that PCN-224 is an excellent photon absorbers from 250 to 700 nm, which allows for promoting the electrons of PCN-224 to an excited state upon visible light irradiation. According to  $(\alpha h\nu)^{1/2} = A(h\nu - E_g)$ , where  $\alpha$ ,  $\nu$ ,  $A$  and  $E_g$  are absorption coefficient, light frequency, proportionality constant and indirect band gap energy, respectively, the calculated indirect bandgap of the PCN-224 is 1.75 eV (Figure 4.9). After the metalation of the porphyrin ring with Fe(III), the Fe@PCN-224 hybrid structure can extend light absorption edge to 1000 nm, which can be ascribed to the fact that the incorporation of Fe(III) in the PCN-224 structure can lower its band gap energy by introducing unoccupied Fe(III) trap levels between the valence band maximum (VBM) and the conduction band minimum (CBM) of PCN-224.<sup>30</sup> These introduced trap levels allow for excitation of electrons from VBM of PCN-224 to the trap levels when subjected to near-infrared illumination.

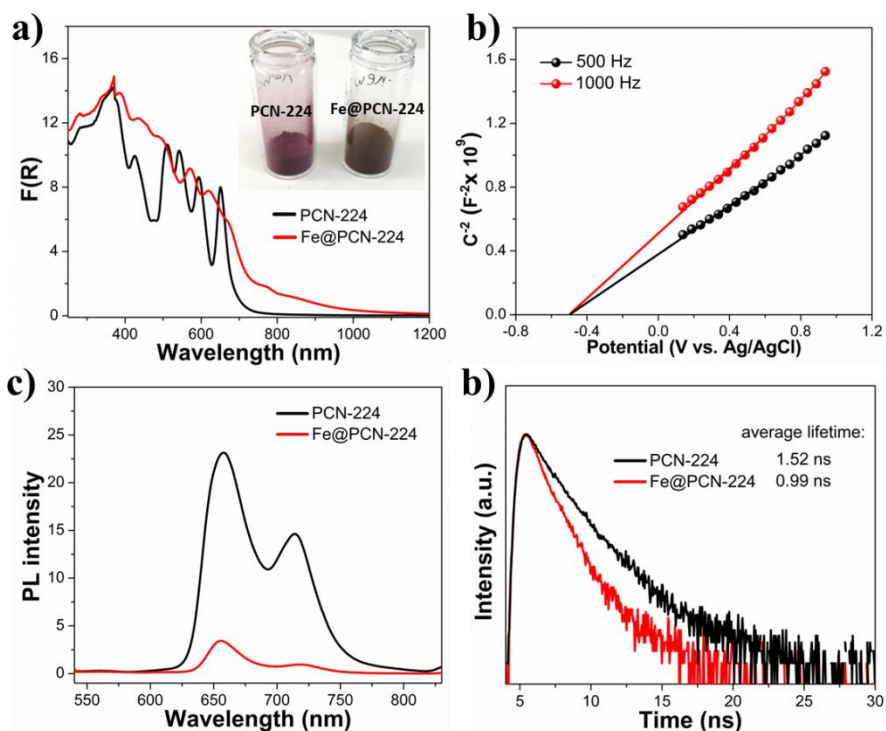


Figure 4.8. (a) UV-vis spectra and photograph (inset) of PCN-224 and Fe@PCN-224, respectively; (b) Mott-Schottky plots of PCN-224; (c)-(d) PL spectra and lifetime decay curves of PCN-224 and Fe@PCN-224, respectively.

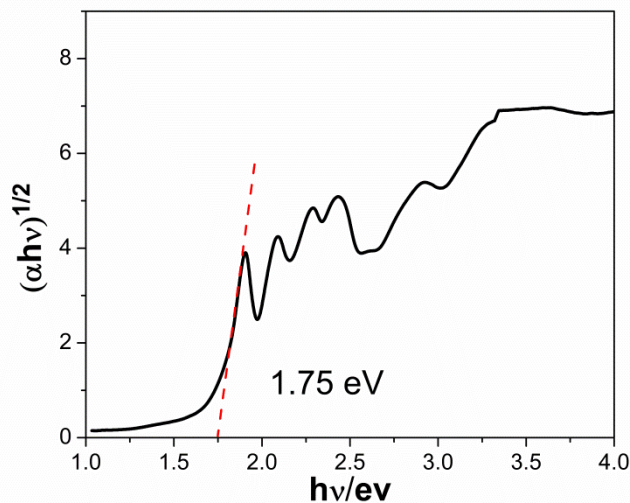


Figure 4.9. Bandgap energy of PCN-224.

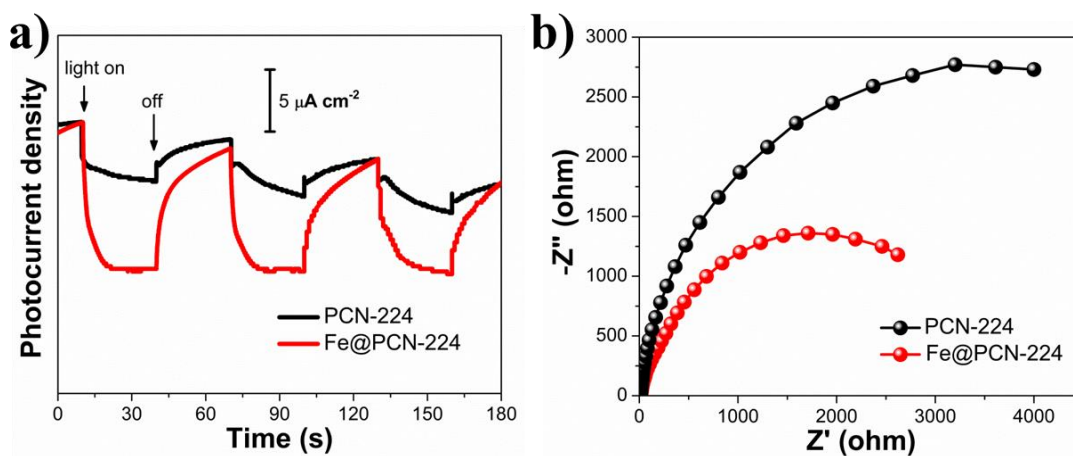


Figure 4.10. (a) Transient photocurrent response and (b) electrochemical impedance spectra of PCN-224 and Fe@PCN-224, respectively.

In order to elucidate the semiconductor character of PCN-224, Mott-Schottky measurements on PCN-224 photoanode were conducted at frequencies of 500 and 1000 Hz (Figure 4.8b). The positive slope of the obtained  $C^2$  to potential plot is consistent with that of typical n-type semiconductors,<sup>43</sup> and the derived flat-band potential for PCN-224 is -0.50 V versus Ag/AgCl (Figure 4.8b). Considering the small difference between the flat-band potential and the lower CB edge for n-type semiconductors, the

## Chapter 4

CBM position of PCN-224 can be roughly estimated to be +0.11 V (vs. RHE). With the bandgap energy of PCN-224 estimated to be 1.75 eV from the Tauc plot (Figure 4.9), its VBM position is then calculated to be +1.86 V (vs. RHE). Moreover, the PCN-224 photoanode produces an obvious photocurrent response to on-off cycles of light illumination with the bias potential applied under visible light irradiation, demonstrating that electron-hole pairs are generated over PCN-224 under visible light irradiation (Figure 4.10). These results indicate that PCN-224 should be a suitable candidate for light harvesting and photocatalysis.

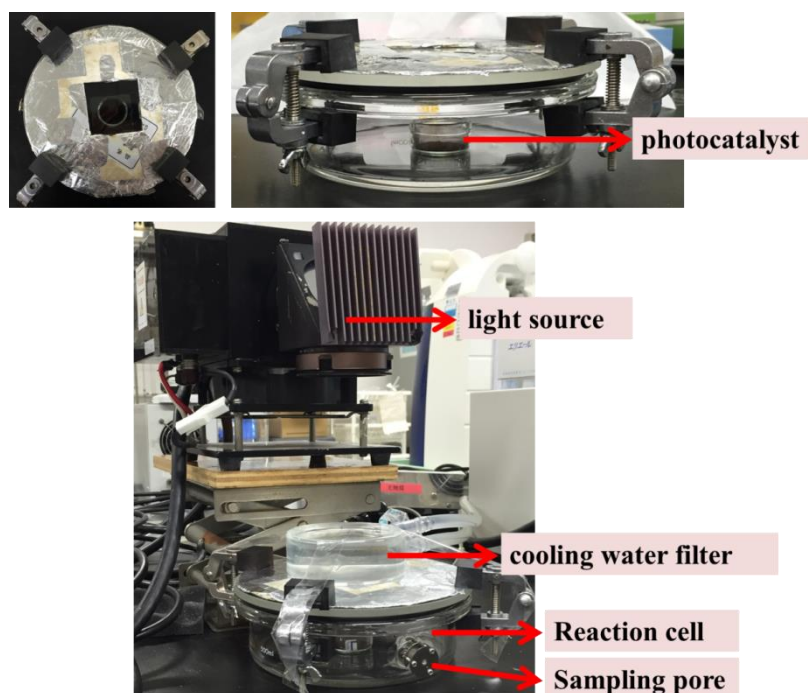


Figure 4.11. The setup of the photocatalytic IPA oxidation experiment.

### 4.3.2 Photocatalytic performance

IPA as a typical volatile organic compound in industry is a serious pollutant of indoor air.<sup>35</sup> In order to test the photocatalytic activity of PCN-224 and assess the validity of the Fe(III) implantation on improving photocatalytic efficiency, I designed a solid-gas reaction system for photocatalytic IPA oxidation (Figure 4.11). It is notable that the IPA photo-oxidation includes both a single-photon route to generate the initial product of acetone and a multiphoton route to yield the complete degradation product

## Chapter 4

of CO<sub>2</sub> (see equations in Experimental section).<sup>35,44</sup> The clear reaction mechanism and typical intermediate product enable us to evaluate the photocatalytic performance of PCN-224 and Fe@PCN-224. Figure 4.12a presents the time-dependent photocatalytic acetone evolution over PCN-224 and Fe@PCN-224, respectively. Since the generation of each acetone molecule from IPA usually requires one hole, while the reaction of IPA to CO<sub>2</sub> is a more complex multiphoton-involved process, it's understandable that the photocatalytic oxidation of IPA to acetone is easier than that to CO<sub>2</sub>. As shown in Figure 4.12b, the generation rate of acetone is much higher than that of CO<sub>2</sub> for both PCN-224 and Fe@PCN-224, which indicates that one-photon reaction takes the predominance role. The calculated acetone evolution rate of Fe@PCN-224 is 280.7 ppm/h, which delivers over 8.9 folds higher than that of PCN-224 (31.6 ppm/h). Moreover, the CO<sub>2</sub> evolution rate of Fe@PCN-224 is also much higher than PCN-224, further indicating the much higher photocatalytic activity of Fe@PCN-224 compared with PCN-224. This experiment demonstrates the superiority of the Fe(III) incorporation into the PCN-224 for the photocatalytic IPA oxidation. Fe@PCN-224 also exhibits much higher photocatalytic activity for IPA oxidation than NH<sub>2</sub>-MIL-125 (Ti), NH<sub>2</sub>-UiO-66 (Zr), MIL-88B (Fe), g-C<sub>3</sub>N<sub>4</sub> and commercial α-Fe<sub>2</sub>O<sub>3</sub> under the same reaction conditions (Figure 4.13, 4.14). Moreover, as shown in Table 4.1, the achieved photocatalytic activity of Fe@PCN-224 for IPA oxidation to acetone is also higher than some reported photocatalysts, which further demonstrates the superiority of Fe@PCN-224 for photooxidation of IPA.<sup>45-</sup>

49

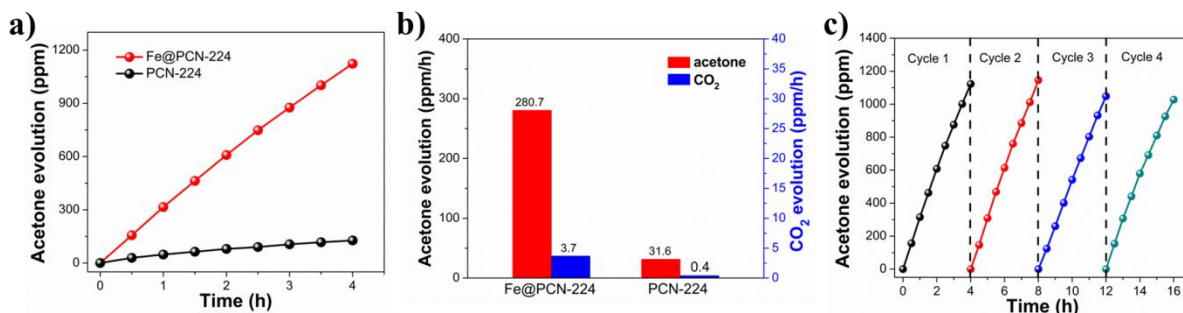


Figure 4.12. (a) Time-dependent acetone evolution from photocatalytic IPA oxidation by PCN-224 and Fe@PCN-224; (b) acetone and CO<sub>2</sub> evolution rate comparison between PCN-224 and Fe@PCN-224; (c) photocatalytic acetone evolution stability test on Fe@PCN-224.

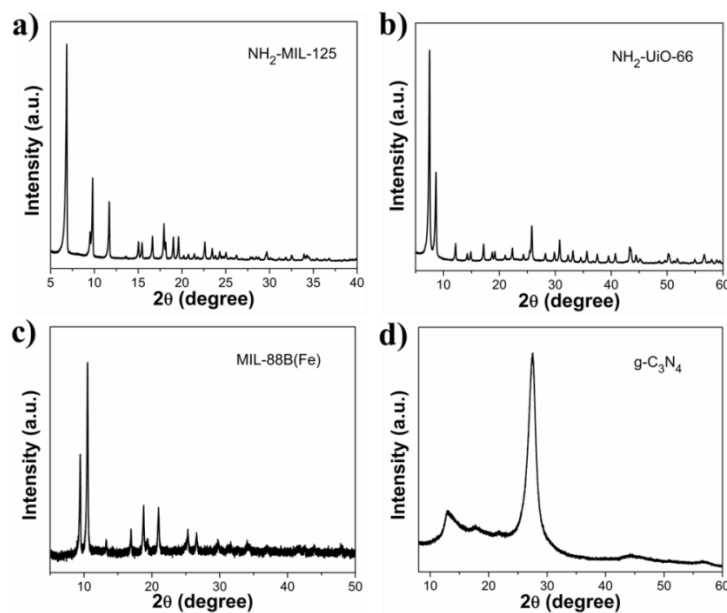


Figure 4.13. (a)-(d) XRD patterns of  $\text{NH}_2\text{-MIL-125}$  (Ti),  $\text{NH}_2\text{-Uio-66}$  (Zr),  $\text{MIL-88B}$  (Fe) and  $\text{g-C}_3\text{N}_4$ , respectively.

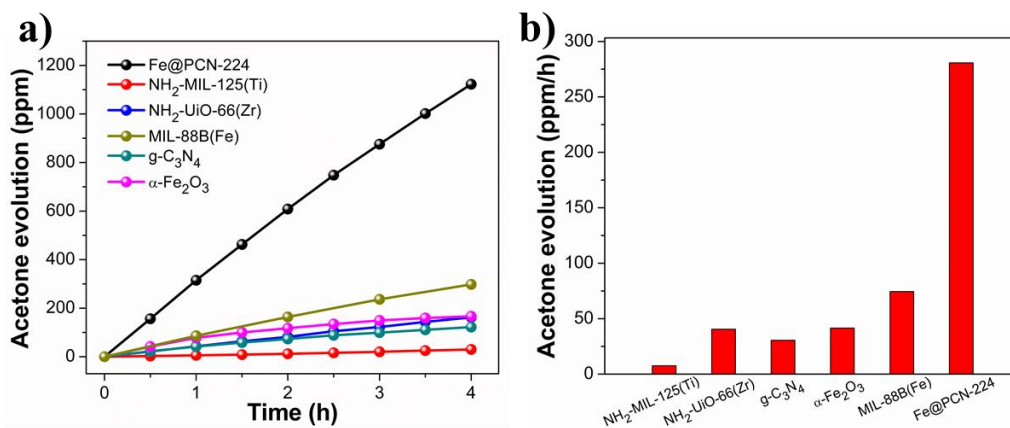


Figure 4.14. (a) Time-dependent acetone evolution from photocatalytic IPA oxidation by various photocatalysts. (b) Acetone evolution rate comparison between different photocatalysts under the same conditions.

## Chapter 4

Table 4.1. Summary of the some reported photocatalysts employed for IPA oxidation to acetone.

photocatalyst	Light source	Acetone evolution rate	Ref.
Fe@PCN-224	Visible light: 300 W Xe lamp with a cut-off filter (i.e., $\lambda > 400$ nm, 21A).	280.7 ppm h <sup>-1</sup>	This study
$\beta$ -Bi <sub>2</sub> O <sub>3</sub>	Visible light: 300 W Xe lamp with a cut-off filter (i.e., $420 \leq \lambda \leq 800$ nm, 10A).	130.6 ppm h <sup>-1</sup>	<i>J. Mater. Chem. A</i> , 2015, 3, 5119.
CuO <sub>x</sub> / $\alpha$ -Bi <sub>2</sub> O <sub>3</sub>	Visible light: 300 W Xe lamp with a cut-off filter (i.e., $420 \leq \lambda \leq 800$ nm, 10A).	150.0 ppm h <sup>-1</sup>	<i>Appl. Catal. B: Environ.</i> 2015, 163, 267.
Ag <sub>3</sub> PO <sub>4</sub> /Sr <sub>2</sub> Nb <sub>2</sub> O <sub>7</sub>	Visible light: 300 W Xe lamp with a cut-off filter (i.e., $420 \text{ nm} < \lambda < 800 \text{ nm}$ , 7A).	173.3 ppm h <sup>-1</sup>	<i>Nanoscale</i> , 2014, 6, 7303.
Nanoporous SrTiO <sub>3</sub>	UV-visible light: 300 W Xe lamp (i.e., $\lambda > 300$ nm, 21A).	ca. 72.0 ppm h <sup>-1</sup>	<i>ACS Appl. Mater. Interfaces</i> 2014, 6, 22726.
HKUST-1@TiO <sub>2</sub>	AM 1.5	ca. 177.0 ppm/h	<i>Ind. Eng. Chem. Res.</i> 2016, 55, 8096.

The stability and reusability of the Fe@PCN-224 photocatalyst were investigated. After the reaction, the Fe@PCN-224 was removed from the reaction system and characterized by FTIR spectra (Figure 4.15), XRD pattern (Figure 4.16) and morphology analyses (Figure 4.17). The results show that the Fe@PCN-224 has strong resistance to chemical structure, crystal structure and morphology changes during the photocatalytic IPA oxidation reaction. The reusability of the photocatalyst was studied by reusing the photocatalyst for four times. As shown in Figure 4.12c, slight decline of activity was observed after four cycling reaction, decreasing from 280.7 ppm/h in the first cycle to 256.8 ppm/h in the fourth cycle. However, it still showed good activity and maintained 91.5 % of the initial activity after four cycling reaction. The slight decline of the acetone evolution rate observed in this work may be partially induced by the accumulation of Fe<sup>2+</sup> during the continuous photocatalysis, as revealed by the XPS measurement (Figure 4.18), which may lead to the slight decrease of the separation efficiency of electron-hole pairs. Moreover, the limited diffusion of reactant to the active sites might also lead to the slightly decreased

## Chapter 4

activity during continuous photoreaction. The suitable activation process to recover the efficient photocatalytic activity is still under exploration.

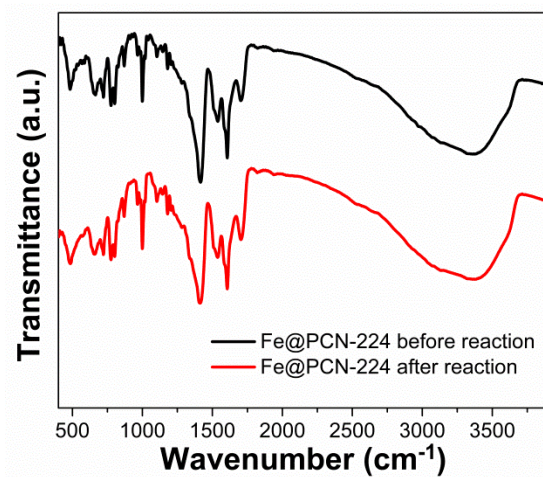


Figure 4.15. FTIR spectra of Fe@PCN-224 before and after reaction.

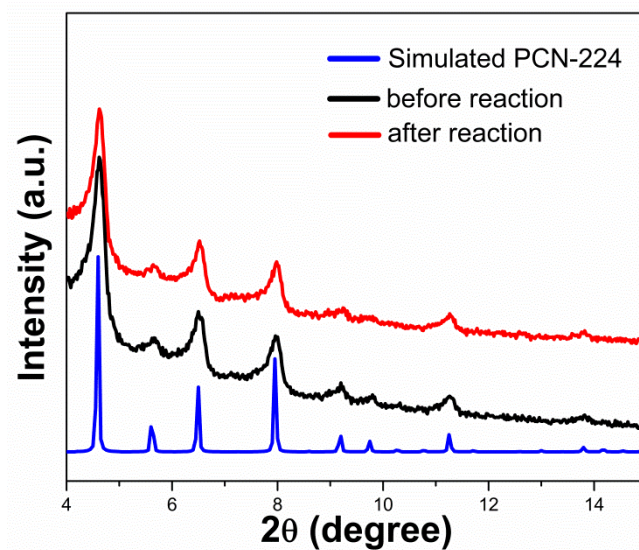


Figure 4.16. The XRD patterns of Fe@PCN-224 before and after photocatalytic reaction.

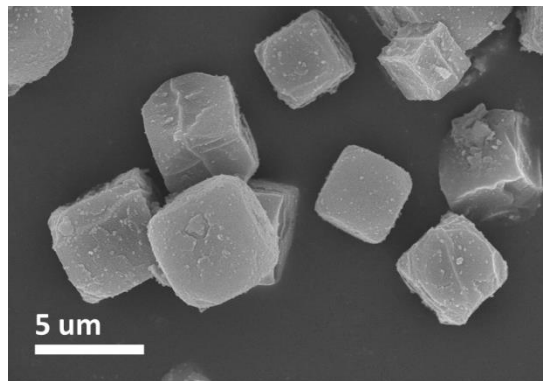


Figure 4.17. SEM image of Fe@PCN-224 after photocatalytic reaction.

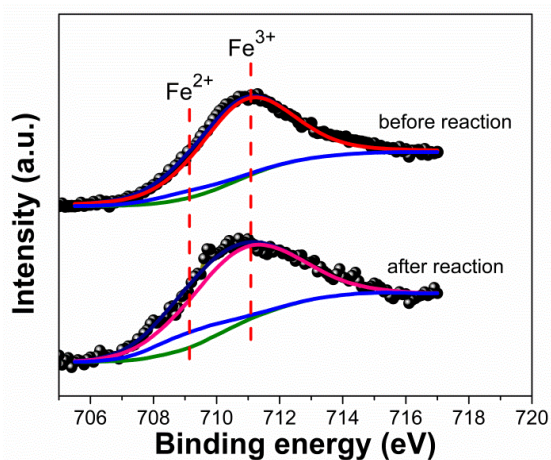


Figure 4.18. High resolution Fe XPS spectrum of Fe@PCN-224 before and after reaction.

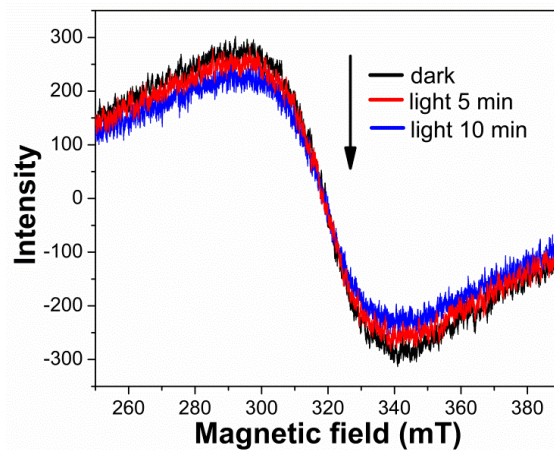


Figure 4.19. In-situ ESR spectra of a mixture of Fe@PCN-224 and isopropanol in the dark and under visible light irradiation. The ESR measurement was conducted under vacuum at room temperature, and the isopropanol was used to scavenge photo-generated holes.

### 4.3.3 Mechanism investigation

The above results clearly demonstrate the superiority of Fe(III) implantation in porphyrin MOF for photocatalysis. I am now in a position to understand the mechanisms behind the function of the newly developed structures. To gain insight into the enhancement of photocatalytic activity, I firstly explored the influence of Fe(III) implantation on the transfer and utilization of the photocarriers (photoexcited electrons and holes) of PCN-224 photocatalyst. Quick recombination of photocarriers is one of the main reasons to limit the photocatalytic activity of a photocatalyst.<sup>50</sup> However, Fe(III) implantation into PCN-224 can effectively improve the the separation efficiency of the photoinduced electron-hole pairs and decrease electron transfer resistance of PCN-224, as revealed by transient photocurrent response and electrochemical impedance characterizations (see more details in Figure 4.10). This is reasonable because the unoccupied Fe(III) trap sites formed below the CBM of PCN-224, and thus some part of photogenerated electrons from PCN-224 can transfer to the Fe(III) site. To gain further evidence of electron transfer process, *in-situ* ESR studies were also carried out. As shown in Figure 4.19, Fe@PCN-224 in the dark gives a typical ESR signal ascribed to Fe<sup>3+</sup>. When visible light is irradiated on the above reaction system, the ESR signal is gradually quenched. The decrease of Fe<sup>3+</sup> ESR signal intensity could be attributed to the trapping of electrons by Fe(III) site in Fe@PCN-224. The electron transfer in Fe@PCN-224 can effectively improve the the separation efficiency of electron-hole pairs. To gain a deeper understanding of the photophysical characteristics of the photogenerated charge carriers in PCN-224 before and after Fe(III) implantation, the photoluminescence (PL) and fluorescence lifetime measurements were conducted (Figure 4.8c, d). The pronounced PL emission quenching and slightly decreased fluorescence lifetime is due to the fast capture of photogenerated electrons from the CBM of PCN-224 by Fe(III) trap site, which indeedly demonstrated the electron transfer from PCN-224 to Fe(III) trap site, implying the greatly suppressed radiative electron-hole recombination in PCN-224 after Fe(III) implantation. The VBM position of PCN-224 is estimated to be +1.86 V (vs. RHE), which can reach the oxidation potential of IPA (+0.32 V vs. SHE).<sup>51</sup> Therefore, the photogenerated holes in PCN-224 can

## Chapter 4

oxidize IPA, and the suppressed radiative electron-hole recombination in PCN-224 after Fe(III) implantation is one of the reasons that the photocatalytic activity is improved for Fe@PCN-224.

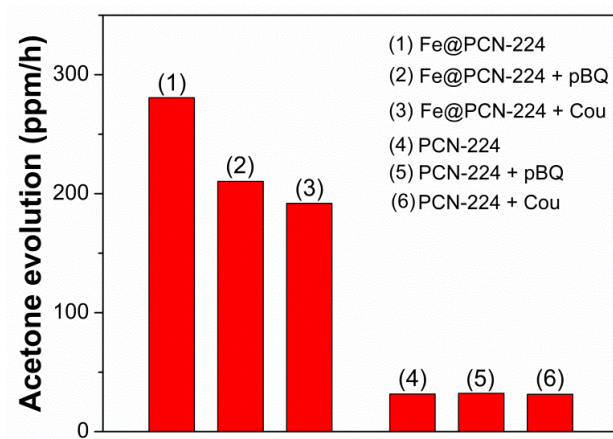
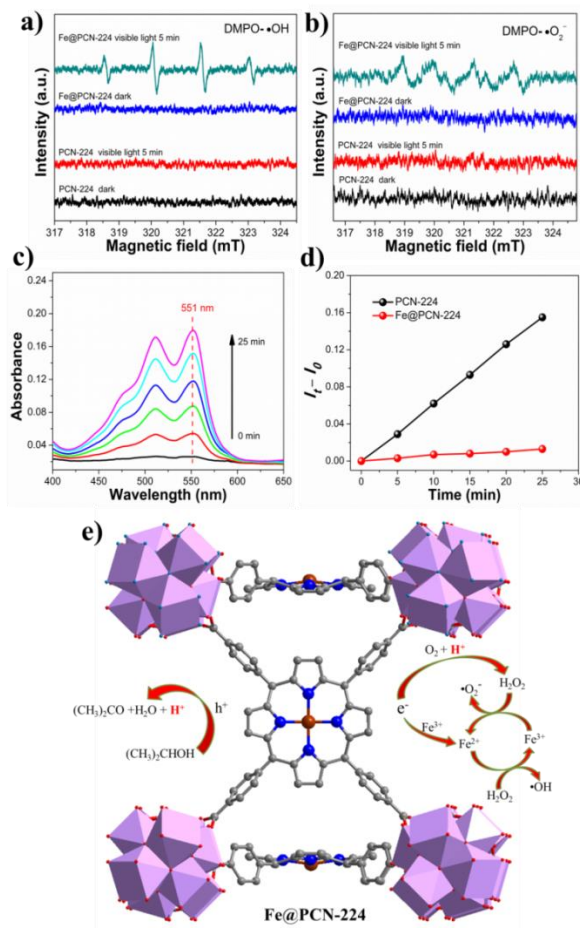


Figure 4.20. Photocatalytic acetone evolution by Fe@PCN-224 and PCN-224 with and without different reactive-species scavengers, respectively.

In the photocatalytic IPA oxidation process, in addition to the direct hole oxidation, the oxygen-related radicals are considered as highly active species (see equations in Experimental section). To verify if the oxygen-related radicals are participated in the photocatalytic IPA oxidation reactions, the radicals trapping experiments were performed by adding *p*-benzoquinone (pBQ) and coumarin (Cou) as  $\bullet\text{O}_2^-$  and  $\bullet\text{OH}$  radicals scavenger, respectively, to the photocatalytic reaction system. For the PCN-224 sample, the addition of pBQ and Cou hardly blocks the photocatalytic process, indicating that the oxygen-related radicals did not participate in the photocatalytic IPA oxidation reaction (Figure 4.20). However, the pBQ and Cou can obviously suppress the photocatalytic process for the Fe@PCN-224, indicating that  $\bullet\text{O}_2^-$  and  $\bullet\text{OH}$  radicals join its IPA photooxidation reaction (Figure 4.20). The generation of the  $\bullet\text{O}_2^-$  and  $\bullet\text{OH}$  radicals over Fe@PCN-224 can be evidenced by ESR and 5,5-dimethyl-1-pyrroline-*N*-oxide (DMPO) spin-trapping technique.<sup>52</sup> Figure 4.21a, b show the ESR spectra of PCN-224 and Fe@PCN-224 in the presence of DMPO as spin-trapping agent. Obviously, PCN-224 cannot produce  $\bullet\text{O}_2^-$  and  $\bullet\text{OH}$  radicals, since neither DMPO- $\bullet\text{OH}$  signals nor DMPO- $\bullet\text{O}_2^-$  signals were detected under visible light irradiation.

## Chapter 4

This is largely due to the fact that the potential of the VBM and CBM positions of PCN-224 is located at +1.86 V (vs. RHE) and +0.11 V (vs. RHE), respectively, which thermodynamically disfavors for the oxidation of  $\text{OH}^-$  to  $\bullet\text{OH}$  (+1.9 V vs. NHE, pH=7) or reduction of  $\text{O}_2$  to  $\bullet\text{O}_2^-$  (-0.33 V vs. NHE, pH=7).<sup>53</sup> However, the production of  $\bullet\text{O}_2^-$  and  $\bullet\text{OH}$  was observed over Fe@PCN-224 under visible light, as confirmed by the formation of characteristic peaks of DMPO- $\bullet\text{OH}$  and DMPO- $\bullet\text{O}_2^-$  adducts (Figure 4.21a, b). In most case, the  $\bullet\text{O}_2^-$  and  $\bullet\text{OH}$  radicals are generated under Fenton reactions and the  $\text{H}_2\text{O}_2$  is one of the important reactant.<sup>35</sup> In a photocatalytic process for degradation of gaseous organic compounds,  $\text{H}_2\text{O}_2$  can be produced via photocatalytic reduction of  $\text{O}_2$  ( $\text{O}_2 + 2 \text{H}^+ + 2 \text{e}^- \rightarrow \text{H}_2\text{O}_2$ , +0.695 V vs. SHE).<sup>54</sup> Since the CBM of PCN-224 has more negative potential, it is believed that this reaction can be achieved in theory. However, convincing experimental results are still necessary to prove the capability of PCN-224 to photogenerate  $\text{H}_2\text{O}_2$  under visible light irradiation.

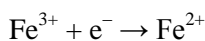
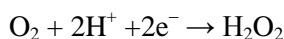


## Chapter 4

---

Figure 4.21. (a)-(b) ESR signals of DMPO- $\cdot$ OH adducts and DMPO- $\cdot$ O $_2^-$  adducts produced by PCN-224 and Fe@PCN-224 samples, respectively; (c) time-dependent absorption spectra of the DPD/POD-PCN-224 solution; (d) time-dependent concentration evolution of H $_2$ O $_2$  produced by PCN-224 and Fe@PCN-224, respectively; (e) proposed mechanism of oxygen related radicals generation in photocatalytic systems with Fe@PCN-224.

To determine the generated H $_2$ O $_2$  in our photocatalytic process, I designed the experiment as following. The sample powder was irradiated under visible-light for several min with gaseous IPA and air addition, and then was dispersed into an as-prepared solution; the filtrate was used to measure the generated H $_2$ O $_2$  via *N,N*-diethyl-*p*-phenylenediamine (DPD)–horseradish peroxidase (POD) method (See more details in Experimental section).<sup>35</sup> Figure 4.21c shows the time-dependent absorption spectra of the DPD/POD-PCN-224 solution and Figure 4.22 shows the time-dependent absorption spectra of the DPD/POD-Fe@PCN-224 solution. The concentration of H $_2$ O $_2$  can be monitored by the absorption intensity of the solution at 551 nm. Figure 4.21d shows the time-dependent concentration evolution of H $_2$ O $_2$  produced by PCN-224 and Fe@PCN-224, respectively. For PCN-224, the concentration of H $_2$ O $_2$  increases almost linearly as irradiation time prolongs, indicating that PCN-224 is able to produce H $_2$ O $_2$  in the photocatalytic reaction system. H $_2$ O $_2$  was not formed in a control experiment when air was replaced by Ar in the photocatalytic reaction, indicating that H $_2$ O $_2$  was indeed generated from photocatalytic O $_2$  reduction by PCN-224. It shows that the evolved H $_2$ O $_2$  is difficult to be observed over Fe@PCN-224 (Figure 4.21d, Figure 4.22), which can be reasonably explained that the generated H $_2$ O $_2$  by PCN-224 quickly reacts with Fe $^{2+}$ /Fe $^{3+}$  pairs, which derives from Fe $^{3+}$  reduced by photoelectron to form  $\cdot$ O $_2^-$  and  $\cdot$ OH radicals via Fenton reactions.<sup>35</sup> The reactions can be described as below:<sup>35</sup>



## Chapter 4

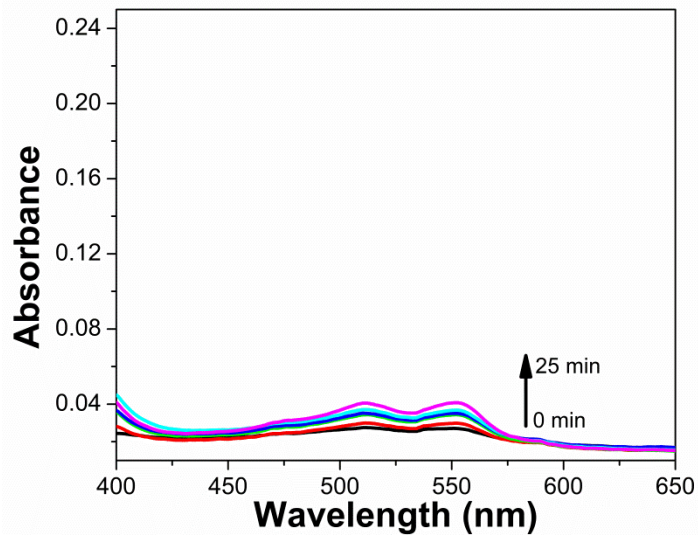
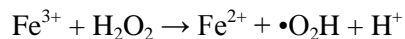


Figure 4.22. Time-dependent absorption spectra of the DPD/POD-Fe@PCN-224 solution.

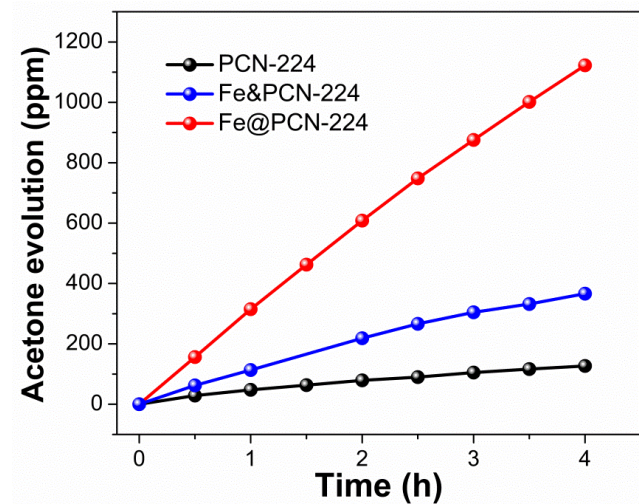


Figure 4.23. Time-dependent photocatalytic acetone evolution over PCN-224, Fe&PCN-222 and Fe@PCN-224.

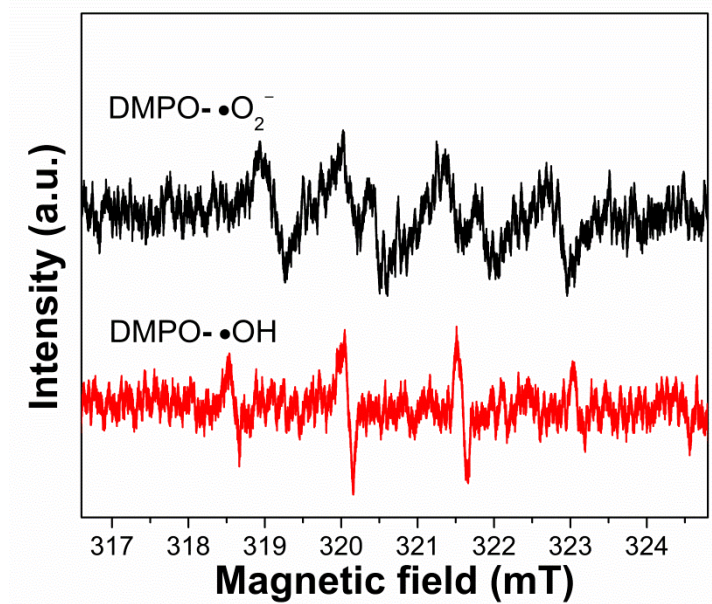


Figure 4.24. ESR signals of DMPO-•O<sub>2</sub><sup>-</sup> adducts and DMPO-•OH adducts produced by Fe&PCN-224 sample under visible light.

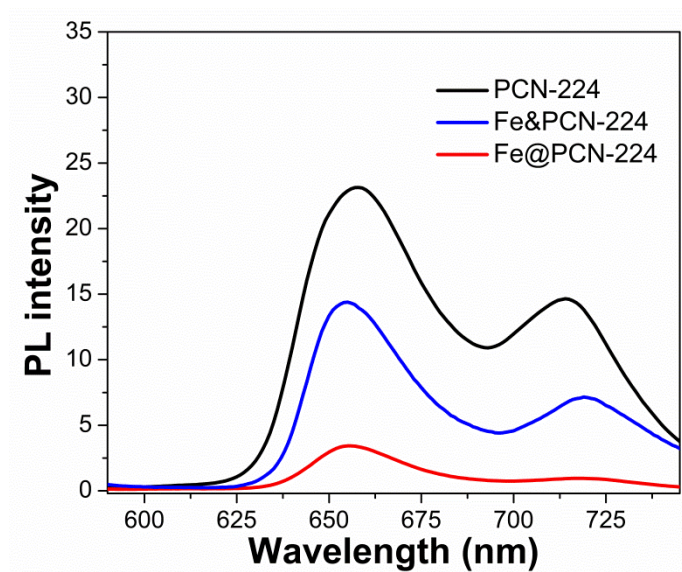


Figure 4.25. PL spectra of PCN-224, Fe&PCN-224 and Fe@PCN-224, respectively.

## Chapter 4

---

On the basis of the above results, a tentative photocatalytic process for gaseous IPA oxidation over the Fe(III)@PCN-224 hybrid structure was proposed in Figure 4.21e. Under visible light irradiation, the PCN-224 structure is photoexcited to generate electron-hole pairs, and the separation efficiency can be significantly improved after incorporation of Fe(III) into the structure of PCN-224. The long-lived holes remained in the VBM of PCN-224 can oxidize the IPA to produce acetone and  $H^+$ , and a few of photoelectrons in the CBM are consumed to form  $H_2O_2$ . Simultaneously, a few of electrons may also reduce the incorporated  $Fe^{3+}$  to  $Fe^{2+}$  ions, and then the formed  $Fe^{2+}/Fe^{3+}$  pairs interact with the formed  $H_2O_2$  to generate active  $\cdot O_2^-$  and  $\cdot OH$  radicals through the Fenton reactions, and therefore greatly enhances photoactivity. In order to further demonstrate the superiority of the Fe(III) implantation into the porphyrin unit of PCN-224 for photocatalysis, the Fe(III) loaded at the surface of PCN-224, named as Fe&PCN-224, was prepared through mixing Fe(III) and PCN-224 at room temperature (see experimental section), and its photocatalytic activity for IPA oxidation was also investigated. The result showed that the photocatalytic activity of Fe@PCN-224 was much higher than Fe&PCN-224 (Figure 4.23). It was found that the Fenton reactions could also be constructed on Fe&PCN-224 (Figure 4.24). However, its lower efficiency in charge carriers separation would result in much lower photocatalytic activity compared with Fe@PCN-224 (Figure 4.25). Fe@PCN-224 also showed great advantages compared with PCN-224 in other photocatalytic reactions, such as formaldehyde mineralization, methyl orange (MO) photo-degradation, ciprofloxacin photo-degradation and Cr(VI) reduction (see more details in Figure 4.26, 4.27).

Since the Fe(III) implantation in PCN-224 have a great effect on improving its photocatalytic performance, it is very interesting to investigate the photocatalytic performance of other porphyrinic MOFs based photocatalysts. PCN-222 was selected because this kind of porphyrinic MOF has been proven to be a stable photocatalyst and contain the  $H_2TCPP$  organic linker similar to that in PCN-224 but have different structure.<sup>19</sup> Moreover, Fe(III) implanted Fe@PCN-222 can also be obtained through a post-synthetic modification method. The formation of these MOFs has been confirmed by their XRD

## Chapter 4

patterns (Figure 4.28). Those XRD patterns were in good agreement with the simulated PCN-222 structure. The photocatalytic oxidation of IPA was also investigated over PCN-222 and Fe@PCN-222. It is obvious that Fe@PCN-222 shows an greatly improved photocatalytic performance compared to PCN-222 without Fe(III) implantation (Figure 4.29). This observation indicated that Fe(III) implantation in porphyrinic MOFs could be a general method to improve the photocatalytic performance for the oxidation of IPA.

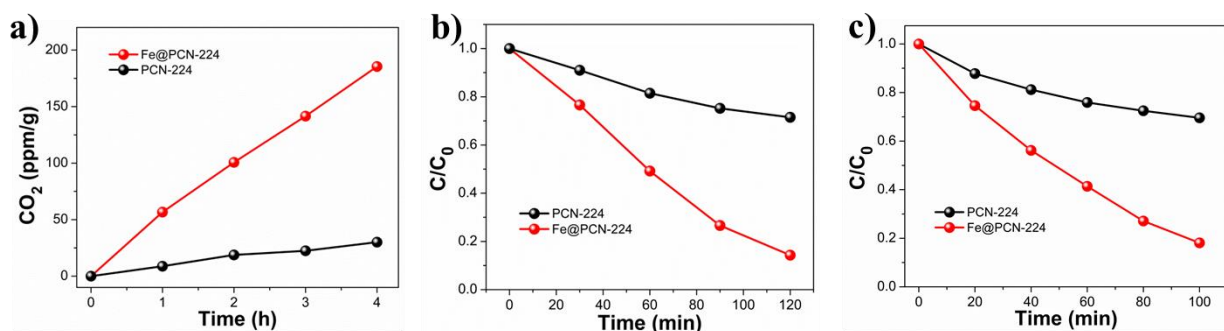


Figure 4.26. (a) photocatalytic oxidation of formaldehyde to CO<sub>2</sub> by PCN-224 and Fe@PCN-224. The setup of the experiment of formaldehyde oxidation is similar as the photooxidation of isopropanol, expect that formaldehyde instead of isopropanol was injected into the reaction cell. (b) Photocatalytic degradation of MO by PCN-224 and Fe@PCN-224; 80 ml 40 mg/L MO adjusted to pH=3.0, bubbled with O<sub>2</sub> for 30 min, 5 mg photocatalyst. The reaction solution was firstly stirred in dark for 90 min to reach absorption-desorption equilibrium, and then irradiated with visible light. (c) Photocatalytic degradation of ciprofloxacin by PCN-224 and Fe@PCN-224; 50 ml 10 mg/L ciprofloxacin adjusted to pH=3.0, bubbled with O<sub>2</sub> for 30 min, 5 mg photocatalyst. The reaction solution was firstly stirred in dark for 60 min to reach absorption-desorption equilibrium, and then irradiated with visible light. The concentration of ciprofloxacin was determined by an UV-visible spectrophotometer.

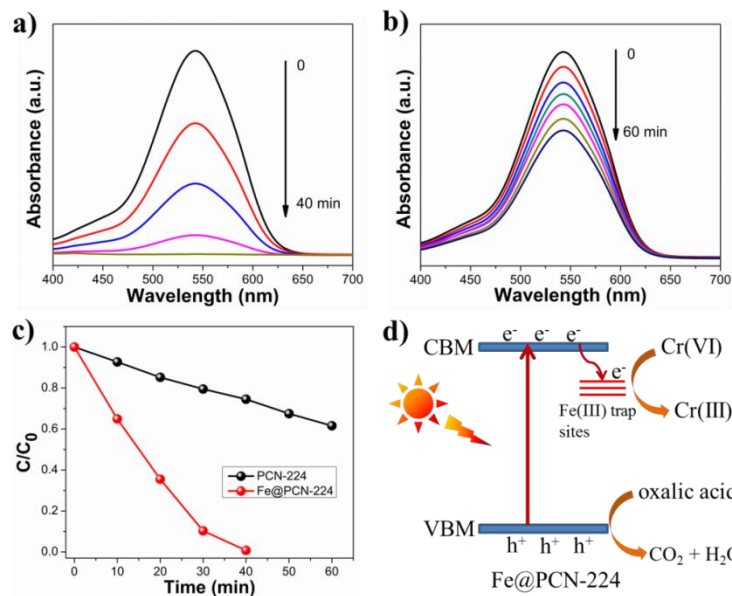


Figure 4.27. (a)-(b) Time-dependent absorption spectral pattern of DPC- Cr(VI) complex solutions after reduced by Fe@PCN-224 and PCN-224 at various exposure times at pH 3.0, respectively. (c) Reduction profiles of photocatalytic reduction of Cr(VI) over Fe@PCN-224 and PCN-224. (d) Mechanisms underlying the photoexcited dynamics involved in photocatalytic Cr(VI) reduction over Fe@PCN-224.

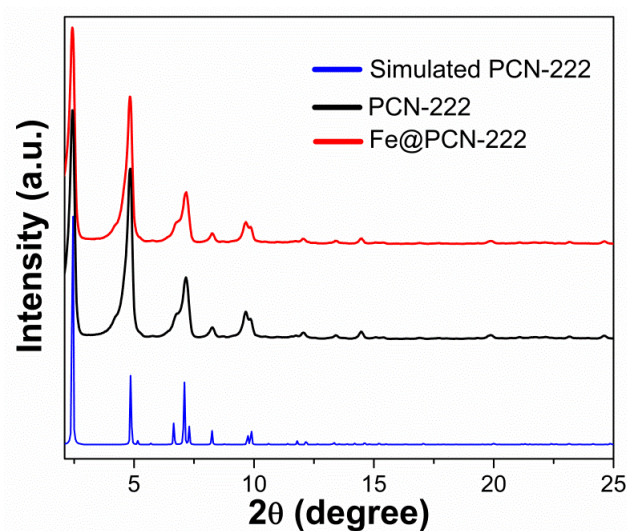


Figure 4.28. XRD patterns of the as-prepared PCN-222 and Fe@PCN-222.

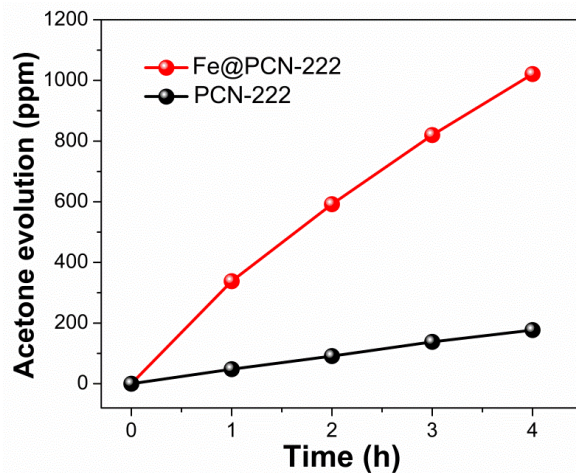


Figure 4.29. Time-dependent photocatalytic acetone evolution over PCN-222 and Fe@PCN-222.

## 4.4 Conclusion

In summary, I herein propose a novel strategy to boost the photocatalytic efficiency of a porphyrinic MOF photocatalyst (PCN-224) for IPA oxidation via post-synthetic implantation of Fe(III). Mechanism study indicates that the implantation of Fe(III) ions in PCN-224 can not only improve the separation efficiency of photogenerated electron-hole pairs, but also construct Fenton reactions to convert *in-situ* formed inactive  $\text{H}_2\text{O}_2$  into reactive radicals (such as  $\cdot\text{O}_2^-$  and  $\cdot\text{OH}$ ), which play significant roles in the oxidation of IPA. The effect of Fe(III) implantation in another porphyrinic MOF (PCN-222) on the visible light photocatalytic activity for the oxidation of IPA has been also studied. The same trend is observed, namely Fe@PCN-222 also shows enhanced activity for photocatalytic oxidation of IPA compared with bare PCN-222. This work provides a simple Fe(III) implantation strategy to improve the photocatalytic performance of MOFs based photocatalysts for organic compounds oxidation, and it is anticipated that the metal ions implantation strategy can also be applicable to other photocatalytic reactions, such as  $\text{H}_2$  evolution and  $\text{CO}_2$  reduction, by flexibly implanting specific metal ions in the MOFs structure.

## Chapter 4

---

### References

1. G. Zhang, G. Liu, L. Wang, J. T. S. Irvine, *Chem. Soc. Rev.*, **2016**, *45*, 5951.
2. W. -J. Ong, L. -L. Tan, Y. H. Ng, S. -T. Yong, S. -P. Chai, *Chem. Rev.* **2016**, *116*, 7159.
3. M. Ge, Q. Li, C. Cao, J. Huang, S. Li, S. Zhang, Z. Chen, K. Zhang, S. S. Al-Deyab, Y. Lai, *Adv. Sci.* **2017**, *4*, 1600152.
4. H. Tong, S. Ouyang, Y. Bi, N. Umezawa, M. Oshikiri, J. Ye, *Adv. Mater.*, **2012**, *24*, 229.
5. T. Zhang, W. Lin, *Chem. Soc. Rev.*, **2014**, *43*, 5982.
6. S. Wang, X. Wang, *Small*, **2015**, *11*, 3097.
7. A. Dhakshinamoorthy, A. M. Asiri, H. García, *Angew. Chem., Int. Ed.*, **2016**, *55*, 5414.
8. L. Chi, Q. Xu, X. Liang, J. Wang, X. Su, *Small*, **2016**, *12*, 1351.
9. T. Toyao, M. Saito, S. Dohshi, K. Mochizuki, M. Iwata, H. Higashimura, Y. Horiuchi, M. Matsuoka, *Chem. Commun.*, **2014**, *50*, 6779.
10. W. Wang, X. Xu, W. Zhou, Z. Shao, *Adv. Sci.* **2017**, 1600371.
11. C. -C. Wang, J. -R. Li, X. -L. Lv, Y. -Q. Zhang, G. Guo, *Energy Environ. Sci.*, **2014**, *7*, 2831.
12. K. G. M. Laurier, F. Vermoortele, R. Ameloot, D. E.D. Vos, J. Hofkens, M. B. J. Roeffaers, *J. Am. Chem. Soc.*, **2013**, *135*, 14488.
13. J. -L. Wang, C. Wang, W. Lin, *ACS Catal.*, **2012**, *2*, 2630.
14. R. Liang, L. Shen, F. Jing, W. Wu, N. Qin, R. Lin, L. Wu, *Appl. Catal. B: Environ.* **2015**, *162*, 245.
15. R. Liang, F. Jing, L. Shen, N. Qin, L. Wu, *J. Hazard. Mater.*, **2015**, *287*, 364.
16. Y. Fu, D. Sun, Y. Chen, R. Huang, Z. Ding, X. Fu, Z. Li, *Angew. Chem. Int. Ed.*, **2012**, *51*, 3364.
17. D. Wang, R. Huang, W. Liu, D. Sun, Z. Li, *ACS Catal.*, **2014**, *4*, 4254.
18. H. He, J. A. Perman, G. Zhu, S. Ma, *Small*, **2016**, *12*, 6309.
19. H. -Q. Xu, J. Hu, D. Wang, Z. Li, Q. Zhang, Y. Luo, S. -H. Yu, H. -L. Jiang, *J. Am. Chem. Soc.*, **2015**, *137*, 13440.
20. K. M. Choi, D. Kim, B. Rungtaweivoranit, C. A. Trickett, J. T. D. Barmanbek, A. S. Alshammari, P. Yang, O. M. Yaghi, *J. Am. Chem. Soc.*, **2017**, *139*, 356.

## Chapter 4

---

21. M. A. Nasalevich, M. van der Veen, F. Kapteijn, J. Gascon, *CrystEngComm*, **2014**, *16*, 4919.
22. H. Zhang, G. Liu, L. Shi, H. Liu, T. Wang, J. Ye, *Nano Energy*, **2016**, *22*, 149.
23. D. Sun, Y. Fu, W. Liu, L. Ye, D. Wang, L. Yang, X. Fu, Z. Li, *Chem. Eur. J.* **2013**, *19*, 14279.
24. A. W. Peters, Z. Li, O. K. Farha, J. T. Hupp, *ACS Appl. Mater. Interfaces*, **2016**, *8*, 20675.
25. Z. Sha, J. Wu, *RSC Adv.*, **2015**, *5*, 39592.
26. S. Wang, X. Wang, *Appl. Catal. B: Environ.* **2015**, *162*, 494.
27. R. Li, J. Hu, M. Deng, H. Wang, X. Wang, Y. Hu, H. -L. Jiang, J. Jiang, Q. Zhang, Y. Xie, Y. Xiong, *Adv. Mater.*, **2014**, *26*, 4783.
28. M. Wen, K. Mori, T. Kamegawa, H. Yamashita, *Chem. Commun.*, **2014**, *50*, 11645.
29. Y. Mi, L. Wen, Z. Wang, D. Cao, R. Xu, Y. Fang, Y. Zhou, Y. Lei, *Nano Energy*, **2016**, *30*, 109.
30. M. Liu, X. Qiu, M. Miyauchi, K. Hashimoto, *J. Am. Chem. Soc.*, **2013**, *135*, 10064.
31. E. Brillas, I. Sires, M. A. Oturan, *Chem. Rev.*, **2009**, *109*, 6570.
32. D. Yang, J. Feng, L. Jiang, X. Wu, L. Sheng, Y. Jiang, T. Wei, Z. Fan, *Adv. Funct. Mater.* **2015**, *25*, 7080.
33. Y. Su, Z. Wu, Y. Wu, J. Yu, L. Sun, C. Lin, *J. Mater. Chem. A*, **2015**, *3*, 8537.
34. X. Geng, W. Li, F. Xiao, D. Wang, L. Yang, *Catal. Sci. Technol.*, **2017**, *7*, 658.
35. Y. Li, S. Ouyang, H. Xu, X. Wang, Y. Bi, Y. Zhang, J. Ye, *J. Am. Chem. Soc.*, **2016**, *138*, 13289.
36. I. A. Menon, M. A. C. Beker, S. D. Persad, H. F. Haberman, *Clin. Chim. Acta*, **1989**, *186*, 375.
37. K. Komagoe and T. Katsu, *Anal. Sci.*, **2006**, *22*, 255.
38. B. Abeykoon, J. M. Grenèche, E. Jeanneau, D. Chernyshov, C. Goutaudier, A. Demessence, T. Devic, A. Fateeva, *Dalton Trans.*, **2017**, *46*, 517.
39. J. S. Anderson, A. T. Gallagher, J. A. Mason, T. D. Harris, *J. Am. Chem. Soc.*, **2014**, *136*, 16489.
40. D. Feng, W. -C, Chung, Z. Wei, Z. -Y, Gu, H. -L. Jiang, Y. -P. Chen, D. J. Darensbourg, H. -C. Zhou, *J. Am. Chem. Soc.*, **2013**, *135*, 17105.
41. M. Jahan, Q. Bao, K. P. Loh, *J. Am. Chem. Soc.*, **2012**, *134*, 6707.
42. B. Yao, C. Peng, W. Zhang, Q. Zhang, J. Niu, J. Zhao, *Appl. Catal. B: Environ.* **2015**, *174-175*, 77.

## Chapter 4

---

43. L. Yang, J. Huang, L. Cao, L. Shi, Q. Yu, X. Kong, Y. Jie, *Sci. Rep.* **2016**, *6*, 27765.
44. S. Ouyang, J. Ye, *J. Am. Chem. Soc.* **2011**, *133*, 7757.
45. H. –Y. Jiang, P. Li, G. Liu, J. Ye, J. Lin, *J. Mater. Chem. A*, **2015**, *3*, 5119.
46. J. Guo, H. Zhou, S. Ouyang, T. Kako, J. Ye, *Nanoscale*, **2014**, *6*, 7303.
47. H. –Y. Jiang, G. Liu, M. Li, J. Liu, W. Sun, J. Ye, J. Lin, *Appl. Catal. B: Environ.* **2015**, *163*, 267.
48. H. Wang, T. Yu, X. Tan, H. Zhang, P. Li, H. Liu, L. Shi, X. Li, J. Ye, *Ind. Eng. Chem. Res.* **2016**, *55*, 8096.
49. S. Ouyang, P. Li, H. Xu, H. Tong, L. Liu, J. Ye, *ACS Appl. Mater. Interfaces* **2014**, *6*, 22726.
50. L. Shen, W. Wu, R. Liang, R. Lin, L. Wu, *Nanoscale*, **2013**, *5*, 9374.
51. S. Naya, T. Niwa, T. Kume, H. Tada, *Angew. Chem. Int. Ed.* **2014**, *53*, 7305.
52. J. Sun, X. Li, Q. Zhao, M. O. Tadé, S. Liu, *J. Mater. Chem. A*, **2015**, *3*, 21655.
53. G. Liu, P. Niu, L. Yin, H. –M. Cheng, *J. Am. Chem. Soc.* **2012**, *134*, 9070.
54. H. Katsumata, M. Taniguchi, S. Kaneco and T. Suzuki, *Catal. Commun.*, **2013**, *34*, 30.

# Chapter 5 Boosting charge separation *via* single cobalt atom implantation in MOFs for efficient visible-light driven CO<sub>2</sub> reduction

## 5.1 Introduction

Atomically dispersed catalysts with mononuclear metal complexes or single metal atoms anchored on supports have recently drew increasing research attention, which offer the maximum atom efficiency and provide the most ideal strategy to create highly efficient catalysts.<sup>1-2</sup> Moreover, the catalysts with atomically dispersed active sites make them a model system to understand heterogeneous catalysis at the molecular level, bridging the gap between heterogeneous and homogeneous catalysis. However, fabrication of practical and stable single-atom catalysts remains a significant challenge because, typically, single atoms are too mobile and easy to sinter under realistic reaction conditions.<sup>3-5</sup> Metal organic frameworks (MOFs), a class of porous and crystalline materials—provide the most effective coordination sites to anchor individual metal atoms therein prevent them from sintering during catalysis.<sup>6-7</sup>

Global energy demands and climate change underpin broad interest in the sustainable reductive transformation of carbon dioxide (CO<sub>2</sub>) to value-added carbon products such as carbon monoxide (CO), and hydrocarbon fuels. Photocatalytic reduction of CO<sub>2</sub> is a highly important route for solar-to-chemical energy conversion by mimicking the natural photosynthetic process.<sup>8-10</sup> A great deal of effort has been devoted to explore photocatalysts that are capable of capturing and reducing CO<sub>2</sub>. However, the photocatalytic efficiency of currently developed catalyst is far from satisfaction, largely due to its low specific surface area, confined active sites and the fast recombination of the photogenerated electron–hole pairs.<sup>11-12</sup> In photocatalytic processes, as the photocatalysts are excited by light absorption to generate

## Chapter 5

---

electron–hole pairs which are then separated and transferred to different sites for redox reactions, the separation efficiency of the photoinduced charge carriers, the highly directional excitons transfer, play an important role for the final catalytic activity.<sup>13-14</sup> Besides, increasing the CO<sub>2</sub> adsorption ability of photocatalysts is also an effective strategy to improve the CO<sub>2</sub> conversion efficiency, as the electron transfer from the catalytically active sites of the photocatalysts to the CO<sub>2</sub> molecules largely relies on their intimate and stable bind interaction with CO<sub>2</sub> molecular, nevertheless, investigations for photocatalytic CO<sub>2</sub> reduction using MOFs or MOFs based composite are still at their early stage, low efficiency for charge separation and energy transfer, as well as inconsistent between catalytic active and adsorption sites are main drawbacks for visible light driven CO<sub>2</sub> reduction.<sup>15-16</sup>

Bearing these in mind and motivated by the fact that exciton migration in natural photosynthesis primarily occurs in highly ordered porphyrin-like pigments, I considered that equally ordered porphyrin-based metal–organic frameworks might be expected to exhibit similar behavior, thereby facilitating antenna-like light-harvesting and positioning such materials for use in solar energy conversion schemes.<sup>17-</sup>

<sup>19</sup> MOF-525, formulated as Zr<sub>6</sub>O<sub>4</sub>(OH)<sub>4</sub>(TCPP-H<sub>2</sub>)<sub>3</sub> [TCPP = 4,4',4'',4'''-(porphyrin-5,10,15,20-tetrayl) tetrabenzoate], which integrate the Zr<sub>6</sub> clusters and porphyrin based molecular units into 3D network, has been selected as a MOF matrix for its excellent performances in CO<sub>2</sub> capture and visible light utilization.<sup>17</sup> Coordinatively unsaturated cobalt sites are incorporated into porphyrin unit and generate a new composite MOF-525-Co, in which guarantee each active site is simultaneously exposed to the CO<sub>2</sub> molecular and can avoid the aggregation of active sites (Figure 5.1a and Figure 5.2). The introduction of unsaturated cobalt sites can not only generate efficient catalytic active sites, but also enhance CO<sub>2</sub> adsorption over open sites of cobalt porphyrin, thus realizing the activation of CO<sub>2</sub> molecular.<sup>19</sup> Furthermore, directional energy migration within MOF are greatly facilitated with the introduction of cobalt sites, which substantially suppresses electron–hole recombination in MOF, as well as supplies long-lifetime electrons for the reduction of CO<sub>2</sub> molecules adsorbed on the MOF.<sup>17-19</sup>

### 5.2 Experimental section

#### 5.2.1 Materials

N, N-dimethylformamide (DMF), Tetrakis(4-carboxyphenyl)porphyrin ligand, zirconium chloride ( $ZrCl_4$ ), acetonitrile (MeCN), acetic acid, and triethanolamine (TEOA) were purchased commercially and used as received. Ultrapure water (18.2  $M\Omega \cdot cm$  resistivity at 25 °C) was used in all experiments.

#### 5.2.2 Synthesis of MOF-525

MOF-525 samples were prepared according to a previous report.<sup>17</sup> In the synthesis of MOF-525, Zirconyl chloride octahydrate (125 mg, 0.37 mmol) was added to N, N-dimethylformamide (DMF, 60 mL) and sonicated for thirty minutes. Following sonication, tetrakis(4-carboxyphenyl)porphyrin (25 mg, 0.37 mmol) was added to the solution. After ten minutes further sonication, acetic acid (10 mL) was added to the solution. The solution was placed in a 100 mL scintillation vial and heated at 80 °C for three days. The microcrystalline powder was filtered and washed with DMF ( $5 \times 10$  mL) over a three-hour period. The DMF was then replaced with acetone ( $5 \times 30$  mL) over a five-day period. Finally, the volatile acetone was removed by heating at 120 °C under vacuum (30 mTorr) for 48 hrs.

#### 5.2.3 Postmetalation of MOF-525 to form MOF-525-Co and MOF-525-Zn

**MOF-525-Co:** Cobalt nitrate (70 mg) was dissolved in to DMF (10 mL). MOF-525 (50 mg) was added to this solution, the solution was heated at 100 °C for 48 hrs. The microcrystalline powder were collected by filtration and washed with DMF ( $5 \times 10$  mL) over a three-hour period. The DMF was then replaced with acetone ( $5 \times 30$  mL) over a five-day period. Finally, the volatile acetone was removed by heating at 120 °C under vacuum (30 mTorr) for 48 hrs.

**MOF-525-Zn:** The synthesis process of MOF-525-Zn is much similar to that of MOF-525-Co, expect that zinc nitrate (75 mg) was used to replace the cobalt nitrate (70 mg).

#### 5.2.4 Characterization

X-ray diffraction (XRD) patterns were recorded on an X-Pert diffractometer equipped with graphite monochromatized  $Cu-K\alpha$  radiation. The UV-Vis absorption was measured with a UV-visible spectrophotometer (Shimadzu, UV-2600) using  $BaSO_4$  as the reflectance standard reference. PL spectra were recorded by a JASCO FP-6500 spectrofluorometer. Scanning electron microscope (SEM) images were recorded on a Hitachi S4800 microscope. Gas adsorption measurement was performed in the ASAP (Accelerated Surface Area and Porosimetry) 2020 System. The specific surface area of the photocatalysts

## Chapter 5

---

was calculated by the Brunauer–Emmett–Teller (BET) method. The fluorescence decay curve was measured using a fluorescent spectrophotometer (Horiba Jobin Yvon, Fluorolog-3) with a nano-LED lamp. ESR measurements were carried out at room temperature on a JEOL JES-FA-200 with the samples adsorbed with TEOA. The Co, Zn and Zr contents of hybrids were analyzed by inductively coupled plasma optical emission spectrometry (ICP-OES, SPS3520UV-DD, SII nano technology Inc., Japan). Surface chemical analysis was performed by X-ray photoelectron spectroscopy (XPS, PHI Quantera SXM, ULVAC-PHI Inc., Japan).

### 5.2.5 Photocatalytic Experiments

The photocatalytic activities of all samples were carried out in a batch-type reaction system with a total volume of about 330 mL. The setup of the photocatalytic system is illustrated in Figure S8 in the Supporting Information. 2 mg sample was uniformly dispersed on a porous quartzose film in the reaction cell, and 2 mL of solution (MeCN/TEOA = 4:1) was injected into the cell. After complete evacuation of the reaction system (no O<sub>2</sub> or N<sub>2</sub> could be detected), 80 kPa of pure CO<sub>2</sub> gas was injected into the airtight system. A 300 W xenon arc lamp with a UV-cut filter, to remove light with wavelengths lower than 400 nm, and an IR-cut filter to remove wavelengths longer than 800 nm light filters (400 nm <  $\lambda$  < 800 nm) was used as the light source. Prior to testing, the catalysts were degassed at 160 °C for 12 hours under vacuum to remove any possible organic contaminants. The gas products were measured using gas chromatography (GC- 14B, Shimadzu Co., Japan). The isotope of <sup>13</sup>C was analyzed using gas chromatography-mass spectrometry (JEOL-GCQMS, JMS-K9 and 6890N Network GC system, Agilent Technologies).

### 5.2.6 X-ray absorption data collection, analysis, and modelling

Co K-edge X-ray absorption spectra were acquired at beamline 1W1B of the Beijing Synchrotron Radiation Facility (BSRF) in fluorescence mode at room temperature using a Si (111) double-crystal monochromator. The storage ring of BSRF was operated at 2.5 GeV with a maximum current of 250 mA in decay mode. The energy was calibrated using Co foil; the intensities of the incident and fluorescence X-ray were monitored by using standard N<sub>2</sub>-filled ion chamber and Ar-filled Lytle-type detector, respectively. All air sensitive Co-MOF samples are prepared in glove box. In order to achieve the best signal-to-noise ratio, the powdered samples were uniformly mixed with BN powder and pressed to a pellet, which was sealed in a cell holder with Kapton windows for XAFS measurement. A detuning of about 20 % by misaligning the silicon crystals was also performed to suppress the high harmonic content.

## Chapter 5

---

The XAFS raw data were background-subtracted, normalized, and Fourier transformed by the standard procedures with the ATHENA program. Least-squares curve fitting analysis of the EXAFS  $\chi(k)$  data was carried out using the ARTEMIS program, with the theoretical scattering amplitudes, phase shifts and the photoelectron mean free path for all paths calculated by ab-initio code FEFF9. All fits were performed in the  $R$  space with  $k$ -weight of 3. Due to the important non-MT effects in asymmetrical or sparse systems, the Co K-edge theoretical XANES calculations were carried out with the FDMNES code in the framework of full-potential finite difference method (FDM). The energy dependent exchange-correlation potential was calculated in the real Hedin-Lundqvist scheme, and then the spectra are convoluted using a Lorentzian function with an energy-dependent width to account for the broadening due both to the core-hole width and to the final state width. A cluster of 6.0 Å radius having about 40 atoms surrounding the absorber was used for the self-consistency and a cluster of 11.0 Å radius having about 80 atoms for FDM, satisfactory convergence being achieved. The  $\text{CoN}_x\text{C}_y$  moiety was built by situating Co at the center of the porphyrinic unit within the crystal structure obtained by XRD Rietveld refinement and geometrically optimized by density functional theory calculation.

### 5.2.7 Photoelectrochemical measurements

The measurements were carried out in a three-electrode, single-compartment quartz cell. All the experiments were performed at room temperature in 0.5-M  $\text{Na}_2\text{SO}_4$  electrolyte (100 mL, pH = 6.6) deoxygenated using an Ar stream. The working electrode was prepared by depositing the as-prepared samples on indium tin oxide (ITO) glass (1 cm<sup>2</sup> in deposition area). The suspension for the deposition was 500- $\mu\text{L}$  ethanol containing 1 mg of the synthesized samples. The counter and reference electrodes were platinum gauze and Ag/AgCl, respectively.

### 5.2.8 Computational methods

The Vienna ab initio Simulation (VASP) package was used to simulate the electronic structures of various interfaces. Calculations were performed at the spin-polarized density functional theory (DFT) level using frozen-core all-electron projector augmented wave (PAW) model with the generalized gradient approximation (GGA) and Perdew-Burke-Ernzerhof (PBE) functions. An energy cutoff of 400 eV was used for the plane-wave expansion of the electronic wave function. The force and energy convergence criterion was set to 0.01 eV/Å and 10<sup>-5</sup> eV, respectively. Based on the optimized structure from the VASP calculations, the cluster of a  $\text{CO}_2$  molecule adsorbed to the small porphyrin-cobalt unit was extracted. Then the Gaussian09 program was employed to simulate potential energy surface along the variation of C-O bond, to obtain the activation energy barrier for  $\text{CO}_2$  reduction.

## 5.2.10 Energy transfer efficiency, $\Phi_{ET}$

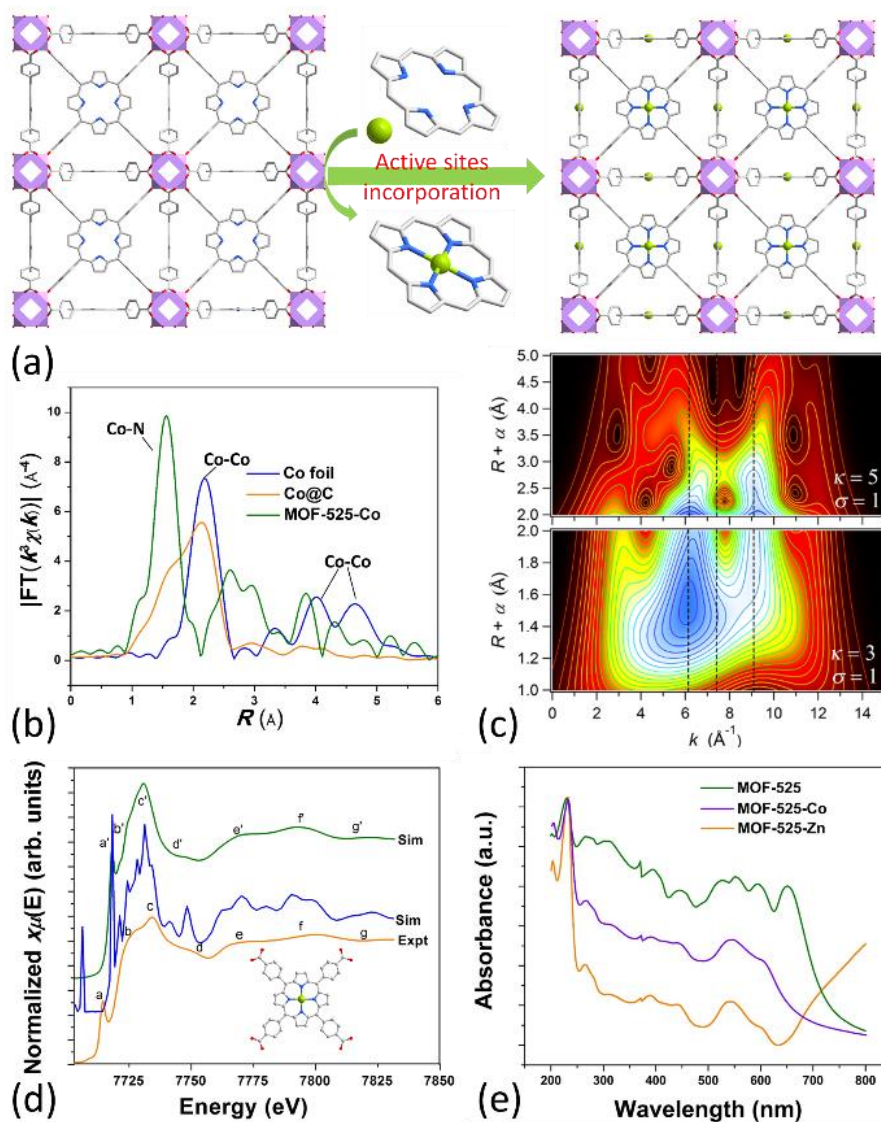
The energy transfer efficiency,  $\Phi_{ET}$  were calculated using the following equation:

$$\Phi_{ET} = k_e / (k_r + k_{nr} + k_e) = k_e / (k_o + k_e), \text{ (eq. 1)}$$

where  $k_r$ ,  $k_{nr}$ , and  $k_e$  = radiative decay, non-radiative decay, and energy transfer constants, respectively. The  $k_o$  and  $k_e$  values were found from the lifetimes for donor molecule ( $\tau_D$ ) and donor molecule in the presence of acceptor ( $\tau_{D-A}$ ), which are  $\tau_D = 1/k_o$  and  $\tau_{D-A} = 1/(k_o + k_e)$ , respectively.

## 5.3 Results and discussion

### 5.3.1 Characterization of photocatalysts



## Chapter 5

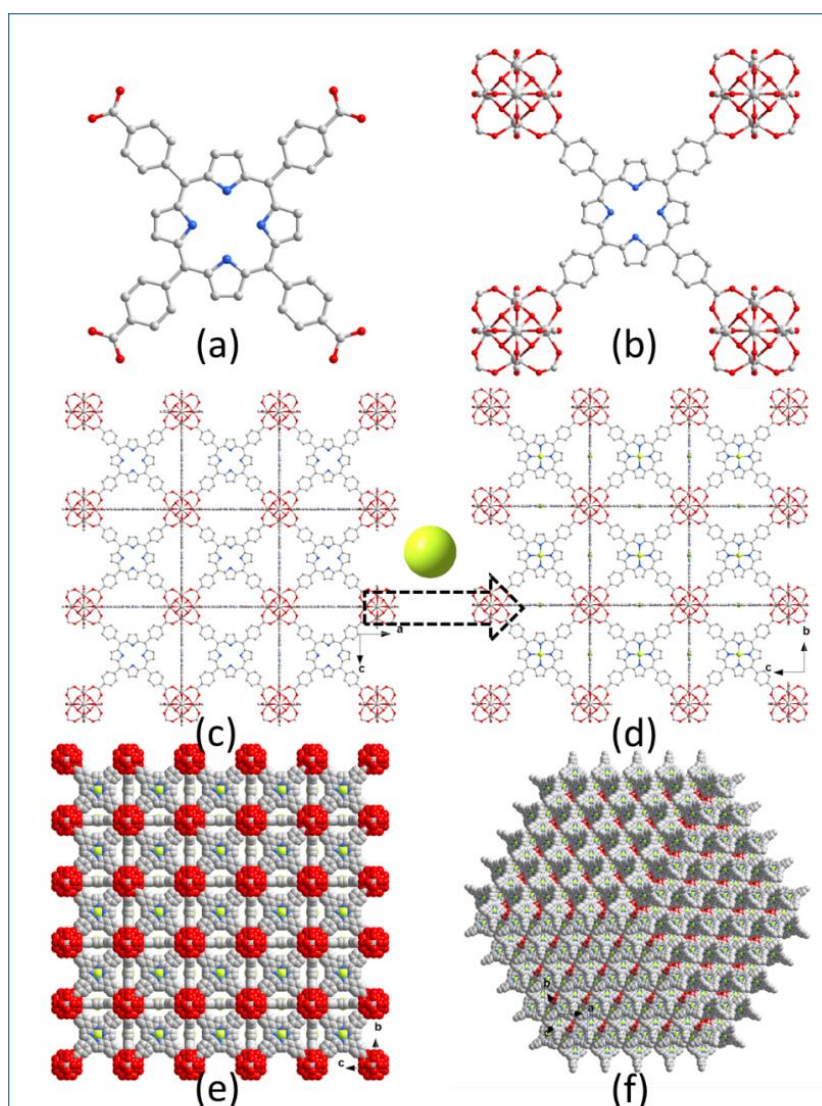
---

Figure 5.1. (a) View of the 3D network of MOF-525 featuring highly porous framework as well as the incorporation of active sites into the MOF-525 framework; (b) Fourier transform magnitudes of the experimental Co K-edge EXAFS spectra of samples. The Fourier transforms are not corrected for phase shift; (c) Wavelet transform for the  $k^3$ -weighted EXAFS signal of MOF-525-Co based on Morlet wavelets with optimum resolution at the first (lower panel) and higher (upper panel) coordination shells. The vertical dashed lines that denote the  $k$ -space positions of the Co-N and Co-Co contributions are provided to guide the eye; (d) Comparison between the Co K-edge XANES experimental spectrum of MOF-525-Co and the theoretical spectrum calculated with the depicted structure. For clarity, the non-convoluted theoretical spectrum is also shown; (e) UV/vis spectra of MOF-525, MOF-525-Co and MOF-525-Zn.

The successful synthesis of MOF was confirmed by the XRD pattern at room temperature (Figure 5.3). To confirm the local coordination environment of the cobalt atom upon insertion within the framework, the Co K-edge extended X-ray absorption fine structure (EXAFS) and X-ray absorption near-edge structure (XANES) spectroscopies were investigated.<sup>20</sup> The EXAFS Fourier transforms (FTs) and wavelet transforms (WTs) are shown in Figure 5.1b and 5.1c. The assignment of the signals from 1.0 to 5.0 Å to either Co–N(C) or Co–Co interaction is based on a detailed WT-EXAFS wavelet transform analysis. For MOF-525-Co, one WT intensity maximum near 6.0 Å<sup>-1</sup> associated with a shoulder around 9.0 Å<sup>-1</sup> is well resolved at 1.0-5.0 Å (Figure 5.1c), which can be assigned to the Co-N bond. In comparison, WT intensity maximum at 7.5 Å<sup>-1</sup> corresponding to the Co-Co bond is not detected in MOF-525-Co, indicating that almost all cobalts exists as mononuclear centers.<sup>21-22</sup> EXAFS curve fitting analysis reveals that the coordination number of the nearest-neighbor N atoms surrounding the isolated cobalt atom is 3.9 at 1.95 Å (Table 5.1), further confirmed the square-planar configuration of cobalt in the newly developed MOF, leaving unsaturated active sites for catalytic reaction (Table 5.1). Due to the high sensitivity to the three-dimensional arrangement of atoms around the photo-absorber, XANES was applied to better identify the newly developed MOF. From Figure 5.4, it can be observed that the overall profile of the Co  $K$ -edge XANES spectrum of MOF-525-Co is drastically different from that of metallic

## Chapter 5

Co, which suggested the existence of the Co-N species. The square-planar configuration of cobalt center with high  $D_{4h}$  symmetry was further qualitatively evidenced by the strong characteristic pre-edge peak at 7715 eV due to a  $1s \rightarrow 4p_z$  shakedown transition.<sup>21-22</sup> Moreover, I resorted to XANES simulation of the  $\text{CoN}_x\text{C}_y$  moiety built by situating cobalt atom at the center of the porphyrinic unit within the crystal structure obtained by XRD rietveld refinement. As shown in Figure 5.1d, the seven features (denote as a-g) of the experimental XANES spectrum for MOF-525-Co are all satisfactorily reproduced, thus fully corroborating the unsaturated single atom implanted MOF-525-Co.



## Chapter 5

Figure 5.2. The structure of TCPP ligand (a), the TCPP ligand connected with four  $Zr_6$  cluster (b) to realize the organization of MOF-525 framework(c). The implantation of active sites into new hybrid (d). Three dimensional framework of MOF-525-Co in different directions (e) and (f).

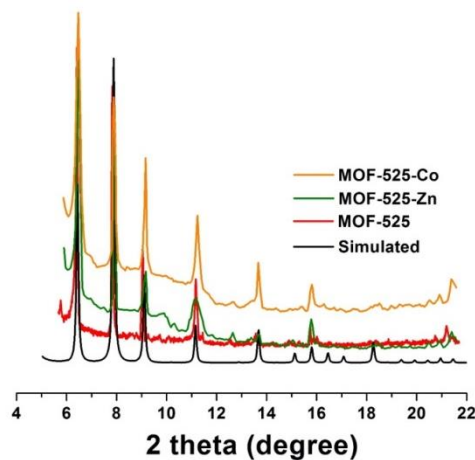


Figure 5.3. XRD patterns of MOF-525, as well as single atom implanted MOF-525-Co and MOF-525-Zn. The standard pattern MOF-525 has also been shown as references. After incorporation of active sites into the framework, powder X-ray diffraction (PXRD) patterns remained nearly unchanged, which suggests that cobalt and zinc insertion does not destroy the framework structure.

Table 5.1. Co K-edge EXAFS curve Fitting Parameters<sup>a</sup>

Sample	Shell	$N$	$R$ (Å)	$\sigma^2$ ( $\times 10^3$ Å <sup>-2</sup> )	$\Delta E_0$ (eV)	$R_f$ , %
Co foil <sup>b</sup>	Co-Co	12	2.494 (2)	7.4 (1)	0.4 (4)	0.01
Co@C <sup>c</sup>	Co-C	2.6 (2)	2.023 (8)	11.5 (10)	0.6 (7)	0.01
	Co-Co	4.3 (2)	2.474 (4)	13.2 (5)	-7.5 (6)	
MOF-525-Co <sup>d</sup>	Co-N(O)	3.9 (7)	1.951 (8)	3.0 (10)	3.9 (15)	0.01

<sup>a</sup> $N$ , coordination number;  $R$ , distance between absorber and backscatter atoms;  $\sigma^2$ , Debye-Waller factor to account for both thermal and structural disorders;  $\Delta E_0$ , inner potential correction;  $R$ -factor ( $R_f$ , %)

## Chapter 5

indicates the goodness of the fit. Errors are given in brackets.  $S_0^2$  was fixed to 0.93 as determined from Co foil fitting. Bold numbers indicate fixed coordination number according to the crystal structure. <sup>b</sup>Fitting range:  $3.2 \leq k (\text{\AA}) \leq 12.5$  and  $1.4 \leq R (\text{\AA}) \leq 2.7$ . <sup>c</sup>Fitting range:  $2.0 \leq k (\text{\AA}) \leq 12.5$  and  $1.0 \leq R (\text{\AA}) \leq 2.7$ . <sup>d</sup>Fitting range:  $2.0 \leq k (\text{\AA}) \leq 12.5$  and  $1.0 \leq R (\text{\AA}) \leq 2.0$ .

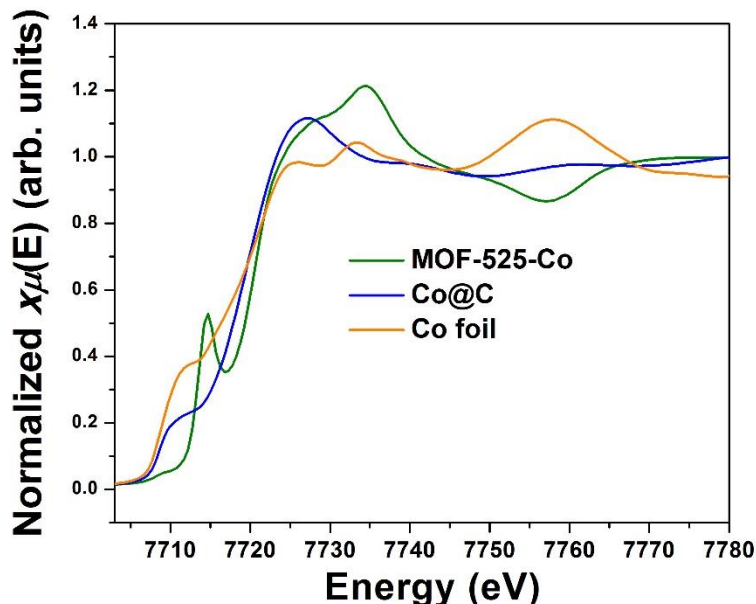


Figure 5.4. The normalized Co K-edge XANES spectra of different samples and references.

Metallization of zinc in the MOF (MOF-525-Zn) has also been developed as reference compound under similar strategy. UV-Vis spectra indicated that MOF-525, MOF-525-Co, as well as MOF-525-Zn were excellent photon absorbers from 200 to 800 nm (Figure 5.1e). MOF-525 displays a strong S band and four Q bands, which are characteristic bands for the porphyrin family (Figure 5.5). After the metallation of the porphyrin ring with cobalt and zinc, the four Q bands become two due to the higher symmetry of porphyrin unit in MOF-525-Zn and MOF-525-Co.<sup>23</sup> These results combined with the Fourier transform infrared spectroscopy (FTIR) and inductively coupled plasma (ICP)-elemental analysis confirmed the successful incorporation of zinc and cobalt into the framework (Table 5.2, Figure 5.6). Compared with TCPP ligand, the asymmetric vibrational absorption was disappeared after coordination

## Chapter 5

between  $Zr^{4+}$  and -COOH group in MOF-525, indicating that all the -COOH groups are participated in the coordination with  $Zr^{4+}$ . N-H bond absorption was observed in MOF-525, which confirmed that the uncoordinated nitrogen sites in the framework. By post-synthetic modification of MOF-525 with cobalt ions, I observed that there is no N-H bond adsorption in the as-synthesized MOF-525-Co, these results support the successfully incorporate of cobalt into the porphyrin unit in MOF-525. These facts were further revealed by the survey of XPS spectra, the free base porphyrin in MOF-525 contains two chemically different types of nitrogen atoms, (=N-, and -NH), while cobalt and zinc incorporated MOF-525-Zn and MOF-525-Co produced single signal for Co-N or Zn-N bonding in the asymmetric N 1s XPS spectra, respectively (Figure 5.7).<sup>23</sup> The presence of  $Co_{2p}$  XPS or  $Zn_{2p}$  spectra, also evidenced the introduction of these components into the framework (Figure 5.8).  $N_2$  adsorption measurements at 77 K (Figure 5.9) for MOF-525, MOF-525-Zn and MOF-525-Co show a type I isotherm, MOF-525 has the maximum  $N_2$  adsorption with the Brunauer-Emmett-Teller (BET) surface areas of  $2127.7 \text{ m}^2 \text{ g}^{-1}$ , which is higher than that of MOF-525-Zn ( $1264.2 \text{ m}^2 \text{ g}^{-1}$ ) and MOF-525-Co ( $1317.8 \text{ m}^2 \text{ g}^{-1}$ ). The reason may be ascribed to the introduction of cobalt and zinc sites, which can slightly diminish the surface area.

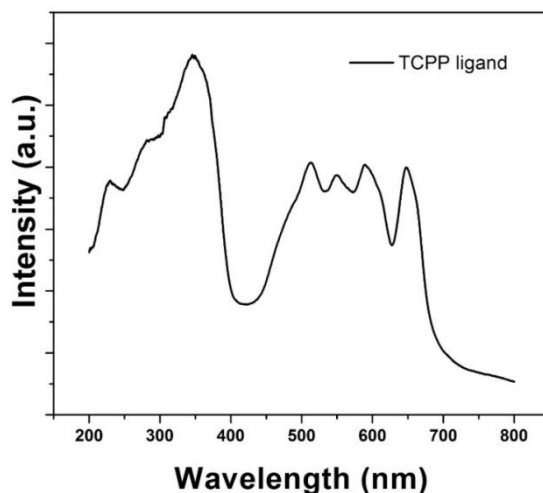


Figure 5.5. UV/vis spectra of TCPP ligand, UV-vis spectra indicated that TCPP ligand is excellent photon absorbers from 200 to 800 nm, which displays a series of characteristic bands (a strong S band and four Q bands) for the porphyrin family.

## Chapter 5

Table 5.2. Elemental analysis of the MOF-525, MOF-525-Co, mof-525-Zn.

Elemental Analysis	Zr (%) <sup>b</sup>		Zn (%) <sup>b</sup>		Co (%) <sup>b</sup>	
	Calcd	Found	Calcd	Found	Calcd	Found
MOF-525	20.9	21.32	0	0	0	0
MOF-525-Co	19.64	19.97	0	0	6.35	6.01
MOF-525-Zn	19.50	19.83	6.99	6.42	0	0

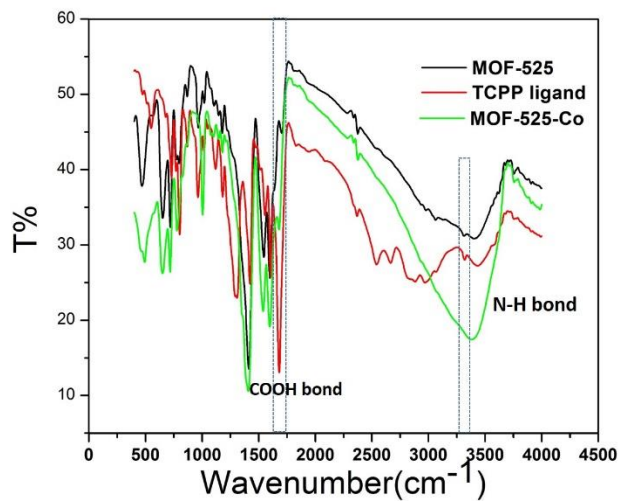


Figure 5.6. FTIR (Fourier transform infrared spectroscopy) of MOF-525, TCPP ligand, and MOF-525-Co.

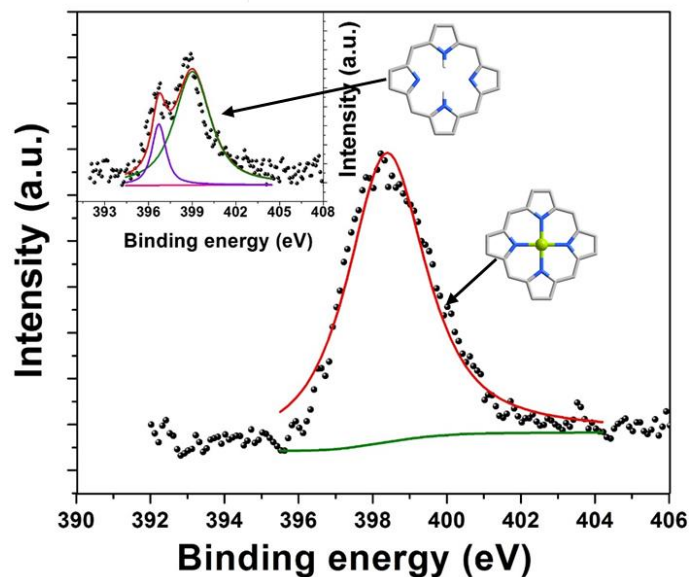


Figure 5.7. XPS spectra of the as-prepared samples: N1s spectra of MOF-525-Co and MOF-525 (inset).

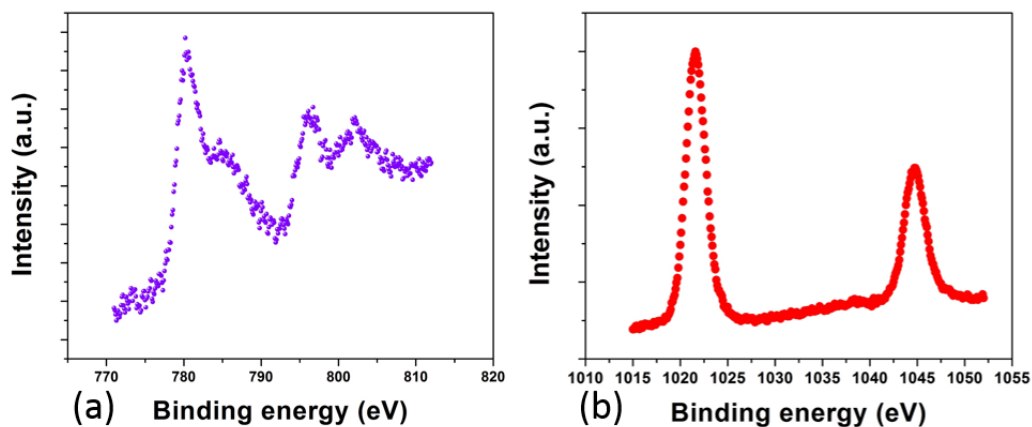


Figure 5.8. XPS spectra of the as-prepared samples: Co 2p spectra for MOF-525-Co and Zn 2p spectra for MOF-525-Zn.

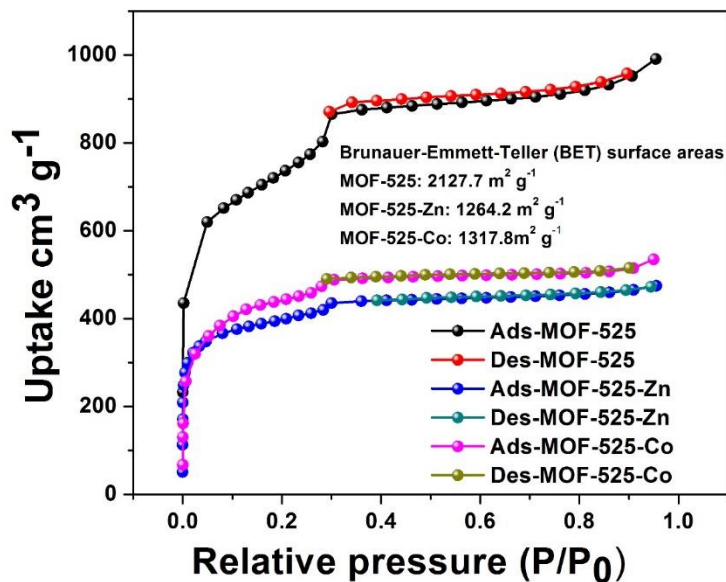


Figure 5.9.  $N_2$  isotherms of MOF-525, MOF-525-Co, as well as MOF-525-Zn.

### 5.3.2 Photocatalytic $CO_2$ reduction

To elucidate the effect of metallization over porphyrin based MOF, the catalytic behaviors of MOF-525-Co and MOF-525-Zn in the photochemical reduction of  $CO_2$  was examined and compared with that of MOF-525. The reduction proceeded upon irradiation with visible light by using triethanolamine (TEOA) as an electron donor, giving two-electron reduction products CO together and eight-electron reduction product  $CH_4$ . As shown in Figure 5.10a and 5.10b, the generation of CO and  $CH_4$  increased almost linearly with irradiation time. It is clear that MOF-525-Co composite showed the highest CO evolution rate of  $200.6 \mu\text{mol g}^{-1}\text{h}^{-1}$  (yield of  $2.42 \mu\text{mol}$ ), and  $CH_4$  evolution rate of  $36.76 \mu\text{mol g}^{-1}\text{h}^{-1}$  (yield of  $0.42 \mu\text{mol}$ ) under light illumination for 6 hours, much higher than that of MOF-525-Zn (CO evolution rate of  $111.7 \mu\text{mol g}^{-1}\text{h}^{-1}$  and  $CH_4$  evolution rate of  $11.635 \mu\text{mol g}^{-1}\text{h}^{-1}$ ) and MOF-525 (CO evolution rate of  $64.02 \mu\text{mol g}^{-1}\text{h}^{-1}$  and  $CH_4$  evolution rate of  $6.2 \mu\text{mol g}^{-1}\text{h}^{-1}$ ). These results also reveal that MOF-525-Co is an active catalyst for  $CO_2$  reduction and comparable with previously reported catalysts under similar condition.<sup>24-27</sup> As demonstrated that superior efficiency in the  $CO_2$  conversion was realized with the incorporation of unsaturated single atoms into zirconium-porphyrin MOF: i)  $CO_2$

## Chapter 5

conversion enhancement is more obvious over MOF-525-Co than MOF-525-Zn. ii) Compared with MOF-525, MOF-525-Co possessed 3.13 fold higher photocatalytic activity in CO (two-electron reduction products) evolution and meanwhile produced 5.93 fold enhancements in CH<sub>4</sub> (eight-electron reduction products) evolution, which clearly confirmed that the selectivity of CH<sub>4</sub> was significantly improved with the metalization of cobalt (Table 5.3).

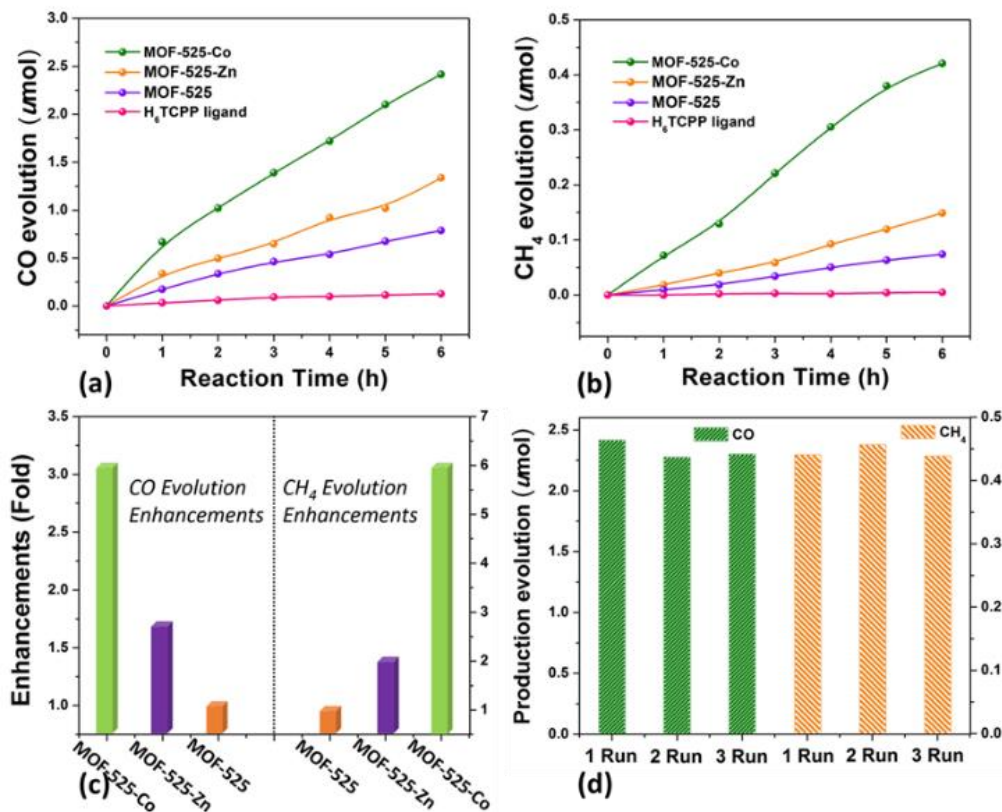


Figure 5.10. Time dependent CO (a) and CH<sub>4</sub> (b) evolution over MOF-525-Co, MOF-525-Zn, and MOF-525 photocatalysts; c) Enhancement of production evolution over MOF-525-Co and MOF-525-Zn. d) Production yield of CO and CH<sub>4</sub> over MOF-525-Co photocatalyst to measure reproducibility by cycling tests.

## Chapter 5

Table 5.3. Comparison of the properties and photocatalytic activity of samples.

Catalyst	CO <sub>2</sub> uptake <sup>[a]</sup>	$\Phi_{ET}$ <sup>[b]</sup>	Evolution rate <sup>[c]</sup>		CH <sub>4</sub> Selectivity <sup>[e]</sup>
			CO	CH <sub>4</sub>	
<b>TCP ligand</b>	4.8	–	4.5	n.d. <sup>[d]</sup>	0
<b>MOF-525</b>	25.3	–	64.02	6.2	8.83
<b>MOF-525-Zn</b>	28.1	24.9	111.7	11.635	9.43
<b>MOF-525-Co</b>	33.6	62.1	200.6	36.76	15.4

[a] in cm<sup>3</sup> g<sup>-1</sup>. [b] Energy transfer efficiency. [c] In  $\mu\text{mol g}^{-1}\text{h}^{-1}$ . [d] Not detectable. [e] Calculated by the ratio of CH<sub>4</sub> (in moles) to the total products formed (in moles).

In addition, MOF-525-Co also exhibits excellent performance stability in a recycling test, and produces a fairly reproducible photocatalytic activity for all three cycles. Catalytic behaviors comparison between MOF-525-Co and its molecular units (such as porphyrin cobalt (TCP-Co) unit and (TCP-Co)/ZrO<sub>2</sub> composite) have also been conducted, which greatly manifested the advantage of MOF-525-Co in photocatalytic CO<sub>2</sub> reduction (Figure 5.11 and 5.12). To well demonstrate the advantage of MOF-525-Co, the photocatalytic CO<sub>2</sub> reduction performances of TCP(Co), as well as the hybrid of ZrO<sub>2</sub>/TCP(Co) have also been investigated. As shown in Figure 5.11, the catalytic performance of TCP(Co) is higher than of ZrO<sub>2</sub>/TCP, but much lower than that of MOF-525-Co, which greatly demonstrated the advantage of MOF-525-Co in photocatalytic CO<sub>2</sub> reduction. The BET surface area as well as CO<sub>2</sub> adsorption ability of TCP(Co) and ZrO<sub>2</sub>/TCP(Co) have also been investigated, which show rather lower ability than that of MOF-525-Co in N<sub>2</sub> and CO<sub>2</sub> adsorption. These results not only can partly account for the enhanced catalytic capability observed in MOF-525-Co, but also provide further evidences to demonstrate the advantages of MOF-525-Co. I also investigated the origin for those difference between ZrO<sub>2</sub>/TCP(Co) and TCP(Co) in CO<sub>2</sub> reduction, generally speaking, the hybrid always produce enhanced performance as the enhanced electron-hole separation efficiency. To answer this question, Mott-Schottky measurements on TCP(Co) were conducted at frequencies of 500, 1000, and 1500 Hz (Figure 5.12) for investigating its semiconductor character. The positive slope of the obtained C<sup>-2</sup> values (vs the applied potentials) is consistent with that of the typical n-type semiconductors. The intersection point is independent of the frequency, and the flat band position determined from the intersection is  $\sim -0.56$  V vs NHE. Since it is

## Chapter 5

generally accepted that the bottom of the conduction band (LUMO) in n-type semiconductors is approximately equal to the flat-band potential, the LUMO of TPP(Co) is estimated to be  $-0.56$  V vs NHE. This value is more positive than the conduction band of  $\text{ZrO}_2$ , and thus energy transfer from TCP(Co) to  $\text{ZrO}_2$  is not supported in hybrid of  $\text{ZrO}_2/\text{TCP}(\text{Co})$ . These results not only accounted for the much weakened  $\text{CO}_2$  reduction ability in  $\text{ZrO}_2/\text{TCP}(\text{Co})$  but also confirmed the porphyrins cobalt active sites in TCP(Co). When the experiment was conducted in the absence of photocatalysts or light illumination, no detectable products was formed in the reaction system (Figure 5.13). To further validate the source of the generated CO and  $\text{CH}_4$  products, an isotopic experiment using  $^{13}\text{CO}_2$  as substrate was performed under identical photocatalytic reaction conditions, and the products were analyzed by gas chromatography and mass spectra. As shown in Figure Figure 5.14, the peak at  $m/Z=29$  and  $m/Z= 17$  could be assigned to  $^{13}\text{CO}$  and  $^{13}\text{CH}_4$ , indicating that the carbon source of CO and  $\text{CH}_4$  indeed originate from the used  $\text{CO}_2$ .

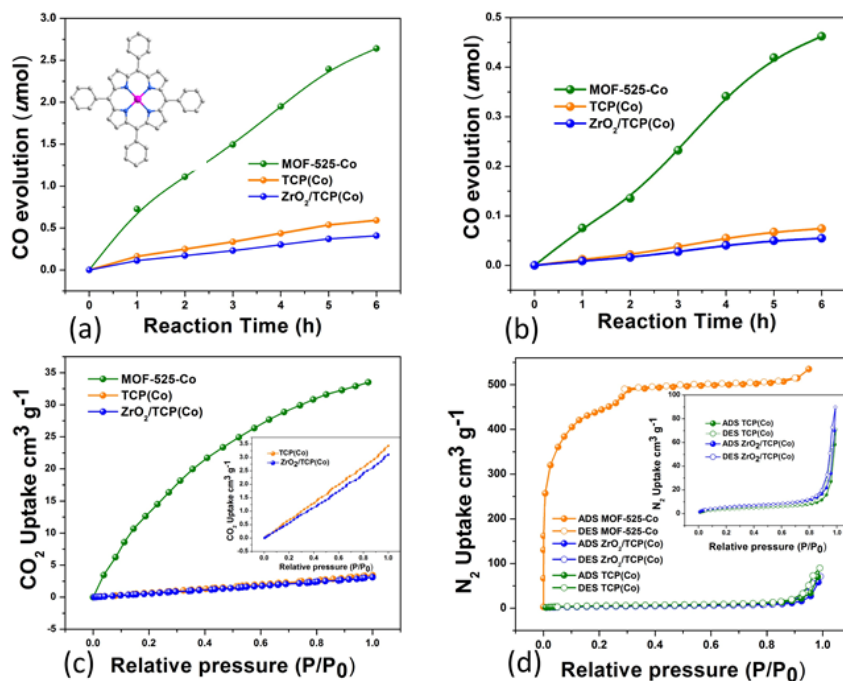


Figure 5.11. Time dependent CO (a) and  $\text{CH}_4$  (b) evolution over MOF-525-Co, TCP(Co), and  $\text{ZrO}_2/\text{TCP}(\text{Co})$  photocatalysts; (c)  $\text{CO}_2$  and (d)  $\text{N}_2$  adsorption behaviors for MOF-525-Co, TCP(Co) and  $\text{ZrO}_2/\text{TCP}(\text{Co})$  photocatalysts.

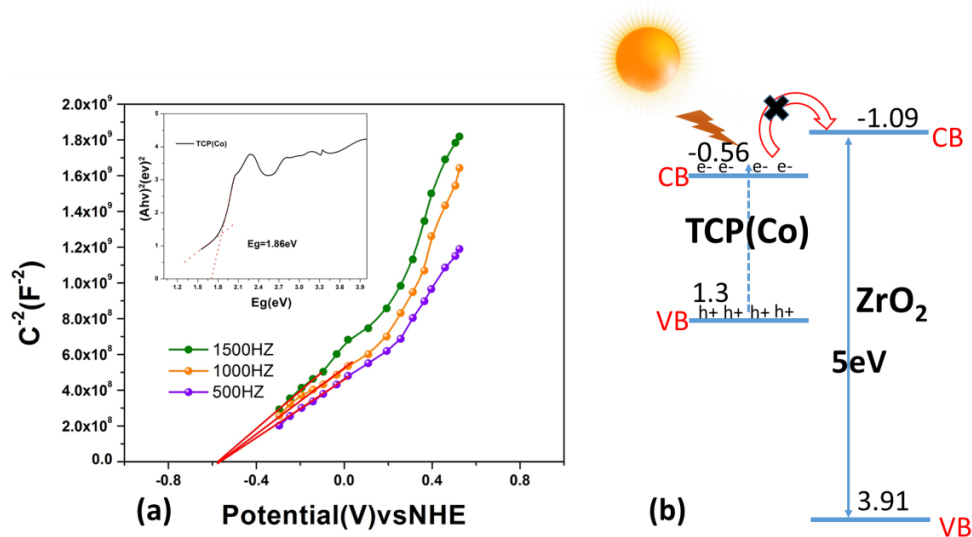


Figure 5.12. (a) Mott–Schottky plots for TCP(Co) in 0.2 M Na<sub>2</sub>SO<sub>4</sub> aqueous solution (pH 6.8). inset is Tauc plot of TCP(Co) (b) inset is the energy diagram of the CB and VB levels of TCP(Co) and ZrO<sub>2</sub>, as well as unsupported charge transfer route in composite of ZrO<sub>2</sub>/TCP(Co).

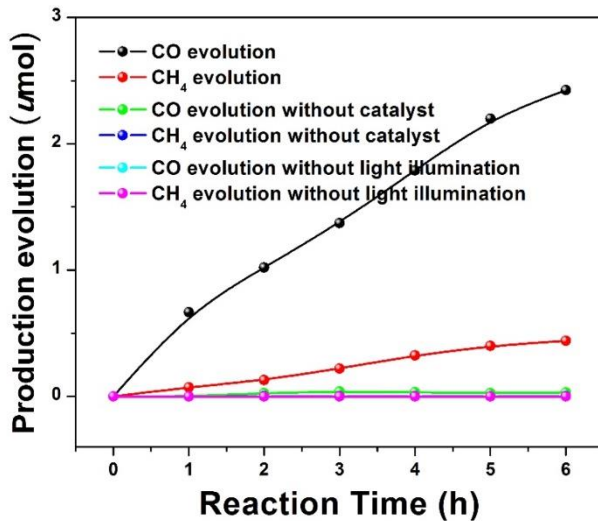


Figure 5.13. Time course of production evolution in different reaction condition.

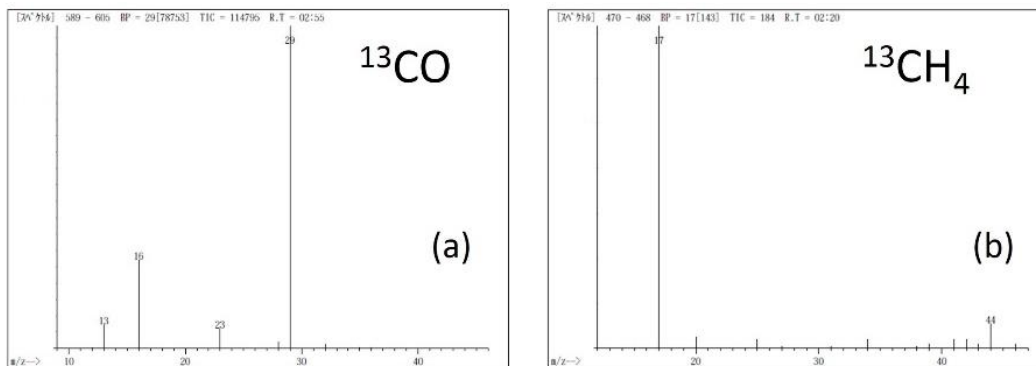


Figure 5.14. Gas chromatogram and mass spectra of  $^{13}\text{CO}$  ( $m/z=29$ ) and  $\text{CH}_4$  ( $m/z=17$ ) produced over MOF-525-Co in the photocatalytic reduction of  $^{13}\text{CO}_2$ .

### 5.3.3 Clarification of mechanism

The above results clearly demonstrate the niche of metalation of zirconium-porphyrin MOF in photocatalysis. I am now in a position to understand the mechanisms behind the function of the newly developed structures.  $\text{CO}_2$  adsorption, the first prerequisite event before further reduction reactions can take place, is of vital importance for the final catalytic result. Volumetric  $\text{CO}_2$  adsorption measurement reveals increased uptakes after metallization at all pressures up to 100 kPa (Figure 5.15a and Table 5.3). These results can be interpreted in terms of increase in the affinity sites for adsorbates after metallization, which should partly account for the enhanced catalytic capability observed. *In-situ* FTIR technology has shown to be a crucial tool to investigate the local interaction between the active sites and  $\text{CO}_2$  molecular, in which asymmetric stretching mode ( $\nu_3 = 2349 \text{ cm}^{-1}$ ) of  $\text{CO}_2$  are infrared active and thus can serve as a handle for identifying the nature of the adsorption behavior. As shown in Figure 5.16, infrared spectra collected from blank sample in  $\text{CO}_2$  atmosphere exhibit a strong peak centered at  $2334 \text{ cm}^{-1}$ , which should be attributed to the  $\nu_3$  band of  $\text{CO}_2$ .<sup>28</sup> In the case of MOF-525-Co, the adsorption of  $\text{CO}_2$  onto the exposed Co(II) adsorption sites resulted in a  $31 \text{ cm}^{-1}$  red shift of the  $\nu_3$  band due to the electron donation from the oxygen lone pairs on the  $\text{CO}_2$  to the unoccupied Co(II) orbitals. The enhanced  $\text{CO}_2$  adsorption activity over MOF-525-Co and MOF-525-Zn as well as the *in situ* FT-IR spectra not only reveal the strong

## Chapter 5

interaction between the CO<sub>2</sub> molecular and adsorption sites, but also demonstrate the integration of the active centers and reagents adsorption sites, and thus enhanced CO<sub>2</sub> reduction activity can be guaranteed with the implantation of metal ions into the porphyrin moiety.

In photocatalytic process, photo-generated electron-hole pairs separate from each other and vigorously move to catalytically active sites. Taking into account that MOF-525-Co and MOF-525-Zn have a similar surface area and CO<sub>2</sub> adsorption ability, the significant difference in the activity enhancement for the two catalysts should be partially ascribed to the difference in charge separation efficiencies as a function of donor-acceptor interaction. Porphyrin-containing struts are the primary building blocks used in MOFs that target solar light harvesting. These porphyrin-units have been proven to have exciton propagation capabilities, displaying anisotropic energy transport over several tens of struts from the initially excited strut.<sup>17-19</sup>

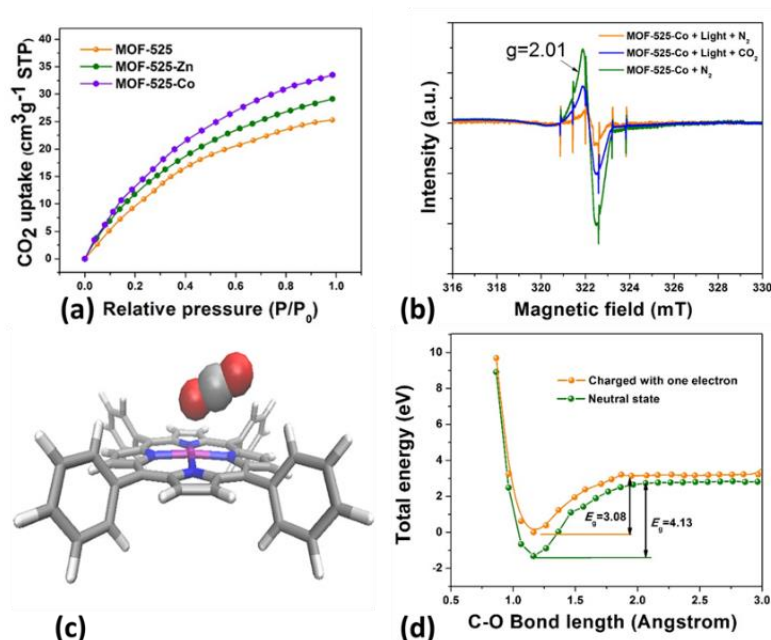


Figure 5.15. (a) CO<sub>2</sub> adsorption behaviors for MOF-525 as well as single atom implanted MOF-525-Co, MOF-525-Zn; (b) ESR spectra of MOF-525-Co under different conditions; (c) The optimized structure for CO<sub>2</sub> adsorption on porphyrin-cobalt unit; (d) O-C bond length dependent CO<sub>2</sub> activation energies barrier.

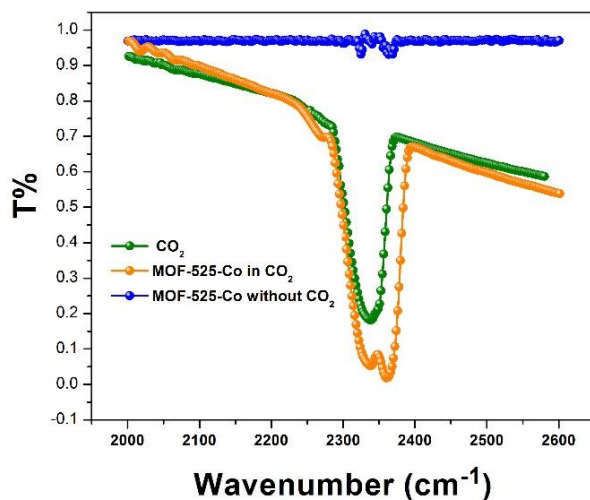


Figure 5.16. *In-situ* FTIR spectra collected from blank sample and MOF-525-Co in different conditions.

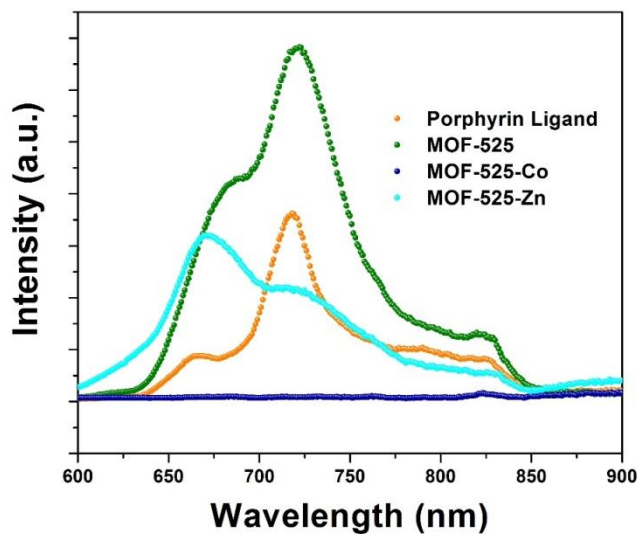


Figure 5.17. (a) Photo-luminescent spectra of porphyrin ligand, MOF-525, MOF-525-Zn as well as MOF-525-Co.

Further insight into the electron transfer behavior was revealed by photo-luminescent (PL) - quenching experiments, with the incorporation of metal ions into the porphyrin ring, significant quenching of the PL intensities of the porphyrin emission are observed, especially for porphyrin-Co units, indicating that the recombination of photoexcited electron-hole pairs is significantly suppressed and the separation of electron-hole pairs is efficiently improved (Figure 5.17). Time-resolved decays for metal

## Chapter 5

---

sites implanted MOF-525-Co and MOF-525-Zn demonstrated more rapid decay than unmodified MOF-525. Analysis of the curves with a reconvolution fit supported a triexponential decay model in each case and revealed a shortening of the amplitude-weighted average lifetimes from 90.25 (MOF-525) to 68.35 and 34.15 ns in the presence of the acceptor molecules in MOF-525-Zn and MOF-525-Co, respectively. To describe quantitatively the energy transfer (ET) processes occurring in photocatalytic process, I sought an independent measurement of the ET efficiency ( $\Phi_{ET}$ ) based on the time-resolved fluorescence decay lifetimes (eq 1).<sup>28</sup> The  $\Phi_{ET}$  was determined based on donor lifetimes in the presence and absence of the acceptor molecules. Compared with MOF-525-Zn ( $\Phi_{ET} = 24.9\%$ ), relative larger  $\Phi_{ET}$  ( $\Phi_{ET} = 62.1\%$ ) was observed for MOF-525-Co, which could further accounted for the more enhanced catalytic activity in MOF-525-Co (Table 5.3). Thus, directional migration of photo-generated exciton from porphyrin to electron trapping sites was realized by the implantation of catalytic cobalt single atoms, and which achieved the supply of long-lived electrons for the reduction of CO<sub>2</sub> molecules that are adsorbed on cobalt centers.

After making clear the charge transfer route from the excited porphyrin to the reaction centers, I now turn my attention to the reaction kinetic over the activation sites. ESR spectroscopy can provide valuable fingerprinting information about trapped electrons and interface states in reaction process. For MOF-525, a  $g$  value of 1.9984 was observed at room temperature under nitrogen gas atmosphere, which could be ascribed to the free radicals produced by the porphyrin-based ligand.<sup>29</sup> With light irradiation, enhanced ESR signal with  $g$  value of 1.9984 as well as a new ESR signal with a  $g$  value of 2.0048 were observed, which provided a clue about the promoted photogeneration of radical pairs in the MOF-525 and charge transfer process was occurred (Figure 5.18). According to the literature, the new signal can be attributed to Zr(III) species formed from the optically induced hopping of electrons from Zr(IV) to Zr(III) sites in the zirconium oxo-clusters.<sup>30</sup> These studies conclusively demonstrated that without the intention of additional sites in the MOF matrix, charge transfer from porphyrin ligand to zirconium oxo-clusters is expected. However, in the case of the MOF-525-Co composite without irradiation, strong signal for the high-spin state Co(II) accompanied by signal from porphyrin unit were observed (Figure 5.15b). With the

## Chapter 5

irradiation of visible light, the peak intensity of Co(II) was greatly weakened, which clearly indicated that the optically induced valence transformation from high-spin state Co(II) to Co(I) in low-spin state.<sup>31</sup> When CO<sub>2</sub> was introduced into the irradiated MOF-525-Co system, this ESR signal corresponding to Co(II) becomes much enhanced, implying that amounts of Co(I) was oxidized back to Co(II) species during CO<sub>2</sub> photoreduction process. This kinetic behavior also indicates that the photoexcited electrons transferred to the cobalt center and realize the valence transformation of cobalt center. It is rather interesting that the Zr(III) signal in MOF-525-Co nearly disappeared under light irradiation, I may tentatively draw the conclusion that the coordination between the porphyrin ring and Co center is most likely leads to effective shuttering of the electron-transfer channels from the porphyrin units to zirconium oxo-clusters.

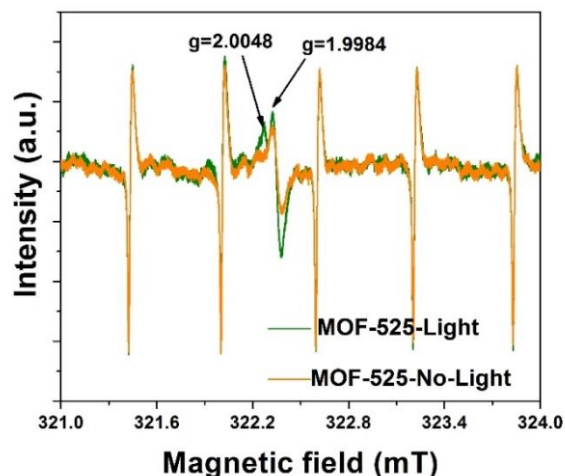


Figure 5.18. ESR spectra of MOF-525 under light irradiation and without light interference.

From the analysis above, it can be concluded that in the hybrid structures the porphyrin unit is photoexcited to generate electron-hole pairs and the electrons are transferred to the coordinatively unsaturated metal sites to accomplish the valence transformation of cobalt center, where CO<sub>2</sub> can be adsorbed on during the reduction process (Figure 5.19). The improved efficiency of charge separation in our designed hybrid system was clearly demonstrated in above discussion. Theoretical model has also

## Chapter 5

been constructed to simulate the reaction process and examine whether the CO<sub>2</sub> molecules can be activated well on the coordinately unsaturated cobalt sites of the MOFs upon receiving the photoexcited electrons from the porphyrin unit (Figure 5.15c). The activation of CO<sub>2</sub> molecules is attributed to a high concentration of localized electrons in the near-surface region and a corrugation of the surface that can trap oxygen atoms from carbon monoxide and carbon dioxide molecules. First-principles simulations reveal that the addition of electron charges can greatly improve the adsorption of CO<sub>2</sub> to the active sites, resulting in the calculated adsorption energy increase from 0.865 to 2.189 eV. The simulated potential energy surfaces along the variation of the O–C bond of the CO<sub>2</sub> molecule adsorbed on active sites are plotted in Figure 5.15d. The addition of a one-electron charge can barely alter the activation-energy barrier (EB) for CO<sub>2</sub>, and substantially lowers the EB from 4.13 to 3.08 eV. These results clearly indicate that upon receiving the photo-excited electrons from porphyrin units, the coordinatively unsaturated cobalt centers can turn into an active catalytic material for the activation of CO<sub>2</sub> molecules.

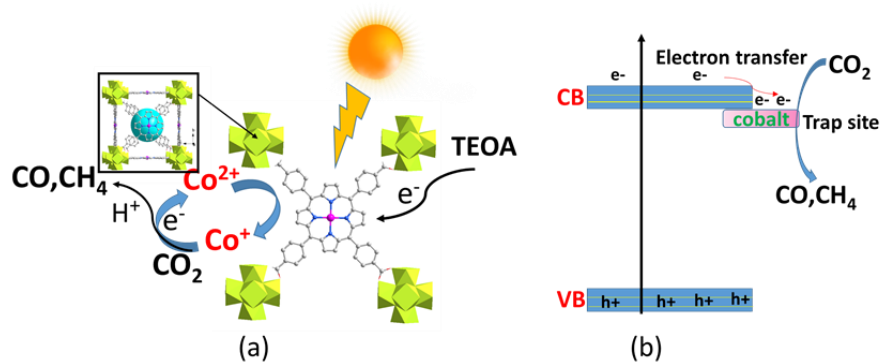


Figure 5.19. (a)-(b) Mechanisms underlying the photoexcited dynamics involved in MOF-525-Co.

### 5.4 Conclusion

In conclusion, I realized the atomically dispersed active sites into extended MOF, and thus give rise to the photocatalysts that perform high activity to CO<sub>2</sub> reduction. The unique structural characters of developed catalyst possessed a large surface area and strong CO<sub>2</sub> adsorption ability. As demonstrated by

## Chapter 5

---

the energy transfer efficiency investigation, the photogenerated electrons can be effectively transferred to the active sites, which not only facilitates charge separation in the semiconducting MOF but supplies energetic electrons to gas molecules adsorbed on the MOF. After active sites incorporation, CO<sub>2</sub> can be easily captured and followed by photocatalytic reduction to CO and CH<sub>4</sub> with dramatically improved performance in terms of both activity and CH<sub>4</sub> selectivity. I anticipate that this implantation strategy combined with the molecular material platforms will be applicable to a broad range of catalytic applications, particularly those that require solar harvesting and gaseous compatibility.

### References

1. J. Lin, A. Wang, B. Qiao, X. Liu, X. Yang, X. Wang, J. Liang, J. Li, J. Liu, T. Zhang, *J. Am. Chem. Soc.* **2013**, *135*, 15314–15317.
2. P. Liu, Y. Zhao, R. Qin, S. Mo, G. Chen, D. M. Chevrier, P. Zhang, Q. Guo, D. Zang, B. Wu, G. Fu, N. Zheng, *Science*. **2016**, *352*, 797–801.
3. Y. Lei, F. Mehmood, S. Lee, J. Greeley, B. Lee, S. Seifert, R. E. Winans, J. W. Elam, M. J. Pellin, L. A. Curtiss, S. Vajda, *Science*. **2010**, *328*, 224–228.
4. C. Liu, B. Yang, E. Tyo, S. Seifert, J. DeBartolo, B. Issendorff, P. Zapol, S. Vajda, L. A. Curtiss, *J. Am. Chem. Soc.* **2015**, *137*, 8676–8679.
5. F. Li, Y. Li, X. C. Zeng, Z. Chen, *ACS Catal.* **2015**, *5*, 544–552.
6. K. Manna, T. Zhang, F.X. Greene, W. Lin, *J. Am. Chem. Soc.* **2015**, *137*, 2665–2673.
7. H. Zhang, G. Liu, L. Shi, J. Tang, H. Pang, K. Wu, T. Takei, J. Zhang, Y. Yamauchi, J. Ye, *NPG Asia Materials*. **2016**, *8*, DOI:10.1038/am.2016.102.
8. H. Xu, J. Hu, D. Wang, Z. Li, Q. Zhang, Y. Luo, S-H. Yu, H-L. Jiang, *J. Am. Chem. Soc.* **2015**, *137*, 13440–13443.
9. S. Wang, W. Yao, J. Lin, Z. Ding, X. Wang, *Angew. Chem. Int. Ed.* **2014**, *53*, 1034–1038.
10. H. Zhang, T. Wang, J. Wang, T. D. Dao, M. Li, G. Liu, X. Meng, K. Chang, L. Shi, T. Nagao, J. Ye, *Adv. Mater.* **2016**, *28*, 3703–3710.

## Chapter 5

---

11. L. Long, J. Chen, X. Zhang, A. Zhang, Y. Huang, Q. Rong, H. Yu, *NPG Asia Materials*. **2016**, 8, DOI:10.1038/am.2016.46.
12. L. Duan, L. Wang, F. Li, L. Sun, *Acc. Chem. Res.* **2015**, 48, 2084–2096.
13. M. Yamamoto, L. Wang, F. Li, T. Fukushima, K. Tanaka, L. Sun, H. Imahori, *Chem. Sci.* **2016**, 7, 1430–1439.
14. H. Li, F. Li, B. Zhang, X. Zhou, F. Yu, L. Sun, *J. Am. Chem. Soc.* **2015**, 137, 4332–4335.
15. N. Kornienko, Y. Zhao, C. Zhu, D. Kim, S. Lin, C. Chang, O. M. Yaghi, P. Yang, *J. Am. Chem. Soc.*, **2015**, 137, 14129–14135.
16. D. J. Darensbourg, W.-C. Chung, K. Wang, H.-C. Zhou, *ACS Catal.*, **2014**, 4, 1511–1515.
17. W. Morris, P. L. McGrier, H. Furukawa, D. Cascio, J. F. Stoddart, O. M. Yaghi, *Inorg. Chem.*, **2012**, 51, 6443–6445.
18. I. Hod, M. D. Sampson, P. Deria, O. K. Farha, J. T. Hupp, *ACS Catalysis.*, **2015**, 5, 6302–6309.
19. J. A. Johnson, J. Luo, X. Zhang, Y.-S. Chen, M. D. Morton, E. Echeverría, F. E. Torres, J. Zhang, *ACS Catalysis*. **2015**, 5, 5283–5291.
20. D. C. Koningsberger, R. Eds. Prins, In X-ray absorption: principles, applications, techniques of EXAFS, SEXAFS, and XANES. **1988**, 92, Wiley: New York.
21. H. Fei, J. Dong, M. J. A-Jimenez, G. Ye, N. D. Kim, E. L.G. Samuel, Z. Peng, Z. Zhu, F. Qin, J. Bao, M. J. Yacaman, P. M. Ajayan, D. Chen, J. M. Tour, *Nat. Commun.* **2015**, 6, 8668.
22. T. E. Westre, P. Kennepohl, J. G. DeWitt, B. Hedman, K. O. Hodgson, E. I. Solomon, *J. Am. Chem. Soc.*, **1997**, 119, 6297–6314.
23. S. Afzal, W. A. Daoud, S. J. Langford, *ACS Appl. Mater. Interfaces.*, **2013**, 5, 4753–4759.
24. D. Wang, R. Huang, W. Liu, D. Sun, Z. Li, *ACS Catal.*, **2014**, 4, 4254–4260.
25. Y. Lee, S. Kim, J. K. Kang, S. M. Cohen, *Chem. Commun.*, **2015**, 51, 5735–5738.
26. Y. Fu, D. Sun, Y. Chen, R. Huang, Z. Ding, X. Fu, Z. Li, *Angew. Chem. Int. Ed.* **2012**, 51, 3364–3367.
27. H. Zhang, G. Liu, L. Shi, H. Liu, T. Wang, J. Ye, *Nano Energy*. **2016**, 22, 149–168.

## Chapter 5

---

28. J. R. Lakowicz, *Principles of Fluorescence Spectroscopy* Principles of Fluorescence Spectroscopy, Springer, Heidelberg, **2007**.
29. D. Feng, H. Jiang, Y. Chen, Z. Gu, Z. Wei, H-C, Zhou, *Inorg. Chem.* **2013**, *52*, 12661–12667.
30. J. Long, S. Wang, Z. Ding, C. Wang, Y. Zhou, L. Huang, X, Wang, *Chem. Commun.*, **2012**, *48*, 11656–11658.
31. J. McAlpin, G. Surendranath, M. Dincă, T. A. Stich, S. A. Stoian, W. H. Casey, D. G. Nocera, R. D. Britt, *J. Am. Chem. Soc.* **2010**, *132*, 6882–6883.

# Chapter 6 General conclusions and future prospects

## 6.1 General conclusions

This thesis carried out a systematic study on the construction of efficient MOFs based photocatalysts for visible light photocatalytic reactions, including Cr(VI) reduction, CO<sub>2</sub> reduction and IPA oxidation. Organic ligand modification, heterojunction fabrication and metal ion implantation were proved to be effective strategies to improve the photocatalytic efficiencies of the constructed MOFs based photocatalysts. The findings in this study present some potential applications of MOFs based materials, aid to understand the mechanism of photocatalysis, and more importantly, highlight some universal design principles to the efficient MOFs based photocatalysis. The detailed conclusions for each part are summarized as follows:

1. Construction of an amine-functionalized iron(III) metal-organic framework as efficient visible-light photocatalyst for Cr(VI) reduction

In this part, an iron(III) based MOF structured as MIL-88B structure was successfully produced through a rapid microwave-assisted solvothermal synthesis method, and it was explored for photocatalytic Cr(VI) reduction under visible light. An organic ligand modification strategy, namely amine functionalization, was demonstrated to be effective for enlarging the light absorption and improving the carrier separation and transfer efficiency of MIL-88B (Fe). It was found that in addition to the direct excitation of Fe<sub>3</sub>-μ<sub>3</sub>-oxo clusters in MIL-88B (Fe), the amine functionalized organic linker could also be excited and then transferred an electron to Fe<sub>3</sub>-μ<sub>3</sub>-oxo clusters to reduce Cr(VI). As a result, the amine functionalized MIL-88B (Fe) showed much enhanced photocatalytic activity for Cr(VI) reduction than bare MIL-88B (Fe). The effect of amine functionalization in the other two Iron(III)-based MOFs (MIL-53 (Fe) and MIL-101 (Fe) ) on the visible light photocatalytic activity for the reduction of Cr(VI) was also

## Chapter 6

---

studied. The same trend was observed, namely all of the amine functionalized MOFs showed enhanced activity for photocatalytic Cr(VI) reduction compared with those of their parent MOFs. This part elucidated the mechanism of iron(III) based MOFs as photocatalysts for Cr(VI) reduction. It also proves that MOFs can serve as stable and efficient photocatalysts and the light harvesting efficiency can be flexibly tuned by simply modifying the organic linker in the MOFs structure.

### 2. Construction of nano-sized g-C<sub>3</sub>N<sub>4</sub> nanosheet/UiO-66 composite photocatalyst for enhanced photocatalytic CO<sub>2</sub> Reduction

In this part, a MOF based heterostructure photocatalyst that composed of a zirconium MOF (UiO-66) and g-C<sub>3</sub>N<sub>4</sub> nanosheet (CNNS) was constructed for photocatalytic CO<sub>2</sub> reduction under visible light. The designed hybrid structure possesses not only a large surface area and strong CO<sub>2</sub> adsorption ability, but also an improved electron separation and prolonged lifetime of charge carriers as a result of efficient electron transfer across the interface between CNNS and UiO-66. As a result, the UiO-66/CNNS heterostructure photocatalyst exhibited a CO yield of 59.4  $\mu\text{mol g}_{\text{CN}}^{-1}$  after visible light illumination for 6 hours, which is 3.4-fold larger than that of CNNS under mild reaction conditions. This part provides a strategy to design more active photocatalysts for CO<sub>2</sub> conversion reaction, as well as open up the opportunities to develop various MOFs based photocatalysts for gaseous reaction.

### 3. Implantation of iron(III) in porphyrinic metal organic frameworks for highly improved photocatalytic performance

In this part, I proposed a novel strategy to boost the photocatalytic efficiency of a porphyrinic MOF photocatalyst (PCN-224) for IPA oxidation via post-synthetic implantation of Fe(III). The implantation of Fe(III) ions in PCN-224 can not only improve the separation efficiency of photogenerated electron-hole pairs, but also construct Fenton reactions to convert *in-situ* formed inactive H<sub>2</sub>O<sub>2</sub> into reactive radicals (such as  $\cdot\text{O}_2^-$  and  $\cdot\text{OH}$ ) during the photocatalytic IPA oxidation reaction. As a result, the newly developed Fe@PCN-224 exhibited significantly enhanced photocatalytic activity, which was equivalent to an 8.9-fold improvement in acetone evolution rate and 9.3-fold enhancement in CO<sub>2</sub> generation rate

## Chapter 6

---

compared with the PCN-224. The effect of Fe(III) implantation in another porphyrinic MOF (PCN-222) on the visible light photocatalytic activity for the oxidation of IPA has also been studied. The same trend is observed, namely Fe@PCN-222 also shows enhanced activity for photocatalytic oxidation of IPA compared with bare PCN-222. This work provides a simple Fe(III) implantation strategy to improve the photocatalytic performance of MOFs based photocatalysts for organic compounds oxidation.

4. Boosting charge separation via single cobalt atom implantation in MOFs for efficient visible-light driven CO<sub>2</sub> reduction

In this part, a porphyrinic MOF, named as MOF-525, was constructed for photocatalytic CO<sub>2</sub> reduction under visible light. I realized the atomically disperse of active sites into extended MOF-525, and thus gave rise to the photocatalysts that performed high activity to CO<sub>2</sub> reduction. The unique structural characters of developed catalyst possessed a large surface area and strong CO<sub>2</sub> adsorption ability. As demonstrated by the energy transfer efficiency investigation, the photogenerated electrons can be effectively transferred to the active sites, which not only facilitates charge separation in the MOF-525 but also supplies energetic electrons to gas molecules adsorbed on the MOF-525. As a result, the MOF-525 comprising atomically dispersed catalytic centers exhibits significantly enhanced photocatalytic conversion of CO<sub>2</sub>, which is equivalent to a 3.1-fold improvement in CO evolution rate (200.6 μmol g<sup>-1</sup>h<sup>-1</sup>) and 5.9-fold enhancement in CH<sub>4</sub> generation rate (36.7 μmol g<sup>-1</sup>h<sup>-1</sup>) compared with bare MOF-525.

### 6.2 Future prospects

The search for suitable materials as photocatalysts for water splitting, CO<sub>2</sub> reduction and pollutant degradation using solar energy is one of the noble missions of material science. In contrast to the overwhelming attention given to conventional photocatalysts (inorganic metal-containing semiconductors, such as TiO<sub>2</sub>, WO<sub>3</sub>, CdS, *etc.*) over the past several decades, recent efforts in searching for new visible light active photocatalysts have paid attention to MOFs based photocatalysts. MOFs based photocatalysts represent another new and unconventional class of photocatalysts. Their high dispersion of components, tunable adsorption properties, and pore size and topology, along with their intrinsic hybrid nature, all

## Chapter 6

---

point at applications in diverse photocatalytic reactions. However, despite the significant advantages described above, the use of MOFs as photocatalysts still requires significant additional improvements to become fully competitive. The research in this direction is still in an early stage and thereby leaves a much room for further development.

One important challenge is that the catalytic efficiencies of most MOFs based photocatalysts are moderate or even very low, especially in the heterogenous reaction system, and thus much work need to be remarkably improved to satisfy the requirements of practical applications, including the optimization of the combination of MOFs and functional materials, introduction of additional active sites to the framework, regulation of the crystal structures and improvement of energy transfer efficiency between the chromophore and catalytic centers. Secondly, although a number of research groups have performed a lot of work in the developing of MOFs for artificial photosynthesis, no satisfactory understanding of the mechanisms involved in this filed has been arrived at. For example, the question of how multiple-electron reactions take place in MOFs based photocatalysts has long been confusing to researchers studying water oxidation or CO<sub>2</sub> reduction, as well as the real role of surrounding organic environment over the metal cluster to the final catalytic performances. To answer these questions, it is very essential to analysis the surface energies of different surface orientations by conducting molecular dynamics simulation for revealing chemical reaction pathways. Therefore, rapid development of the computational methods is required to advance theoretical studies and achieve a thorough understanding of photocatalysis processes in MOFs materials, which may result in the development of fundamental paradigm for the MOFs based photocatalyst designing.

The last but not the least limitation of this kind of materials is their poor stability, in particular in the presence of strong alkaline and acid, and intense radiation. This limitation can be overcome by design of new MOFs materials with highly stable structure. Surface modification is another important strategy to improve the stability of MOFs photocatalyst. For example, coating the surface of MOFs with a protective layer to form core-shell structure should be intensively investigated and the improved stability of MOFs photocatalysts can be anticipated. What's more, the screening of MOFs with optimized coordination

## Chapter 6

---

between metal cluster and organic linker is of great necessity, as the stability of MOFs materials is heavily dependent on the coordination between ligands and metal centers.

## Acknowledgement

---

### Acknowledgement

First of all, I would like to extend my sincere gratitude to my supervisor, Prof. Jinhua Ye, for her helpful guidance, valuable suggestions and constant encouragement both in my study and in my life. She has given me patient instructions and profound insight throughout the process of selecting the research topic, discussing the experimental results and writing the thesis during my PhD course. Her inspirational and conscientious teachings will always be of great value to my future academic research. I am deeply grateful of her help in my research and the completion of this thesis.

Secondly, I want to express my heartfelt thanks to my supervisors, Prof. Kiyoharu Tadanaga and Prof. Kazunari Yamaura. Their insightful comments on my thesis, which provides me with many enlightening ideas, have inspired me to a great extent.

I would like to express my sincere gratitude to Dr. Tetsuya Kako, Dr. Naoto Umezawa and Dr. Hideki Abe, for their insightful comments and suggestions about my research. I also owe many thanks to Haruna-san, Aya-san and Atsuko-san for their generous help about my daily life and research in Japan.

Also, I want to thank all the group members in our lab. I would like to express my thanks to Dr. Wang Tao, Dr. Li Peng, Dr. Chang Kun, Dr. Liu Huimin, Dr. Liu Lequan, Dr. Kang Qing, Dr. Zhang Huabin, Dr. Zhao Guixia, Dr. Meng Xianguang, Mr. Liu Guigao, Ms. Yu Qing, Mr. Li Mu, Mr. Hai Xiao, Mr. Lu Hao, Ms. Pang Hong, Ms. Yang Liuqing, Ms. Wang Hongmei and Mr. Ichihara Fumihiko. Without their kind help, I would not undertake the research smoothly or enjoy a happy life in NIMS.

Finally, I would like to extend my deep gratefulness to my parents and friends who support me without a word of complaint and shared with me my worries, frustrations, and happiness.